Current Oscillations Arising from Nonlinear Chemical Dynamics in Solid Oxide Fuel Cells

by

Jonathan David Sands

A thesis submitted to the University of Birmingham
for the degree of Doctor of Philosophy

Doctoral Training Centre for Hydrogen,
Fuel Cells and their Applications
Schools of Mathematics &
Chemical Engineering
University of Birmingham
December 2014

University of Birmingham
Schools of Mathematics and Chemical Engineering

PhD in Hydrogen, Fuel Cells, and their Applications as part
of the EPSRC funded Doctoral Training Centre

Current Oscillations Arising from Nonlinear Chemical Dynamics in Solid Oxide Fuel Cells

Supervisors

Prof. David Needham .....

Dr. Jamal Uddin .....

Candidate

Jonathan David Sands .....

Schools of Mathematics & Chemical Engineering,
University of Birmingham,
Edgbaston, Birmingham,
B15 2TT, United Kingdom

Abstract

Fuel cells are becoming increasingly important in the conversion of our society to clean, and renewable energy sources. However, there are some technical, as well as commercial barriers, which remain to be overcome before the fuel cell industry may be counted a success. One such problem is that of nonlinear current fluctuations, which have been observed under quite general conditions, in solid oxide fuel cells.

This thesis attempts to elucidate the mechanisms driving this undesirable behaviour, by developing a rational mathematical model based on fundamental chemical kinetics, and mass transfer effects, which take place within the porous anode of the fuel cell. A system of nonlinear, coupled ordinary differential equations is derived to describe the reaction and transfer processes associated with this fundamental model. This system is then rationally reduced to a planar dynamical system and the cases of weakly and fully humidified fuel streams are considered.

Self-sustained, temporal oscillations are shown to arise through Hopf bifurcations in each case, and key parameter regimes leading to oscillatory behaviour are identified. The structural dynamics of the fuel cell change significantly as the water content of the fuel stream increases.

Experiments have been conducted on commercial fuel cells, the results of which are presented in Chapter 5. Model predictions are confirmed for the weakly humidified case, with exceptional agreement between the unfolding plane diagrams in the model and the experimental conditions which were found to

induce current oscillations. Conclusions are then drawn, and further work is discussed in Chapter 6.

Chapters 3, 4, and 5 in this thesis have appeared as papers in Proceedings of the Royal Society A [1], Journal of Engineering Mathematics [2], and Journal of Power Sources [3].

To my family for all their love and support,
and Chantelle for giving me faith in myself.

Acknowledgment

I would like to express deep and sincere gratitude to my supervisors, Professor David Needham and Doctor Jamal Uddin, for their support of my studies throughout my doctorate. Over the years, their guidance has been invaluable in both my personal development, and in the writing of this thesis.

I would also like to thank both Professor Kevin Kendall and Professor Robert Steinberger-Wilckens for facilitating this project at the hydrogen and fuel cell research centre, as well as the EPSRC for their generous funding.

Contents

List of Figures

Chapter 1

Introduction

Fuel cells are powerful energy conversion devices which directly extract both electrical power and useful heat from various chemical species. They are a relatively old technology, predating the four-stroke internal combustion engine (ICE) which is prevalent in today's modern vehicles. Despite their age, fuel cell technologies have not yet been adopted into the mainstream, due to a number of technical and commercial barriers. Even from their inception, it has been noted (see for example [4]) that the performance of a fuel cell can vary widely depending on a number of factors. Such factors include, but are not limited to, the type of fuel used, the operating conditions, the cell's previous usage, and the manufacturing processes used to fabricate both the cell and its materials.

One undesirable characteristic of fuel cells is that of oscillatory phenomena. Most applications require that the fuel cell give a steady power output during its working life. However, fuel cells have been known to exhibit periodic oscillations of both current and voltage. It is the aim of this thesis to help elucidate the fundamental mechanisms behind these oscillations, and present a mathematical

model which can be used as a tool for avoiding this unwanted behaviour. A series of experiments have been conducted in order to verify certain predictions of the model, the results of which, are presented in Chapter 5.

The purpose of this opening chapter is to give the reader a basic understanding of what fuel cells are, outline the most common types, and discuss their operating principles and applications. For a historical overview of solid oxide fuel cell technology, the reader is referred to the opening chapters of some of the standard texts on the subject (see for example [5, 6]). For a more comprehensive treatise of the general history of fuel cells, Blomen & Mugerwa [4] provide an accurate chronological sequence of key discoveries in the fuel cell industry, whilst Behling [7] describes in great detail, the geopolitical events associated with the development of each individual type of fuel cell, as well as some of their common applications.

1.1 Types of Fuel Cell

Fuel cells may be categorised in a number of different ways. The three most common classifications are, their operating temperature, the type of electrolyte, and the type of fuel. The type of electrolyte and fuel used influence the fuel cell's mode of operation, whilst the operating temperature tends to dictate the area of application. For example, it is less appropriate to use a high temperature fuel cell in applications where power is required immediately from startup. This is due to the length of time it takes to heat up the cell, or series of cells (stack). More recently, however, high temperature microtubular fuel cells have been implemented, which greatly reduce startup time due to an increased surface area

to volume ratio [5, 8].

The most commonly used fuel cells are now briefly discussed in order to give the reader an understanding of the various types, and the nature of some of their applications.

1.1.1 High Temperature Fuel Cells

Solid Oxide Fuel Cells (SOFC)

SOFCs are one of the most widely used fuel cells. They typically operate between $600 - 1000^{o}C$, placing them in the high temperature range. Their name derives from the fact that they utilise a solid oxide ion-conducting electrolyte, which conducts an O^{2-} ion from the cathode to the anode. This differs significantly from the traditional fuel cell designs, which incorporated a liquid electrolyte. The solid electrolyte used in an SOFC is made from a ceramic material, usually yttria-stabilised zirconia (YSZ), and only starts to become an effective conductor of O^{2-} ions at high temperatures. Generally, the hotter the electrolyte, the greater ease with which it conducts ions. However, raising the operating temperature of an SOFC has its drawbacks in terms of thermal stresses, mismatches in thermal expansion coefficients, and the greater parasitic start-up energy that is required.

The anode is usually made from a composite of nickel and yttria-stabilised zirconia (Ni/YSZ), whilst the cathode is commonly made from various compositions of lanthanum strontium manganate (LSM), or lanthanum strontium cobaltite ferrite (LSCF). Fuel cell materials is still a highly active research field, and new materials are frequently engineered [9–13]. However, the materials mentioned here have gained favour with the SOFC community, due to their

favourable physical and chemical properties. Each of the fuel cell's three layers (anode, electrolyte and cathode) must not only perform well in their prescribed task, but also be compatible with each other in terms of thermal expansion coefficients. Materials which do not match well may cause cracks to propagate, rendering the fuel cell inefficient, if not entirely unable to operate.

There is a lot of research being directed into lowering the operating temperature of SOFCs in order to negate some of the disadvantages of being a high temperature fuel cell (see for example [14–16]). One of the advantages, however, of operating at such a high temperature is that it reduces manufacturing costs. This may seem counterintuitive initially, as one would think that robust materials are required for operating at such high temperatures. Whilst this is true, by operating at high temperatures, the need for an expensive catalyst is significantly reduced, meaning that cheaper catalysts may be selected. In low temperature fuel cells, platinum, which is an expensive and rare metal, is frequently required to catalyse the electrochemical reaction. In an SOFC, however, nickel may be used as the catalyst, which is a relatively common and cheap material that is often doped with YSZ for compatibility with the electrolyte. In addition to this, the high temperature allows for greater fuel flexibility and greater tolerance to impurities compared with low temperature fuel cells.

One of the major barriers for low temperature fuel cells in the market place is that high purity hydrogen is not as widely available as other fuels, which are usually hydrocarbon based. SOFCs have been demonstrated to operate extremely well on methane or coal syngas [17–20], as well as longer chain hydrocarbon fuels such as propane and butane [21–23]. This is usually achieved by an internal or external reforming process, but is sometimes possible by direct oxidation de-

pending on the design of the fuel cell. A disadvantage of using hydrocarbons as a fuel is that carbon deposition can occur (coking). This problem is often addressed by adjusting the gas composition supplied to the anode of the fuel cell [18, 24].

SOFCs are well suited for stationary power plants since they can operate continuously and utilise widley available fuels. They may also be integrated with other power generating technologies, such as in combined heat and power (CHP) units, that are often used in domestic applications [25–27]. Their suitability for this application derives from high grade waste heat which is produced through the standard operation of an SOFC. The high grade waste heat can be utilised in gas turbines, for instance [28, 29], making them ideal for combined systems. These properties also make SOFCs an excellent choice for auxiliary power units (APU) [30].

The main technical challenges that remain to be overcome include, the reduction of start-up time and parasitic energy losses, utilising readily available hydrocarbon fuels without performance degradation, systems integration, and finding suitable inexpensive materials for more stable and efficient operation.

Molten Carbonate Fuel Cells (MCFC)

MCFCs are functionally quite similar to SOFCs and share many of the same properties. For example they typically operate around $650^{o}C$, which means that they are able to function on hydrocarbon fuels, as well as utilise the high grade waste heat which is produced from standard operation. They often use the same catalyst (nickel) as an SOFC for the electrochemical reaction.

The fundamental difference between an MCFC and an SOFC is the electrolyte. Instead of conducting oxide ions (O^{2-}), the MCFC electrolyte permits carbonate ions (CO_3^{2-}) to pass from the cathode to the anode. Additionally, whilst the SOFC electrolyte is made from a solid ceramic, the electrolyte of an MCFC achieves a molten state at its operating temperature. This has a number of consequences, particularly since the electrolyte is corrosive. Long term durability remains a challenge for MCFCs, as the cathode has a tendency to dissolve due to the corrosive nature of the electrolyte [31]. Also, since the electrolyte is in the liquid phase, MCFCs are prone to leaks which cause degradation in performance.

Whilst MCFCs are endowed with many of the same benefits as SOFCs, the problems associated with them mean that many turn to SOFCs for applications where both may be suitable. However it should be noted that MCFCs still have a higher tolerance to impurities such as hydrogen sulfide (H_2S), which even in minute amounts can cause severe degradation in SOFCs [7, 32]. Thus it may be more suitable in applications where contamination of fuel sources is likely.

1.1.2 Low-Intermediate Temperature Fuel Cells

Alkaline Fuel Cells (AFC)

Another fuel cell which derives its name from the type of electrolyte used is the AFC. It uses the liquid alkali, potassium hydroxide (KOH), as the electrolyte in order to facilitate ionic transfer between electrodes. The ions transferred in this case are hydroxyl ions (OH^{-1}), and they migrate from the cathode (where they are produced), to the anode where they are consumed in an electrochemical reaction which releases electrons.

The operating temperature for an AFC is typically under 220^oC and can even continue to function below room temperature. This gives them a major advantage when it comes to start-up time, since preheating may not necessarily be required for power generation. However this does mean that high grade waste heat isn't readily available for applications such as CHP.

AFCs utilise cheap and easily manufactured electrodes made from carbon and plastic. This has been part of their appeal, since one of the major barriers for fuel cells has been the cost. AFCs even made their way into the National Aeronautics and Space Administration (NASA) through the Gemini project in the 1960's. AFCs were used to power onboard electronics and produce drinking water for the astronauts [33]. However, in modern fuel cells, electrodes are usually manufactured using nanoparticles, some of which may become dislodged in the exit stream. This would have serious detrimental effects on the human body [34], and long term, comprehensive research, on the potential effects on the human body of ingesting water from fuel cells, should be carried out before advocating drinking of such water.

A significant disadvantage of this particular type of fuel cell is their sensitivity to carbon dioxide. This means that hydrocarbons cannot be used as a fuel, and high purity hydrogen is required. Even trace amounts of CO_2 cause the formation of carbonate crystals which block chemical diffusion, as well as ionic pathways. Additionally, the corrosive nature of the electrolyte causes life span issues due to the corrosion of materials.

Phosphoric Acid Fuel Cells (PAFC)

The PAFC was the first type of fuel cell to be sold commercially and has been widely demonstrated in long term tests [7]. They operate at approximately 200^oC and therefore do not take as long to start up as either SOFCs or MCFCs. Similarly to the AFC, the tradeoff for this lower operating temperature is not being able to utilise high grade waste heat.

Unlike the fuel cells mentioned up to this point, the electrochemical mechanism which generates power in a PAFC involves ionic migration from anode to cathode. Hydrogen is split into its subatomic constituents, a proton and an electron, at the anode. The proton (H^+) then passes through the electrolyte which is composed of phosphoric acid, whilst the electron is forced to go around an external circuit. They meet at the cathode and combine with oxygen in order to form water as steam.

Fundamental to its commercial adoption, is the fact that unlike the AFC, it is tolerant to CO_2. This gives it a greater fuel flexibility than other types, including AFCs, at the cost of lower efficiency and decreased power output. Platinum is also required to compose the electrodes, which increases the cost of production.

Polymer Electrolyte Membrane Fuel Cells (PEMFC)

Also known as proton exchange membrane fuel cells, PEMFCs have become the first choice of fuel cell for use in the automotive industry. Both acronymically equivalent names refer once again to the nature of the electrolyte, which is made from a polymer which conducts protons from the anode to the cathode. This mechanism is similar to the PAFC, however, in a PEMFC the electrolyte is solid.

The electrolyte (usually nafion) is only capable of efficiently conducting protons at the right humidity. Thus, careful water management must be implemented in order to maintain the desired performance. Local wet or dry spots may appear due to an uneven distribution of water, particularly when in multiple phases. These can cause instabilities as well as other unwanted performance characteristics [35–37]. For instance, too much water in the membrane (flooding) blocks ionic migration pathways, whereas too little water (dehydration), and the ionic conductivity is reduced.

PEMFCs typically operate between $5 - 100^oC$ meaning that they have a fast start-up time. They also give a relatively high power density compared with other types of fuel cell, which makes the stacks that are produced for a required output, light and compact. These attributes are the main reasons why PEMFCs have attracted so much attention from the automotive industry. Electric vehicles are being designed which utilise PEMFCs in conjunction with batteries, internal combustion engines, or even as the sole power source for the vehicle (see for example, [38, 39]).

A consequence of operating the fuel cell close to 100^oC is that the water in the membrane can often be in two phases simultaneously, namely, liquid and gas. The effect on the fuel cell's performance is not well understood and makes modelling far more difficult. As a consequence, research is being done into membranes which can stably function at up to 120^oC in order to ensure that the water is all in the gas phase [40].

The main drawbacks of the PEMFC are the requirements for both high purity hydrogen as the fuel, as well as platinum loading at the electrodes. The platinum is required to catalyse the electrochemical reaction for the operating condi-

tions of the cell, and since it is a rare and expensive material, platinum loading must be reduced in order to make PEMFCs a viable competitor in the commercial automotive industry. Also, since the hydrogen fuelling infrastructure is not widespread, and high purity hydrogen is difficult to obtain, a "chicken-egg" scenario is created where vehicle manufacturers do not want to make PEMFC power cars when nobody will buy them due to lack of infrastructure, and infrastructure is being inadequately funded because there aren't enough end users. In recent years however, the hydrogen fuelling infrastructure has been slowly gathering support, and there are an ever increasing number of stations emerging globally.

1.1.3 Specially Designed Fuel Cells

Single Chamber Solid Oxide Fuel Cells (SC-SOFC)

This type of fuel cell is a special type of SOFC. Instead of having separate channels for the fuel and the oxidant, there is only a single gas chamber which exposes both the anode and the cathode to the same gas mixture. This gas mixture is a combination of any of the usual fuels and oxidants used in standard SOFCs, with the idea being that each electrode acts as a specific catalyst to the half-cell reaction it is designed for. So at the anode, ideally hydrogen is oxidised and no oxygen reacts, whilst at the cathode the ideal situation is where oxygen is reduced but no hydrogen reacts.

The advantage of this type of fuel cell lies in its simplicity. Since one of the major barriers to the fuel cell market is cost, these cells may help to overcome this barrier, since the number of parts required to fabricate the cell are greatly reduced. Additionally fuel crossover is not a problem and thus expensive sealants

are not required.

Unfortunately, the challenge of materials is a major problem [41], with more specific electrode materials still being required. Problems may manifest in unwanted nonlinear behaviour, as reported by Kellogg et al. [42], who found that cyclic oxidation/reduction of the nickel-based anode was causing voltage oscillations. Although autonomous oscillations are not unique to SC-SOFCs, the mechanism in this case also causes expansion and contraction of the anode which may cause cracks to propagate and destroy the cell [43]. Furthermore, the power output from a SC-SOFC is often less than its dual chamber counterpart as hydrogen and oxygen are known to react together, in the absence of a catalyst, at temperatures exceeding $550^{o}C$ [44]. This reduces the efficiency of the fuel cell, and leads to the build up oxygen ions in the electrolyte which cause an increase in overpotential [42]. The term overpotential refers to the potential difference between the thermodynamically determined reduction potential for a half cell reaction and the actual potential at which the the reaction is observed experimentally. It can be thought of as the thermodynamic losses of the system during practical operation, such as internal resistance and mass transfer limitations.

Direct Methanol Fuel Cells (DMFC)

DMFCs are a special type of PEMFC. They contain a solid polymer electrolyte which permits the passage of protons, however, the fuel used is methanol, which flows directly over the anode with no prereforming. This requires that water be available at the anode in order oxidise the methanol, producing 6 protons, 6 electrons, and CO_2. Similarly to the PEMFC, the protons migrate across the

polymer membrane electrolyte, whilst the electrons go around an external circuit. They meet at the cathode and combine with oxygen to form water.

The ability to utilise methanol as a fuel gives the DMFC a distinct advantage over the regular PEMFC. Methanol is more easily obtained and stored, meaning that novel commercial products may be implemented without the need for a large overhaul of infrastructure.

Laminar Flow-based Fuel Cells (LFFC)

A laminar flow-based fuel cell (or microfluidic fuel cell) adopts a unique design which allows the fuel and oxidant streams to flow adjacent to one another, thereby simplifying the design. There is no electrolyte separating the two fluid streams. Instead, the flowrates of each stream are kept at very low Reynold's number, and the properties of a Stokes' flow regime are utilised to keep the fuel and oxidant separate.

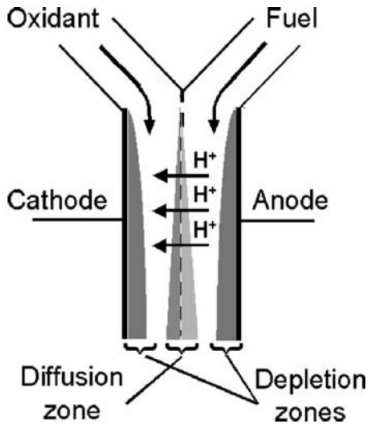

Figure 1.1: Laminar-flow based fuel cell.

A liquid electrolyte is used for the transportation of ions and is mixed with

both the fuel and oxidant streams. This is analogous to impregnating the porous anode of an SOFC with YSZ, which facilitates the transfer of oxygen ions. In LFFCs, it is the protons which migrate across the electrolyte (Figure 1.1 reproduced from [45]).

The fuel and oxidant streams are introduced through a Y-shaped channel and flow adjacent to each other. Since the viscous boundary layer spans the channel width, a fluid-fluid interface ideally keeps the streams from mixing. However, in actual operation there is some interdiffusion, causing a diffusion region to form in the middle of the channel. Further down the fuel channel the diffusion layer in the middle gets wider, thus increasing the risk of fuel crossover. This behaviour is detrimental to the fuel cell as oxygen crossover leads to oxidation of the anode. This in turn diminishes performance.

In addition to the the diffusion layer, concentration boundary layers (depletion zones) form on the outer walls of the channel. These regions are depleted in reactive species due to the electrochemical reactions which take place at the walls. A model which accounts for these effects was presented in [46], whilst alternative designs which negate some of the effects of the diffusion and depletion zones are given in [47]. The power output of these cells is comparable with, and sometimes better in performance than traditional PEMFCs [45].

1.2 Operating Principle of an SOFC

The primary function of a fuel cell is to generate electricity. It achieves this by means of an electrochemical reaction which liberates electrons from the chemical reactants, and passes them through an external circuit, thus generating electrical

current. In this sense it is similar to a battery, however, the fundamental difference lies in the fact that a battery stores its chemical reactants internally. This means that when the reactants are used up, the battery must either be discarded, or recharged from an external power source. Conversely, fuel cells have their reactants supplied from an external source, which ensures that a fresh supply of fuel is always available to the electrodes. Additionally, the electrodes of a battery actively participate in the electrochemical reaction, hence they are consumed during the power generation process. By contrast, the electrodes of a fuel cell merely act as catalysts for the half-cell reactions. This endows them with the extremely useful ability to generate power on a continuous basis. However, limitations lie in the fact that certain mechanisms (related to fuel composition, operating conditions, and manufacturing processes) lead to eventual degradation of the electrodes (particularly the anode).

The main reaction in an SOFC is the electrochemical oxidation of hydrogen to form water. This is achived through the two half-cell reactions given by (1.1) and (1.2).

$$\mathrm{H_2} + \mathrm{O^{2-}} - 2e^- \rightarrow \mathrm{H_2O} \quad \text{anode} \tag{1.1}$$

$$\frac{1}{2}\mathrm{O_2} + 2e^- \rightarrow \mathrm{O^{2-}} \quad \text{cathode} \tag{1.2}$$

Hydrogen is reduced at the anode, forming protons and electrons. The electrons (represented by e^-) are forced around an external circuit whilst oxygen ions migrate across the electrolyte. The oxygen ions bond with the protons, forming

water as steam. The full reaction given by,

$$2H_2 + O_2 \rightarrow 2H_2O, \tag{1.3}$$

is exothermic. A typical SOFC is also capable of electrochemically oxidising carbon monoxide. The full reaction is given by,

$$2CO + O_2 \rightarrow 2CO_2. \tag{1.4}$$

Since pure hydrogen can be difficult to obtain, methane, syngas (which is mostly a mixture of hydrogen and carbon monoxide), natural gas (a mixture of mostly hydrocarbons but primarily methane), and other longer chain hydrocarbons are often used as the primary fuel. The hydrocarbons are reformed either externally before being passed into the cell, or passed directly to the SOFC anode where nickel also catalyses the steam reforming process. Both systems have certain advantages. However, the internal reforming design is generally favoured due to its simplicity. Having an external reformer introduces a higher cost, although may bring advantages in that even greater fuel flexibility can be achieved [48]. On the other hand, one of the major barriers to fuel cell commercialisation is cost, thus making the internal reforming SOFC more applicable for the commercial market since syngas/natural gas (which is easily reformed inside the fuel cell) is adequately available [49].

The operation of an internal reforming SOFC primarily fuelled with methane is shown in Figure 1.2. There are 4 reactions occurring within the anode, and a single reaction at the cathode. **R1** is the steam reforming of methane (SR)

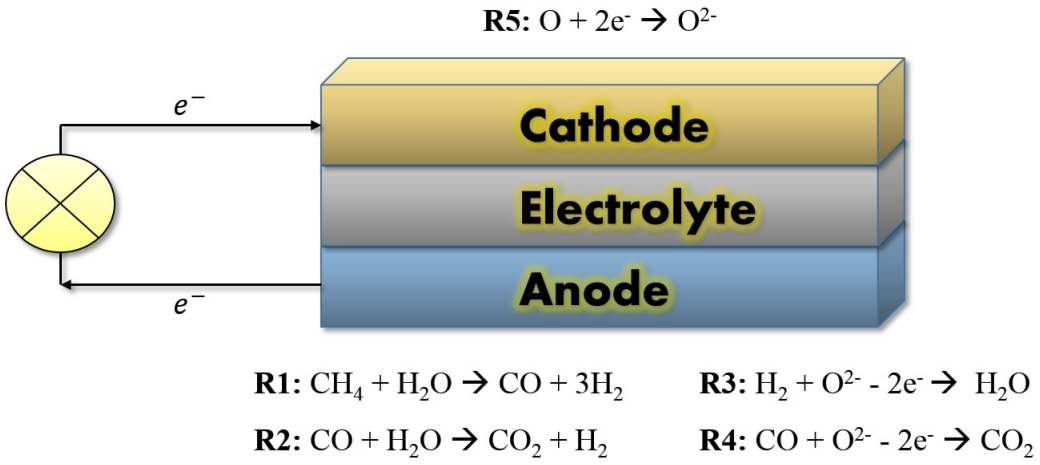

Figure 1.2: Operating principle of an internal reforming SOFC.

which is promoted by nickel in the anode. This reaction generally occurs at over 800^oC which coincides with the standard operating temperature of an SOFC [5, 10, 50]. **R2** is the water-gas shift reaction (WGS) which is also promoted by the nickel catalyst and is known to be extremely fast relative to the other reactions [51–54]. Reactions **R3** and **R4** are the anode-side half-cell reactions corresponding with the electrochemical oxidation of hydrogen and carbon monoxide respectively. These are paralleled by **R5**, which is the cathode-side half-cell reaction corresponding with the two electrochemical reactions **R3** and **R4**.

An important property of the fuel cell is that the electrochemical oxidation of hydrogen, which is the main current producing reaction, is exothermic. This has both advantages and disadvantages depending on the type of cell and its application. Each type of fuel cell can only operate within a certain temperature range, usually depending on the type of electrolyte used. This means that the cell temperature must be managed in order to maintain consistent operation. The thermal management of a stack is often more complex than an individual

fuel cell, and modelling plays a crucial role since it is difficult to measure the temperature distribution of a stack directly [55].

During thermal cycles, as a cell heats up and cools down, its materials expand and contract accordingly. Thus it is imperative that the materials chosen to make the cell have closely matched thermal expansion coefficients, in order to avoid cracking and delamination. The planar design is much more prone to cracking during thermal expansions than the tubular design [56–58], meaning that tubular SOFCs can be utilised for quick startup applications [5, 59, 60].

In addition to the problem of thermal cycling, temperature gradients along the cell can lead to stress distributions that eventually cause the cell to crack [61, 62]. A leading cause of intolerable temperature gradients in SOFCs is due to the fact that the SR reaction is endothermic. This introduces a cool region at the anode inlet, where much of the reforming takes place [63]. If the temperature gradient becomes too steep, a crack will occur. Even without steam reforming, Achenbach [64] showed that various temperature distributions across an SOFC stack can be induced by different flow configurations. This makes thermal management of a stack a challenge even when external reforming is used.

An individual fuel cell can only produce a certain amount of electrical power which is determined by the free enthalpy of reaction between the fuel and its oxidant. In addition to this, it is subject to a number of losses which further reduce the cell voltage. In order to generate enough power for practical applcations, fuel cells may be connected in series, much like batteries, in order to produce the required voltage. This is called stacking. Fuel cell stacks have a range of sizes and designs depending on the application, and are often associated with their own unique phenomena as compared with single cells. This creates a requirement for

careful management strategies, especially when integrating the stacks with other technologies such as in hybrid vehicles.

To summarise, SOFCs are an efficient means of obtaining electrical energy and useful heat from renewable sources. However, more common hydrocarbon-based fuels may also be utilised using methods such as internal reforming. Their performance at low fuel compositions is superior to that of ICEs [18], however in order for them to compete realistically in the commercial market their cost must be greatly reduced. Additionally, some of the undesirable performance characteristics, such as anode poisoning and oscillatory phenomena, must be addressed. The latter of these problems shall be the primary focus of this thesis.

1.3 Literature Review

A well known phenomenon in the fuel cell community is that of autonomous current, or voltage oscillations. Many of the standard texts make no mention of them (for example [5, 6, 65]), and there are only a small number of reports in the literature. This is particularly true for SOFCs. Bavarian et al. [66] point out in their review of the mathematical modelling of fuel cells, that it is crucial that we understand the oscillatory phenomena in fuel cells, and are able to identify regions where oscillatory or chaotic behaviour occur. They state that several publications report that steady state instability is caused by a negative differential resistance, where the differential resistance is defined as $R_{diff} = dU/dI$, with U being voltage and I being the current. However Wolf et al. [67] found through a bifurcation analysis that potential oscillations, during the oxidation of hydrogen on a platinum electrode in the presence of various metal ions, occurred on the branch with a positive differential resistance. Certain other publications offer explanations for the observed oscillatory outputs, related to, the oxygen vacancy content of the anode [68], the temperature dependence of the electrolyte conductivity [69], concentration polarization at the cathode [70], or surface species adsorption/desorption cycles at the anode[71]. Moreover, the explanations for the occurrence of oscillatory phenomena vary for the different types of fuel cell and the operating conditions imposed on them.

It is the objective of the present work to investigate the current oscillations that occur in an SOFC utilising methane as the primary fuel. A review of the literature surrounding fuel cell oscillatory phenomena is now presented.

Chemical and electrochemical systems have been known to exhibit autonomous periodic oscillations, quasiperiodicity, as well as chaotic behaviour [72–75]. Hudson & Tsotis [75] present a review of important results in the field of electrochemical oscillations between the 1970's and the early 1990's. Many electrochemical systems exhibit autonomous oscillations as a result of periodic changes to the surface of the working electrode. However they note that in some cases, the observed oscillations are of a much shorter time scale than the changing of the electrode surface, or that oscillations occur with only minor surface changes, indicating a decoupling of the surface changes from the observed oscillatory effect. For example, Wolf et al. [67, 76] investigated oscillations during hydrogen oxidation at a platinum electrode in the presence of metal ions, and modelled the process in terms of surface coverage. Whilst it is well known (see [75]) that cyclic surface coverage of electrodes can occur in electrochemical systems with extraneous species, which in turn result in electrical oscillations, in [76] they remark that their model is unable to account for the transition between large, slower oscillations, to small, faster oscillations.

Hudson & Tsotis [75] also indicate that thermokinetic instabilities may lead to observed oscillatory phenomena, caused by large temperature gradients between the surface and the bulk solution as a result of the heat released by the electrochemical reactions at the electrode surface. Temperature effects have also been theoretically demonstrated to contribute towards periodic oscillations by Scott [74], for multiple exothermic reactions in a continuously stirred tank reactor.

One study by Wojtowicz et al. [77] on the oscillatory kinetics in fuel oxidation, found that it was the coupling of diffusion and electrochemical oxidation effects, that was the driving mechanism for potentiostatic current oscillations during the

oxidation of ethylene on a spinning platinum electrode. They noted that oscillations ceased for high enough rotation speeds, indicating that diffusion to the reaction site played a critical role in the current instabilities. Several other studies also suggest mass transfer effects play a crucial role in oscillatory phenomena for electrochemical systems [78–83]. As most fuel cells now use gas diffusion electrodes (GDE) in order to supply the reactant gases, it is clear from the results of [77] that a coupled reaction-diffusion system must be accounted for when examining current instabilities in the porous anode of an SOFC.

As the operating principles of an SOFC are closely related to that of a PEMFC, to begin with, a review of autonmous oscillations in PEMFC systems, is presented. As will be seen, many of the mechanisms for the oscillatory behaviour presented in PEMFCs have analogues in SOFCs.

1.3.1 Oscillations in PEMFCs

There are significantly more papers published on PEMFC oscillations than any other type of fuel cell. Here, a selection of the various results from the literature are presented, in order to give an overview of the conditions under which oscillations are observed, and the corresponding mechanisms.

Katsaounis et al. [37] investigated the role of potential-dependent electrolyte resistance in steady state multiplicities and oscillatory phenomenon in PEMFCs. They note that steady state multiplicities (which imply hysteretic behaviour) occur frequently in PEMFCs, and that for certain fuel compositions, self-sustained oscillations of either current or voltage are observed, depending on whether the fuel cell is operated in potentiostatic or galvanostatic mode. Experimentally ob-

served steady state multiplicities are shown in Figure 1.3, which is taken from the results of [37]. They assert that the steady state multiplicities and oscillatory phenomena are intimately linked, and both depend upon the potential-dependent electrolyte resistance. The steady state multiplicities and oscillations which they

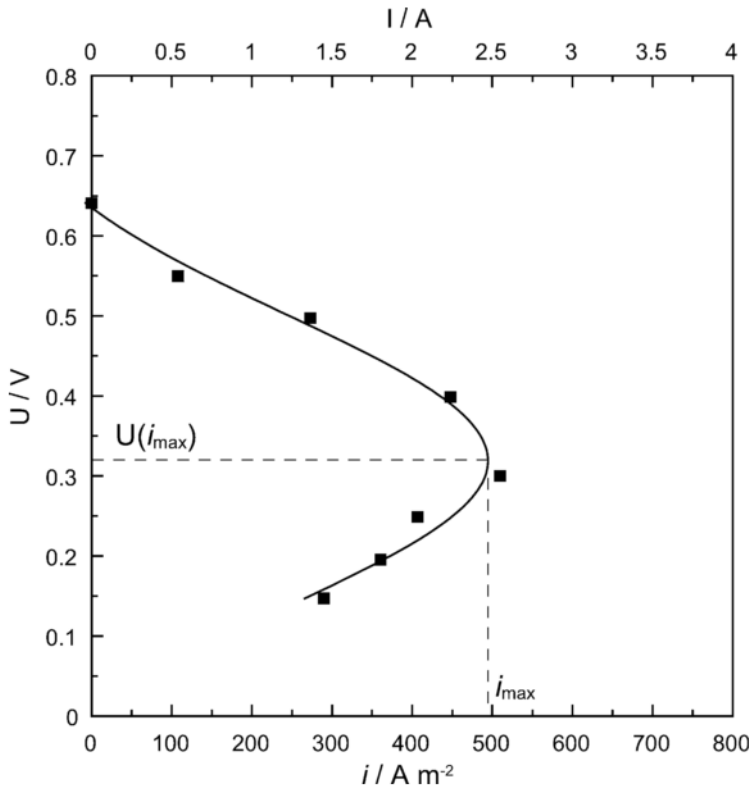

Figure 1.3: Steady state multiplicity in a PEMFC. The horizontal axis is the current density measured in amps per square metre. The vertical axis is the cell potential measured in volts.

observe occur with a fully hydrated membrane, thus, they attribute non-uniform electrolyte resistance to a nonlinear relationship with cell potential. They develop a model in [84] which is capable of semiquantitatively reproducing the (I, U) curve shown in Figure 1.3. However no mention of oscillations is given in

relation to this model.

Contrary to [37], the steady state multiplicities observed experimentally are explained in [36] as a result of the liquid water saturation of the cell. They perform a bifurcation analysis on the governing system of ordinary differential equations and find two stable equilibrium points when operated potentiostatically. This is consistent with experimentally observed steady state multiplicity, and they are able to qualitatively reproduce the type of (I, U) curves which were found in [37], despite the fact that the experiments in [37] were performed with a fully hydrated membrane. They give physical explanations for the two steady states, where the low current state is a product of high liquid water saturation which leads to high transport resistance at the cathode, thus increasing the concentration polarisation at the cathode. Conversley, low liquid water saturation leads to a high active catalyst surface area and low transport resistance at the cathode, leading to a high current output. The physical explanation is contrasting to [37], however the fuel cell outputs are the same. Both mechanisms appear plausible and are specific to the test conditions.

Oscillatory dynamics of a PEMFC with a Pt/Ru catalyst and an H2/CO fuel composition were studied in [85]. The dynamic states of the cell potential were observed as functions of current and fuel stream flow rate. They attribute the oscillations to the cyclic poisoning and cleansing of the anode by CO. The mechanism is explained by a build up of CO on the anode until the blocked surface can no longer maintain the set cell current via hydrogen electro-oxidation. The anodic overpotential then increases, which allows the adsorption of an oxygenated species. This oxygenated species proceeds to react with the adsorbed CO, thus cleansing the surface, and the cycle is repeated. They found that regular periodic

oscillations of cell voltage occurred for high flow rates, whilst more chaotic patterns were observed for high current density. Mixed mode periodic oscillations were favoured at intermediate values of both current density and flow rate. They relate the amplitude of the oscillation to the efficiency of the anode cleansing, in that large amplitude oscillations are indicative of an efficient desorption process.

Sustained potential oscillations were observed in a PEMFC with a Pt/Ru catalyst with an H_2/CO fuel mixture [86]. The oscillations did not occur when pure hydrogen was used on either the Pt/Ru, or the pure Pt catalyst. Nor did they observe any oscillations for the H_2/CO mixture on a pure Pt catalyst. Furthermore, they found that with an H_2/CO mixture on a Pt/Ru catalyst, the operating temperature of the cell determined whether the cell would oscillate under the studied test conditions. Under 70^oC the oscillations were commonly observed, however, above 80^oC there were no oscillations. Proper control of temperature, current density, and anode flow rate is required in order to induce the oscillations. The mechanism they describe for the potential oscillation is that of cyclic poisoning and cleansing of the anode by CO. The period of the oscillation decreases with increasing temperature until the point where the oscillations are extinguished and a new steady state is reached.

Zhang et al. [87] further elucidate the mechanism presented in [86] with a bifurcation analysis that uses temperature as the bifurcation parameter. They found that the oscillations arose from a supercritical Hopf bifurcation and that further from the Hopf point, both the period and amplitude of the oscillations increased. The anode exit stream was analysed. However, they failed to find any corresponding oscillations of CO. They point out, that this may be due to the inadequacy of the experimental setup. The reason for potential oscillations on

Pt/Ru as compared with the pure Pt catalyst is also justified by the model. They say that there is a decrease in the water adsorption rate when changing from Pt/Ru to pure Pt, which, according to the model, pushes the operating point of the fuel cell out of the bifurcation region corresponding with an oscillatory output.

The same mechanism of cyclic adsorption/desorption of CO on the surface of the anode is described by other studies [88–90]. Lu et al. [88, 89] detected an oscillation of CO in the anode outlet stream which accompanied the observed potential oscillations on a Pt/Ru catalyst. The period of the oscillations was found to increase for higher concentrations of CO in the fuel stream, however decreased monotonically as the cell current was increased. Additionally it was discovered that after inducing oscillations by introducing CO into the fuel stream, the cell performance could be fully recovered by switching back to pure hydrogen, thus demonstrating that the poisoning process is somewhat reversible. Kadyk et al. [90] agree that self cleaning of the adsorbed CO due to changes in anode overpotential was the primary cause of their observed oscillations. They not only found potential oscillations, but also current oscillations as the cell was operated galvanostatically. Interestingly, they observed oscillations on a pure Pt catalyst which is contrary to the other studies.

Atkins et al. [91] observed current oscillations in a PEMFC which utilised Pt on a carbon support as the catalyst. In this case, hydrogen at the anode side with no CO content, and oxygen at the cathode side were humidified to various degrees. They found that the performance of the cell was best (higher current output and more stable) when the humidification was high. As the humidification was decreased, current oscillations set in and overall cell performance decreased.

This is in contrast with the studies in [86–89] which found that the average power output in the oscillatory regions were higher than the corresponding steady state.

Two possible explanations for the observed oscillations are offered in [91]. The first is that the oscillations are caused by cyclic hydration/dehydration of the membrane-electrode assembly (similar to [36]). At high current, the electroosmotic drag is high, decreasing the migration of water from anode to cathode, which causes the MEA to dehydrate. The dehydration manifests as an increase in ohmic resistance which leads to a low current output. At the low output, the membrane-electrode assembly rehydrates due to reduced electroosmotic drag, leading to a decrease in ohmic resistance and therefore a high current output.

The second mechanism suggested is that of cathodic flooding. At high current there is a greater water production at the cathode which hinders the mass transport of oxygen. This concentration polarisation thus diminishes cell performance leading to a lower current output. At the low output less water is produced at the cathode, allowing for the cathode fuel stream to clear the blocked pathways and oxygen to be transported to the reaction site with greater ease, thus increasing the cell current. Both mechanisms are plausible and the latter is given by [36] to explain the occurrence of steady state multiplicities. However, the authors express their opinion that the first mechanism is more likely since the amplitude of the current oscillations was greatest at high cell potential, where water generation from the electrochemical reaction is lowest, and dehydration is most likely.

Steady state multiplicities and current/voltage oscillations were found by Benziger et al. [92] in a PEMFC with a Pt/C catalyst. They report that up to 3 stable steady states may be achieved for the same set of operating parameters (temperature, resistive load, flow rate, humidification). They characterise

the steady states by the water content of the membrane, where the dry state corresponded with a zero current output (extinguished state), an intermediate current output for low water content, and a high current output for high water content. Oscillations were observed at low load resistance, which were damped out as the resistance was increased until a steady state was reached. The humidity fluctuations correlated with the fluctuations in current, and they rule out the possibility of cathodic flooding since the humidity was always below 75%. After 5000 hours of testing, autonomous oscillations were observed under nearly all operating conditions, indicating a structural change in the cell over time. They believe the potential mechanism for the oscillations is to do with the swelling and contraction of the membrane as a product of humidity, which then causes the contact area with the current collectors to increase and decrease respectively, creating the observed oscillations.

Chia et al. [35] offer another explanation for the occurrence of oscillations via the formation of "wet spots", where, the local current is higher due to greater proton conductivity. The cyclic formation/dispersion of numerous "wet spots" could then lead to an observed oscillation in electrical current.

1.3.2 Oscillations in SOFCs

The reports of autonomous oscillations in the literature are few and varied for SOFCs, although the problem is well known within the SOFC community. The results available in the literature are presented in order to clarify the state of knowledge with regard to the oscillatory phenomena.

Autonomous voltage oscillations were observed by Kellogg et al. [42] in an

SOFC under single chamber conditions, using a standard Ni/YSZ anode. A dual chamber SOFC was used in order to isolate the mixed gas phenomena occurring at the anode in an SC-SOFC. The fuel used was dry hydrogen mixed with oxygen. The mixture was diluted with 95% argon, and the fuel ranged from pure H_2, through the stoichiometric values, to a slightly oxygen rich mixture. Voltage oscillations were observed at various fuel compositions at 600^oC, and the authors note that the mechanism cannot be down to cyclic carbon-based molecule deposition on the surface since pure H_2 was used as the fuel. Instead they attribute the oscillations to periodic oxidation/reduction cycles of Ni/NiO at the anode. They propose that as H_2 is consumed by the Ni during regular operation, there is a local depletion of fuel, and the Ni is exposed to a locally rich oxygen atmosphere. The Ni then oxidises to form NiO, causing the overpotential to increase, simultaneously reducing the effectiveness of the catalytic surface area. Further decreasing the voltage during this stage of the cycle, NiO has a much lower electronic conductivity than Ni, which causes an increase in ohmic resistance. Whilst the NiO is not consuming fuel, the inlet fuel stream replenishes the local atmosphere with H_2, which in turn oxidises as the NiO is reduced. This completes the cycle, with the only difference in the cell being potential cracks in the anode from the expansion and contraction of Ni/NiO. It is noted that oscillations did not occur when the test was reversed, and the dual mixture was exposed to the cathode whilst the anode was fed pure H_2. The period of the oscillations varied between 45-90 seconds.

A study was done by Marina et al. [93] on the effect of various contaminants in the fuel stream of an SOFC. The contaminants, H_2Se and H_2S, were added to synthetic coal gas (H_2, CO, CO_2, H_2O), and tested separately. They found

that for high enough current densities and parts per million of H_2Se, voltage oscillations settled in after a considerable number of hours of degradation from a steady state. No oscillations were found when the cell was operated potentiostatically, or with sulphur in the fuel stream under the same operating conditions. The oscillations favoured higher concentrations of H_2Se, and could also be induced in a fuel stream containing purely hydrogen and steam along with the contaminant. This shows that cyclic behaviour involving carbon is not required for the oscillations under these conditions. The mechanism they propose is a periodic adsorption/desorption of Se on the anode catalyst layer. As the solid layer of adsorbed Se forms, it blocks the reaction sites which increases polarisation resistance and causes an increase in oxygen partial pressure. As a critical concentration is reached NiO forms, simultaneously releasing Se_2 as a gas and lowering the polarisation resistance. The NiO in turn decomposes due to the favoured oxidation of H_2, returning the anode to its initial state. This mechanism is analogous to many of the electrochemical systems reviewed in [75], when extraneous species form part of the bulk solution. The period of these oscillations varied from a few hours, to up to 50 hours.

Converse to the results of Marina et al. [93], voltage oscillations were found by Noponen et al. [24] in an SOFC with pre-reformed natural gas containing sulphur. An online gas analyser was used to record the species, and it was found that minute fluctuations in methane and hydrogen occurred regardless of whether the cell was exhibiting voltages oscillations or not. Thus they believe that the primary cause was to do with inconsistent injection of sulphur into the reformate gas prior to entering the fuel cell, which in turn would adsorb/desorb on the nickel surface, causing variations in overpotential.

Microtubular SOFCs were operated under single chamber conditions, using methane and air as the gas mixture which was supplied to both the anode and the cathode [94]. Various gas mixture ratios were tested and it was found that if the methane content was too high, coking would occur causing a diminished cell performance. However, for high enough oxygen content the nickel on the anode would begin to oxidise. The critical ratio at which NiO would begin to form was at a methane/air ratio of 1/4.76, and after around 24 hours of testing at this ratio, for a constant voltage of 0.5V, the cell began to exhibit current oscillations after initial degradation, which were attributed to the cyclic oxidation/reduction of Ni/NiO. This seems to indicate that some microstructural changes were taking place inside the anode over the first 24 hour period, after which the physical attributes of the anode entered a critical region which facilitated the oscillatory mechanism. The period of these oscillations was on the order of a few hours.

Mangold et al. [95] attempt to show through a bifurcation analysis, that thermokinetic instabilities can occur due to temperature dependant electrolyte conductivity, in a similar manner to the mechanism given for oscillations in PEMFCs for hydration dependant electrolyte conductivity in studies such as [35, 91]. Their findings indicate that "hot spots" may indeed occur in the electrolyte, causing local regions of high ionic conductivity. However, they state that these thermokinetic instabilities in the spatial domain are not enough to cause current oscillations. Thus, the conclusions drawn by Atkins et al. [91] on the mechanism behind oscillations in PEMFCs cannot be carried over to the analogous situation in SOFCs. This is further confirmed in another theoretical study by Mangold et al. on the dynamic instabilities of SOFCs [69]. The paper establishes that multiple steady states can arise due to thermokinetic instabilities in the electrolyte,

however they may not result in an oscillatory current output.

An SC-SOFC was tested by Wang et al. [96] and oscillations of cell voltage, temperature, and resistance were observed with a $CH_4/O_2/N_2$ gas mixture. They believe that the oscillatory behaviour was down to periodic oxidation/reduction cycles of the nickel in the anode, and they cite work from Zhang et al. [97–99] which report oscillations in species concentration and temperature, during the partial oxidation of methane over a nickel catalyst as a consequence of Ni/NiO oxidation/reduction cycles. The results of Wang et al. [96] show that the voltage and resistance oscillations were of roughly the same period, giving evidence to the hypothesis that Ni/NiO oxidation/reduction cycles were the primary cause. The temperature oscillations, on the other hand, did not correlate well with the voltage and resistance oscillations. They state that the this may be a consequence of the inadequacy of the thermocouple placement when measuring the temperature. The period of the oscillations was between 294-358 seconds.

Degradation mechanisms were studied by Matsui et al. [100] by feeding various mixtures of H_2O and H_2 to the Ni/YSZ anode of an SOFC. They found that for low humidity in the fuel stream, gradual degradation in current output would occur, however performance was recoverable. Increasing the humidity, the degradation became more severe and was not recoverable. Under these conditions various types of current oscillation were observed. Oscillations with faster period and smaller amplitude appeared during the slow degradation of the curent output until a critical point was reached. After this critical point, a sudden large drop in current signified the beginning of current oscillations with larger amplitude and much longer period. They believe the mechanism involves microstructural changes to the anode, including the change in the length

of the triple phase boundary, and the formation of NiO. The results suggest, however, that there is perhaps more than one mechanism triggering the oscillatory behaviour. The fast period oscillations reflect an instability which has a fast response time, and as the anode microstructure continues to change according to the degradation mechanism, an instability with a much slower response time takes over. Unfortunately the period and frequency of the oscillations were not made available.

Potential oscillations were also observed by Yoshizumi et al. [71] in an SOFC with a Ni/ScSZ anode in the presence of sulphur. They observed no oscillations without sulphur in the fuel stream, but with the addition of sulphur the voltage would exhibit oscillatory behaviour even under open circuit conditions (0% fuel utilisation). They believe the oscillations to be a combination of both surface adsorption of sulphur species, combined with the oxidation and reduction of Ni/NiO in the anode since at higher fuel utilisations, they noticed the oxide formation in a post analysis of the cell. However, there was no oxide formation under open circuit conditions when the voltage was oscillating with sulphur in the fuel stream, suggesting that perhaps the role of the Ni/NiO redox cycles were not crucial to the onset of periodic oscillatory phenomena for the particular test conditions. Furthermore, surface coverage of CO was not responsible for the oscillations as the cell exhibited oscillations when there were no hydrocarbons in the fuel stream. They believe that as sulphur species forms on the anode surface, the anodic overpotential increases which accelerates the oxidation of Ni particles. As the potential drops further, the sulphur species has a tendency to oxidise again, freeing up reaction sites and causing a recovery in cell voltage. They note that at high current density the oxidation of Ni particles is accelerated, causing

irreversible damage to the cell, meaning that the cell could not recover its initial voltage. They give no indication as to the period or frequency of the oscillations, however they generally set in after a long initial period, perhaps indicating the slow change of the surface structure until it reaches a critical oscillatory region.

Huang et al. [68] found current oscillations in an SOFC using LSCF-GDC, or Ni added LSCF-GDC for the anode, using methane as the primary fuel. They found that the presence of Ni actually reduced the likelihood of oscillations, and when oscillations in current were detected, the amplitudes were much smaller. Following an analogous hypothesis to [42, 94, 96], they attribute the current oscillations to periodic reduction/oxidation cycles of the anode material. The mechanism given is that methane dissociates, producing a surface C species. This is oxidised either by oxygen ions transported from the cathode side, or from the bulk lattice of the anode leaving behind oxygen vacancies. A build up of oxygen vacancies is the determining factor for the onset of the current oscillations, which eventually get replenished by oxygen ions from the cathode. They do not explicitly state the period or frequency of the oscillations, however the period is estimated from their results to be in the order of minutes, following a relatively long induction time.

In a departure from the previously mentioned studies, Murakami et al. [70] investigated potential oscillations for a fuel cell with the standard Ni/YSZ-YSZ-LSM set up under cathodic current loading. They found that for low oxygen partial pressure, high cathodic current loading, or low porosity, potential oscillations could be induced in the cell. The period of the oscillations were much faster than reported elsewhere [42, 68, 93, 94], at around 1.5 seconds. They thus attribute the potential oscillations to variations in the oxygen concentration over-

potential, although the mechanism is not elaborated upon. It is clear that the oscillations here have nothing to do with oxidation/reduction cycles of the anode or surface coverage, since the cell was operated under cathodic current loading and only O2/N2 was supplied to the working electrode. These results appear to characterise a very different type of electrical oscillation in an SOFC.

1.3.3 Summmary

A review of the literature available on fuel cell oscillatory phenomena has been presented. It is clear that there are a number of possible mechanisms which can induce an oscillatory response depending on the type of fuel cell, the fuel composition, and various other operating parameters. In the case of PEMFCs, hydration and CO surface coverage appear to be critical to the onset of oscillations. However in SOFCs, oscillations in voltage and current have been attributed to surface coverage of contaminants such as sulphur or selenium, oxidation/reduction cycles of the nickel-based anodes, chemical kinetics and mass transfer at the cathode, and inconsistent fuel supply from balance of plant.

The numerous processes taking place within SOFCs, and fuel cells in general, are highly sensitive to fabrication processes and operating conditions. It is thus necessary to isolate the particular physicochemical phenomena of interest when testing and modelling fuel cells. Mangold et al. [69, 95] theoretically examine the effects of temperature dependant electrolyte conductivity on instabilities in SOFCs. Their bifurcation analysis shows that whilst various "hot spots" exist, they are not enough to cause current oscillations. Additionally, there has been investigation into Ni/NiO cycling of the anode by various groups in relation

to various electrical oscillations. These investigations have generally been conducted on SC-SOFCs. Thus, an opportunity arises to investigate the chemical kinetics and mass transfer effects at the anode, for a non-contaminated, methane fuelled SOFC, as a potential source for oscillations. Other studies on electrochemical systems which exhibit nonlinear oscillations, also indicate the importance of the reaction-diffusion coupling at the working electrode [70, 77–83]. To this end, a theoretical investigation similar to [69] is conducted, alongside an experimental programme to test model predictions, in order to determine the possibility for oscillatory phenomena, based on chemical kinetics and mass transfer effects at the anode of an SOFC.

Chapter 2

Mathematical Modelling

In this chapter a mathematical model is developed which describes the dynamics of an SOFC fuelled primarily by methane. The model is based on fundamental chemical kinetics and Fickian mass transfer through a porous medium, which provides a suitably accurate description of the processes occurring at the anode. The cell is assumed to be an internal reforming SOFC, where methane is steam reformed at the nickel catalyst near the surface of the anode. The hydrogen produced by the reforming reaction is then electrochemically oxidised, resulting in the main contribution to the current drawn from the cell. Carbon monoxide will also be produced by the steam reforming of methane, which can then proceed to either participate in the WGS reaction, or be directly consumed by electrochemical oxidisation at the TPB.

The principal electrochemical and chemical reactions which take place within the anode of an SOFC operated on methane, using the internal reforming method,

are given by Singhal & Kendall [5] as,

$$CH_4 + H_2O \rightarrow CO + 3H_2 \quad : \quad k_1[CH_4][H_20] \tag{2.1}$$

$$CO + H_2O \rightarrow CO_2 + H_2 \quad : \quad k_2[CO][H_20] \tag{2.2}$$

$$2H_2 + O_2 \rightarrow 2H_2O \quad : \quad k_3[H_2]^2[O_2] \tag{2.3}$$

$$2CO + O_2 \rightarrow 2CO_2 \quad : \quad k_4[CO]^2[O_2] \tag{2.4}$$

Here k_i, $(i = 1, 2, 3, 4)$, are the reaction rate constants for each respective reaction step. Since the operating temperature range of an SOFC is approximately $600 - 1000^oC$ [5, 101], all the reactants will be in the gas phase. This means that the water involved in the reactions will be in the form of steam and there will be no water management issues to resolve which are commonly associated with the PEMFCs [102]. This is due to the negligible effect that hydration has on an SOFC electrolyte's conductivity, as compared with that of PEMFCs, which often requires careful management in both the gas and liquid phase.

The reactions (2.1)-(2.4) will be adopted as the fundamental reaction scheme where (2.1) is the endothermic steam reforming of methane, (2.2) is the slightly exothermic water-gas shift (WGS) reaction, (2.3) and (2.4) are the electrochemical oxidation of hydrogen and carbon monoxide respectively. In the electrochemical reactions (2.3) and (2.4) electrons are liberated, then the current is collected and distributed along an external circuit.

Various other reactions may take place within the anode of an SOFC, for example the direct oxidation of methane, represented by the half cell reaction

(2.5), or the reactions (2.6) and (2.7) which can lead to a build up of solid deposits on the anode.

$$CH_4 + 4O^{2-} \rightarrow CO_2 + 2H_2O + 8e^- \tag{2.5}$$

$$CH_4 \rightarrow C + 2H_2 \tag{2.6}$$

$$2CO \rightarrow C + CO_2 \tag{2.7}$$

However it is noted in [103] that currently SOFCs are rarely manufactured to allow the direct oxidation of methane to occur, and that the main conusmption of CH_4 is through the SR reaction. Confirming this assumption, Sato et al. [104] report that when dry methane is supplied to the anode, methane is initially oxidised which leads to the production of H_2O. At this point the primary reaction mechanism becomes the steam reforming of methane as it is favoured thermodynamically. It requires specific oxide catalysts such as rare earth-doped ceria in order to significantly increase the catalytic activity for the direct oxidation of methane. Additionally the build up of carbon deposits on the anode may be avoided through careful operation of an SOFC [18, 105]. Thus reactions (2.5)-(2.7) will be neglected in the model.

A further simplification can be made to the reaction scheme (2.1)-(2.4), since the reaction given by (2.2) proceeds much faster than the other reactions [51–54]. In general, for reactions (2.1)-(2.4) in SOFCs it has been confirmed (see for

example [5, 53, 54]), that,

$$k_2 \gg \frac{k_1[CH_4]}{[CO]}, \tag{2.8}$$

$$k_2 \gg \frac{k_3[H_2]^2[O_2]}{[CO][H_2O]}, \tag{2.9}$$

$$k_2 \gg \frac{k_4[CO][O_2]}{[H_2O]}, \tag{2.10}$$

which allows us to reduce the reaction scheme (2.1)-(2.4) to,

$$CH_4 + 2H_2O \rightarrow CO_2 + 4H_2 \quad : \quad k_1[CH_4][H_20] \tag{2.11}$$

$$2H_2 + O_2 \rightarrow 2H_2O \quad : \quad k_3[H_2]^2[O_2] \tag{2.12}$$

with the composite reaction (2.11) being governed by the slowest component rate of reaction. This reduction is supported by Ho et al. [51] who note that the reaction step (2.2) reaches equilibrium because it is kinetically fast and almost all of the CO is consumed in this reaction. Any remaining CO may participate in the reaction given by (2.4) which contributes electrical current, however the CO oxidation rate is around $2-3$ times slower than that of hydrogen oxidation. Hence the dominant current contribution is from hydrogen oxidation alone. This is confirmed by Yakabe et al. [52] who found that the WGS reaction (2.2) was fast enough to significantly reduce the concentration polarization downstream of the fuel inlet.

It is worth observing at this stage, that if we (tentatively) regard reaction (2.11) as significantly faster than reaction (2.12), then these two reactions may be

combined to give, overall,

$$CH_4 + O_2 + 2H_2 \rightarrow CO_2 + 4H_2 \quad : \quad k_3[H_2]^2[O_2] \tag{2.13}$$

which is a cubic autocatalytic reaction, with reactant CH_4, pool chemical O_2, and autocatalyst H_2. The effect of Fickian transfer in CH_4 and H_2O, with O_2 acting as a pool chemical, puts this cubic autocatalytic reaction in a continuous stirred-tank reactor (CSTR) environment. It is well established that cubic autocatalytic reactions in appropriate CSTR environments can sustain autonomous nonlinear oscillatory regimes (see, for example, Gray and Scott [106]). This gives us confidence that at the anode of an SOFC, it is the core chemistry encapsulated in reactions (2.11)-(2.12), when coupled with Fickian transfer from the fuel stream, which provides the principle mechanism of self-sustained autonomous oscillations observed in SOFCs.

Specifically, when calculating electrical current, the accuracy of the model will be increased by considering the electrochemical oxidation of CO in addition to the hydrogen oxidation. However in the present model the aim is primarily to capture the qualitative characteristics of the most predominant reaction kinetics of an SOFC in order to investigate the principal dynamic behaviour, and so the reduction of (2.1)-(2.4) to the reaction scheme (2.11)-(2.12) is justified on the grounds outlined above.

The chemical concentrations of the reactant species are now introduced as,

$$[CH_4] = a, \tag{2.14}$$

$$[H_2] = b, \tag{2.15}$$

$$[H_2O] = c, \tag{2.16}$$

$$[O_2] = x. \tag{2.17}$$

The configuration within which the reaction scheme (2.11) and (2.12) is embedded is illustrated in Figure 2.1. There are two principle zones. In zone B, the species CH_4, H_2 and H_2O (steam) are present and advected through the system from the inlet to the outlet and, in particular, we note that oxygen is available in abundance from the oxidant stream through the porous cathode, so that, throughout, we may regard the oxygen concentration x as fixed at the oxidant stream concentration. The inlet flow contains only CH_4 and H_2O, at inlet concentrations a_0 and c_0 respectively.

We restrict attention to the situation when the flow rate q is sufficiently rapid, relative to the Fickian transfer rates between zone B and zone A, so that zone B provides a steady transfer pool of CH_4 and H_2O, at the inlet concentration, for Fickian transfer into zone A. This is a reasonable assumption as at higher velocities the depletion zone of a reactant stream flowing over a catalytic surface becomes very small in comparison with the width of the channel [46]. This assumption is further justified by the results of Cooper et al. [107] and King et al. [108] who model the fluid dynamics and reaction kinetics of a tubular SOFC.

Their results show that, for typical flow rates used in experiments, the reactants in the gas mixture in the fuel channel are well mixed in the radial direction, and the order of magnitudes of each of the mass fractions for the chemical species in the longitudinal direction remain constant over the anode region. This model is concerned with the reaction and diffusion phenomena occurring at the anode of the SOFC, therefore the assumption of a well mixed, uniform flow can be justified.

The main reactions, given by the reduced scheme (2.11) and (2.12), take place in zone A, which represents the porous anode. Within zone A, O_2 is present at the pool concentration x, whilst CH_4, H_2O and H_2 are transferred across the boundary between zone A and zone B via Fickian transfer. More details on the pool chemical approximation can be found in [73]. Zone A represents the porous anode where the reactions take place. Zone B is the fuel stream channel.

We derive the diffusion terms for each chemical species via an application of Fick's law of diffusion [109]. The dimensions of each term are enclosed in square brackets and are given in terms of the fundamental dimensions, length $[L]$, time $[T]$, and amount of substance $[N]$. In general, we have,

$$\text{Accumulation of chemical species in anode volume} = \text{Flux of chemical species through the surface area of transfer}$$

which gives,

$$V[L^3]\frac{d\phi}{dt}\left[\frac{N}{L^3T}\right] = A[L^2]D\left[\frac{L^2}{T}\right]\frac{(\phi_{bulk}-\phi)}{h}\left[\frac{N}{L^4}\right], \tag{2.18}$$

so that,

$$\frac{d\phi}{dt}\left[\frac{N}{L^3T}\right] = \frac{DA}{Vh}(\phi_{bulk} - \phi)\left[\frac{N}{L^3T}\right], \tag{2.19}$$

where, V is the volume of the anode, A is the surface area of transfer between the fuel channel and the anode, h is the thickeness of the anode, t is time, D is the effective diffusion coefficient for Fickian mass transfer, ϕ is the concentration of the chemical species in the anode, and ϕ_{bulk} is the concentration of the chemical species in the fuel channel. We only need to consider the reaction rate equations

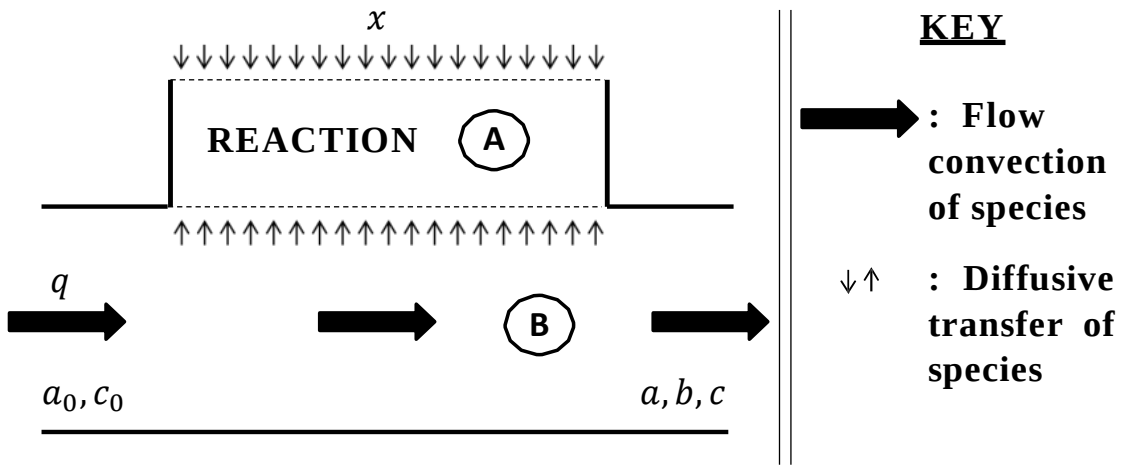

Figure 2.1: Proposed model sketch.

in region A since this is where the reactions occur. The associated reaction rate and Fickian mass transfer balances for a, b, and c lead, via (2.11), (2.12) and (2.19), with the reaction kinetic terms as described in [74, 110], to the three coupled,

nonlinear ordinary differential equations, namely,

$$\dot{a} = \frac{D_a A}{Vh}(a_0 - a) - k_1 ac, \tag{2.20}$$

$$\dot{b} = -\frac{D_b A}{Vh} b + 4k_1 ac - 2k_3 b^2 x, \tag{2.21}$$

$$\dot{c} = \frac{D_c A}{Vh}(c_0 - c) + 2k_3 b^2 x - 2k_1 ac, \tag{2.22}$$

where the dots above the variables represent differentiation with respect to time, t. The parameters D_a, D_b and D_c are respectively, the effective diffusion coefficients for the Fickian transfer of methane, hydrogen and water (as steam) to the reaction site, and h is the scale thickness of the anode. The coefficient $\frac{A}{V}$ is the surface area of transfer to volume ratio, whilst a_0 and c_0 represent the inlet concentrations of species a and c respectively. The first term of each rate equation represents the transfer of the particular species into the reaction zone A as given by (2.19), whilst the remaining terms represent the production/consumption of the species as given by the reduced reaction scheme (2.11) and (2.12).

Typical scales are now established, for each variable in equations (2.20)-(2.22), in line with the nondimensionalisation process detailed in [111]. Let $a \sim a_s$, $b \sim b_s$, $c \sim c_s$, $t \sim T$ with a_s, b_s, c_s and T being typical scales for a, b, c and t re-

spectively. A structured balance of terms in equations (2.20)-(2.22) then requires,

$$\frac{a_s}{T} \sim k_1 a_s c_s, \tag{2.23}$$

$$\frac{b_s}{T} \sim k_1 a_s c_s, \tag{2.24}$$

$$k_1 a_s c_s \sim k_3 b_s^2 x, \tag{2.25}$$

$$\frac{D_c A c_s}{Vh} \sim k_1 a_s c_s. \tag{2.26}$$

This results in the following dimensional scales,

$$a_s = b_s = \frac{D_c A}{Vhk_1}, \tag{2.27}$$

$$c_s = \frac{k_3 x D_c A}{k_1^2 Vh}, \tag{2.28}$$

$$T = \frac{k_1 Vh}{k_3 x D_c A}. \tag{2.29}$$

The equations (2.20)-(2.22) are nondimensionalised with respect to the scales we have determined in (2.27)-(2.29). We write $a = a_s a'$, $b = b_s b'$, $c = c_s c'$, $t = Tt'$. Equations (2.20)-(2.22) then become,

$$\dot{a} = \bar{D}_a(\bar{a_0} - a) - ac, \tag{2.30}$$

$$\dot{b} = -\bar{D}_b b + 4ac - 2b^2, \tag{2.31}$$

$$\varepsilon \dot{c} = (\bar{c_0} - c) + 2b^2 - 2ac, \tag{2.32}$$

where primes are dropped for convenience.

In equations (2.30)-(2.32) we have introduced the following dimensionless parameters.

$$\varepsilon = \frac{xk_3}{k_1}\,, \quad \bar{D}_b = \frac{D_b}{D_c\varepsilon}\,, \quad \bar{D}_a = \frac{D_a}{D_c\varepsilon}\,, \quad \bar{a}_0 = \frac{a_0}{a_s}\,, \quad \bar{c}_0 = \frac{c_0}{c_s}\ .$$

The parameter ε measures the ratio of reaction rates for the reaction scheme (2.11) and (2.12). For $\varepsilon \gg 1$, reaction (2.12) is the faster while for $\varepsilon \ll 1$, reaction (2.11) is the faster. The parameter $\bar{D}_a$ measures the ratio of the diffusivity of methane to the diffusivity of water into the reaction zone A. Similarly the parameter $\bar{D}_b$ measures the ratio of the diffusivity of hydrogen to the diffusivity of water into the reaction zone A. The parameters $\bar{a}_0$ and $\bar{c}_0$ represent the ratios of inlet concentration to the scaled concentration of methane and water respectively.

Experimental studies in SOFCs confirm that, in general, $0 < \varepsilon \ll 1$ which corresponds to reaction (2.11) being significantly faster than reaction (2.12). Specifically, this is confirmed by the following two results. Park et al. [53] found through simulation that there is a decrease of water content along the cell due to the faster consumption of water by the reforming reactions than being produced by the electrochemical oxidation of hydrogen. This is supported by You et al. [112] who found experimentally that there was hydrogen in the anode exit stream indicating that the reforming reactions were producing more hydrogen than was able to be oxidised. These observations support the condition that $0 < \varepsilon \ll 1$.

In what follows we consider $0 < \varepsilon \ll 1$ with $\bar{D}_a$, $\bar{D}_b$, $\bar{a}_0$, $\bar{c}_0 = O(1)$. This is supported by typical values in SOFC experiments (see for example, [64, 109, 113]),

which lead to order of magnitudes,

$$\varepsilon \sim O(10^{-2}), \tag{2.33}$$

$$\bar{D}_a \sim O(10^{1}), \tag{2.34}$$

$$\bar{D}_b \sim O(10^{1}), \tag{2.35}$$

$$\bar{a}_0 \sim O(10^{0}), \tag{2.36}$$

$$\bar{c}_0 \sim O(10^{0}). \tag{2.37}$$

Under these conditions, equations (2.20)-(2.22) can be rationally reduced. At leading order in ε, equations (2.30)-(2.32) become,

$$\dot{a} = \bar{D}_a(\bar{a}_0 - a) - ac, \tag{2.38}$$

$$\dot{b} = -\bar{D}_b b + 4ac - 2b^2, \tag{2.39}$$

$$0 = (\bar{c}_0 - c) + 2b^2 - 2ac, \tag{2.40}$$

From equation (2.40) it follows immediately that,

$$c = \frac{(2b^2 + \bar{c}_0)}{(2a + 1)}. \tag{2.41}$$

It is straightforward to establish that, when $0 < \varepsilon \ll 1$, the manifold (2.41) is attracting in the invariant quadrant $a, b, c \geq 0$ for the dynamical system (2.30)-

(2.32). On substituting for c from (2.41) into (2.38) and (2.39) we obtain,

$$\dot{a} = \bar{D}_a(\bar{a}_0 - a) - \frac{a(2b^2 + \bar{c}_0)}{(2a+1)}, \tag{2.42}$$

$$\dot{b} = -\bar{D}_b b + \frac{4a(2b^2 + \bar{c}_0)}{(2a+1)} - 2b^2. \tag{2.43}$$

Thus we have arrived at a 2-dimensional dynamical system for $(a(t), b(t))$ in $t \geq 0$ which models the temporal dynamics of the concentrations $a(t)$ and $b(t)$ in the anode of an SOFC, with the concentration $c(t)$ then following via (2.41). It is instructive to first analyse the situation when $\bar{c}_0 \ll 1$, which corresponds with a low steam concentration in the inlet flow. The leading order form of equations (2.42)-(2.43) is then,

$$\dot{a} = \bar{D}_a(\bar{a}_0 - a) - \frac{2ab^2}{(2a+1)}, \tag{2.44}$$

$$\dot{b} = -\bar{D}_b b + \frac{8ab^2}{(2a+1)} - 2b^2, \tag{2.45}$$

which determine the temporal dynamics of the concentrations $(a(t), b(t))$ in the case of $\bar{c}_0 \ll 1$.

In Chapter 3 we consider in detail the structure of the planar dynamical system (2.44)-(2.45), which we refer to henceforth as [D-S]. The dynamical system (2.42)-(2.43), which shall henceforth be referred to as $\overline{\text{[D-S]}}$, will be studied in Chapter 4.

Chapter 3

Nonlinear Oscillatory Dynamics in the Reduced Model [D-S]

In this chapter we analyse the structural dynamics of the dynamical system [D-S], given by equations (2.44)-(2.45), derived in the previous chapter. Some general properties of the phase plane are established, then the existence of equilibrium points and equilibrium point bifurcations are determined for various regions of parameter space. Each of the equilibrium points are analysed for stability, and Hopf bifurcations, which are associated with the appearance of limit cycles, are identified. The global phase portraits are constructed, then sample numerical integrations are performed, in order to elucidate the behaviour in the various regions of parameter space presented in the unfolding plane diagram.

3.1 The Phase Portrait of [D-S]

In this section we establish some general properties of [D-S] in the (a, b) phase plane which eventually enable us to construct the global phase portrait of [D-S]. We examine the phase portrait of [D-S] in the quadrant $\bar{Q}$, which is the closure of Q, where,

$$Q = \{(a, b) : a > 0 \text{ and } b > 0\}. \tag{3.1}$$

It is convenient to write [D-S] as,

$$\dot{\mathbf{x}} = \mathbf{F}(\mathbf{x}),\ (\mathbf{x}, t)\ \in\ \bar{Q} \times \mathbb{R},$$

with,

$$\mathbf{F}(\mathbf{x}) = (f(a, b), g(a, b)),$$

where $\mathbf{x} = (a, b)$ and,

$$f(a, b) = \bar{D_a}(\bar{a_0} - a) - \frac{2ab^2}{(2a + 1)}, \tag{3.2}$$

$$g(a, b) = -\bar{D_b}b + \frac{8ab^2}{(2a + 1)} - 2b^2. \tag{3.3}$$

3.1.1 Invariant and Attracting Sets

We first observe that in $\bar{Q}$,

$$\mathbf{F}((a, 0)).\mathbf{j} = g(a, 0) = 0,$$

$$\mathbf{F}((0,b)).\mathbf{i} = f(0,b) = \bar{D}_a \bar{a}_0 > 0, \tag{3.4}$$

where **i** and **j** are unit vectors pointing in the positive a and b directions respectively. We conclude from (3.4) that $\bar{Q}$ is a positively invariant region for [D-S]. Specifically we observe that the non-negative a-axis is a phase path for [D-S], with an equilibrium point at $(a,b) = (\bar{a}_0, 0)$.

Next consider that phase path passing through $(a_i, b_i) \in \bar{Q}$ at $t = 0$, and denote the phase path by $(a,b) = (a^i(t), b^i(t))$ in $t \geq 0$. As $\bar{Q}$ is a positively invariant region for [D-S], we can conclude immediately that,

$$a^i(t) \geq 0,\, b^i(t) \geq 0, \tag{3.5}$$

for all $t \geq 0$. It then follows from (2.44) that,

$$\dot{a}^i + \bar{D}_a a^i \leq \bar{D}_a \bar{a}_0, \quad t \geq 0. \tag{3.6}$$

An integration of (3.6) then gives,

$$a^i(t) \leq \bar{a}_0 + (a_i - \bar{a}_0) e^{-\bar{D}_a t}, \quad t \geq 0, \tag{3.7}$$

from which we obtain, with (3.5),

$$0 \leq a^i(t) \leq a_i + \bar{a}_0, \quad t \geq 0. \tag{3.8}$$

It also follows from (2.44) and (2.45) that, with $w = 4a^i + b^i$,

$$\dot{w} + \bar{D}_m w \leq 4\bar{D}_a \bar{a}_0, \quad t \geq 0, \tag{3.9}$$

where,

$$\bar{D}_m = \min\{\bar{D}_a, \bar{D}_b\}. \tag{3.10}$$

An integration of (3.9) establishes that,

$$w(t) \leq (4a_i + b_i)e^{-\bar{D}_m t} + \frac{4\bar{D}_a \bar{a}_0}{\bar{D}_m}(1 - e^{-\bar{D}_m t}), \quad t \geq 0, \tag{3.11}$$

from which it follows via (3.5), that,

$$0 \leq b^i(t) \leq (4a_i + b_i)e^{-\bar{D}_m t} + \frac{4\bar{D}_a \bar{a}_0}{\bar{D}_m}(1 - e^{-\bar{D}_m t}), \quad t \geq 0, \tag{3.12}$$

and so,

$$0 \leq b^i(t) \leq (4a_i + b_i) + \frac{4\bar{D}_a \bar{a}_0}{\bar{D}_m}, \quad t \geq 0. \tag{3.13}$$

Thus we have established a priori bounds for $(a^i(t), b^i(t))$ in (3.8) and (3.13), and so we can conclude that the phase path $(a^i(t), b^i(t))$ exists globally in $t \geq 0$, and, moreover, remains bounded in $\bar{Q}$ for all $t \geq 0$. We can immediately conclude, via the Poincaré-Bendixson Theorem (see, for example [114]) that the phase path $(a^i(t), b^i(t))$ must approach one of the following as $t \to \infty$, namely,

(i) an equilibrium point of [D-S] in $\bar{Q}$.

(ii) a periodic orbit of [D-S] in $\bar{Q}$.

(iii) a homoclinic or heteroclinic orbit of [D-S] in $\bar{Q}$.

Moreover, it follows from (3.7), (3.11), and (i)-(iii) that the ω-limit set of the phase

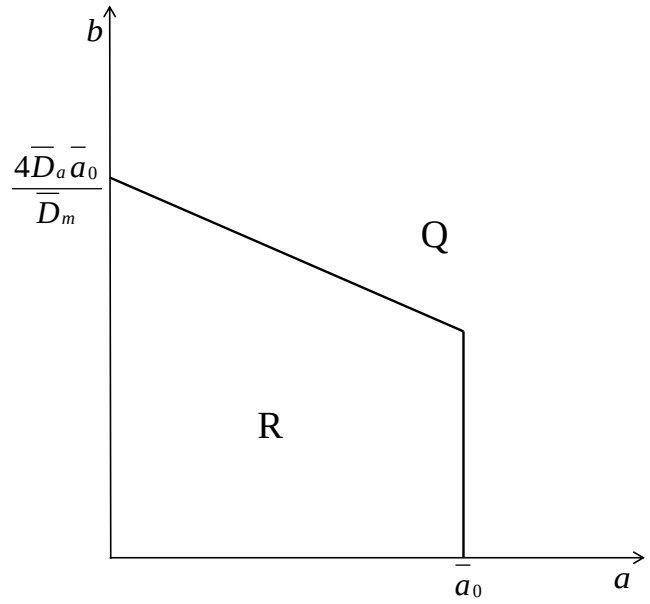

Figure 3.1: The region $R \subset Q$.

path $(a^i(t), b^i(t))$ must be contained in $\bar{R}$, being the closure of R, and so the phase path $(a^i(t), b^i(t))$ must,

(I) enter the region $\bar{R}$ at some $t^* \geq 0$ and remain in $\bar{R}$ for all $t \geq t^*$,

or,

(II) approach the region $\bar{R}$ (having at least one limit point on the boundary of R) as $t \to \infty$,

where R is the interior of a quadrilateral, given by,

$$R = \{(a, b) \,:\, 0 < a < \bar{a}_0,\ 0 < 4a + b < \frac{4\bar{D}_a\bar{a}_0}{\bar{D}_m}\}, \tag{3.14}$$

and is illustrated in Figure 3.1. It also follows from (i), (ii) and (iii), together with

(I) and (II), that,

$$E \cup P \cup H \subset \bar{R}, \tag{3.15}$$

where E is the set of equilibrium points of [D-S] in $\bar{Q}$, P is the set of periodic orbits of [D-S] in $\bar{Q}$ and H is the set of homoclinic and heteroclinic orbits of [D-S] in $\bar{Q}$.

3.1.2 Equilibrium Points and Equilibrium Point Bifurcations

We now identify all equilibrium points of [D-S] in $\bar{Q}$, and their associated bifurcation structure. Let $(a, b) = (\alpha, \beta)$ be an equilibrium point of [D-S] in $\bar{Q}$. It immediately follows from (3.14) and (3.15), that, $(\alpha, \beta) \in \bar{R}$, and so,

$$0 \leq \alpha \leq \bar{a}_0, \qquad 0 \leq \beta \leq 4\left(\frac{\bar{D}_a \bar{a}_0}{\bar{D}_m} - \alpha\right). \tag{3.16}$$

Substitution into [D-S] then requires that,

$$f(\alpha, \beta) = \bar{D}_a(\bar{a}_0 - \alpha) - \frac{2\alpha\beta^2}{(2\alpha + 1)} = 0, \tag{3.17}$$

$$g(\alpha, \beta) = \beta\left(\frac{8\alpha\beta}{(2\alpha + 1)} - 2\beta - \bar{D}_b\right) = 0. \tag{3.18}$$

It follows immediately that,

$$\mathbf{e_0} = (\alpha, \beta) = (\bar{a}_0, 0), \tag{3.19}$$

is an equilibrium point. All other equilibrium points must satisfy,

$$8\alpha\beta - 2(2\alpha+1)\beta - \bar{D}_b(2\alpha+1) = 0, \tag{3.20}$$

$$\bar{D}_a(\bar{a}_0 - \alpha)(2\alpha+1) - 2\alpha\beta^2 = 0, \tag{3.21}$$

with $(\alpha, \beta) \in \bar{R}$. It follows from (3.21) and (3.20) that, $\alpha > 0$ and $\beta > 0$. Then, via (3.21),

$$\beta^2 = \frac{1}{2}\bar{D}_a \frac{(\bar{a}_0 - \alpha)(2\alpha+1)}{\alpha}. \tag{3.22}$$

On substitution from (3.22) into (3.20) and re-arranging, we obtain,

$$F(\alpha; \bar{a}_0) = C \tag{3.23}$$

where,

$$F(\alpha; \bar{a}_0) = \frac{(2\alpha-1)(\bar{a}_0 - \alpha)^{\frac{1}{2}}}{\alpha^{\frac{1}{2}}(2\alpha+1)^{\frac{1}{2}}}, \quad 0 < \alpha \leq \bar{a}_0, \tag{3.24}$$

and,

$$C = \frac{\bar{D}_b}{\sqrt{2}\sqrt{\bar{D}_a}} > 0. \tag{3.25}$$

We must now examine the roots of (3.23) for $\alpha \in (0, \bar{a}_0]$. It is straightforward to establish that (3.23) has no roots when $0 < \bar{a}_0 \leq \frac{1}{2}$. Thus, when $0 < \bar{a}_0 \leq \frac{1}{2}$, the dynamical system [D-S] has just one equilibrium point in $\bar{Q}$, being $\mathbf{e_0}$ as identified in (3.19). However, for $\bar{a}_0 > \frac{1}{2}$ the situation is different. Specifically,

regarding $\bar{D}_b$ as *fixed*, with $\bar{D}_a$ as an *unfolding parameter* and $\bar{a}_0$ as a *bifurcation parameter*, then there is a value $\bar{a}_0 = \bar{a}_0^{SN}(\bar{D}_a)$, for each $\bar{D}_a > 0$, such that (3.23) has no roots for $\frac{1}{2} < \bar{a}_0 < \bar{a}_0^{SN}(\bar{D}_a)$, has a single root (of multiplicity two) for $\bar{a}_0 = \bar{a}_0^{SN}(\bar{D}_a)$, and has two simple roots for $\bar{a}_0 > \bar{a}_0^{SN}(\bar{D}_a)$. We conclude that, in addition to the equilibrium point $\mathbf{e_0}$ given in (3.19), [D-S] has no equilibrium points in $\bar{Q}$ when $0 < \bar{a}_0 < \bar{a}_0^{SN}(\bar{D}_a)$. However, an equilibrium point saddle-node bifurcation occurs when $\bar{a}_0 = \bar{a}_0^{SN}(\bar{D}_a)$, creating two additional equilibrium points in $\bar{Q}$ when $\bar{a}_0 > \bar{a}_0^{SN}(\bar{D}_a)$. We denote these two additional equilibrium points by,

$$\mathbf{e}_+ = (\alpha_+, \beta_+), \quad \mathbf{e}_- = (\alpha_-, \beta_-), \tag{3.26}$$

with $\alpha_+ > \alpha_-$. It follows from Section 3.1 that, $\mathbf{e}_+$, $\mathbf{e}_- \in R$. Moreover, in the $(\bar{a}_0, \bar{D}_a)$ unfolding plane, the curve $\bar{a}_0 = \bar{a}_0^{SN}(\bar{D}_a)$ has the parametric representation,

$$\bar{a}_0 = \alpha + \tfrac{\alpha(2\alpha+1)(2\alpha-1)}{(6\alpha+1)}, \quad \bar{D}_a = \tfrac{\bar{D}_b^2(6\alpha+1)}{2(2\alpha-1)^3}, \tag{3.27}$$

with $\alpha > \frac{1}{2}$. In fact, the parameter α in (3.27) represents the a-coordinate of the bifurcating equilibrium point. We are now in a position to sketch the equilibrium point bifurcation diagrams for [D-S] on the $(\alpha, \bar{a}_0)$ and the $(\beta, \bar{a}_0)$ bifurcation planes, and the equilibrium point bifurcation curves in the $(\bar{a}_0, \bar{D}_a)$ unfolding plane. Qualitative sketches of the bifurcation diagrams are given in Figures 3.2 and 3.3 (which are obtained from (3.19) and the locus of (3.23), together with (3.22)), together with the locus of the equilibrium points (with increasing $\bar{a}_0$) in $\bar{Q}$ on the (a, b) phase plane in Figure 3.4. The qualitative structure of the unfolding plane is sketched in Figure 3.5 (via the locus of (3.27)). We see that, for any

$\bar{D}_b$, $\bar{D}_a > 0$, when $0 \leq \bar{a}_0 < \bar{a}_0^{SN}(\bar{D}_a)$, then the only equilibrium point of [D-S] is that representing the unreacting state. However, with $\bar{a}_0 > \bar{a}_0^{SN}(\bar{D}_a)$, then [D-S] has two additional equilibrium points representing fully reacting states. We now discuss the local dynamic stability of the equilibrium points $\mathbf{e_0}$, $\mathbf{e}_+$ and $\mathbf{e}_-$.

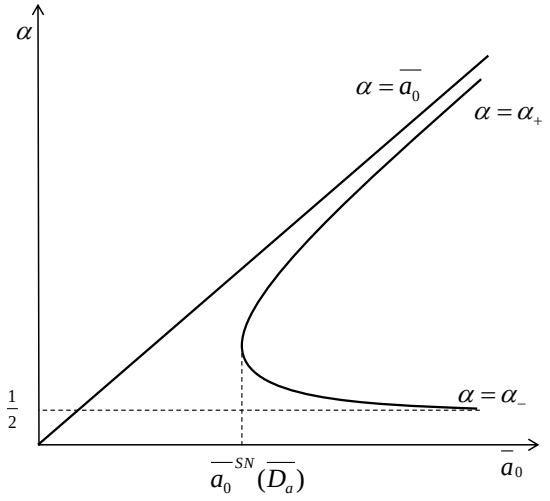

Figure 3.2: Equilibrium point bifurcation diagram in the $(\bar{a}_0, \alpha)$ plane.

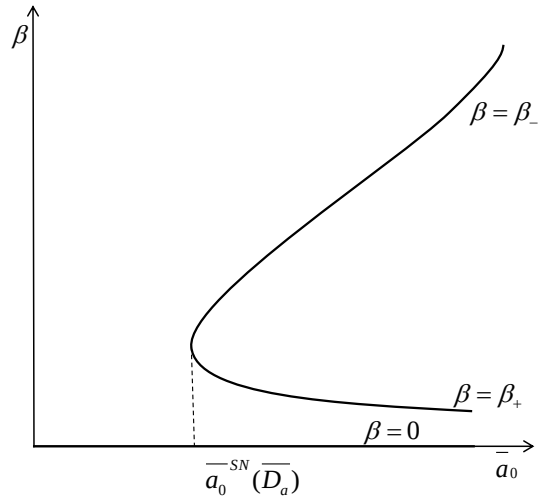

Figure 3.3: Equilibrium point bifurcation diagram in the $(\bar{a}_0, \beta)$ plane.

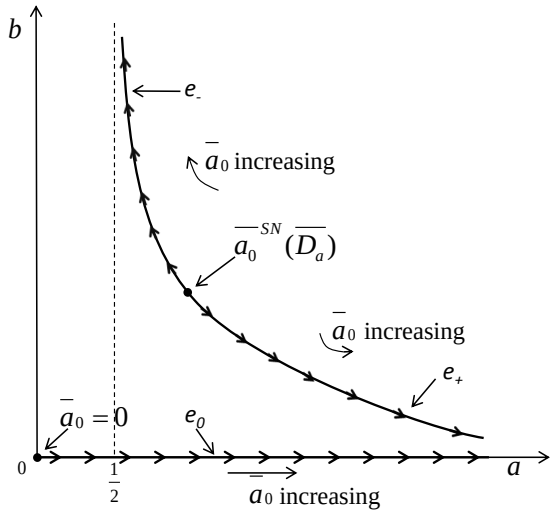

Figure 3.4: Locus of equilibrium points in $\bar{Q}$.

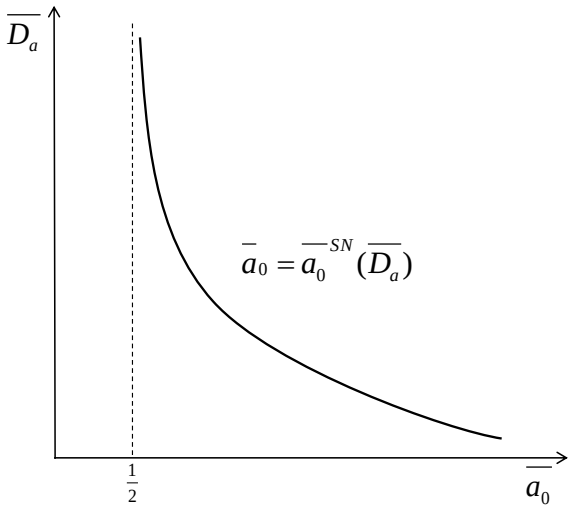

Figure 3.5: The $(\bar{a}_0, \bar{D}_a)$ unfolding plane illustrating the saddle-node bifurcation curve $\bar{a}_0 = \bar{a}_0^{SN}(\bar{D}_a)$.

3.1.3 Local Stability of Equilibrium Points

In this section we examine the local stability of the equilibrium points of [D-S] via the linearisation theorem. The eigenvalues of the associated linearisation of [D-S] at each respective equilibrium point $\mathbf{e_0}$, $\mathbf{e}_+$ and $\mathbf{e}_-$ are the roots of the characteristic equation,

$$\lambda^2 + \gamma(\alpha)\lambda + \delta(\alpha) = 0, \tag{3.28}$$

where,

$$\gamma(\alpha) = \begin{cases} \frac{\bar{D}_b^2}{2(2\alpha-1)^2} + \bar{D}_a - \bar{D}_b & \text{for } \alpha = \alpha_\pm \\ \bar{D}_a + \bar{D}_b & \text{for } \alpha = \bar{a}_0 \end{cases} \tag{3.29}$$

$$\delta(\alpha) = \begin{cases} \frac{\bar{D}_b^3(6\alpha+1)}{2(2\alpha-1)^3} - \bar{D}_a\bar{D}_b & \text{for } \alpha = \alpha_\pm \\ \bar{D}_a\bar{D}_b & \text{for } \alpha = \bar{a}_0 \end{cases} \tag{3.30}$$

It follows from (3.28), (3.29) and (3.30), after a little algebra, that,

$\mathbf{e_0}(\bar{a}_0)$ is a hyperbolic stable node for all $\bar{a}_0 > 0$ and $\bar{D}_a$, $\bar{D}_b > 0$.

$\mathbf{e}_+(\bar{a}_0)$ is a hyperbolic saddle point for all $\bar{a}_0 > \bar{a}_0^{SN}(\bar{D}_a)$ and $\bar{D}_a$, $\bar{D}_b > 0$.

However, an analysis of (3.28)-(3.29) establishes that there exists a value $\bar{D}_a = \bar{D}_a^*$, which depends upon $\bar{D}_b$, with, $0 < \bar{D}_a^* < \bar{D}_b$ for all $\bar{D}_b > 0$, and for which,

$\mathbf{e}_-(\bar{a}_0)$ is a hyperbolic stable node for all $\bar{a}_0 > \bar{a}_0^{SN}(\bar{D}_a)$ and $\bar{D}_a \geq \bar{D}_a^*$.

$\mathbf{e}_-(\bar{a}_0)$ is a hyperbolic unstable node or spiral for all $\bar{a}_0^{SN}(\bar{D}_a) < \bar{a}_0 < \bar{a}_0^H(\bar{D}_a)$ and $0 < \bar{D}_a < \bar{D}_a^*$.

$\mathbf{e}_-(\bar{a}_0)$ is a hyperbolic stable node or spiral for $\bar{a}_0 > \bar{a}_0^H(\bar{D}_a)$ and $0 < \bar{D}_a < \bar{D}_a^*$.

Here $\bar{a}_0^H(\bar{D}_a) > \bar{a}_0^{SN}(\bar{D}_a)$ for all $0 < \bar{D}_a < \bar{D}_a^*$, and the eigenvalues of the associated linearisation of [D-S] at $\mathbf{e}_-$ when $\bar{a}_0 = \bar{a}_0^H(\bar{D}_a)$ $(0 < \bar{D}_a < \bar{D}_a^*)$ are a purely imaginary pair. It is also straightforward, via (3.23) and (3.28)-(3.30), to obtain the following parameterisation for the curve $\bar{a}_0 = \bar{a}_0^H(\bar{D}_a)$ in the $(\bar{a}_0, \bar{D}_a)$ unfolding plane, namely,

$$\bar{a}_0 = \alpha + \tfrac{\bar{D}_b \alpha(2\alpha+1)}{(2(2\alpha-1)^2 - \bar{D}_b)}, \quad \bar{D}_a = \bar{D}_b - \tfrac{\bar{D}_b^2}{2(2\alpha-1)^2}, \tag{3.31}$$

for parameter $\alpha > \frac{1}{2} + \sqrt{\frac{\bar{D}_b}{8}}$. In fact, the parameter α in (3.31) represents the a-coordinate of the equilibrium point $\mathbf{e}_-$ when $\bar{a}_0 = \bar{a}_0^H(\bar{D}_a)$ and $0 < \bar{D}_a < \bar{D}_a^*$.

We next observe that the curves $\bar{a}_0 = \bar{a}_0^H(\bar{D}_a)$ $(0 < \bar{D}_a < \bar{D}_a^*)$ and $\bar{a}_0 = \bar{a}_0^{SN}(\bar{D}_a)$ $(\bar{D}_a > 0)$ intersect tangentially at the point,

$$(\bar{a}_0, \bar{D}_a) = (\bar{a}_0^*, \bar{D}_a^*), \tag{3.32}$$

in the $(\bar{a}_0, \bar{D}_a)$ unfolding plane, with,

$$\bar{a}_0^* = \bar{a}_0^H(\bar{D}_a) = \bar{a}_0^{SN}(\bar{D}_a). \tag{3.33}$$

When $(\bar{a}_0, \bar{D}_a) = (\bar{a}_0^*, \bar{D}_a^*)$ the eigenvalues of the associated linearisation of [D-S] at the coincident equilibrium points $\mathbf{e}_- = \mathbf{e}_+$ are both zero. This point $(\bar{a}_0^*, \bar{D}_a^*)$ in the $(\bar{a}_0, \bar{D}_a)$ unfolding plane is the single unfolding point, with $\bar{D}_b > 0$ fixed. In particular, it has a parameterisation with $\bar{D}_b$, which is readily obtained from (3.27) and (3.31) as,

$$\bar{a}_0^* = \alpha + \tfrac{\alpha(2\alpha+1)(2\alpha-1)}{(6\alpha+1)}, \quad \bar{D}_a^* = \tfrac{(2\alpha-1)^3(6\alpha+1)}{32\alpha^2}, \quad \bar{D}_b = \tfrac{(2\alpha-1)^3}{4\alpha}, \tag{3.34}$$

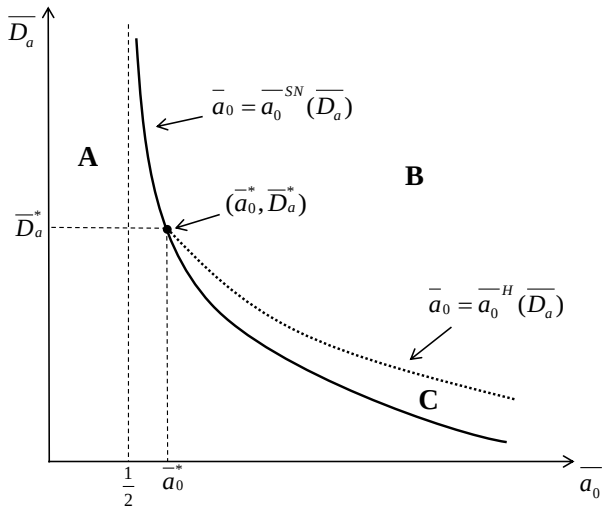

Figure 3.6: The $(\bar{a}_0, \bar{D}_a)$ unfolding plane illustrating the curves $\bar{a}_0 = \bar{a}_0^{SN}(\bar{D}_a)$ and $\bar{a}_0 = \bar{a}_0^{H}(\bar{D}_a)$ with the unfolding point $(\bar{a}_0^*, \bar{D}_a^*)$.

for $\alpha > \frac{1}{2}$, with the parameter α being the a-coordinate of the coincident equilibrium points $\mathbf{e}_+$ and $\mathbf{e}_-$ at the unfolding point $(\bar{a}_0^*, \bar{D}_a^*)$. The curves $\bar{a}_0 = \bar{a}_0^{SN}(\bar{D}_a)$ and $\bar{a}_0 = \bar{a}_0^{H}(\bar{D}_a)$ divide the $(\bar{a}_0, \bar{D}_a)$ unfolding plane into three disjoint regions A, B and C, and this is illustrated in Figure 3.6. We have now characterised the local stability properties of the equilibrium points $\mathbf{e_0}$, $\mathbf{e}_+$ and $\mathbf{e}_-$. We can next use this information to locate local bifurcations at the equilibrium points $\mathbf{e_0}$, $\mathbf{e}_+$ and $\mathbf{e}_-$.

3.1.4 Local Bifurcations

We now examine the possibility of local bifurcations occurring at equilibrium points following the conclusions of Subsection 3.1.3. No local bifurcations occur at the equilibrium point $\mathbf{e_0}$ since this equilibrium point remains a hyperbolic

stable node throughout $A \cup B \cup C$. The equilibrium points $\mathbf{e}_+$ and $\mathbf{e}_-$ are created into $\bar{a}_0 > \bar{a}_0^{SN}(\bar{D}_a)$ at a saddle-node bifurcation in the (a, b) phase plane at $(a, b) = \mathbf{e}_+ = \mathbf{e}_-$ when $\bar{a}_0 = \bar{a}_0^{SN}(\bar{D}_a)$. No further local bifurcations occur at $\mathbf{e}_+$ for all $\bar{a}_0 > \bar{a}_0^{SN}(\bar{D}_a)$ since $\mathbf{e}_+$ remains as a hyperbolic saddle point. However, for each $0 < \bar{D}_a < \bar{D}_a^*$, a further local bifurcation occurs at $\mathbf{e}_-$, when $\bar{a}_0 = \bar{a}_0^H(\bar{D}_a)$, and this is a Hopf bifurcation creating a unique limit cycle into either of $\bar{a}_0 < \bar{a}_0^H(\bar{D}_a)$ (stable) or $\bar{a}_0 > \bar{a}_0^H(\bar{D}_a)$ (unstable). Further details of the nature of this Hopf bifurcation are postponed until Subsection 3.1.7.

3.1.5 Heteroclinic Connections

At the point $\bar{a}_0 = \bar{a}_0^{SN}(\bar{D}_a)$ there exists an equilibrium point $\mathbf{e}_\pm$ which has a zero eigenvalue. The associated centre manifold may be approximated by an equation of the form,

$$b = \phi(a) = A + Ba + Ca^2 + Da^3 + O(a^4), \tag{3.35}$$

which gives,

$$\dot{b} = \phi'(a) = B\dot{a} + 2Ca\dot{a} + 3Da^2\dot{a} + O(a^3)\dot{a}. \tag{3.36}$$

Substituting into the linearised system about the point $\mathbf{e}_\pm$ yields the coefficients in equation 3.35. We find that the coefficient A is zero and so at leading order we have,

$$\phi(a) = Ba + O(a^2), \tag{3.37}$$

where,

$$B = -\frac{8\beta^2}{(2\alpha+1)^2}\left(\frac{1}{\frac{2\beta^2}{(2\alpha+1)^2} + \frac{20\alpha\beta}{(2\alpha+1)} + \bar{D}_b - \bar{D}_a - 4\beta}\right). \tag{3.38}$$

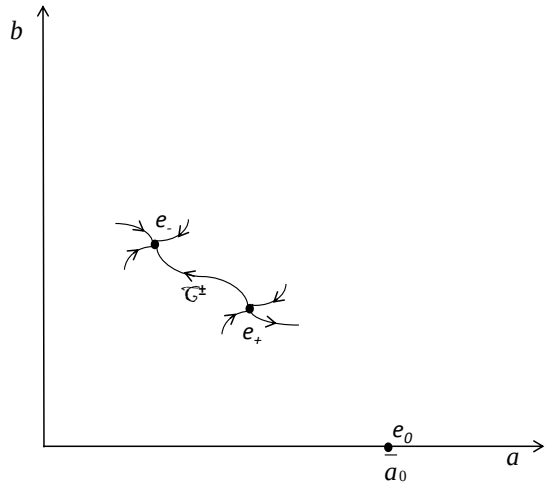

Figure 3.7: Sketch of the (a, b) phase plane showing the heteroclinic connection $\mathcal{C}^{\pm}$.

Thus the centre manifold is attracting for $t > 0$, and by the centre manifold theorem, trajectories starting at $(a, b) \sim \mathbf{e}_{\pm}$ when $\bar{a}_0 \sim \bar{a}_0^{SN}(\bar{D}_a)$ will approach the centre manifold. Hence the equilibrium points $\mathbf{e}_+$ and $\mathbf{e}_-$ have a unique heteroclinic connection, which we label as $\mathcal{C}^{\pm}$, as shown in Figure 3.7. This heteroclinic connection can only subsequently be broken in $\bar{a}_0 > \bar{a}_0^{SN}(\bar{D}_a)$ by either a local bifurcation at $\mathbf{e}_+$ and/or $\mathbf{e}_-$, or a global bifurcation away from $\mathbf{e}_+$ and $\mathbf{e}_-$.

3.1.6 Phase Portrait at Infinity

Here we examine the structure of the phase portrait of [D-S] in the neighbourhood of the arc at infinity in $\bar{Q}$. A straight forward application of the Poincaré projection (see [115]) establishes that in $\bar{Q}$, the circular arc at infinity forms a

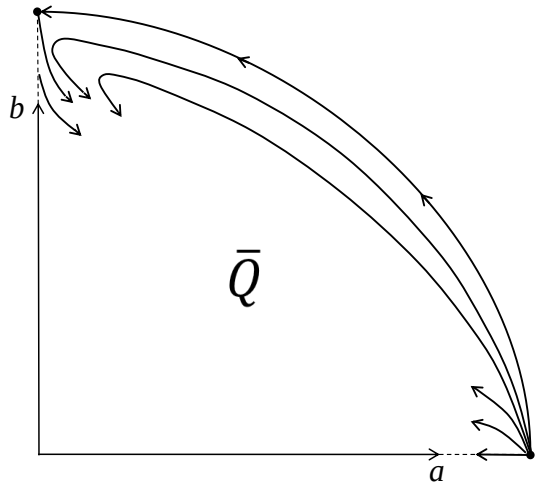

Figure 3.8: The phase portrait at infinity in $\bar{Q}$.

phase path, containing exactly two equilibrium points at infinity at, $\mathbf{e}_\infty = (\infty, 0)$ and $\mathbf{e}_\infty{}' = (0, \infty)$, where, $\mathbf{e}_\infty$ is an unstable node and $\mathbf{e}_\infty{}'$ is a saddle point. The arc at infinity in $\bar{Q}$ forms a heteroclinic connection, connecting $\mathbf{e}_\infty$ to $\mathbf{e}_\infty{}'$. The phase portrait at infinity in $\bar{Q}$ is sketched in Figure 3.8. Observe that no phase paths are attracted to the arc at infinity in $\bar{Q}$, in accord with the conclusions of Subsection 3.1.1.

3.1.7 Periodic Orbits and Bifurcation to Periodic Orbits

We consider the periodic orbits of [D-S] in $\bar{Q}$, and their associated bifurcation structure. Firstly we observe that as $\bar{Q}$ is a positively invariant region for [D-S], then any periodic orbit of [D-S] which has non-trivial intersection with $\bar{Q}$, must lie wholly within $\bar{Q}$. Thus no periodic orbit in $\bar{Q}$ can surround the equilibrium

point $\mathbf{e_0}$. However, it follows via index theory, that any periodic orbit which may exist in $\bar{Q}$ must surround at least one finite equilibrium point in $\bar{Q}$. We conclude, via Subsection 3.1.2, that there are no periodic orbits in $\bar{Q}$ for $(\bar{a}_0, \bar{D}_a) \in A$. Similarly index theory rules out the existence of any periodic orbits in $\bar{Q}$ for $(\bar{a}_0, \bar{D}_a) \in SN$ (the index of $\mathbf{e}_\pm$ at SN is zero). Furthermore, any periodic orbit which may exist in $\bar{Q}$ for $(\bar{a}_0, \bar{D}_a) \in B \cup C \cup H$ must surround the equilibrium point $\mathbf{e}_-$, and no other equilibrium point, which again follows from index theory.

As identified in Subsection 3.1.2, a Hopf bifurcation occurs for each $0 < \bar{D}_a < \bar{D}_a^*$, at the equilibrium point, $\mathbf{e}_-$ when,

$$\bar{a}_0 = \bar{a}_0^H(\bar{D}_a) > \bar{a}_0^{SN}(\bar{D}_a). \tag{3.39}$$

With regard to the criticality of this Hopf bifurcation, there are three cases to consider. In particular there is a value $\bar{D}_a^c$, depending on $\bar{D}_b$, with $0 < \bar{D}_a^c < \bar{D}_a^*$, and for which the Hopf bifurcation at $\mathbf{e}_-$, when $(\bar{a}_0, \bar{D}_a) = (\bar{a}_0^H(\bar{D}_a^c), \bar{D}_a^c)$ is degenerate. The three cases are:

Case (a): $\bar{D}_a^c < \bar{D}_a < \bar{D}_a^*$

In this case the Hopf bifurcation at $\mathbf{e}_-$, when $(\bar{a}_0, \bar{D}_a) = (\bar{a}_0^H(\bar{D}_a), \bar{D}_a)$, is supercritical, creating a unique, unstable limit cycle in $\bar{Q}$, for each $0 < \bar{a}_0 - \bar{a}_0^H(\bar{D}_a) \ll 1$, bifurcating out of the equilibrium point $\mathbf{e}_-$.

Case (b): $\bar{D}_a = \bar{D}_a^c$

In this case the Hopf bifurcation at $\mathbf{e}_-$, when $(\bar{a}_0, \bar{D}_a) = (\bar{a}_0^H(\bar{D}_a^c), \bar{D}_a^c)$ is degenerate, and supercritical, creating a unique, unstable limit cycle in $\bar{Q}$, for each $0 < \bar{a}_0 - \bar{a}_0^H(\bar{D}_a^c) \ll 1$, bifurcating out of the equilibrium point $\mathbf{e}_-$.

Case (c): $0 < \bar{D}_a < \bar{D}_a^c$

In this case the Hopf bifurcation at $\mathbf{e}_-$, when $(\bar{a}_0, \bar{D}_a) = (\bar{a}_0^H(\bar{D}_a), \bar{D}_a)$, is subcritical, creating a unique, stable limit cycle in $\bar{Q}$, for each $0 < \bar{a}_0^H(\bar{D}_a) - \bar{a}_0 \ll 1$, bifurcating out of the equilibrium point $\mathbf{e}_-$.

In each case, we will refer to this periodic orbit as P^-, with period T^- and amplitude (relative to the equilibrium point $\mathbf{e}_-$) A^-, which depend upon $\bar{a}_0$ and $\bar{D}_a$ (with fixed $\bar{D}_b$). In particular, it is straightforward to establish that,

$$A^- = \begin{cases} O(|\bar{a}_0 - \bar{a}_0^H(\bar{D}_a)|^{\frac{1}{2}}), \ \bar{D}_a \in (0, \bar{D}_a^c) \cup (\bar{D}_a^c, \bar{D}_a^*) \\ O((\bar{a}_0 - \bar{a}_0^H(\bar{D}_a^c))^{\frac{1}{4}}), \ \bar{D}_a = \bar{D}_a^c \end{cases} \tag{3.40}$$

as $\bar{a}_0 \to \bar{a}_0^H(\bar{D}_a)$, whilst,

$$T^- = \frac{2\pi}{\Omega(\bar{a}_0^H(\bar{D}_a), \bar{D}_a)} + O(|\bar{a}_0 - \bar{a}_0^H(\bar{D}_a)|), \tag{3.41}$$

as $\bar{a}_0 \to \bar{a}_0^H(\bar{D}_a)$ for all $0 < \bar{D}_a < \bar{D}_a^*$, with,

$$\Omega(\bar{a}_0^H(\bar{D}_a), \bar{D}_a)^2 = \frac{\bar{D}_b^3(6\alpha_-(\bar{a}_0^H(\bar{D}_a)) + 1)}{2(2\alpha_-(\bar{a}_0^H(\bar{D}_a)) - 1)^3} - \bar{D}_a\bar{D}_b. \tag{3.42}$$

Now, numerical evidence establishes that for $0 < \bar{D}_a < \bar{D}_a^*$, a homoclinic bifurcation occurs when, $\bar{a}_0 = \bar{a}_0^\infty(\bar{D}_a)$, via the formation of a homoclinic orbit on the saddle point equilibrium point $\mathbf{e}_+$. This homoclinic bifurcation creates a unique unstable limit cycle in $0 < \bar{a}_0^\infty(\bar{D}_a) - \bar{a}_0 \ll 1$ for $\bar{D}_a^\infty \leq \bar{D}_a < \bar{D}_a^*$, and unique stable limit cycle in $0 < \bar{a}_0 - \bar{a}_0^\infty(\bar{D}_a) \ll 1$ for $0 < \bar{D}_a < \bar{D}_a^\infty$, with the homoclinic bifurcation changing from subcritical for $\bar{D}_a^\infty \leq \bar{D}_a < \bar{D}_a^*$, to supercritical for

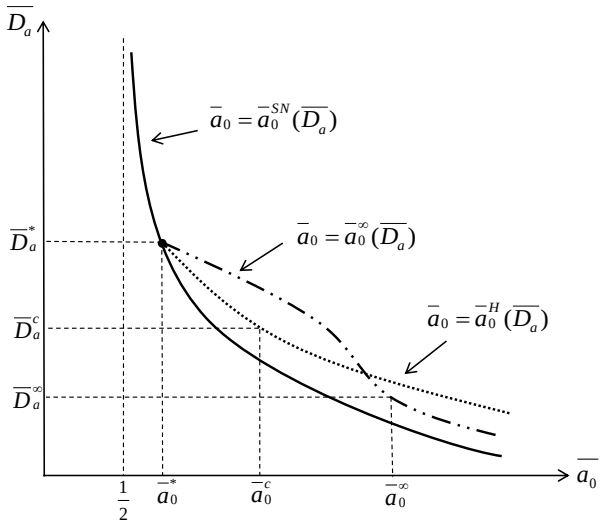

Figure 3.9: The $(\bar{a}_0, \bar{D}_a)$ unfolding plane.

$0 < \bar{D}_a < \bar{D}_a^{\infty}$. The limit cycle is created at finite amplitude from the homoclinic orbit on $\mathbf{e}_+$ at $\bar{a}_0 = \bar{a}_0^H(\bar{D}_a)$. Numerical evidence establishes that $\bar{D}_a^{\infty} < \bar{D}_a^c$ (with $\bar{D}_a^{\infty}$ depending on $\bar{D}_b$). On the unfolding plane we now have the situation which is illustrated in Figure 3.9. The change in criticality of the Hopf bifurcation at $\bar{D}_a = \bar{D}_a^c$ induces a periodic saddle-node bifurcation for each $\bar{D}_a^{\infty} < \bar{D}_a < \bar{D}_a^c$, when, $\bar{a}_0 = \bar{a}_0^P(\bar{D}_a)$, with $\bar{a}_0^P(\bar{D}_a) < min(\bar{a}_0^H(\bar{D}_a), \bar{a}_0^{\infty}(\bar{D}_a))$ for all $\bar{D}_a^{\infty} < \bar{D}_a < \bar{D}_a^c$. The periodic saddle-node bifurcation is absorbed at the homoclinic bifurcation at its change in criticality, when $\bar{D}_a = \bar{D}_a^{\infty}$. The periodic saddle-node bifurcation gives rise to both an unstable (outer) and stable (inner) limit cycle surrounding the equilibrium point $\mathbf{e}_-$, being created at finite amplitude as $\bar{a}_0$ increases through $\bar{a}_0^P(\bar{D}_a)$, with a single bi-stable limit cycle appearing at $\bar{a}_0 = \bar{a}_0^P(\bar{D}_a)$, from which they are created in $\bar{a}_0 > \bar{a}_0^P(\bar{D}_a)$. The inner limit cycle is that which

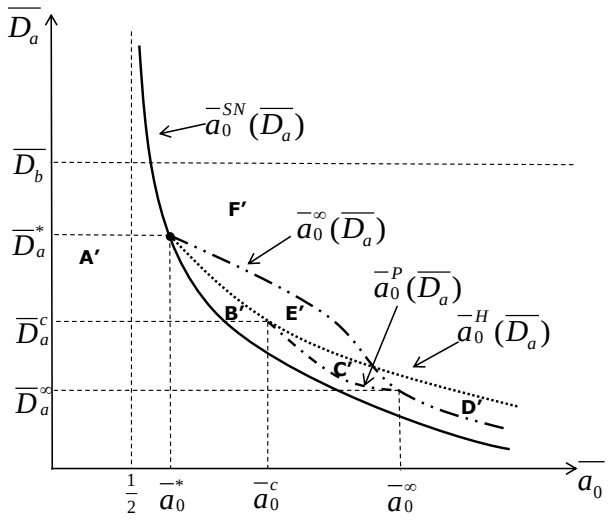

Figure 3.10: The full $(\bar{a}_0, \bar{D}_a)$ unfolding plane.

we have labeled as P^-. We now label the outer limit cycle as P^+.

We remark that the limit cycle created by the homoclinic bifurcation is created at finite amplitude and infinite period, whilst the two limit cycles created by the periodic saddle-node bifurcation are created at finite amplitude and finite period.

Numerical evidence then confirms that, for each $\bar{D}_b > 0$, the full $(\bar{a}_0, \bar{D}_a)$ unfolding plane is as illustrated in Figure 3.10, where the $(\bar{a}_0, \bar{D}_a)$ plane is now subdivided into the disjoint regions A'-F'. We are now in a position to use Figure 3.10 to sketch $(\bar{a}_0, A)$ bifurcation diagrams for periodic orbits at each $0 < \bar{D}_a < \bar{D}_a^*$, with the amplitude A represented as $A = (a_{max} - a_{min})$ on the periodic orbit. These are illustrated in Figure 3.11.

In Figure 3.11 A_∞ represents the amplitude of the periodic orbit at the homoclinic bifurcation and A_p represents the amplitude of the periodic orbit at the

periodic saddle-node bifurcation. It should also be noted that in the (a, b) phase plane, each periodic orbit, P^- and P^+, must lie in the region $\bar{R}$, as a consequence of Subsection 3.1.1, and in particular, (3.15).

The equilibrium point bifurcation diagram in Figure 3.2 can now be combined with the bifurcation diagrams for periodic orbits in Figure 3.11 to construct the full bifurcation diagrams illustrated in Figure 3.12. Again, we remark that, in the (a, b) phase plane, all equilibrium points, periodic orbits and homoclinic orbits identified in the bifurcation diagrams of Figure 3.12 lie in the region $\bar{R}$, as a consequence of Subsection 3.1.1 and equation (3.15).

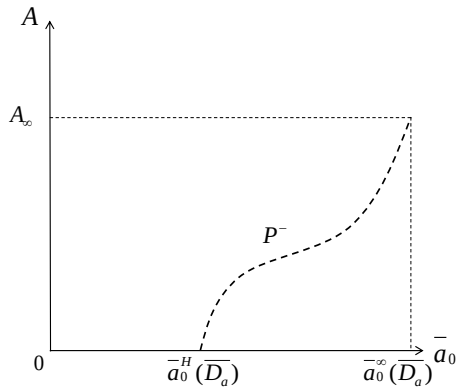

(a) $\bar{\mathbf{D}}_\mathbf{a}^\mathbf{c} \leq \bar{\mathbf{D}}_\mathbf{a} < \bar{\mathbf{D}}_\mathbf{a}^*$

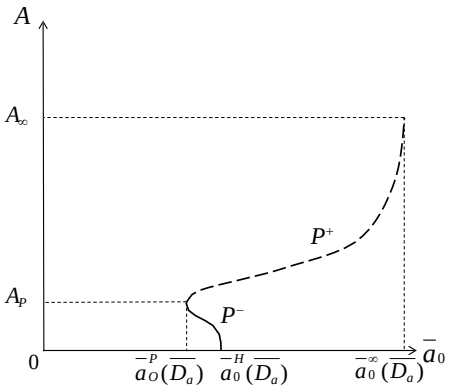

(b) $\bar{\mathbf{D}}_\mathbf{a}^\infty < \bar{\mathbf{D}}_\mathbf{a} < \bar{\mathbf{D}}_\mathbf{a}^\mathbf{c}$ when $\bar{a}_0^H < \bar{a}_0^\infty$

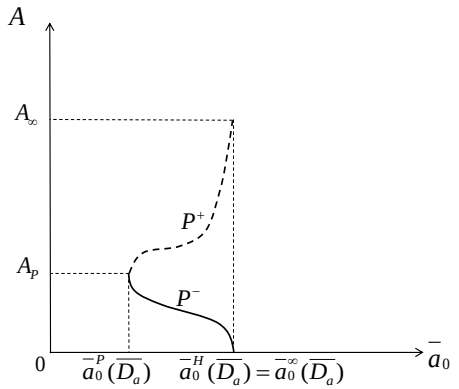

(c) $\bar{\mathbf{D}}_\mathbf{a}^\infty < \bar{\mathbf{D}}_\mathbf{a} < \bar{\mathbf{D}}_\mathbf{a}^\mathbf{c}$ when $\bar{a}_0^H = \bar{a}_0^\infty$

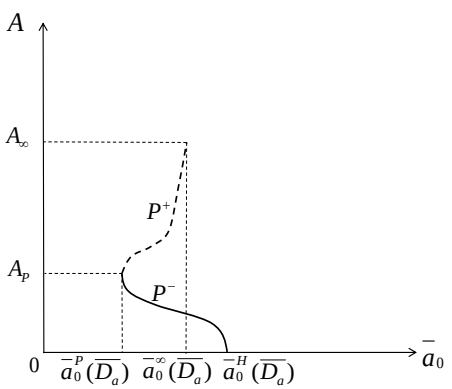

(d) $\bar{\mathbf{D}}_\mathbf{a}^\infty < \bar{\mathbf{D}}_\mathbf{a} < \bar{\mathbf{D}}_\mathbf{a}^\mathbf{c}$ when $\bar{a}_0^H > \bar{a}_0^\infty$

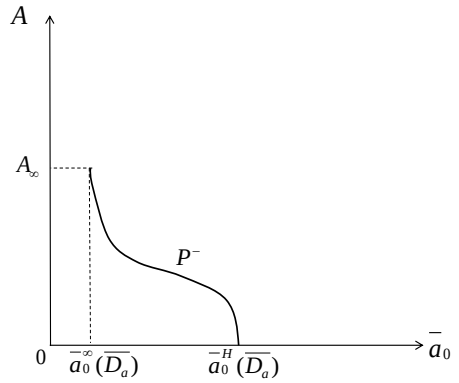

(e) $\mathbf{0} < \bar{\mathbf{D}}_\mathbf{a} \leq \bar{\mathbf{D}}_\mathbf{a}^\infty$

Figure 3.11: Bifurcation diagrams for periodic orbits with dashed lines being unstable and solid lines being stable periodic orbits.

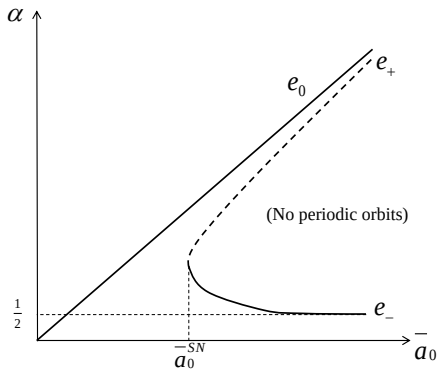

(a) $\bar{\mathbf{D}}_\mathbf{a} \geq \bar{\mathbf{D}}_\mathbf{a}^*$:

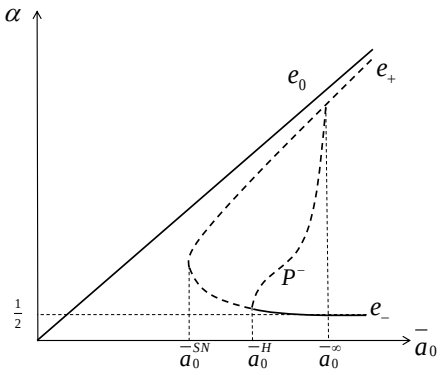

(b) $\bar{\mathbf{D}}_\mathbf{a}^\mathbf{c} \leq \bar{\mathbf{D}}_\mathbf{a} < \bar{\mathbf{D}}_\mathbf{a}^*$

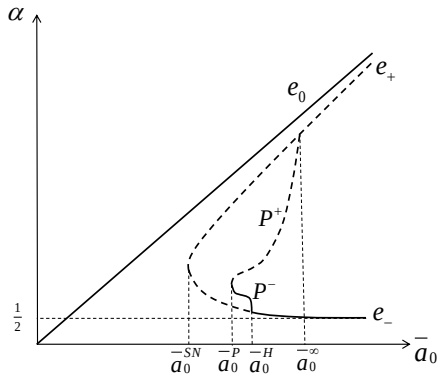

(c) $\bar{\mathbf{D}}_\mathbf{a}^\infty < \bar{\mathbf{D}}_\mathbf{a} < \bar{\mathbf{D}}_\mathbf{a}^\mathbf{c}$ when $\bar{a}_0^H < \bar{a}_0^\infty$

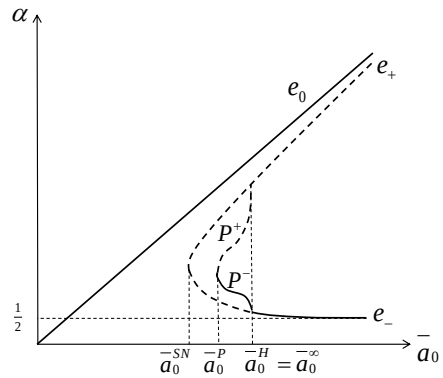

(d) $\bar{\mathbf{D}}_\mathbf{a}^\infty < \bar{\mathbf{D}}_\mathbf{a} < \bar{\mathbf{D}}_\mathbf{a}^\mathbf{c}$ when $\bar{a}_0^H = \bar{a}_0^\infty$

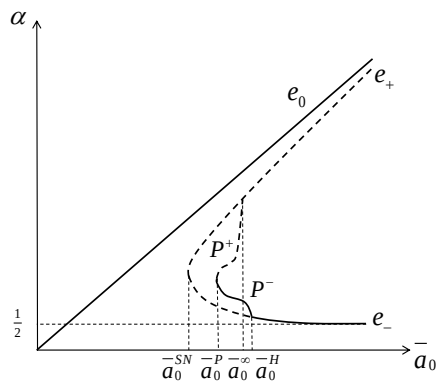

(e) $\bar{\mathbf{D}}_\mathbf{a}^\infty < \bar{\mathbf{D}}_\mathbf{a} < \bar{\mathbf{D}}_\mathbf{a}^\mathbf{c}$ when $\bar{a}_0^H > \bar{a}_0^\infty$

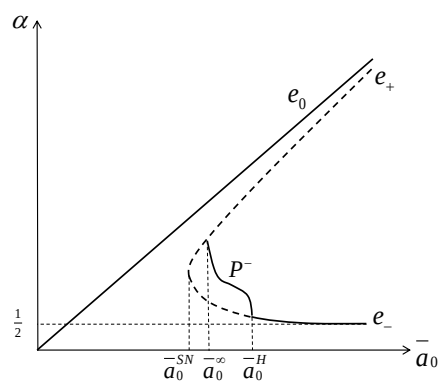

(f) $\mathbf{0} < \bar{\mathbf{D}}_\mathbf{a} \leq \bar{\mathbf{D}}_\mathbf{a}^\infty$

Figure 3.12: Full bifurcation diagrams. Here dashed lines represent unstable and solid lines represent stable for both equilibrium points and periodic orbits.

3.1.8 Attractors for Phase Paths in $\overline{Q}$

We can now determine the attracting set for each phase path in $\bar{Q}$. With $(a_0, b_0) \in \bar{Q}$, in what follows we will denote the phase path passing through (a_0, b_0) at $t = 0$, when $t \geq 0$, as $P_0 \subset \bar{Q}$ (via Subsection 3.1.1). We denote the ω-limit set of P_0 by $\omega_0 \subset \bar{Q}$. Also, at the relevant parameter value in the $(\bar{a}_0, \bar{D}_a)$ unfolding plane, we denote the stable limit cycle as $\mathcal{C}_s \subset \bar{Q}$, the unstable limit cycle as $\mathcal{C}_u \subset \bar{Q}$, and the bistable limit cycle as $\mathcal{C}_b \subset \bar{Q}$. We denote the homoclinic orbit on the saddle point $\mathbf{e}_+$ as $\mathcal{H} \subset \bar{Q}$, and the stable manifold of the saddle point $\mathbf{e}_+$ as $\mathcal{S} \subset \bar{Q}$. Simlarly we write, $\varepsilon_0 = \{\mathbf{e_0}\} \subset \bar{Q}$, $\varepsilon_+ = \{\mathbf{e}_+\} \subset \bar{Q}$, $\varepsilon_- = \{\mathbf{e}_-\} \subset \bar{Q}$, $\varepsilon_\pm = \{\mathbf{e}_\pm\} \subset \bar{Q}$. We now examine ω_0 for each P_0 with $(a_0, b_0) \in \bar{Q}$, for each of the regions $A' - F'$ on the $(\bar{a}_0, \bar{D}_a)$ unfolding plane. In addition we introduce the notation $\partial A'B'$ to be the boundary between regions A' and B' in the $(\bar{a}_0, \bar{D}_a)$ unfolding plane, with similar notation for all other boundaries in the unfolding plane. We have:

$$\underline{(\bar{a}_0, \bar{D}_a) \in A'}: \qquad (a_0, b_0) \in \bar{Q} \Rightarrow \omega_0 = \varepsilon_0 \tag{3.43}$$

$$\underline{(\bar{a}_0, \bar{D}_a) \in B' \cup \partial E'B'}: \qquad (a_0, b_0) \in \bar{Q} \backslash \mathcal{S} \Rightarrow \omega_0 = \varepsilon_0 \tag{3.44}$$

$$(a_0, b_0) \in \varepsilon_- \Rightarrow \omega_0 = \varepsilon_- \tag{3.45}$$

$$(a_0, b_0) \in \mathcal{S} \backslash \varepsilon_- \Rightarrow \omega_0 = \varepsilon_+ \tag{3.46}$$

$\underline{(\bar{a}_0, \bar{D}_a) \in C'}$:

$$(a_0, b_0) \in int\mathcal{C}_u \backslash \varepsilon_- \Rightarrow \omega_0 = \mathcal{C}_s \tag{3.47}$$

$$(a_0, b_0) \in \varepsilon_- \Rightarrow \omega_0 = \varepsilon_- \tag{3.48}$$

$$(a_0, b_0) \in \mathcal{C}_u \Rightarrow \omega_0 = \mathcal{C}_u \tag{3.49}$$

$$(a_0, b_0) \in \mathcal{S} \Rightarrow \omega_0 = \varepsilon_+ \tag{3.50}$$

$$(a_0, b_0) \in \bar{Q} \backslash (\overline{int\mathcal{C}_u} \cup \mathcal{S}) \Rightarrow \omega_0 = \varepsilon_0 \tag{3.51}$$

with $int\mathcal{C}_u \subset \bar{Q}$ being the interior of $\mathcal{C}_u$, and $int\mathcal{C}_s \subset \bar{Q}$ being the interior of $\mathcal{C}_s$.

$\underline{(\bar{a}_0, \bar{D}_a) \in D'}$:

$$(a_0, b_0) \in int\mathcal{S} \backslash \varepsilon_- \Rightarrow \omega_0 = \mathcal{C}_s \tag{3.52}$$

$$(a_0, b_0) \in \mathcal{S} \Rightarrow \omega_0 = \varepsilon_+ \tag{3.53}$$

$$(a_0, b_0) \in \varepsilon_- \Rightarrow \omega_0 = \varepsilon_- \tag{3.54}$$

$$(a_0, b_0) \in \bar{Q} \backslash (\overline{int\mathcal{S}}) \Rightarrow \omega_0 = \varepsilon_0 \tag{3.55}$$

with $int\mathcal{S} \subset \bar{Q}$ being the interior of $\mathcal{S}$.

$\underline{(\bar{a}_0, \bar{D}_a) \in E' \cup \partial E' C'}$:

$$(a_0, b_0) \in int\mathcal{C}_u \Rightarrow \omega_0 = \varepsilon_- \tag{3.56}$$

$$(a_0, b_0) \in \mathcal{C}_u \Rightarrow \omega_0 = \mathcal{C}_u \tag{3.57}$$

$$(a_0, b_0) \in \mathcal{S} \Rightarrow \omega_0 = \varepsilon_+ \tag{3.58}$$

$$(a_0, b_0) \in \bar{Q} \backslash (\overline{int\mathcal{C}_u} \cup \mathcal{S}) \Rightarrow \omega_0 = \varepsilon_0 \tag{3.59}$$

$\underline{(\bar{a}_0, \bar{D}_a) \in F' \cup F'D'}$: $(a_0, b_0) \in int\mathcal{S} \Rightarrow \omega_0 = \varepsilon_-$ (3.60)

$(a_0, b_0) \in \mathcal{S} \Rightarrow \omega_0 = \varepsilon_+$ (3.61)

$(a_0, b_0) \in \bar{Q} \backslash (\overline{int\mathcal{S}}) \Rightarrow \omega_0 = \varepsilon_0$ (3.62)

$\underline{(\bar{a}_0, \bar{D}_a) \in \partial A'B'}$: $(a_0, b_0) \in \mathcal{S}' \Rightarrow \omega_0 = \varepsilon_\pm$ (3.63)

$(a_0, b_0) \in \bar{Q} \backslash \mathcal{S} \Rightarrow \omega_0 = \varepsilon_0$ (3.64)

with $\mathcal{S}'$ being the stable manifold of the saddle-node $\varepsilon_\pm$.

$\underline{(\bar{a}_0, \bar{D}_a) \in \partial A'F'}$: $(a_0, b_0) \in \overline{int\mathcal{S}'} \Rightarrow \omega_0 = \varepsilon_\pm$ (3.65)

$(a_0, b_0) \in \bar{Q} \backslash \overline{int\mathcal{S}} \Rightarrow \omega_0 = \varepsilon_0$ (3.66)

$\underline{(\bar{a}_0, \bar{D}_a) \in \partial F'E'}$: $(a_0, b_0) \in \mathcal{H} \cup \mathcal{S} \Rightarrow \omega_0 = \varepsilon_+$ (3.67)

$(a_0, b_0) \in int\mathcal{H} \Rightarrow \omega_0 = \varepsilon_-$ (3.68)

$(a_0, b_0) \in \bar{Q} \backslash (\overline{int\mathcal{H}} \cup \mathcal{S}) \Rightarrow \omega_0 = \varepsilon_0$ (3.69)

with $int\mathcal{H}$ being the interior of the homoclinic orbit on $\mathbf{e}_+$.

$\underline{(\bar{a}_0, \bar{D}_a) \in \partial B'C'}$: $(a_0, b_0) \in (int\mathcal{C}_b) \backslash \varepsilon_- \Rightarrow \omega_0 = \mathcal{C}_b$ (3.70)

$(a_0, b_0) \in \mathcal{S} \Rightarrow \omega_0 = \varepsilon_+$ (3.71)

$(a_0, b_0) \in \bar{Q} \backslash (\overline{int\mathcal{C}_b} \cup \mathcal{S}) \Rightarrow \omega_0 = \varepsilon_0$ (3.72)

$(a_0, b_0) \in \varepsilon_- \Rightarrow \omega_0 = \varepsilon_-$ (3.73)

$$\underline{(\bar{a}_0, \bar{D}_a) \in \partial B'D'}: \qquad (a_0, b_0) \in (int\mathcal{H})\backslash\varepsilon_- \;\Rightarrow\; \omega_0 = \mathcal{H} \tag{3.74}$$

$$(a_0, b_0) \in \varepsilon_- \;\Rightarrow\; \omega_0 = \varepsilon_- \tag{3.75}$$

$$(a_0, b_0) \in \mathcal{H} \cup \mathcal{S} \;\Rightarrow\; \omega_0 = \varepsilon_+ \tag{3.76}$$

$$(a_0, b_0) \in \bar{Q}\backslash(\overline{int\mathcal{H}} \cup \mathcal{S}) \;\Rightarrow\; \omega_0 = \varepsilon_0 \tag{3.77}$$

All cases are now complete. We can now immediately identify from the above cases the stable attractors in $\bar{Q}$, and this is exhibited in Table 3.1. It is appropriate at this point to interpret the nature of the stable attractors as power generating states for the SOFC. The equilibrium point ε_0 represents a dormant, non-power generating steady state, whilst the equilibrium point ε_- represents a constant, non-zero, power generating steady state. The stable periodic orbit $\mathcal{C}_s$ represents a time-periodic, non-zero, power generating state.

Table 3.1: Summary of attracting sets in $\bar{Q}$ for the various regions of the $(\bar{a}_0, \bar{D}_a)$ unfolding plane.

region in unfolding plane	stable attracting set in $\bar{Q}$
$A' \cup B' \cup \partial A'B' \cup \partial A'F' \cup \partial E'B' \cup \partial B'C' \cup \partial B'D'$	ε_0
$C' \cup D'$	$\varepsilon_0 \cup \mathcal{C}_s$
$E' \cup F' \cup \partial E'F' \cup \partial E'C'$	$\varepsilon_0 \cup \varepsilon_-$

3.1.9 Global Phase Portraits

In this section the global phase portraits are sketched for the regions $A' - F'$ in the $(\bar{a}_0, \bar{D}_a)$ unfolding plane via the information established in Section 3.1. The phase portraits on the boundaries between the regions A'-F' may also be readily constructed, however they are omitted for brevity. The qualitative sketches of

the global phase portraits are given in Figure 3.13, where stable limit cycles are shown with a single dash, whilst unstable ones have a double dash. In addition, the stable manifold $\mathcal{S}$ of the equilibrium point $\mathbf{e}_+$ is shown with a triple dash.

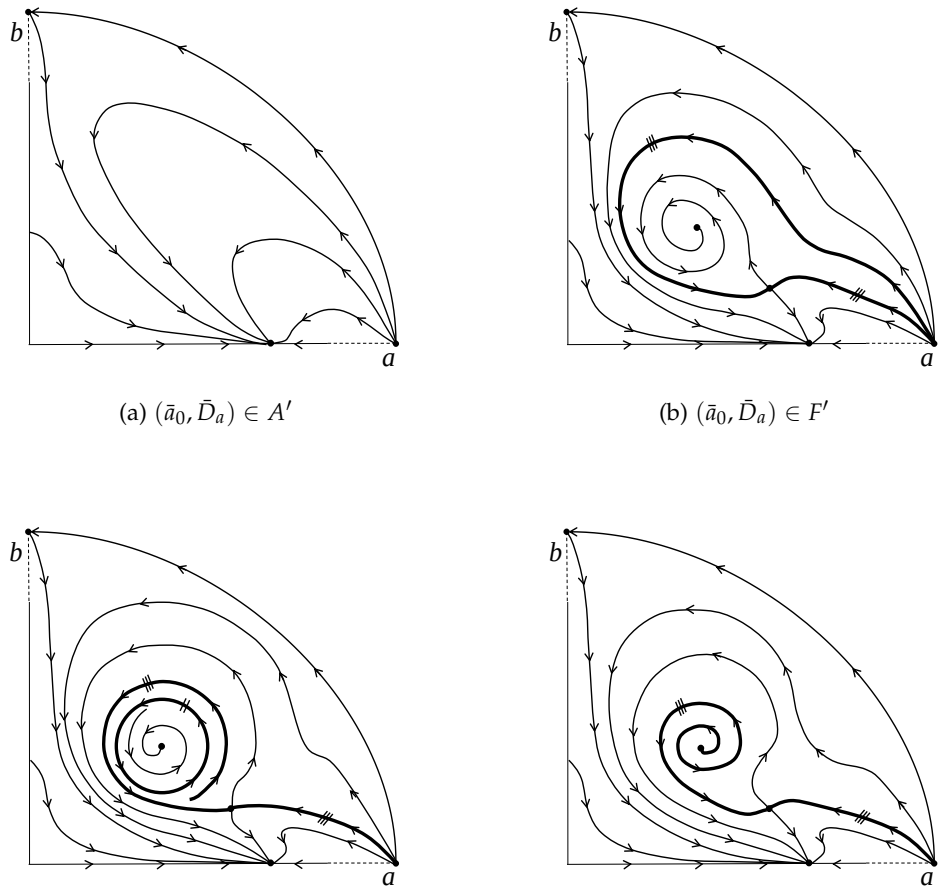

(a) $(\bar{a}_0, \bar{D}_a) \in A'$

(b) $(\bar{a}_0, \bar{D}_a) \in F'$

(c) $(\bar{a}_0, \bar{D}_a) \in E'$

(d) $(\bar{a}_0, \bar{D}_a) \in B'$

Figure 3.13: Global phase portraits for [D-S].

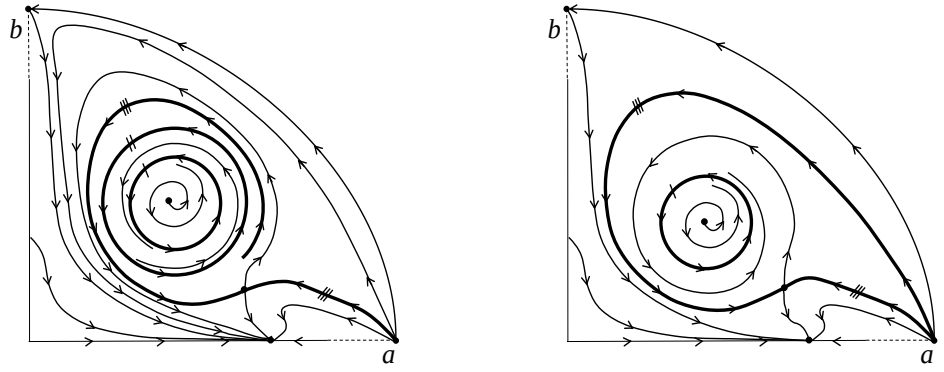

(e) $(\bar{a}_0, \bar{D}_a) \in C'$ (f) $(\bar{a}_0, \bar{D}_a) \in D'$

Figure 3.13: (Continued) Global phase portraits for [D-S].

3.2 Numerical Integration

In this section we exhibit sample numerical integrations to [D-S]. We take $\bar{D}_b = 0.6$ throughout, and select $(\bar{a}_0, \bar{D}_a)$ from illustrative regions in the unfolding plane. [D-S] is integrated forward into $t > 0$, from initial conditions $(a_0, b_0) \in \bar{Q}$, using the MATLAB *ode*23*s* solver. The graphs of $a(t)$ and $b(t)$ against $t \geq 0$ are shown in Figure 3.14. The initial conditions are chosen to illustrate the stable attracting sets in Table 3.1 and are shown in Table 3.2.

In Figure 3.14a all phase paths approach the stable equilibrium point $\mathbf{e_0} = (\bar{a}_0, 0)$ as $t \to \infty$, in accordance with the phase portrait sketched in Figure 3.13a for the region A' in the $(\bar{a_0}, \bar{D}_a)$ unfolding plane.

Figure 3.14b shows the phase paths which approach the stable equilibrium points $\mathbf{e_0}$ and $\mathbf{e}_- = (\alpha_-, \beta_-)$, representative of region F' in the $(\bar{a_0}, \bar{D}_a)$ unfolding plane, whose phase portrait was sketched in Figure 3.13b. Phase paths starting

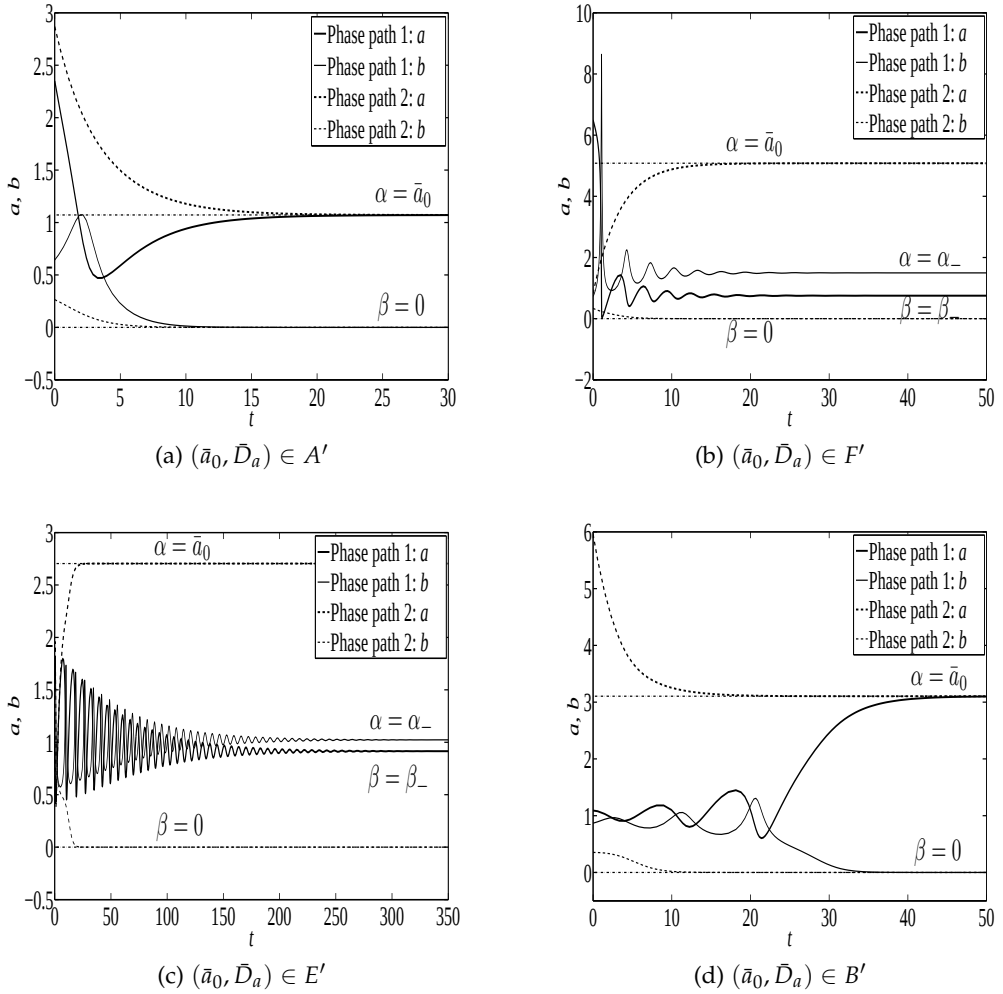

(a) $(\bar{a}_0, \bar{D}_a) \in A'$

(b) $(\bar{a}_0, \bar{D}_a) \in F'$

(c) $(\bar{a}_0, \bar{D}_a) \in E'$

(d) $(\bar{a}_0, \bar{D}_a) \in B'$

Figure 3.14: Graphs of $a(t)$ and $b(t)$ against $t \geq 0$ with $(\bar{a}_0, \bar{D}_a)$ chosen from the unfolding plane regions. Initial conditions from Table 3.2 are selected to illustrate the stable attracting sets in Table 3.1.

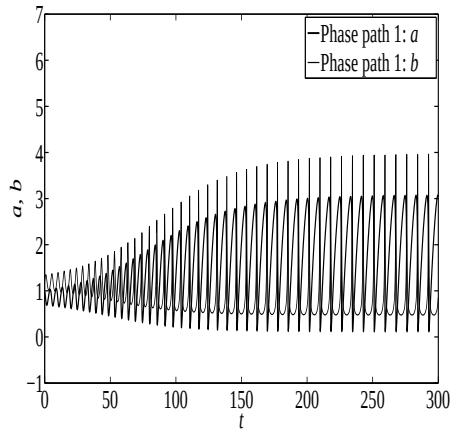

(e) Phase path 1, $(\bar{a}_0, \bar{D}_a) \in C'$

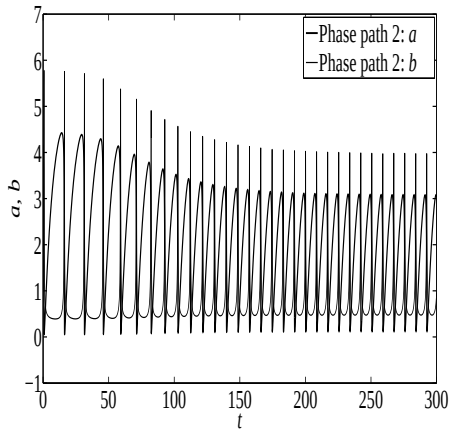

(f) Phase path 2, $(\bar{a}_0, \bar{D}_a) \in C'$

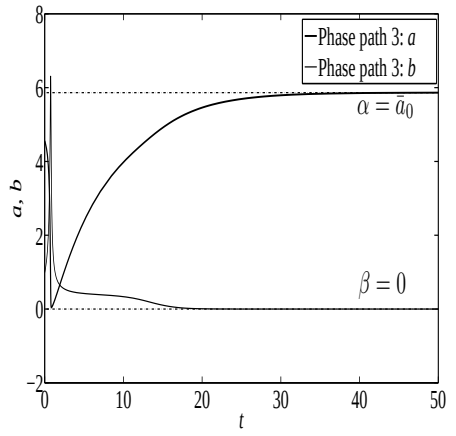

(g) Phase path 3, $(\bar{a}_0, \bar{D}_a) \in C'$

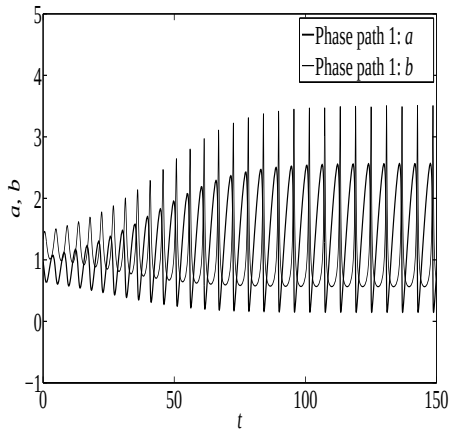

(h) Phase path 1, $(\bar{a}_0, \bar{D}_a) \in D'$

Figure 3.15: (Continued) Graphs of $a(t)$ and $b(t)$ against $t \geq 0$ with $(\bar{a}_0, \bar{D}_a)$ chosen from the unfolding plane regions. Initial conditions from Table 3.2 are selected to illustrate the stable attracting sets in Table 3.1.

Table 3.2: Initial conditions for the calculated phase paths in Figure 3.14.

region in unfolding plane $(\bar{a}_0, \bar{D}_a)$	phase path no.	initial condition $(a(t=0), b(t=0))$
A'	1	$(2.3500, 0.6428)$
$(1.0714, 0.2745)$	2	$(2.8680, 0.2650)$
B'	1	$(1.0910, 0.8673)$
$(3.1037, 0.2519)$	2	$(5.9580, 0.3527)$
C'	1	$(0.9770, 1.2190)$
$(5.8662, 0.1716)$	2	$(4.1692, 1.0503)$
	3	$(4.5557, 0.9900)$
D'	1	$(0.9679, 1.3318)$
$(9.5992, 0.1055)$	2	$(10.2214, 0.4168)$
	3	$(0.0401, 0.9686)$
E'	1	$(1.2827, 1.4412)$
$(2.7044, 0.3781)$	2	$(1.4420, 1.4120)$
F'	1	$(6.4940, 0.7272)$
$(5.0806, 0.3104)$	2	$(0.8250, 0.3393)$

within the interior of $\mathcal{S}$ spiral onto the equilibrium point $\mathbf{e}_-$, whilst those outside approach the equilibrium point $\mathbf{e_0}$.

In Figure 3.14c, which represents the region E' of the $(\bar{a_0}, \bar{D}_a)$ unfolding plane, with phase portrait sketched in Figure 3.13c, we see the same attracting set as in Figure 3.14b. Unique to the region E', however, the set of initial conditions which approach the equilibrium point $\mathbf{e}_-$ is bounded by the unstable limit cycle $\mathcal{C}_u$, as opposed to being bounded by the stable manifold $\mathcal{S}$, of the equilibrium point $\mathbf{e}_+$ for region F'. This is demonstrated in Figure 3.14c by taking the initial conditions for phase path 1 just inside the unstable limit cycle, and the initial conditions for phase path 2 just outside the unstable limit cycle (see Table 3.2).

Figure 3.14d which represents region B' in the $(\bar{a_0}, \bar{D}_a)$ unfolding plane, with phase portrait sketched in Figure 3.13d, has phase paths which approach the stable equilibrium point $\mathbf{e_0}$, although we see the appearance now of the unstable

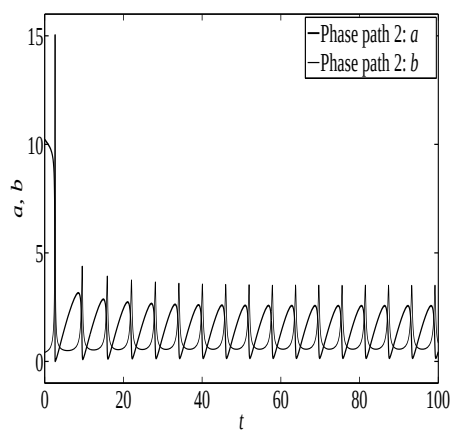

(i) Phase path 2, $(\bar{a}_0, \bar{D}_a) \in D'$

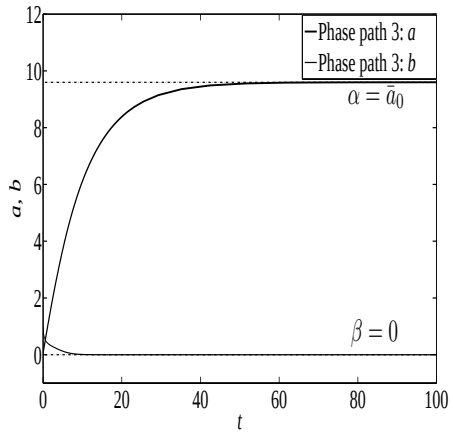

(j) Phase path 3, $(\bar{a}_0, \bar{D}_a) \in D'$

Figure 3.15: (Continued) Graphs of $a(t)$ and $b(t)$ against $t \geq 0$ with $(\bar{a}_0, \bar{D}_a)$ chosen from the unfolding plane regions. Initial conditions from Table 3.2 are selected to illustrate the stable attracting sets in Table 3.1.

equilibrium point $\mathbf{e}_-$ and the saddlepoint $\mathbf{e}_+$. Phase paths can be seen spiraling away from the equilibrium point $\mathbf{e}_-$ towards the stable equilibrium point $\mathbf{e_0}$.

The Figures 3.14e-3.14g show various phase paths for region C' in the $(\bar{a}_0, \bar{D}_a)$ unfolding plane, whilst the phase paths shown in Figures 3.14h-3.14j represent region D'. In Figures 3.14e, showing phase path 1 in region C', and 3.14h, showing phase path 1 in region D', starting close to the equilibrium point $\mathbf{e}_-$ the phase paths can be seen winding onto the stable limit cycle $\mathcal{C}_s$. Figures 3.14f and 3.14g, showing phase paths 2 and 3 in region C', can be seen approaching different attractors in the phase plane, namely, the stable limit cycle $\mathcal{C}_s$ in Figure 3.14f and the equilibrium point $\mathbf{e}_-$ in Figure 3.14g. The initial conditions are taken to be just inside, and just outside of the unstable limit cycle $\mathcal{C}_u$. Phase path 2 shown in Figure 3.14i, representing region D' in the $(\bar{a}_0, \bar{D}_a)$ unfolding plane, approaches the stable limit cycle $\mathcal{C}_s$ but starts much further out than phase path 2 in Figure

3.14f. The set of points which approach $\mathcal{C}_s$ in region D' are bounded only by the stable manifold $\mathcal{S}$ of the equilibrium point $\mathbf{e}_+$, and not by the unstable limit cycle $\mathcal{C}_u$, as in region C'. Hence initial conditions may be taken much further from the equilibrium point $\mathbf{e}_-$ and still approach $\mathcal{C}_s$. Figure 3.14j shows phase path 3 from region D' in the $(\bar{a_0}, \bar{D}_a)$ unfolding plane, which starts outside of the stable manifold $\mathcal{S}$ of the equilibrium point $\mathbf{e}_+$ and approaches the equilibrium point $\mathbf{e_0}$.

3.3 Discussion

The model presented in Chapter 2, which was derived from fundamental chemical kinetics and transfer processes, for an internal reforming SOFC which uses methane as the primary fuel, was analysed in detail. The system was considered to be governed by the reaction scheme set out in (2.1)-(2.4), in accordance with [5]. The dynamical system (2.20)-(2.22), which describes the temporal dynamics of the chemical species within the anode, was derived based on this reaction scheme, in addition to the transfer processes within the cell. Typical scales were chosen and the dynamical system (2.20)-(2.22) was non-dimensionalised with respect to these scales, leading to a reduced planar dynamical system [D-S], represented by equations (2.44)-(2.45). This system describes the temporal dynamics of the concentrations $(a(t), b(t))$, which are the non-dimensional concentrations of methane and hydrogen within the SOFC, respectively, for the case of a weakly humidified fuel stream.

Having obtained the rationally reduced planar dynamical system [D-S], it has been established that the quadrant $\bar{Q}$ is a positively invariant region, and the existence of attracting sets for [D-S] within this region have been determined, with

the ω-limit set for phase paths in $\bar{Q}$ being given by (3.15). Following this, the equilibrium points of [D-S] were identified and were analysed for stability. It was found that there exists a stable equilibrium point $\mathbf{e}_0$, irrespective of the parameter regime, but that two more equilibrium points emerge via a saddle-node bifurcation as the parameter $\bar{a}_0$ passes through the point $\bar{a}_0^{SN}(\bar{D}_a)$. One of these $(\mathbf{e}_+)$ is a saddle point, whilst the other $(\mathbf{e}_-)$ is either stable or unstable depending on the parameter regime. The equilibrium point $(\mathbf{e}_-)$ changes stability via a Hopf bifurcation as the parameter $\bar{a}_0$ passes through the point $\bar{a}_0^{H}(\bar{D}_a) > \bar{a}_0^{SN}(\bar{D}_a)$. The nature of the limit cycles associated with the Hopf bifurcations, which appear in the phase plane, are determined by the regions of the $(\bar{a}_0, \bar{D}_a)$ unfolding plane. Up to two limit cycles may coexist in the phase plane, surrounding the equilibrium point $\mathbf{e}_-$, however, at most, one of these limit cycles is stable. Sketches of the phase portraits in the various regions of the $(\bar{a}_0, \bar{D}_a)$ unfolding plane may be seen in Figure (3.13). Sample numerical integrations were given in Section 3.2 to illustrate the stable attracting sets of [D-S].

3.4 Conclusions

We conclude from the analysis in this chapter, that the temporal dynamics of an internal reforming SOFC fuelled with methane, and supplied with a weakly humidified fuel stream, are capable of displaying a wide range of behaviours. These include bifurcations, multiple steady states, and oscillatory phenomena, which is consistent with the literature (see for example, [69, 71, 96]). However, the approach here is unique in identifying key measurable dimensionless parameters which determine the bifurcation structure, and onset of nonlinear oscillations, in

terms of the diffusivities of the chemical species to the reaction zone, and the composition of the fuel stream. Practical operating conditions for an SOFC may be directly linked to the key dimensionless parameters in the model, and thus oscillations may be induced by controlling these parameters in such a way that they lie within the correct regions of the $(\bar{a}_0, \bar{D}_a)$ unfolding plane. An experimental programme has been implemented in order to verify the results of this chapter. These experiments are presented in detail in Chapter 5. Finally, the fundamental model that we have introduced reveals that the mechanism for autonomous oscillations in SOFCs is intimately related to a cubic autocatalytic reaction mechanism (see [106]) coupled with Fickian transfer from the fuel stream at the anode.

Chapter 4

Nonlinear Oscillatory Dynamics in the Reduced Model with a Humidified Fuel Stream $\overline{\text{[D-S]}}$

In this chapter, we now focus attention on the more general planar dynamical system (2.42)-(2.43) $\overline{\text{[D-S]}}$, which represents a methane fuelled SOFC when the fuel stream is fully humidified. The inclusion of fuel stream humidification will reveal additional bifurcation structure, including, equilibrium-equilibrium, periodic-equilibrium, and periodic-periodic hysteresis loops, which were not present in the case of a weakly humidified fuel stream analysed in chapter 3.

4.1 The Phase Portrait of $\overline{\text{[D-S]}}$

In this section we discuss detailed aspects of the global phase portrait of $\overline{\text{[D-S]}}$, and in particular, the associated bifurcation structure of $\overline{\text{[D-S]}}$.

4.1.1 Invariant and Attracting Sets

Firstly it is readily established that $\bar{Q}$, the closure of the quadrant $Q = \{(a, b) : a > 0, b > 0\}$, is a *strictly* positively invariant region for $\overline{\text{[D-S]}}$. Now let $\Gamma^i = \{(a, b) = (a^i(t), b^i(t)) : t \geq 0\}$ be the phase path of $\overline{\text{[D-S]}}$ which has $(a^i(0), b^i(0)) = (a_i, b_i) \in \bar{Q}$. Following Section 3.1.1 of Chapter 3 we may establish that,

$$0 < 4a^i(t) + b^i(t) \leq (4a_i + b_i)e^{-\bar{D}_m t} + \frac{4\bar{D}_a \bar{a}_0}{\bar{D}_m}(1 - e^{-\bar{D}_m t}), \tag{4.1}$$

$$0 < a^i(t) \leq \bar{a}_0 + (a_i - \bar{a}_0)e^{-\bar{D}_a t}, \tag{4.2}$$

for $t > 0$ recalling that $\bar{D}_m = min\{\bar{D}_a, \bar{D}_b\}$. Therefore each phase path Γ^i exists globally, and remains bounded in Q for all $t > 0$. Let Ω^i be the ω-limit set of Γ^i. It then follows that Ω^i is closed, connected and bounded, with

$$\Omega^i \subset Q \cap \bar{R}, \tag{4.3}$$

where R is the interior of the quadrilateral shown in Figure 4.1, given by

$$R = \{(a, b) : 0 < a < \bar{a}_0,\ b > 0,\ 0 < 4a + b < \frac{4\bar{D}_a \bar{a}_0}{\bar{D}_m}\}. \tag{4.4}$$

In addition, via the Poincarè-Bendixson Theorem [114], Ω^i is either a single equilibrium point of $\overline{\text{[D-S]}}$, a periodic orbit of $\overline{\text{[D-S]}}$, or a homoclinic/heteroclinic orbit of $\overline{\text{[D-S]}}$. We may conclude that every equilibrium point, periodic orbit and homoclinic/heteroclinic orbit of $\overline{\text{[D-S]}}$ in $\bar{Q}$, must lie in $Q \cap \bar{R}$. Moreover Γ^i must approach such an equilibrium point, periodic orbit or homoclinic/heteroclinic orbit as $t \to \infty$. The above conclusions are similar to those in Section 3.1.1 of

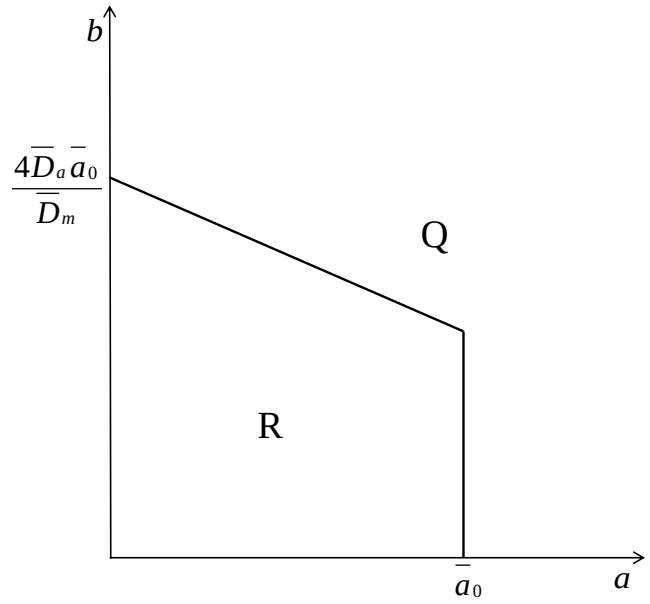

Figure 4.1: The region $R \subset Q$.

Chapter 3 (with $\bar{c}_0 = 0$) except that $\bar{R}$ is replaced by $Q \cap \bar{R}$ when $\bar{c}_0 > 0$.

4.1.2 Equilibrium Points and Equilibrium Point Bifurcations

In this section we identify the equilibrium points of $\overline{\text{[D-S]}}$ in $\bar{Q}$ and discuss the occurrence of equilibrium point bifurcations. We denote an equilibrium point of $\overline{\text{[D-S]}}$ in $\bar{Q}$ by $(a, b) = (\alpha, \beta)$. Then from (4.3) and (4.4) we have that,

$$0 < \alpha \leq \bar{a}_0, \qquad 0 < \beta \leq 4\left(\frac{\bar{D}_a\bar{a}_0}{\bar{D}_m} - \alpha\right). \tag{4.5}$$

From equations (2.42) and (2.43), the equilibrium points of $\overline{\text{[D-S]}}$ are solutions of the two nonlinear algebraic equations,

$$\bar{D}_a(\bar{a}_0 - \alpha) - \frac{\alpha(2\beta^2 + \bar{c}_0)}{(2\alpha + 1)} = 0, \tag{4.6}$$

$$-\bar{D}_b\beta + \frac{4\alpha(2\beta + \bar{c}_0)}{(2\alpha + 1)} - 2\beta^2 = 0. \tag{4.7}$$

From (4.6) we have,

$$\beta^2 = \frac{\bar{D}_a(\bar{a}_0 - \alpha)(2\alpha + 1)}{2\alpha} - \frac{\bar{c}_0}{2}. \tag{4.8}$$

It follows from (4.5) and (4.8) that,

$$0 < \alpha < \alpha_c(\bar{a}_0, \bar{D}_a, \bar{c}_0) < \bar{a}_0, \tag{4.9}$$

where,

$$\alpha_c(\bar{a}_0, \hat{D}_a) = \frac{1}{2}\left(\left(\bar{a}_0 - \frac{1}{2} - \frac{1}{2\hat{D}_a}\right) + \sqrt{\left(\bar{a}_0 - \frac{1}{2} - \frac{1}{2\hat{D}_a}\right)^2 + 2\bar{a}_0}\right) \tag{4.10}$$

Here we have introduced the notation $\hat{D}_a = \frac{\bar{D}_a}{\bar{c}_0}$ and $\hat{D}_b = \frac{\bar{D}_b}{\sqrt{\bar{c}_0}}$. It follows from (4.10) that,

$$\alpha_c(\bar{a}_0, \hat{D}_a) = \begin{cases} \frac{\hat{D}_a\bar{a}_0}{(1+\hat{D}_a)} + o(\bar{a}_0) & \text{as } \bar{a}_0 \to 0^+ \\ \bar{a}_0 - \frac{1}{2\hat{D}_a} + o(1) & \text{as } \bar{a}_0 \to \infty \end{cases} \tag{4.11}$$

Substituting for β from (4.8) into (4.7) we arrive at,

$$F(\alpha; \bar{a}_0, \hat{D}_a, \hat{D}_b) = 0, \qquad 0 < \alpha < \alpha_c(\bar{a}_0, \hat{D}_a), \tag{4.12}$$

where,

$$\begin{aligned} F(\alpha; \bar{a}_0, \hat{D}_a, \hat{D}_b) &= \hat{D}_a(\bar{a}_0 - \alpha)(1 - 2\alpha) - \alpha \\ &+ \frac{\hat{D}_b \alpha^{\frac{1}{2}}}{\sqrt{2}} \left(\hat{D}_a(\bar{a}_0 - \alpha)(2\alpha + 1) - \alpha\right)^{\frac{1}{2}}, \quad 0 < \alpha < \alpha_c(\bar{a}_0, \hat{D}_a) \end{aligned} \tag{4.13}$$

We observe that,

$$F(0; \bar{a}_0, \hat{D}_a, \hat{D}_b) = \hat{D}_a \bar{a}_0, \tag{4.14}$$

$$F(\alpha_c; \bar{a}_0, \hat{D}_a, \hat{D}_b) = -4\hat{D}_a \alpha_c(\bar{a}_0 - \alpha_c), \tag{4.15}$$

which, via (4.9), guarantees the existence of at least one equilibrium point of $\overline{\text{[D-S]}}$. We now examine the roots of (4.12) over the interval, $\alpha \in (0, \alpha_c)$. The parameters $\bar{D}_b$ and $\bar{c}_0$ are treated as fixed, with $\bar{a}_0$ and $\bar{D}_a$ taken as the bifurcation and unfolding parameters respectively, as in the previous chapter. There are three cases to consider:

Case (I): $0 < \bar{c}_0 \leq \frac{1}{16}\bar{D}_b^2$

In this case, the set of equilibrium points is similar to that in Section 3.1.2 of Chapter 3. Fixing $\bar{D}_a > 0$, then there is an equilibrium point $\mathbf{e_0} = (\alpha_0, \beta_0) \in Q \cap \bar{R}$ which exists for each $\bar{a}_0 > 0$. In addition, a saddle-node bifurcation occurs at $\bar{a}_0 = \bar{a}_0^{SN}(\bar{D}_a)$, which creates two additional equilibrium points, $\mathbf{e}_+ = (\alpha_+, \beta_+) \in$

$Q \cap \bar{R}$ and $\mathbf{e}_- = (\alpha_-, \beta_-) \in Q \cap \bar{R}$, when $\bar{a}_0 > \bar{a}_0^{SN}$. The situation is illustrated in Figure 4.2a in the $(\bar{a}_0, \alpha)$ bifurcation diagram. In accord with the Figure 4.2a, we have,

$$\alpha_0 = \begin{cases} \frac{\hat{D}_a \bar{a}_0}{(1+\hat{D}_a)} + o(\bar{a}_0), & \text{as } \bar{a}_0 \to 0^+ \\ \bar{a}_0 - \frac{X^-(\hat{D}_b)}{2\hat{D}_a} + o(1), & \text{as } \bar{a}_0 \to \infty \end{cases} \tag{4.16}$$

$$\alpha_+ = \bar{a}_0 - \frac{X^+(\hat{D}_b)}{2\hat{D}_a} + o(1), \qquad \text{as } \bar{a}_0 \to \infty \tag{4.17}$$

$$\alpha_- = \tfrac{1}{2} + o(1), \qquad \text{as } \bar{a}_0 \to \infty \tag{4.18}$$

with,

$$X^{\pm} = \frac{1}{4}\left((\hat{D}_b^2 - 4) \pm \hat{D}_b (\hat{D}_b^2 - 16)^{\frac{1}{2}} \right). \tag{4.19}$$

Case (II): $\frac{1}{16}\bar{D}_b^2 < \bar{c}_0 < \bar{c}_0^*(\bar{D}_b)$

Here $\bar{c}_0^*(\bar{D}_b) > \frac{1}{16}\bar{D}_b$, and depends upon $\bar{D}_b$. In this case there is a value $\bar{D}_a = \bar{D}_a^{\chi}(\bar{D}_b, \bar{c}_0)$ which divides two sub-cases, namely,

(a) $\bar{D}_a > \bar{D}_a^{\chi}(\bar{D}_b, \bar{c}_0)$

In this case there are two saddle-node bifurcations at $\bar{a}_0 = \bar{a}_0^{SN_-}(\bar{D}_a)$ and $\bar{a}_0 = \bar{a}_0^{SN_+}(\bar{D}_a)$, with $0 < \bar{a}_0^{SN_-}(\bar{D}_a) < \bar{a}_0^{SN_+}(\bar{D}_a)$. Associated with these saddle-node

bifurcations are three equilibrium points, in $Q \cap \bar{R}$,

$$\begin{aligned}
&\mathbf{e_0} = (\alpha_0, \beta_0), && 0 < \bar{a}_0 \leq \bar{a}_0^{SN_+}(\bar{D}_a) \\
&\mathbf{e}_+ = (\alpha_+, \beta_+), && \bar{a}_0^{SN_-}(\bar{D}_a) < \bar{a}_0 < \bar{a}_0^{SN_+}(\bar{D}_a) \\
&\mathbf{e}_- = (\alpha_-, \beta_-), && \bar{a}_0 \geq \bar{a}_0^{SN_-}(\bar{D}_a).
\end{aligned}$$

The situation is shown in the $(\bar{a}_0, \alpha)$ bifurcation diagram in Figure 4.2b. Again, we have,

$$\begin{aligned}
&\alpha_0 = \tfrac{\hat{D}_a \bar{a}_0}{(1+\hat{D}_a)} + o(\bar{a}_0), && \text{as } \bar{a}_0 \to 0^+ \\
&\alpha_- = \tfrac{1}{2} + o(1), && \text{as } \bar{a}_0 \to \infty.
\end{aligned}$$

We note that $\bar{a}_0^{SN_+}(\bar{D}_a^\chi) = \bar{a}_0^{SN_-}(\bar{D}_a^\chi) = \bar{a}_0^\chi$.

(b): $0 < \bar{D}_a \leq \bar{D}_a^\chi(\bar{D}_b, \bar{c}_0)$

In this case there is just a single equilibrium point in $Q \cap \bar{R}$,

$$\mathbf{e_0} = (\alpha_0, \beta_0), \qquad \bar{a}_0 > 0,$$

with no equilibrium point bifurcations occurring. In particular, we have,

$$\alpha_0 = \begin{cases} \tfrac{\hat{D}_a \bar{a}_0}{(1+\hat{D}_a)} + o(\bar{a}_0), & \text{as } \bar{a}_0 \to 0^+ \\ \tfrac{1}{2} + o(1), & \text{as } \bar{a}_0 \to \infty. \end{cases} \tag{4.20}$$

For $\bar{D}_a$ close to $\bar{D}_a^\chi$, the situation is as illustrated in Figure 4.2c. The maximum point in Figure 4.2c disappears in decreasing $\bar{D}_a$, and thereafter adopts the struc-

ture shown in Figure 4.2d.

Case (III): $\bar{c}_0 > \bar{c}_0^*(\bar{D}_b)$

In this case there is just a single equilibrium point in $Q \cap \bar{R}$ for all $\bar{D}_a > 0$,

$$\mathbf{e_0} = (\alpha_0, \beta_0), \qquad \bar{a}_0 > 0,$$

with no equilibrium point bifurcations occurring. In particular we have,

$$\alpha_0 = \begin{cases} \frac{\hat{D}_a \bar{a}_0}{(1+\hat{D}_a)} + o(\bar{a}_0), & \text{as } \bar{a}_0 \to 0^+ \\ \frac{1}{2} + o(1), & \text{as } \bar{a}_0 \to \infty \end{cases} . \tag{4.21}$$

The situation is as illustrated in Figure 4.2d.

We are now in a position to sketch the $(\bar{a}_0, \bar{D}_a)$ unfolding diagrams. In each of the three cases identified above, the $(\bar{a}_0, \bar{D}_a)$ unfolding diagrams are sketched in Figure 4.3, indicating the locus of the associated equilibrium point bifurcations.

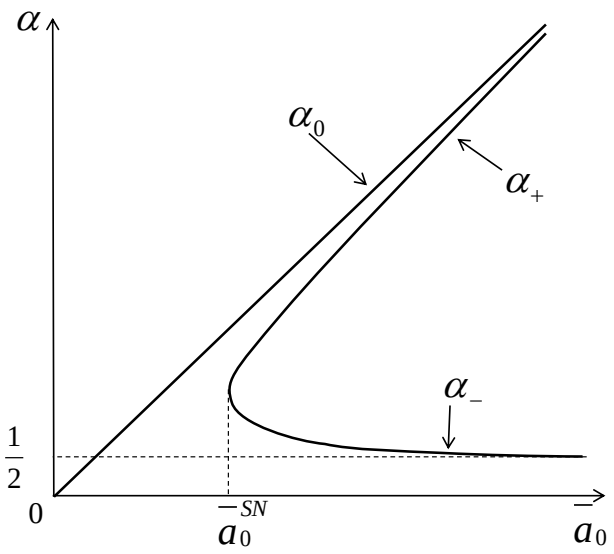

(a) For case (I)

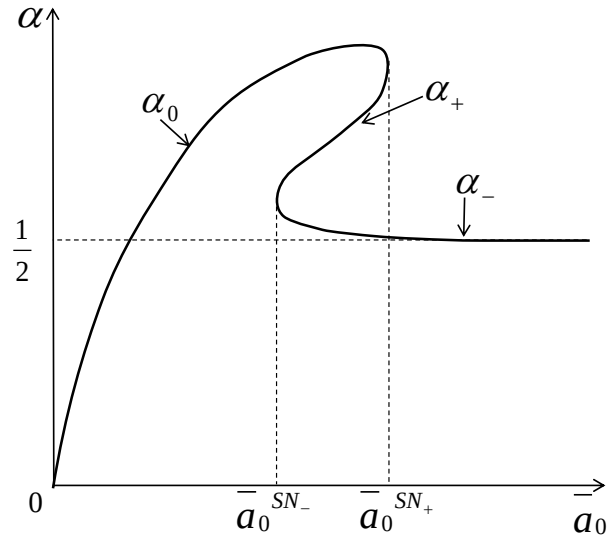

(b) For case (II)(a)

Figure 4.2: Equilibrium point bifurcation diagram in the $(\bar{a}_0, \alpha)$ plane.

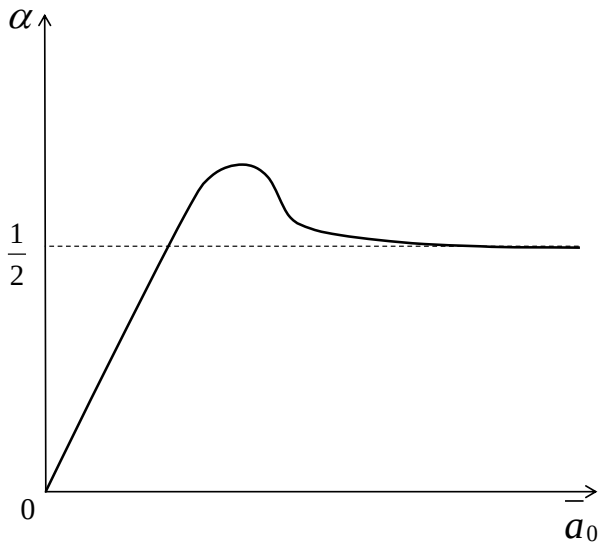

(c) For case (II)(b) and case (III) with $\bar{D}_a$ close to $\bar{D}_a^{\chi}$

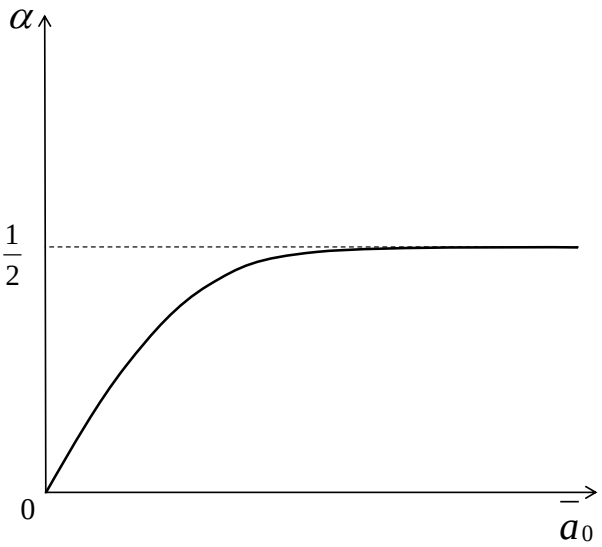

(d) For case (II)(b) and case (III) with $\bar{D}_a$ well below $\bar{D}_a^{\chi}$

Figure 4.2: (Continued) Equilibrium point bifurcation diagram in the $(\bar{a}_0, \alpha)$ plane.

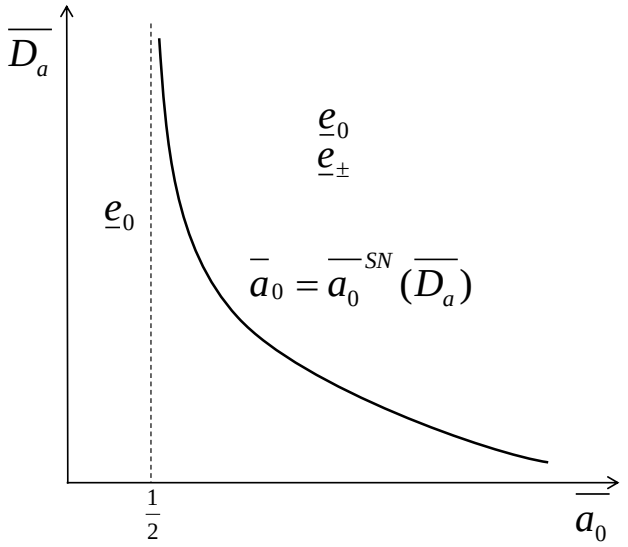

(a) For case (I)

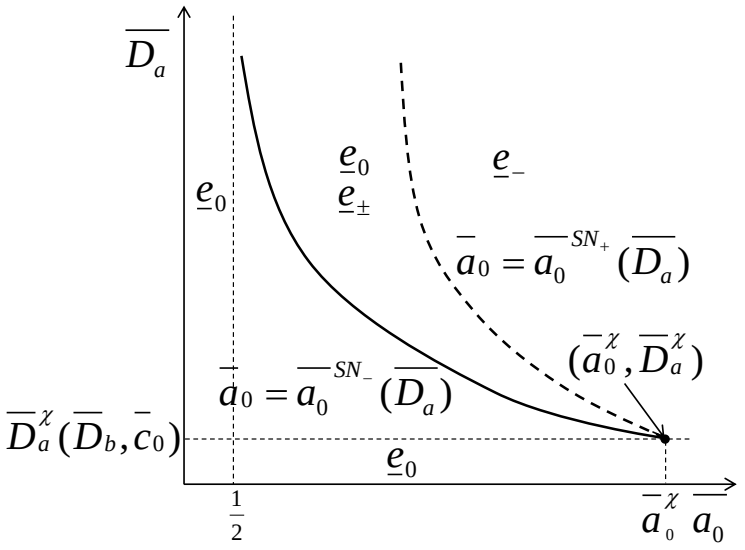

(b) For case (II)(a), (b)

Figure 4.3: The $(\bar{a}_0, \bar{D}_a)$ unfolding plane.

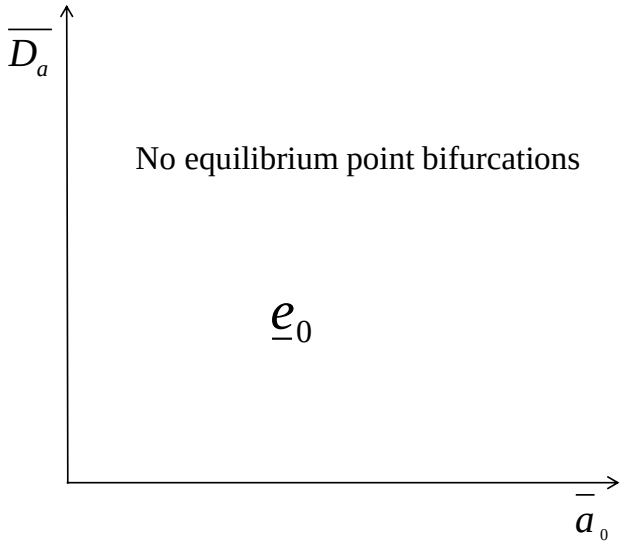

(c) For case (III)

Figure 4.4: (Continued) The $(\bar{a}_0, \bar{D}_a)$ unfolding plane.

4.1.3 Equilibrium Point Stability

Having identified the existence of the equilibrium points of $\overline{\text{[D-S]}}$, we now examine the local stability of $\mathbf{e_0}$, $\mathbf{e}_+$ and $\mathbf{e}_-$ via the linearization theorem. Each of the equilibrium points $\mathbf{e_0}$, $\mathbf{e}_+$ and $\mathbf{e}_-$ have eigenvalues associated with the linearization of $\overline{\text{[D-S]}}$ given by the roots of the characteristic equation,

$$\lambda^2 + \Gamma(\alpha)\lambda + \Delta(\alpha) = 0, \tag{4.22}$$

where,

$$\Gamma(\alpha) = \bar{D}_a + \bar{D}_b + \frac{(2\beta^2 + \bar{c}_0)}{(2\alpha+1)^2} - \frac{4\beta(2\alpha-1)}{(2\alpha+1)}, \tag{4.23}$$

and,

$$\Delta(\alpha) = \bar{D}_a\bar{D}_b - \frac{4\bar{D}_a\beta(2\alpha-1)}{(2\alpha+1)} + \frac{\bar{D}_b(2\beta^2+\bar{c}_0)}{(2\alpha+1)^2} + \frac{4\beta(2\beta^2+\bar{c}_0)}{(2\alpha+1)^2}. \tag{4.24}$$

Equations (4.22)-(4.24) allow us to examine the cases described in Section 3.1.2 for stability of the equilibrium points $\mathbf{e_0}$, $\mathbf{e}_+$ and $\mathbf{e}_-$.

Case (I): $0 < \bar{c}_0 \leq \frac{1}{16}\bar{D}_b^2$

The stability characteristics of the equilibrium points in this case is similar to that in Section 3.1.3 of Chapter 3. Examining the eigenvalues in (4.22)-(4.24) we find that,

$\mathbf{e_0}(\bar{a}_0)$	is a hyperbolic stable node for all $\bar{a}_0 > 0$ and $\bar{D}_a$, $\bar{D}_b > 0$.
$\mathbf{e}_+(\bar{a}_0)$	is a hyperbolic saddle point for all $\bar{a}_0 > \bar{a}_0^{SN}(\bar{D}_a)$ and $\bar{D}_a$, $\bar{D}_b > 0$.

However there exists a value $\bar{D}_a = \bar{D}_a^*$ (which depends upon $\bar{D}_b$ and $\bar{c}_0$), with

$0 < \bar{D}_a^*(\bar{D}_b, \bar{c}_0) < \bar{D}_b$ and for which,

- $\mathbf{e}_-(\bar{a}_0)$ is a hyperbolic stable node for all $\bar{a}_0 > \bar{a}_0^{SN}(\bar{D}_a)$ and $\bar{D}_a \geq \bar{D}_a^*(\bar{D}_b, \bar{c}_0)$.
- $\mathbf{e}_-(\bar{a}_0)$ is a hyperbolic unstable node or spiral for all $\bar{a}_0^{SN}(\bar{D}_a) < \bar{a}_0 < \bar{a}_0^H(\bar{D}_a)$ and $0 < \bar{D}_a < \bar{D}_a^*(\bar{D}_b, \bar{c}_0)$.
- $\mathbf{e}_-(\bar{a}_0)$ is a hyperbolic stable node or spiral for $\bar{a}_0 > \bar{a}_0^H(\bar{D}_a)$ and $0 < \bar{D}_a < \bar{D}_a^*(\bar{D}_b, \bar{c}_0)$.

Here $\bar{a}_0^H(\bar{D}_a) > \bar{a}_0^{SN}(\bar{D}_a)$ for all $0 < \bar{D}_a < \bar{D}_a^*(\bar{D}_b, \bar{c}_0)$, and we note that $\bar{a}_0^{SN}(\bar{D}_a^*) = \bar{a}_0^H(\bar{D}_a^*) = a^*$, with $(a^*, \bar{D}_a^*)$ being the unfolding point in the unfolding diagram. The situation is illustrated in Figure 4.5a on the $(\bar{a}_0, \bar{D}_a)$ unfolding diagram.

Case (II): $\frac{1}{16}\bar{D}_b^2 < \bar{c}_0 < \bar{c}_0^*(\bar{D}_b)$

Here there are two sub-cases.

(a) $\bar{D}_a > \bar{D}_a^{\chi}(\bar{D}_b, \bar{c}_0)$

In this case we have that,

- $\mathbf{e_0}(\bar{a}_0)$ is a hyperbolic stable node for all $\bar{D}_a > \bar{D}_a^{\chi}(\bar{D}_b, \bar{c}_0)$ and $0 < \bar{a}_0 < \bar{a}_0^{SN_+}(\bar{D}_a)$.
- $\mathbf{e}_+(\bar{a}_0)$ is a hyperbolic saddle point for all $\bar{D}_a > \bar{D}_a^{\chi}(\bar{D}_b, \bar{c}_0)$and $\bar{a}_0^{SN_-}(\bar{D}_a) < \bar{a}_0 < \bar{a}_0^{SN_+}(\bar{D}_a)$.

When considering $\mathbf{e}_-(\bar{a}_0)$, we find that there exists a value $\frac{1}{16}\bar{D}_b^2 < \bar{c}_0^{\phi}(\bar{D}_b) <$

$\bar{c}_0^*(\bar{D}_b)$, such that for $\bar{c}_0^{\phi}(\bar{D}_b) < \bar{c}_0 < \bar{c}_0^*(\bar{D}_b)$,

$$\mathbf{e}_-(\bar{a}_0) \quad \text{is a hyperbolic stable node for } \bar{D}_a > \bar{D}_a^{\chi}(\bar{D}_b, \bar{c}_0) \text{ and } \bar{a}_0 > \bar{a}_0^{SN_-}(\bar{D}_a).$$

However for $\frac{1}{16}\bar{D}_b^2 < \bar{c}_0 < \bar{c}_0^{\phi}(\bar{D}_b)$, there exists a value $\bar{D}_a^*(\bar{D}_b, \bar{c}_0) > \bar{D}_a^{\chi}(\bar{D}_b, \bar{c}_0)$, with, for $\bar{D}_a > \bar{D}_a^*(\bar{D}_b, \bar{c}_0)$,

$$\mathbf{e}_-(\bar{a}_0) \quad \text{is a hyperbolic stable node or spiral for } \bar{D}_a > \bar{D}_a^*(\bar{D}_b, \bar{c}_0) \text{ and } \bar{a}_0 > \bar{a}_0^{SN_-}(\bar{D}_a),$$

whilst for $\bar{D}_a^{\chi}(\bar{D}_b, \bar{c}_0) < \bar{D}_a < \bar{D}_a^*(\bar{D}_b, \bar{c}_0)$ there exists $\bar{a}_0 = \bar{a}_0^{H^+}(\bar{D}_a)$ such that,

$$\mathbf{e}_-(\bar{a}_0) \quad \text{is a hyperbolic unstable node or spiral for } \bar{D}_a^{\chi}(\bar{D}_b, \bar{c}_0) < \bar{D}_a < \bar{D}_a^*(\bar{D}_b, \bar{c}_0) \text{ and } \bar{a}_0^{SN_-}(\bar{D}_a) < \bar{a}_0 < \bar{a}_0^{H^+}(\bar{D}_a).$$

$$\mathbf{e}_-(\bar{a}_0) \quad \text{is a hyperbolic stable node or spiral for } \bar{D}_a^{\chi}(\bar{D}_b, \bar{c}_0) < \bar{D}_a < \bar{D}_a^*(\bar{D}_b, \bar{c}_0) \text{ and } \bar{a}_0 > \bar{a}_0^{H^+}(\bar{D}_a).$$

(b) $0 < \bar{D}_a \leq \bar{D}_a^{\chi}(\bar{D}_b, \bar{c}_0)$

In this case, when $\bar{c}_0^{\phi}(\bar{D}_b) < \bar{c}_0 < \bar{c}_0^*(\bar{D}_b)$, there exists $0 < \bar{D}_a^*(\bar{D}_b, \bar{c}_0) < \bar{D}_a^{\chi}(\bar{D}_b, \bar{c}_0)$, such that when $\bar{D}_a^*(\bar{D}_b, \bar{c}_0) < \bar{D}_a < \bar{D}_a^{\chi}(\bar{D}_b, \bar{c}_0)$, then,

$$\mathbf{e_0}(\bar{a}_0) \quad \text{is a hyperbolic stable node or spiral for } \bar{D}_a^*(\bar{D}_b, \bar{c}_0) < \bar{D}_a < \bar{D}_a^{\chi}(\bar{D}_b, \bar{c}_0) \text{ and } \bar{a}_0 > 0,$$

whilst, when $0 < \bar{D}_a < \bar{D}_a^*(\bar{D}_b, \bar{c}_0)$, there exist values $\bar{a}_0^{H^+}(\bar{D}_a)$ and $\bar{a}_0^{H^-}(\bar{D}_a)$, with

$\bar{a}_0^{H^+}(\bar{D}_a) > \bar{a}_0^{H^-}(\bar{D}_a)$, such that,

- $\mathbf{e_0}(\bar{a}_0)$ is a hyperbolic stable node or spiral for $\bar{D}_a < \bar{D}_a^*(\bar{D}_b, \bar{c}_0)$ and $0 < \bar{a}_0 < \bar{a}_0^{H^-}(\bar{D}_a)$.
- $\mathbf{e_0}(\bar{a}_0)$ is a hyperbolic unstable node or spiral for $0 < \bar{D}_a < \bar{D}_a^*(\bar{D}_b, \bar{c}_0)$ and $\bar{a}_0^{H^-}(\bar{D}_a) < \bar{a}_0 < \bar{a}_0^{H^+}(\bar{D}_a)$.
- $\mathbf{e_0}(\bar{a}_0)$ is a hyperbolic stable node or spiral for $0 < \bar{D}_a < \bar{D}_a^*(\bar{D}_b, \bar{c}_0)$ and $\bar{a}_0 > \bar{a}_0^{H^+}(\bar{D}_a)$.

When $\frac{1}{16}\bar{D}_b^2 < \bar{c}_0 < \bar{c}_0^{\phi}(\bar{D}_b)$, then there exist values $\bar{a}_0^{H^+}(\bar{D}_a)$ and $\bar{a}_0^{H^-}(\bar{D}_a)$, with $\bar{a}_0^{H^+}(\bar{D}_a) > \bar{a}_0^{H^-}(\bar{D}_a)$, such that,

- $\mathbf{e_0}(\bar{a}_0)$ is a hyperbolic stable node or spiral for $0 < \bar{D}_a < \bar{D}_a^{\chi}(\bar{D}_b, \bar{c}_0)$ and $0 < \bar{a}_0 < \bar{a}_0^{H^-}(\bar{D}_a)$.
- $\mathbf{e_0}(\bar{a}_0)$ is a hyperbolic unstable node or spiral for $0 < \bar{D}_a < \bar{D}_a^{\chi}(\bar{D}_b, \bar{c}_0)$ and $\bar{a}_0^{H^-}(\bar{D}_a) < \bar{a}_0 < \bar{a}_0^{H^+}(\bar{D}_a)$.
- $\mathbf{e_0}(\bar{a}_0)$ is a hyperbolic stable node or spiral for $0 < \bar{D}_a < \bar{D}_a^{\chi}(\bar{D}_b, \bar{c}_0)$ and $\bar{a}_0 > \bar{a}_0^{H^+}(\bar{D}_a)$.

We note in this case that there are two unfolding points in the $(\bar{a}_0, \bar{D}_a)$ unfolding diagram, at $(\bar{a}_0^*, \bar{D}_a^*)$ and $(\bar{a}_0^{\chi}, \bar{D}_a^{\chi})$. The situation is illustrated on the $(\bar{a}_0, \bar{D}_a)$ unfolding diagram in Figures 4.5b and 4.5c.

Case (III): $\bar{c}_0 > \bar{c}_0^*(\bar{D}_b)$

In this case there is only the single equilibrium point $\mathbf{e_0}$. Also, there exists a value

$\bar{D}_a^*(\bar{D}_b, \bar{c}_0)$ such that when $\bar{D}_a > \bar{D}_a^*(\bar{D}_b, \bar{c}_0)$,

$$\mathbf{e_0}(\bar{a}_0) \quad \text{is a hyperbolic stable node or spiral for } \bar{a}_0 > 0,$$

whilst for $\bar{D}_a < \bar{D}_a^*(\bar{D}_b, \bar{c}_0)$,

$\mathbf{e_0}(\bar{a}_0)$ is a hyperbolic stable node or spiral for $0 < \bar{a}_0 < \bar{a}_0^{H^-}(\bar{D}_a)$.

$\mathbf{e_0}(\bar{a}_0)$ is a hyperbolic unstable node or spiral for $\bar{a}_0^{H^-}(\bar{D}_a) < \bar{a}_0 < \bar{a}_0^{H^+}(\bar{D}_a)$.

$\mathbf{e_0}(\bar{a}_0)$ is a hyperbolic stable node or spiral for $\bar{a}_0 > \bar{a}_0^{H^+}(\bar{D}_a)$.

Here, $0 < \bar{a}_0^{H^-}(\bar{D}_a) < \bar{a}_0^{H^+}(\bar{D}_a)$ for $0 < \bar{D}_a < \bar{D}a(\bar{D}_b, \bar{c}_0)$, and $\bar{a}_a^{H^-}(\bar{D}_a) = \bar{a}_0^{H^+}(\bar{D}_a)$ when $\bar{D}_a = \bar{D}_a^*(\bar{D}_b, \bar{c}_0)$.

We note in this case that there is a single unfolding point in the $(\bar{a}_0, \bar{D}_a)$ unfolding plane at $(\bar{a}_0^*, \bar{D}_a^*)$. The situation is illustrated on the $(\bar{a}_0, \bar{D}_a)$ unfolding diagram in Figure 4.5d.

We have now characterized the local stability properties of the equilibrium points $\mathbf{e_0}$, $\mathbf{e}_+$ and $\mathbf{e}_-$ and may use this information to locate any local bifurcations to periodic orbits.

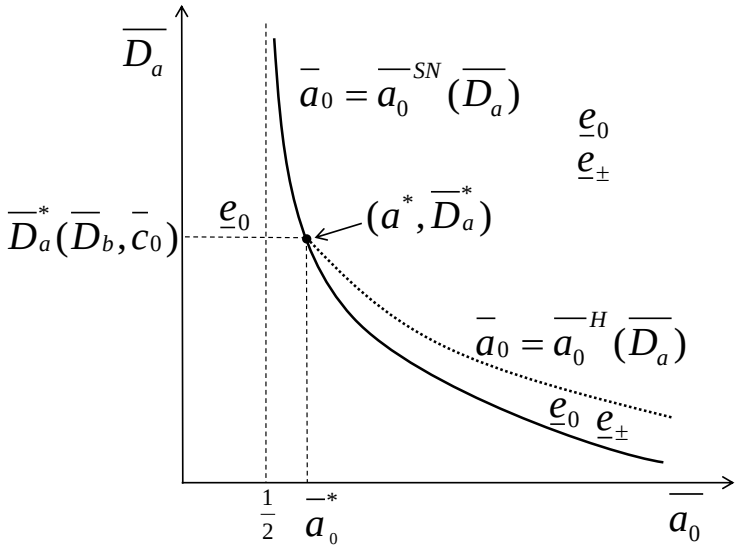

(a) For case (I)

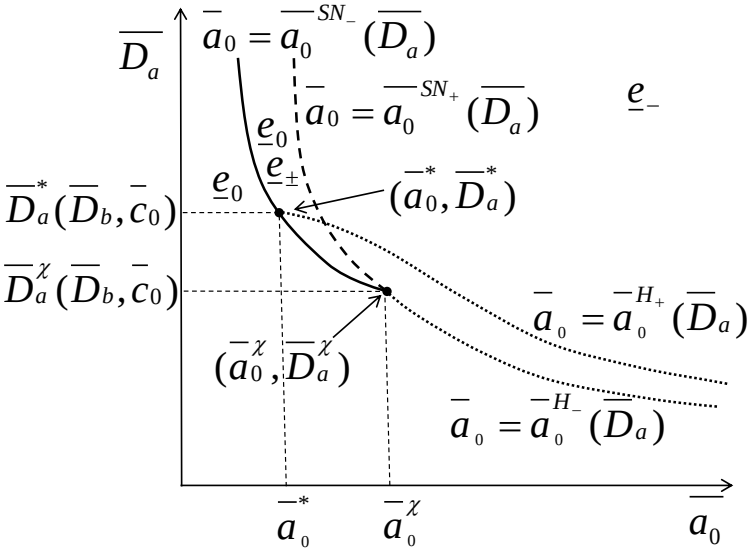

(b) For case (II)(a) and (b) with $\frac{1}{16}\bar{D}_b^2 < \bar{c}_0 < \bar{c}_0^\phi(\bar{D}_b)$ and $\bar{D}_a^*(\bar{D}_a, \bar{c}_0) > \bar{D}_a^\chi(\bar{D}_b, \bar{c}_0)$

Figure 4.5: The $(\bar{D}_a, \bar{a}_0))$ unfolding plane.

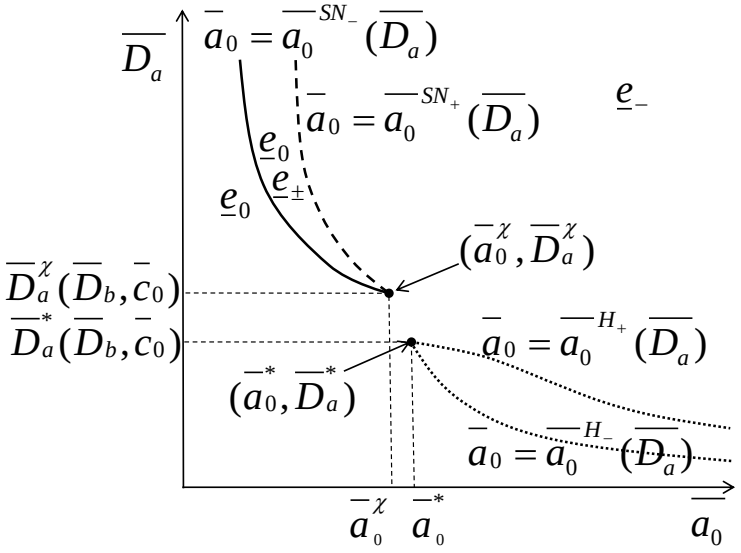

(c) For case (II)(a) and (b) with $\bar{c}_0^\phi(\bar{D}_b) < \bar{c}_0 < \bar{c}_0^*(\bar{D}_b)$ and $\bar{D}_a^*(\bar{D}_a, \bar{c}_0) < \bar{D}_a^\chi(\bar{D}_b, \bar{c}_0)$

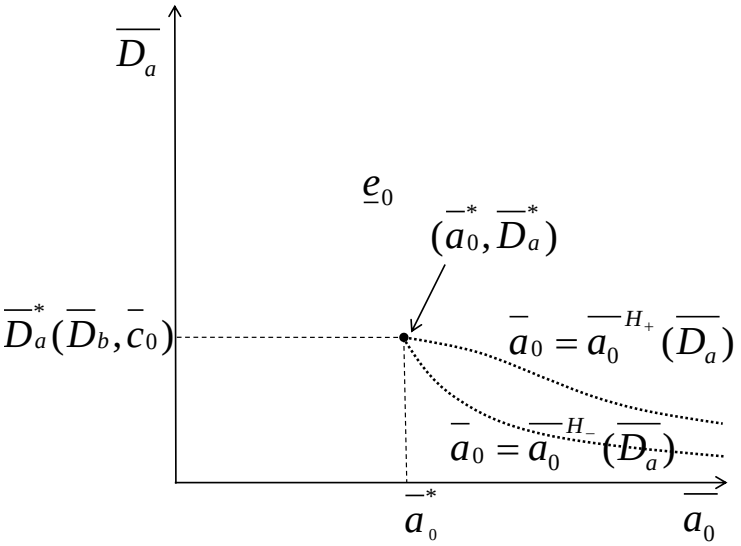

(d) For case (III)

Figure 4.5: (Continued) The $(\bar{D}_a, \bar{a}_0))$ unfolding plane.

4.2 Bifurcation to Periodic Orbits

We can now identify the periodic orbits in the phase portrait of $\overline{\text{[D-S]}}$ arising via Hopf bifurcations at the equilibrium points for the cases presented in Section 4.1.3.

Case (I): $0 < \bar{c}_0 \leq \frac{\bar{D}_b^2}{16}$

The occurrence of periodic orbits for this case is detailed in Section 3.1.7 of Chapter 3, and is summarised here.

A Hopf bifurcation occurs for each $0 < \bar{D}_a < \bar{D}_a^*(\bar{D}_b, \bar{c}_0)$, at the equilibrium point $\mathbf{e}_-$ when, $\bar{a}_0 = \bar{a}_0^H(\bar{D}_a) > \bar{a}_0^{SN}(\bar{D}_a)$. There exists a value $\bar{D}_a^c$, which depends on $\bar{D}_b$ and $\bar{c}_0$, with $0 < \bar{D}_a^c(\bar{D}_b, \bar{c}_0) < \bar{D}_a^*(\bar{D}_b, \bar{c}_0)$, that subdivides three cases, namely:

(a) $\bar{D}_a^c(\bar{D}_b, \bar{c}_0) < \bar{D}_a < \bar{D}_a^*(\bar{D}_b, \bar{c}_0)$

In this case the Hopf bifurcation at $\mathbf{e}_-$, when $(\bar{a}_0, \bar{D}_a) = (\bar{a}_0^H(\bar{D}_a), \bar{D}_a)$, is supercritical, creating a (unique) unstable, limit cycle in $\bar{Q}$ for each $0 < \bar{a}_0 - \bar{a}_0^H(\bar{D}_a) \ll 1$, bifurcating out of the equilibrium point $\mathbf{e}_-$.

(b) $\bar{D}_a = \bar{D}_a^c(\bar{D}_b, \bar{c}_0)$

In this case the Hopf bifurcation at $\mathbf{e}_-$, when $(\bar{a}_0, \bar{D}_a) = (\bar{a}_0^H(\bar{D}_a^c), \bar{D}_a^c)$ is degenerate, and supercritical, creating a (unique) unstable limit cycle in $\bar{Q}$ for each $0 < \bar{a}_0 - \bar{a}_0^H(\bar{D}_a^c) \ll 1$, bifurcating out of the equilibrium point $\mathbf{e}_-$.

(c) $0 < \bar{D}_a < \bar{D}_a^c(\bar{D}_b, \bar{c}_0)$

In this case the Hopf bifurcation at $\mathbf{e}_-$, when $(\bar{a}_0, \bar{D}_a) = (\bar{a}_0^H(\bar{D}_a), \bar{D}_a)$, is subcritical, creating a (unique) stable limit cycle in $\bar{Q}$ for each $0 < \bar{a}_0^H(\bar{D}_a) - \bar{a}_0 \ll 1$,

bifurcating out of the equilibrium point $\mathbf{e}_-$.

The nature of the homoclinic bifurcations for case (I) is as in Section 3.1.7 of Chapter 3. For each $0 < \bar{D}_a < \bar{D}_a^*(\bar{D}_b, \bar{c}_0)$, a homoclinic bifurcation occurs when $\bar{a}_0 = \bar{a}_0^\infty(\bar{D}_a)$. This homoclinic bifurcation changes from subcritical, for $\bar{D}_a^\infty(\bar{D}_b, \bar{c}_0) \leq \bar{D}_a < \bar{D}_a^*(\bar{D}_b, \bar{c}_0)$, creating a unique unstable limit cycle in $0 < \bar{a}_0^\infty(\bar{D}_a) - \bar{a}_0 \ll 1$, to supercritical, for $0 < \bar{D}_a < \bar{D}_a^\infty(\bar{D}_b, \bar{c}_0)$, creating a unique stable limit cycle in $0 < \bar{a}_0 - \bar{a}_0^\infty(\bar{D}_a) \ll 1$. A periodic saddle-node bifurcation, giving rise to both an unstable (outer) and stable (inner) limit cycle which surrounds the equilibrium point $\mathbf{e}_-$, occurs for each $\bar{D}_a^\infty(\bar{D}_b, \bar{c}_0) < \bar{D}_a < \bar{D}_a^c(\bar{D}_b, \bar{c}_0)$, when $\bar{a}_0^P(\bar{D}_a)$, with $\bar{a}_0^P(\bar{D}_a) < min(\bar{a}_0^H(\bar{D}_a), \bar{a}_0^\infty(\bar{D}_a))$. The limit cycles created by the Hopf and homoclinic bifurcations have zero and finite amplitude respectively at creation. However the limit cycle associated with the homoclinic bifurcation has infinite period, whilst the two limit cycles arising from the Hopf bifurcation have finite period at creation.

We represent the amplitude of the limit cycles as $A = (a_{max} - a_{min})$, and label the inner and outer limit cycles P^- and P^+ respectively. The periodic orbit bifurcation diagrams are sketched in Figure 4.6, with A_∞ representing the amplitude of the periodic orbit at the homoclinic bifurcation, and A_p representing the amplitude of the periodic orbit at the periodic saddle-node bifurcation.

Case (II): $\frac{1}{16}\bar{D}_b^2 < \bar{c}_0 < \bar{c}_0^*(\bar{D}_b)$

We examine the periodic orbits in the phase portrait of $\overline{\text{[D-S]}}$ for the two subcases defined in Section 4.1.3.

(a) $\bar{D}_a > \bar{D}_a^{\chi}(\bar{D}_b, \bar{c}_0)$

In this case, when $\frac{1}{16}\bar{D}_b^2 < \bar{c}_0 < \bar{c}_0^{\phi}(\bar{D}_b)$, there is a Hopf bifurcation for each $\bar{D}_a^{\chi}(\bar{D}_b, \bar{c}_0) < \bar{D}_a < \bar{D}_a^{*}(\bar{D}_b, \bar{c}_0)$, at the equilibrium point $\mathbf{e}_-$ when, $\bar{a}_0 = \bar{a}_0^{H^+}(\bar{D}_a) > \bar{a}_0^{SN_-}(\bar{D}_a)$. The Hopf bifurcation is subcritical, creating a unique stable limit cycle in $\bar{Q}$ for each $0 < \bar{a}_0^{H^+} - \bar{a}_0 \ll 1$, bifurcating out of the equilibrium point $\mathbf{e}_-$. In addition, a supercritical homoclinic bifurcation occurs for each $\bar{D}_a^{\chi}(\bar{D}_b, \bar{c}_0) < \bar{D}_a < \bar{D}_a^{*}(\bar{D}_b, \bar{c}_0)$, when $\bar{a}_0 = \bar{a}_0^{\infty}(\bar{D}_a)$, creating a unique stable limit cycle in $0 < \bar{a}_0 - \bar{a}_0^{\infty}(\bar{D}_a) \ll 1$. Here $\bar{a}_0^{SN_-}(\bar{D}_a) < \bar{a}_0^{\infty}(\bar{D}_a) < \bar{a}_0^{H_+}(\bar{D}_a)$. However, when $\bar{c}_0^{\phi}(\bar{D}_b) < \bar{c}_0 < \bar{c}_0^{*}(\bar{D}_b)$, there are no Hopf or homoclinic bifurcations.

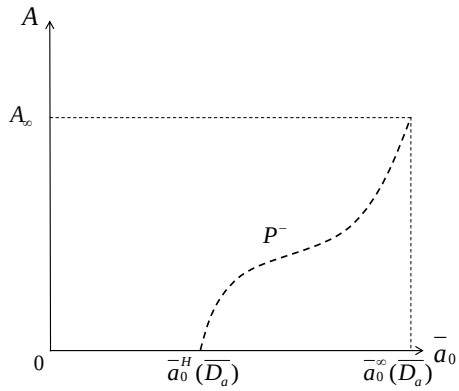

(e) $\bar{D}_a^c \leq \bar{D}_a < \bar{D}_a^*$

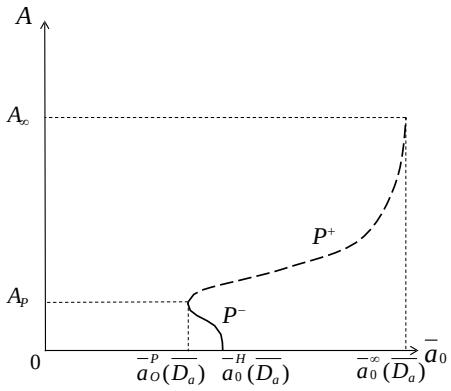

(f) $\bar{D}_a^\infty < \bar{D}_a < \bar{D}_a^c$ when $\bar{a}_0^H < \bar{a}_0^\infty$

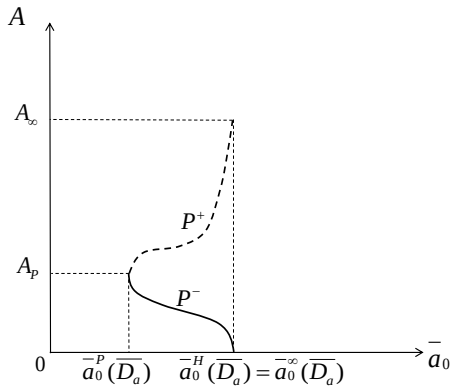

(g) $\bar{D}_a^\infty < \bar{D}_a < \bar{D}_a^c$ when $\bar{a}_0^H = \bar{a}_0^\infty$

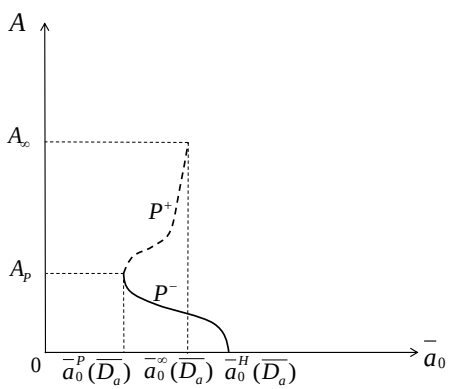

(h) $\bar{D}_a^\infty < \bar{D}_a < \bar{D}_a^c$ when $\bar{a}_0^H > \bar{a}_0^\infty$

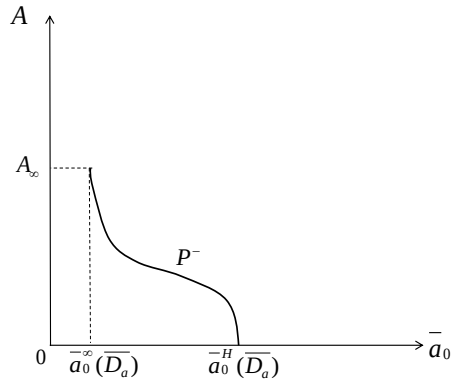

(i) $0 < \bar{D}_a \leq \bar{D}_a^\infty$

Figure 4.6: Periodic orbit bifurcation diagrams in case (I) when $0 < \bar{c}_0 \leq \frac{\bar{D}_b^2}{16}$, with dashed lines being unstable and solid lines being stable periodic orbits.

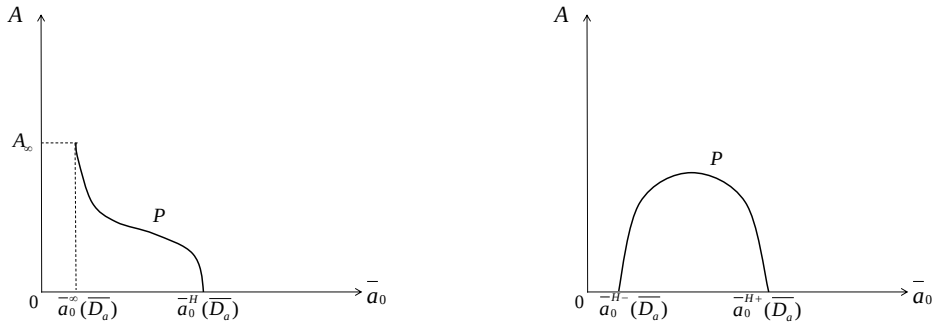

(a) $\frac{\bar{D}_b^2}{16} < \bar{c}_0 < \bar{c}_0^{\phi}$ with $\bar{D}_a^{\chi} \leq \bar{D}_a < \bar{D}_a^*$

(b) $\frac{\bar{D}_b^2}{16} < \bar{c}_0 < \bar{c}_0^{\phi}$ with $0 < \bar{D}_a < \bar{D}_a^{\chi}$, and $\bar{c}_0^{\phi} < \bar{c}_0 < \bar{c}_0^*$ with $0 < \bar{D}_a < \bar{D}_a^*$

Figure 4.7: Periodic orbit bifurcation diagrams in case (II) when $\frac{1}{16}\bar{D}_b^2 < \bar{c}_0 < \bar{c}_0^*(\bar{D}_b)$.

(b) $0 < \bar{D}_a < \bar{D}_a^{\chi}(\bar{D}_b, \bar{c}_0)$

In this case, when $\frac{1}{16}\bar{D}_b^2 < \bar{c}_0 < \bar{c}_0^{\phi}(\bar{D}_b)$, there are two Hopf bifurcations, when $\bar{a}_0 = \bar{a}_0^{H^-}(\bar{D}_a)$, and $\bar{a}_0 = \bar{a}_0^{H^+}(\bar{D}_a)$, with $\bar{a}_0^{H^-}(\bar{D}_a) < \bar{a}_0^{H^+}(\bar{D}_a)$, for all $0 < \bar{D}_a < \bar{D}_a^{\chi}(\bar{D}_b, \bar{c}_0)$. However, when $\bar{c}_0^{\phi}(\bar{D}_b) < \bar{c}_0 < \bar{c}_0^*(\bar{D}_b)$, there exists $\bar{D}_a^*(\bar{D}_b, \bar{c}_0) < \bar{D}_a^{\chi}(\bar{D}_b, \bar{c}_0)$, such that for $0 < \bar{D}_a < \bar{D}_a^*(\bar{D}_b, \bar{c}_0)$, there are two Hopf bifurcations, when $\bar{a}_0 = \bar{a}_0^{H^-}(\bar{D}_a)$, and $\bar{a}_0 = \bar{a}_0^{H^+}(\bar{D}_a)$, with $\bar{a}_0^{H^-}(\bar{D}_a) < \bar{a}_0^{H^+}(\bar{D}_a)$, for all $0 < \bar{D}_a < \bar{D}_a^*(\bar{D}_b, \bar{c}_0)$. There are no Hopf bifurcations when $\bar{D}_a^*(\bar{D}_b, \bar{c}_0) < \bar{D}_a < \bar{D}_a^{\chi}(\bar{D}_b, \bar{c}_0)$ for any $\bar{a}_0 > 0$.

The Hopf bifurcation at $\bar{a}_0^{H_-}(\bar{D}_a)$ is supercritical, creating a unique stable limit cycle in $0 < \bar{a}_0 - \bar{a}_0^{H^-}(\bar{D}_a) \ll 1$, whilst the Hopf bifurcation at $\bar{a}_0^{H_+}(\bar{D}_a)$ is subcritical, creating a unique stable limit cycle in $0 < \bar{a}_0^{H^+}(\bar{D}_a) - \bar{a}_0 \ll 1$. There are no homoclinic bifurcations in this case.

The periodic orbit bifurcation diagrams in case (II) are illustrated in Figure 4.7, with the single periodic orbit labelled as P.

Case (III): $\bar{c}_0 > \bar{c}_0^*(\bar{D}_b)$

In this case, there exists a value $\bar{D}_a = \bar{D}_a^*(\bar{D}_b, \bar{c}_0)$, such that for $0 < \bar{D}_a < \bar{D}_a^*(\bar{D}_b, \bar{c}_0)$, there are two Hopf bifurcations, when $\bar{a}_0 = \bar{a}_0^{H^-}(\bar{D}_a)$, and $\bar{a}_0 = \bar{a}_0^{H^+}(\bar{D}_a)$, with $\bar{a}_0^{H^-}(\bar{D}_a) < \bar{a}_0^{H^+}(\bar{D}_a)$, for all $0 < \bar{D}_a < \bar{D}_a^*(\bar{D}_b, \bar{c}_0)$. The Hopf bifurcation at $\bar{a}_0^{H^-}(\bar{D}_a)$ is supercritical, creating a unique stable limit cycle in $0 < \bar{a}_0 - \bar{a}_0^{H^-}(\bar{D}_a) \ll 1$, whislt the Hopf bifurcation at $\bar{a}_0^{H^+}(\bar{D}_a)$ is subcritical, creating a unique stable limit cycle in $0 < \bar{a}_0^{H^+}(\bar{D}_a) - \bar{a}_0 \ll 1$. There are no homoclinic bifurcations in this case. The periodic orbit bifurcation diagram in this case is qualitatively the same as that in Figure 4.7b.

It is worth mentioning here, that following Section 4.1.1, we can infer that all equilibrium points and periodic orbits in the phase portrait of $\overline{\text{[D-S]}}$ must lie in the region $Q \cap \bar{R}$. Finally we can now sketch the full $(\bar{a}_0, \bar{D}_a)$ unfolding plane in each of the three cases. These are illustrated in Figure 4.8.

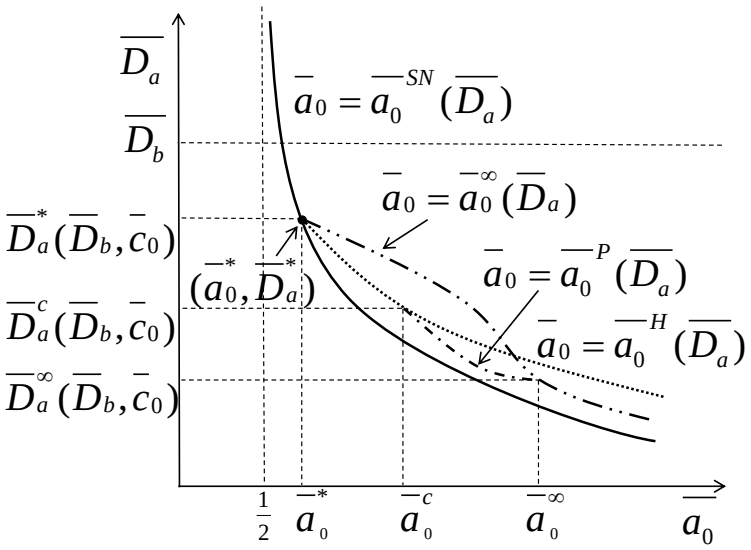

(a) For case (I)

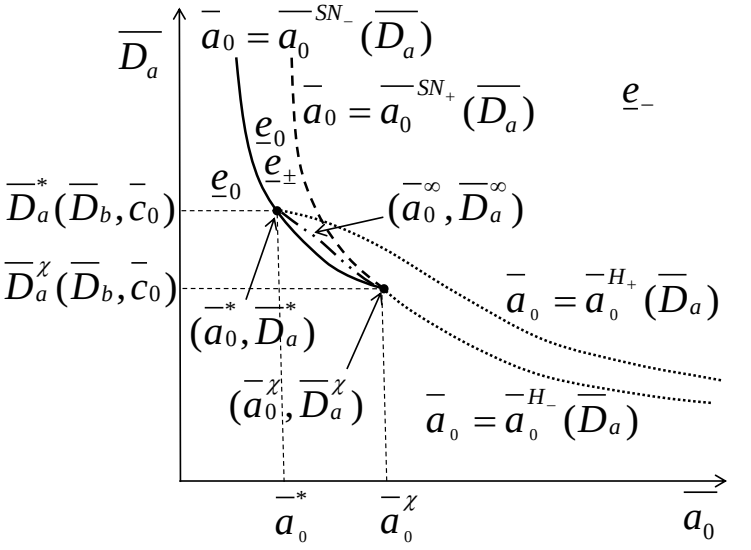

(b) For case (II)(a) and (b) with $\frac{1}{16}\bar{D}_b^2 < \bar{c}_0 < \bar{c}_0^{\phi}(\bar{D}_b)$ and $\bar{D}_a^*(\bar{D}_a, \bar{c}_0) > \bar{D}_a^{\chi}(\bar{D}_b, \bar{c}_0)$

Figure 4.8: The full $(\bar{D}_a, \bar{a}_0))$ unfolding planes.

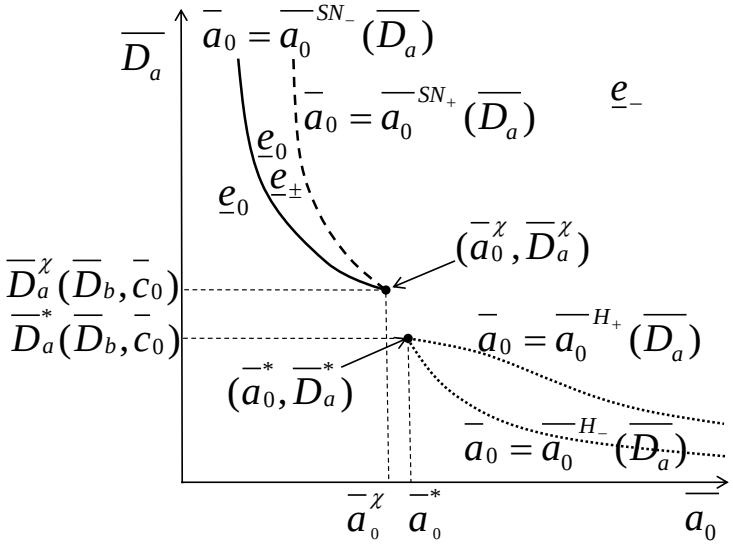

(c) For case (II)(a) and (b) with $\bar{c}_0^\phi(\bar{D}_b) < \bar{c}_0 < \bar{c}_0^*(\bar{D}_b)$ and $\bar{D}_a^*(\bar{D}_a, \bar{c}_0) < \bar{D}_a^\chi(\bar{D}_b, \bar{c}_0)$

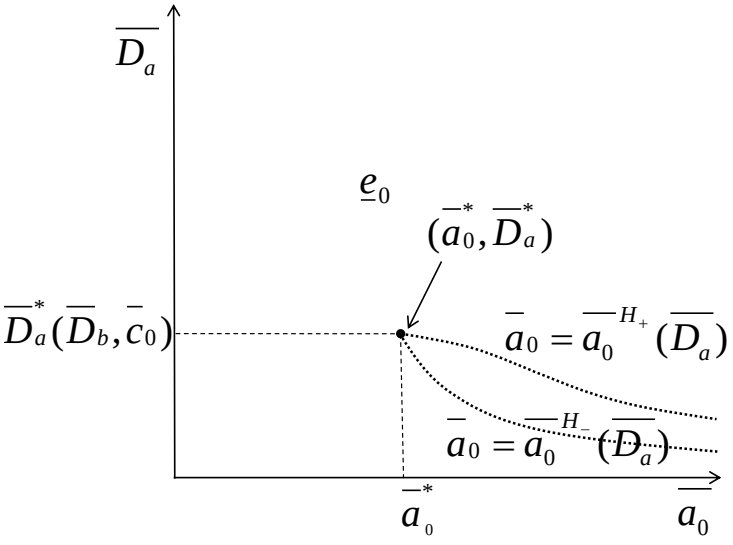

(d) For case (III)

Figure 4.8: The full $(\bar{D}_a, \bar{a}_0))$ unfolding planes.

4.3 Periodic Orbits and Hysteresis

In this section we identify in parameter space when $\overline{\text{[D-S]}}$ can exhibit equilibrium point hysteresis, or periodic orbit hysteresis. To this end, we construct the family of distinct full bifurcation diagrams for $\overline{\text{[D-S]}}$. This can be done via the full $(\bar{D}_a, \bar{a}_0)$ unfolding plane in Figure 4.8. The distinct cases are detailed below. In what follows, we refer to the unique stable and unstable limit cycles in the phase plane as $\mathcal{C}_{\mathcal{S}}$ and $\mathcal{C}_{\mathcal{U}}$ respectively, and the stable manifold of the saddle equilibrium point $\mathbf{e}_+$ as $\mathcal{S}$.

Case (I): $0 < \bar{c}_0 < \frac{1}{16}\bar{D}_b^2$

(i) $\bar{D}_a > 0$ and $0 < \bar{a}_0 < \bar{a}_0^{SN}(\bar{D}_a)$

There exists the single, stable equilibrium point, $\mathbf{e_0}$, which is globally attracting in the phase plane. All phase paths, Γ^i of $\overline{\text{[D-S]}}$, are attracted to $\mathbf{e_0}$ as $t \to +\infty$.

(ii) $\bar{D}_a > \bar{D}_a^*(\bar{D}_b, \bar{c}_0)$, and $\bar{a}_0 > \bar{a}_0^{SN}(\bar{D}_a)$

There exist three equilibrium points, $\mathbf{e_0}$, $\mathbf{e}_-$ and $\mathbf{e}_+$. The equilibrium points $\mathbf{e_0}$ and $\mathbf{e}_-$ are attracting in the phase plane, whilst the equilibrium point $\mathbf{e}_+$ is a saddlepoint. All phase paths, Γ^i of $\overline{\text{[D-S]}}$, which start on the interior of the stable manifold, $\mathcal{S}$, of $\mathbf{e}_+$, are attracted to the equilibrium point $\mathbf{e}_-$ as $t \to +\infty$. However all phase paths starting outside $\mathcal{S}$ are attracted to the equilibrium point $\mathbf{e_0}$ as $t \to +\infty$.

(iii) $\bar{D}_a^c(\bar{D}_b, \bar{c}_0) < \bar{D}_a < \bar{D}_a^*(\bar{D}_b, \bar{c}_0)$, and $\bar{a}_0^{SN}(\bar{D}_a) < \bar{a}_0 < \bar{a}_0^{H}(\bar{D}_a)$

There exist three equilibrium points, $\mathbf{e_0}$, $\mathbf{e}_-$ and $\mathbf{e}_+$. The equilibrium point $\mathbf{e_0}$ is attracting in the phase plane, the equilibrium point $\mathbf{e}_-$ is repelling in the phase plane, and the equilibrium point $\mathbf{e}_+$ is a saddlepoint. All phase paths, Γ^i of $\overline{\text{[D-S]}}$,

which do not lie on the stable manifold, $\mathcal{S}$, of $\mathbf{e}_+$ are attracted to the equilibrium point $\mathbf{e_0}$ as $t \to +\infty$.

(iv) $\bar{D}_a^c(\bar{D}_b, \bar{c}_0) < \bar{D}_a < \bar{D}_a^*(\bar{D}_b, \bar{c}_0)$, and $\bar{a}_0^H(\bar{D}_a) < \bar{a}_0 < \bar{a}_0^\infty(\bar{D}_a)$

There exist three equilibrium points, $\mathbf{e_0}$, $\mathbf{e}_-$ and $\mathbf{e}_+$, and a unique unstable limit cycle, $\mathcal{C}_\mathcal{U}$ which surrounds the equilibrium point $\mathbf{e}_-$. The equilibrium points $\mathbf{e_0}$ and $\mathbf{e}_-$ are attracting in the phase plane, whilst the equilibrium point $\mathbf{e}_+$ is a saddlepoint. All phase paths, Γ^i of $\overline{\text{[D-S]}}$, that start inside the unstable limit cycle, $\mathcal{C}_\mathcal{U}$, are attracted to the equilibrium point $\mathbf{e}_-$ as $t \to +\infty$. However all phase paths starting outside $\mathcal{C}_\mathcal{U}$, and which do not lie on the stable manifold, $\mathcal{S}$, of $\mathbf{e}_+$, are attracted to the equilibrium point $\mathbf{e_0}$ as $t \to +\infty$.

(v) $\bar{D}_a^c(\bar{D}_b, \bar{c}_0) < \bar{D}_a < \bar{D}_a^*(\bar{D}_b, \bar{c}_0)$, and $\bar{a}_0 > \bar{a}_0^\infty(\bar{D}_a)$

This case is the same as case (ii).

(vi) $\bar{D}_a^\infty(\bar{D}_b, \bar{c}_0) < \bar{D}_a < \bar{D}_a^c(\bar{D}_b, \bar{c}_0)$, and $\bar{a}_0^{SN}(\bar{D}_a) < \bar{a}_0 < \bar{a}_0^P(\bar{D}_a)$

This case is the same as case (iii).

(vii) $\bar{D}_a^\infty(\bar{D}_b, \bar{c}_0) < \bar{D}_a < \bar{D}_a^c(\bar{D}_b, \bar{c}_0)$, and $\bar{a}_0^P(\bar{D}_a) < \bar{a}_0 < \bar{a}_0^H(\bar{D}_a)$ with $\bar{a}_0^\infty(\bar{D}_a) > \bar{a}_0^H(\bar{D}_a)$

There exist three equilibrium points, $\mathbf{e_0}$, $\mathbf{e}_-$ and $\mathbf{e}_+$, and both a unique stable limit cycle, $\mathcal{C}_\mathcal{S}$, which surrounds the equilibrium point $\mathbf{e}_-$, and a unique unstable limit cycle, $\mathcal{C}_\mathcal{U}$, which surrounds the stable limit cycle, $\mathcal{C}_\mathcal{S}$. The equilibrium point $\mathbf{e_0}$ is attracting in the phase plane, the equilibrium point $\mathbf{e}_-$ is repelling in the phase plane, and the equilibrium point $\mathbf{e}_+$ is a saddlepoint. All phase paths, Γ^i of $\overline{\text{[D-S]}}$, which start on the interior of the unstable limit cycle, $\mathcal{C}_\mathcal{U}$ are attracted to the stable limit cycle, $\mathcal{C}_\mathcal{S}$ as $t \to +\infty$. However all phase paths starting on the

outside of $\mathcal{C}_{\mathcal{U}}$, and which do not lie on the stable manifold, $\mathcal{S}$, of $\mathbf{e}_+$, are attracted to the equilibrium point $\mathbf{e_0}$ as $t \to +\infty$.

(viii) $\bar{D}_a^{\infty}(\bar{D}_b, \bar{c}_0) < \bar{D}_a < \bar{D}_a^{c}(\bar{D}_b, \bar{c}_0)$, and $\bar{a}_0^{P}(\bar{D}_a) < \bar{a}_0 < \bar{a}_0^{\infty}(\bar{D}_a)$ with $\bar{a}_0^{\infty}(\bar{D}_a) < \bar{a}_0^{H}(\bar{D}_a)$

This case is the same as case (vii).

(ix) $\bar{D}_a^{\infty}(\bar{D}_b, \bar{c}_0) < \bar{D}_a < \bar{D}_a^{c}(\bar{D}_b, \bar{c}_0)$, and $\bar{a}_0^{\infty}(\bar{D}_a) < \bar{a}_0 < \bar{a}_0^{H}(\bar{D}_a)$ with $\bar{a}_0^{\infty}(\bar{D}_a) < \bar{a}_0^{H}(\bar{D}_a)$

There exist three equilibrium points, $\mathbf{e_0}$, $\mathbf{e}_-$ and $\mathbf{e}_+$, and a unique stable limit cycle, $\mathcal{C}_{\mathcal{S}}$, which surrounds the equilibrium point $\mathbf{e}_-$. The equilibrium point $\mathbf{e_0}$ is attracting in the phase plane, the equilibrium point $\mathbf{e}_-$ is repelling in the phase plane, and the equilibrium point $\mathbf{e}_+$ is a saddlepoint. All phase paths, Γ^i of $\overline{\text{[D-S]}}$, that start on the interior of the stable manifold, $\mathcal{S}$, of the equilibrium point $\mathbf{e}_+$ are attracted to the stable limit cycle, $\mathcal{C}_{\mathcal{S}}$ as $t \to +\infty$. However phase paths starting outside $\mathcal{S}$ are attracted to the equilibrium point $\mathbf{e_0}$ as $t \to +\infty$.

(x) $\bar{D}_a^{\infty}(\bar{D}_b, \bar{c}_0) < \bar{D}_a < \bar{D}_a^{c}(\bar{D}_b, \bar{c}_0)$, and $\bar{a}_0^{H}(\bar{D}_a) < \bar{a}_0 < \bar{a}_0^{\infty}(\bar{D}_a)$ with $\bar{a}_0^{\infty}(\bar{D}_a) > \bar{a}_0^{H}(\bar{D}_a)$

This case is the same as case (iv).

(xi) $\bar{D}_a^{\infty}(\bar{D}_b, \bar{c}_0) < \bar{D}_a < \bar{D}_a^{c}(\bar{D}_b, \bar{c}_0)$, and $\bar{a}_0 > \bar{a}_0^{\infty}(\bar{D}_a)$ with $\bar{a}_0^{\infty}(\bar{D}_a) > \bar{a}_0^{H}(\bar{D}_a)$

This case is the same as cases (ii) and (v).

(xii) $\bar{D}_a^{\infty}(\bar{D}_b, \bar{c}_0) < \bar{D}_a < \bar{D}_a^{c}(\bar{D}_b, \bar{c}_0)$, and $\bar{a}_0 > \bar{a}_0^{H}(\bar{D}_a)$ with $\bar{a}_0^{\infty}(\bar{D}_a) < \bar{a}_0^{H}(\bar{D}_a)$
This case is the same as cases (ii), (v) and (xi).

(xiii) $0 < \bar{D}_a < \bar{D}_a^{\infty}(\bar{D}_b, \bar{c}_0)$, and $\bar{a}_0^{SN}(\bar{D}_a) < \bar{a}_0 < \bar{a}_0^{\infty}(\bar{D}_a)$

This case is the same as case (iii).

(xiv) $0 < \bar{D}_a < \bar{D}_a^{\infty}(\bar{D}_b, \bar{c}_0)$, and $\bar{a}_0^{\infty}(\bar{D}_a) < \bar{a}_0 < \bar{a}_0^{H}(\bar{D}_a)$

This case is the same as case (ix).

(xv) $0 < \bar{D}_a < \bar{D}_a^{\infty}(\bar{D}_b, \bar{c}_0)$, and $\bar{a}_0 > \bar{a}_0^{H}(\bar{D}_a)$

This case is the same as cases (ii), (v), (xi) and (xii).

Case (II): $\frac{1}{16}\bar{D}_b^2 < \bar{c}_0 < \bar{c}_0^{\phi}(\bar{D}_a)$ and $\bar{D}_a^{*}(\bar{D}_a, \bar{c}_0) > \bar{D}_a^{\chi}(\bar{D}_b, \bar{c}_0)$

(i) $\bar{D}_a > \bar{D}_a^{\chi}(\bar{D}_b, \bar{c}_0)$ and $0 < \bar{a}_0 < \bar{a}_0^{SN_-}(\bar{D}_a)$

There exists the single, stable equilibrium point, $\mathbf{e_0}$, which is globally attracting in the phase plane. All phase paths, Γ^i of $\overline{\text{[D-S]}}$, are attracted to $\mathbf{e_0}$ as $t \to +\infty$.

(ii) $\bar{D}_a > \bar{D}_a^{*}(\bar{D}_b, \bar{c}_0)$ and $\bar{a}_0^{SN_-}(\bar{D}_a) < \bar{a}_0 < \bar{a}_0^{SN_+}(\bar{D}_a)$

There exist three equilibrium points, $\mathbf{e_0}$, $\mathbf{e}_-$ and $\mathbf{e}_+$. The equilibrium points $\mathbf{e_0}$ and $\mathbf{e}_-$ are attracting in the phase plane, whilst the equilibrium point $\mathbf{e}_+$ is a saddlepoint. All phase paths, Γ^i of $\overline{\text{[D-S]}}$, which start on the interior of the stable manifold, $\mathcal{S}$, of the equilibrium point, $\mathbf{e}_+$, are attracted to the equilibrium point, $\mathbf{e}_-$, as $t \to +\infty$. However all phase paths starting on the outside of $\mathcal{S}$, are attracted to the equilibrium point $\mathbf{e_0}$ as $t \to +\infty$.

(iii) $\bar{D}_a > \bar{D}_a^{*}(\bar{D}_b, \bar{c}_0)$ and $\bar{a}_0 > \bar{a}_0^{SN_+}(\bar{D}_a)$

There exists the single equilibrium point, $\mathbf{e}_-$, which is attracting in the phase plane. All phase paths, Γ^i of $\overline{\text{[D-S]}}$, are attracted to $\mathbf{e}_-$ as $t \to +\infty$.

(iv) $\bar{D}_a^{\chi}(\bar{D}_b, \bar{c}_0) < \bar{D}_a < \bar{D}_a^{*}(\bar{D}_b, \bar{c}_0)$ and $\bar{a}_0^{SN_-}(\bar{D}_a) < \bar{a}_0 < \bar{a}_0^{\infty}(\bar{D}_a)$

There exist three equilibrium points, $\mathbf{e_0}$, $\mathbf{e}_-$ and $\mathbf{e}_+$. The equilibrium point $\mathbf{e_0}$ is attracting in the phase plane, the equilibrium point $\mathbf{e}_-$ is repelling in the phase plane, and the equilibrium point $\mathbf{e}_+$ is a saddlepoint. All phase paths, Γ^i of $\overline{\text{[D-S]}}$,

are attracted to the equilibrium point, $\mathbf{e_0}$, as $t \to +\infty$.

(v) $\bar{D}_a^{\chi}(\bar{D}_b, \bar{c}_0) < \bar{D}_a < \bar{D}_a^{*}(\bar{D}_b, \bar{c}_0)$ and $\bar{a}_0^{\infty}(\bar{D}_a) < \bar{a}_0 < \bar{a}_0^{m}(\bar{D}_a)$, where $\bar{a}_0^{m}(\bar{D}_a) = min\{\bar{a}_0^{SN_+}(\bar{D}_a), \bar{a}_0^{H_+}(\bar{D}_a)\}$

There exist three equilibrium points, $\mathbf{e_0}$, $\mathbf{e}_-$ and $\mathbf{e}_+$, and a unique stable limit cycle, $\mathcal{C}_{\mathcal{S}}$, which surrounds the equilibrium point $\mathbf{e}_-$. The equilibrium point $\mathbf{e_0}$ is attracting in the phase plane, the equilibrium point $\mathbf{e}_-$ is repelling in the phase plane, and the equilibrium point $\mathbf{e}_+$ is a saddlepoint. All phase paths, Γ^i of $\overline{\text{[D-S]}}$, which start on the interior of the stable manifold, $\mathcal{S}$, of the equilibrium point $\mathbf{e}_+$, are attracted to the stable limit cycle, $\mathcal{C}_{\mathcal{S}}$, as $t \to +\infty$. However all phase paths starting outside of $\mathcal{S}$ are attracted to the equilibrium point $\mathbf{e_0}$ as $t \to +\infty$.

(vi) $\bar{D}_a^{\chi}(\bar{D}_b, \bar{c}_0) < \bar{D}_a < \bar{D}_a^{*}(\bar{D}_b, \bar{c}_0)$ and $\bar{a}_0^{SN_+}(\bar{D}_a) < \bar{a}_0 < \bar{a}_0^{H_+}(\bar{D}_a)$

There exists the single equilibrium point, $\mathbf{e}_-$, which is repelling in the phase plane, and a unique stable limit cycle, $\mathcal{C}_{\mathcal{S}}$, which surrounds the equilibrium point $\mathbf{e}_-$. All phase paths, Γ^i of $\overline{\text{[D-S]}}$, are attracted to $\mathcal{C}_{\mathcal{S}}$ as $t \to +\infty$.

(vii) $\bar{D}_a^{\chi}(\bar{D}_b, \bar{c}_0) < \bar{D}_a < \bar{D}_a^{*}(\bar{D}_b, \bar{c}_0)$ and $\bar{a}_0^{H_+}(\bar{D}_a) < \bar{a}_0 < \bar{a}_0^{SN_+}(\bar{D}_a)$

This case is the same as case (ii).

(viii) $0 < \bar{D}_a < \bar{D}_a^{\chi}(\bar{D}_b, \bar{c}_0)$ and $0 < \bar{a}_0 < \bar{a}_0^{H_-}(\bar{D}_a)$

This case is the same as case (i).

(ix) $0 < \bar{D}_a < \bar{D}_a^{\chi}(\bar{D}_b, \bar{c}_0)$ and $\bar{a}_0^{H_-}(\bar{D}_a) < \bar{a}_0 < \bar{a}_0^{H_+}(\bar{D}_a)$

There exists the single equilibrium point, $\mathbf{e_0}$, which is repelling in the phase plane, and a unique stable limit cycle, $\mathcal{C}_{\mathcal{S}}$, which surrounds the equilibrium point

$\mathbf{e_0}$. All phase paths, Γ^i of $\overline{\text{[D-S]}}$, are attracted to $\mathcal{C}_S$ as $t \to +\infty$.

(x) $0 < \bar{D}_a < \bar{D}_a^*(\bar{D}_b, \bar{c}_0)$ and $\bar{a}_0 > \bar{a}_0^M(\bar{D}_a)$, where $\bar{a}_0^M(\bar{D}_a) = max\{\bar{a}_0^{H_+}(\bar{D}_a), \bar{a}_0^{SN_+}(\bar{D}_a)\}$

This case is the same as case (iii).

Case (II): When $\bar{c}_0^{\phi}(\bar{D}_a) < \bar{c}_0 < \bar{c}_0^*(\bar{D}_a)$ and $\bar{D}_a^*(\bar{D}_b, \bar{c}_0) < \bar{D}_a^{\chi}(\bar{D}_b, \bar{c}_0)$

(i) $\bar{D}_a > \bar{D}_a^{\chi}(\bar{D}_b, \bar{c}_0)$ and $0 < \bar{a}_0 < \bar{a}_0^{SN_-}(\bar{D}_a)$

There exists the single, stable equilibrium point, $\mathbf{e_0}$, which is globally attracting in the phase plane. All phase paths, Γ^i of $\overline{\text{[D-S]}}$, are attracted to $\mathbf{e_0}$ as $t \to +\infty$.

(ii) $\bar{D}_a > \bar{D}_a^{\chi}(\bar{D}_b, \bar{c}_0)$ and $\bar{a}_0^{SN_-}(\bar{D}_a) < \bar{a}_0 < \bar{a}_0^{SN_+}(\bar{D}_a)$

There exist three equilibrium points, $\mathbf{e_0}$, $\mathbf{e}_-$ and $\mathbf{e}_+$. The equilibrium points $\mathbf{e_0}$ and $\mathbf{e}_-$ are attracting in the phase plane, whilst the equilibrium point $\mathbf{e}_+$ is a saddlepoint. All phase paths, Γ^i of $\overline{\text{[D-S]}}$, which start on the interior of the stable manifold, $\mathcal{S}$, of the equilibrium point, $\mathbf{e}_+$, are attracted to the equilibrium point, $\mathbf{e}_-$, as $t \to +\infty$. However all phase paths starting on the outside of $\mathcal{S}$, are attracted to the equilibrium point $\mathbf{e_0}$ as $t \to +\infty$.

(iii) $\bar{D}_a > \bar{D}_a^{\chi}(\bar{D}_b, \bar{c}_0)$ and $\bar{a}_0 > \bar{a}_0^{SN_+}(\bar{D}_a)$

There exists the single equilibrium point, $\mathbf{e}_-$, which is attracting in the phase plane. All phase paths, Γ^i of $\overline{\text{[D-S]}}$, are attracted to $\mathbf{e}_-$ as $t \to +\infty$.

(iv) $\bar{D}_a^*(\bar{D}_b, \bar{c}_0) < \bar{D}_a < \bar{D}_a^{\chi}(\bar{D}_b, \bar{c}_0)$ and $\bar{a}_0 > 0$

This case is the same as case (i).

(v) $0 < \bar{D}_a < \bar{D}_a^*(\bar{D}_b, \bar{c}_0)$ and $\bar{a}_0 < \bar{a}_0^{H_-}(\bar{D}_a)$

This case is the same as cases (i) and (iv).

(vi) $0 < \bar{D}_a < \bar{D}_a^*(\bar{D}_b, \bar{c}_0)$ and $\bar{a}_0^{H_-}(\bar{D}_a) < \bar{a}_0 < \bar{a}_0^{H_+}(\bar{D}_a)$

There exists the single equilibrium point, $\mathbf{e_0}$, which is repelling in the phase plane, and a unique stable limit cycle, $\mathcal{C}_S$, which surrounds the equilibrium point $\mathbf{e_0}$. All phase paths, Γ^i of $\overline{\text{[D-S]}}$, are attracted to $\mathcal{C}_S$ as $t \to +\infty$.

(vii) $0 < \bar{D}_a < \bar{D}_a^*(\bar{D}_b, \bar{c}_0)$ and $\bar{a}_0 > \bar{a}_0^{H_+}(\bar{D}_a)$

This case is the same as cases (i), (iv) and (v).

Case (III): When $\bar{c}_0 > \bar{c}_0^*(\bar{D}_a)$

(i) $\bar{D}_a > \bar{D}_a^*(\bar{D}_b, \bar{c}_0)$ and $\bar{a}_0 > 0$

There exists the single, stable equilibrium point, $\mathbf{e_0}$, which is globally attracting in the phase plane. All phase paths, Γ^i of $\overline{\text{[D-S]}}$, are attracted to $\mathbf{e_0}$ as $t \to +\infty$.

(ii) $0 < \bar{D}_a < \bar{D}_a^*(\bar{D}_b, \bar{c}_0)$ and $0 < \bar{a}_0 < \bar{a}_0^{H_-}(\bar{D}_a)$

This case is the same as case (i).

(iii) $0 < \bar{D}_a < \bar{D}_a^*(\bar{D}_b, \bar{c}_0)$ and $\bar{a}_0^{H_-}(\bar{D}_a) < \bar{a}_0 < \bar{a}_0^{H_+}(\bar{D}_a)$

There exists the single equilibrium point, $\mathbf{e_0}$, which is repelling in the phase plane, and a unique stable limit cycle, $\mathcal{C}_S$, which surrounds the equilibrium point $\mathbf{e_0}$. All phase paths, Γ^i of $\overline{\text{[D-S]}}$, are attracted to $\mathcal{C}_S$ as $t \to +\infty$.

(iv) $0 < \bar{D}_a < \bar{D}_a^*(\bar{D}_b, \bar{c}_0)$ and $\bar{a}_0 > \bar{a}_0^{H_+}(\bar{D}_a)$

This case is the same as cases (i) and (ii).

It is now instructive to sketch the full bifurcation diagrams for $\overline{\text{[D-S]}}$ in each of the distinct cases outlined above. In Figures 4.9-4.12, the equilibrium points and limit cycles are stable when represented by a solid line, and unstable when repre-

sented by a dashed line. Hysteresis loops are marked by bold lines with arrows, and the following convention is used when identifying the hysteretic behaviour: We classify the hysteresis loop as e-e, when the system jumps between two stable equilibrium points, e-p when the system jumps between an equilibrium point and a stable limit cycle, and e-p-e when then system jumps from an equilibrium point to a stable limit cycle, and then to a different equilibrium point. The classifications defined above may be preceded by a $\frac{1}{2}$ to indicate that the system only exhibits a "half" hysteresis loop.

The full bifurcation diagrams for case (I) are shown in Figure 4.9. It can be seen from Figure 4.9a that when $\bar{D}_a \geq \bar{D}_a^*$ there exists a $\frac{1}{2}$e-e loop, where, starting on the lower branch and decreasing $\bar{a}_0$, the system jumps from the stable equilibrium point $\mathbf{e}_-$ to the stable equilibrium point $\mathbf{e_0}$ at the point $\bar{a}_0 = \bar{a}_0^{SN}(\bar{D}_a)$. In Figure 4.9b, when $\bar{D}_a^c \leq \bar{D}_a < \bar{D}_a^*$, another $\frac{1}{2}$e-e loop appears when starting on the lower branch and decreasing $\bar{a}_0$, but in this case the system jumps from the stable equilibrium point $\mathbf{e}_-$ to the stable equilibrium point $\mathbf{e_0}$ at the point $\bar{a}_0 = \bar{a}_0^H(\bar{D}_a)$. In Figures 4.9c-4.9e, when $\bar{D}_a^\infty < \bar{D}_a < \bar{D}_a^c$, there exists a $\frac{1}{2}$e-p-e loop, where, starting on the lower branch and decreasing $\bar{a}_0$, the system moves from the stable equilibrium point $\mathbf{e}_-$ to the stable limit cycle $\mathcal{C}_S$ at the point $\bar{a}_0 = \bar{a}_0^H(\bar{D}_a)$, afterwhich the system then jumps to the stable equilibrium point $\mathbf{e_0}$ at the point $\bar{a}_0 = \bar{a}_0^P(\bar{D}_a)$. In Figure 4.9f, when $0 < \bar{D}_a \leq \bar{D}_a^\infty$, we see another $\frac{1}{2}$e-p-e loop, where, starting on the lower branch and decreasing $\bar{a}_0$, the system moves from the stable equilibrium point $\mathbf{e}_-$ to the stable limit cycle $\mathcal{C}_S$ at the point $\bar{a}_0 = \bar{a}_0^H(\bar{D}_a)$, except that in this case the jump from the stable limit cycle $\mathcal{C}_S$ to the stable equilibrium $\mathbf{e_0}$ occurs at the point $\bar{a}_0 = \bar{a}_0^\infty(\bar{D}_a)$.

The full bifurcation diagrams for case (II)(a) and (b) with $\frac{1}{16}\bar{D}_b^2 < \bar{c}_0 < \bar{c}_0^\phi(\bar{D}_b)$

and $\bar{D}_a^*(\bar{D}_a, \bar{c}_0) > \bar{D}_a^\chi(\bar{D}_b, \bar{c}_0)$ are shown in Figure 4.10. In Figure 4.10a, when $\bar{D}_a \geq \bar{D}_a^*$, there exists a full e-e loop, where, starting on the lower branch and decreasing $\bar{a}_0$, the system jumps from the stable equilibrium point $\mathbf{e}_-$ to the stable equilibrium point $\mathbf{e_0}$ at the point $\bar{a}_0 = \bar{a}_0^{SN_-}(\bar{D}_a)$. Increasing $\bar{a}_0$ again up to the point $\bar{a}_0 = \bar{a}_0^{SN_+}(\bar{D}_a)$ causes the system to jump back down to the stable equilibrium point $\mathbf{e}_-$. In Figure 4.10b, when $\bar{D}_a^\chi < \bar{D}_a < \bar{D}_a^*$ and $\bar{a}_0^{H_+} < \bar{a}_0^{SN_+}$, there exists a full e-p-e loop, where, starting on the lower branch and decreasing $\bar{a}_0$, the system moves from the stable equilibrium point $\mathbf{e}_-$ to the stable limit cycle $\mathcal{C}_\mathcal{S}$ at the point $\bar{a}_0 = \bar{a}_0^{H_+}(\bar{D}_a)$. Further decreasing $\bar{a}_0$ to the point $\bar{a}_0 = \bar{a}_0^{\infty}(\bar{D}_a)$ causes the system to jump from the stable limit cycle $\mathcal{C}_\mathcal{S}$ to the stable equilibrium point $\mathbf{e_0}$. Now increasing $\bar{a}_0$ again to the point $\bar{a}_0 = \bar{a}_0^{SN_+}(\bar{D}_a)$ will cause the system to jump back down to the stable equilibrium point $\mathbf{e}_-$. In Figure 4.10c, when $\bar{D}_a^\chi < \bar{D} < \bar{D}_a^*$ and $\bar{a}_0^{H_+} = \bar{a}_0^{SN_+}$, there exists a full e-p loop, where, starting on the upper branch and increasing $\bar{a}_0$, the system jumps from the stable equilibrium point $\mathbf{e_0}$ down to the stable limit cycle $\mathcal{C}_\mathcal{S}$ at the point $\bar{a}_0 = \bar{a}_0^{SN_+}(\bar{D}_a) = \bar{a}_0^{H_+}(\bar{D}_a)$. Decreasing $\bar{a}_0$ to the point $\bar{a}_0 = \bar{a}_0^{\infty}(\bar{D}_a)$ causes the system to jump from the stable limit cycle $\mathcal{C}_\mathcal{S}$ back up to the stable equilibrium point $\mathbf{e_0}$. Another e-p loop exists when $\bar{D}_a^\chi < \bar{D}_a < \bar{D}_a^*$ and $\bar{a}_0^{H_+} > \bar{a}_0^{SN_+}$, as shown in Figure 4.10d. Starting on the upper branch and increasing $\bar{a}_0$, the system jumps from the stable equilibrium point $\mathbf{e_0}$ down to the stable limit cycle $\mathcal{C}_\mathcal{S}$ at the point $\bar{a}_0 = \bar{a}_0^{SN_+}(\bar{D}_a)$. Decreasing $\bar{a}_0$ to the point $\bar{a}_0 = \bar{a}_0^{\infty}(\bar{D}_a)$ causes the system to jump from the stable limit cycle $\mathcal{C}_\mathcal{S}$ back up to the stable equilibrium point $\mathbf{e_0}$. There are no hysteresis loops for $0 < \bar{D}_a < \bar{D}_a^\chi$.

The full bifurcation diagrams for case (II)(a) and (b) with $\bar{c}_0^\phi(\bar{D}_b) < \bar{c}_0 < \bar{c}_0^*(\bar{D}_b)$ and $\bar{D}_a^*(\bar{D}_a, \bar{c}_0) < \bar{D}_a^\chi(\bar{D}_b, \bar{c}_0)$ are shown in Figure 4.11. In Figure 4.11a,

when $\bar{D}_a \geq \bar{D}_a^{\chi}$, there exists a full e-e loop where, starting on the lower branch and decreasing $\bar{a}_0$, the system jumps from the stable equilibrium point $\mathbf{e}_-$ to the stable equilibrium point $\mathbf{e_0}$ at the point $\bar{a}_0 = \bar{a}_0^{SN_-}(\bar{D}_a)$. Increasing $\bar{a}_0$ again up to the point $\bar{a}_0 = \bar{a}_0^{SN_+}(\bar{D}_a)$ causes the system to jump back down to the stable equilibrium point $\mathbf{e}_-$. There are no hysteresis loops when $0 < \bar{D}_a < \bar{D}_a^{\chi}$.

The full bifurcation diagrams for case (III) are shown in Figure 4.12. There are no hysteresis loops for this case.

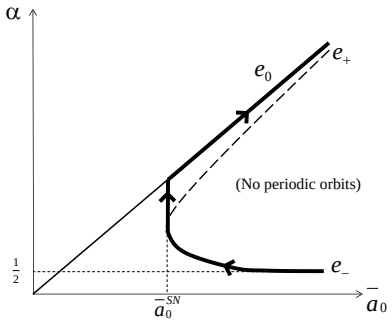

(a) $\bar{D}_a \geq \bar{D}_a^*$

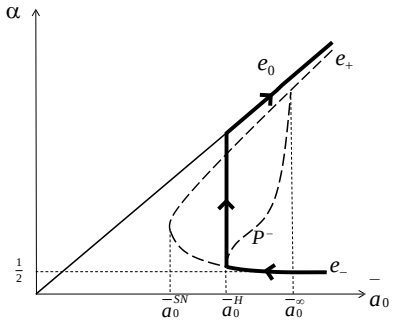

(b) $\bar{D}_a^c \leq \bar{D}_a < \bar{D}_a^*$

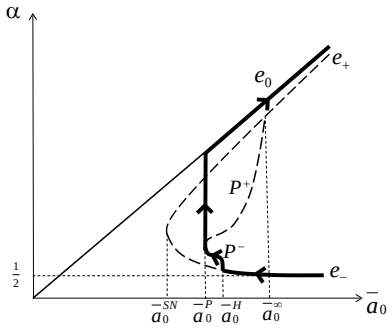

(c) $\bar{D}_a^\infty < \bar{D} < \bar{D}_a^c$ when $\bar{a}_0^H < \bar{a}_0^\infty$

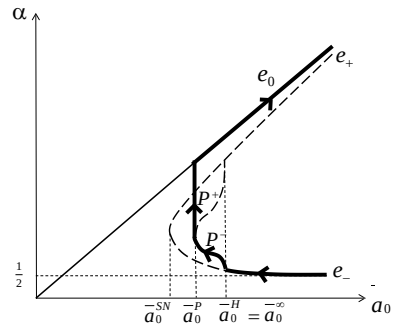

(d) $\bar{D}_a^\infty < \bar{D} < \bar{D}_a^c$ when $\bar{a}_0^H = \bar{a}_0^\infty$

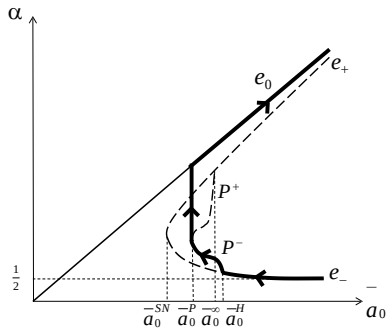

(e) $\bar{D}_a^\infty < \bar{D} < \bar{D}_a^c$ when $\bar{a}_0^H > \bar{a}_0^\infty$

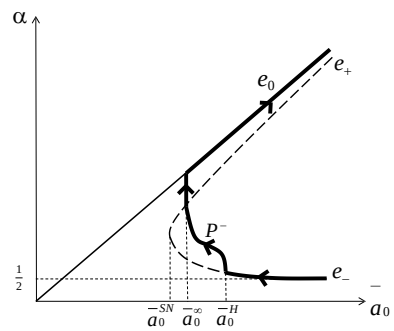

(f) $0 < \bar{D}_a \leq \bar{D}_a^\infty$

Figure 4.9: The full bifurcation diagrams for case (I).

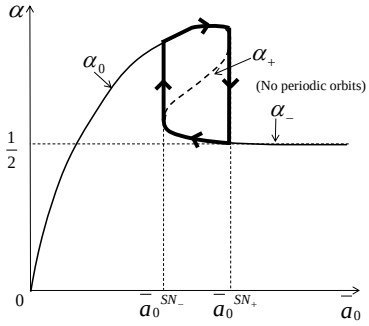

(a) $\bar{D}_a \geq \bar{D}_a^*$

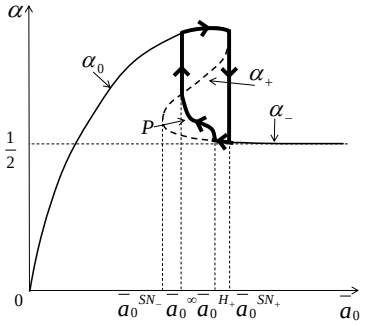

(b) $\bar{D}_a^\chi < \bar{D}_a < \bar{D}_a^*$ when $\bar{a}_0^{H_+} < \bar{a}_0^{SN_+}$

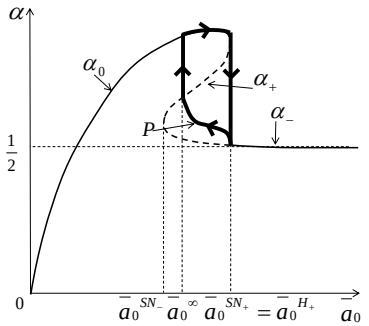

(c) $\bar{D}_a^\chi < \bar{D} < \bar{D}_a^*$ when $\bar{a}_0^{H_+} = \bar{a}_0^{SN_+}$

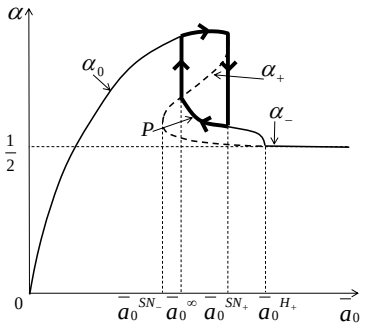

(d) $\bar{D}_a^\chi < \bar{D} < \bar{D}_a^*$ when $\bar{a}_0^{H_+} > \bar{a}_0^{SN_+}$

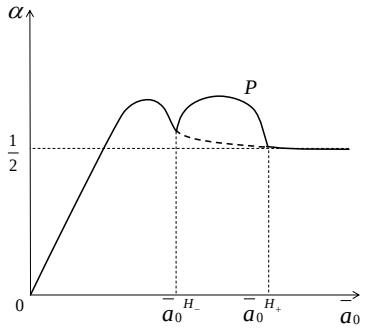

(e) $0 < \bar{D}_a < \bar{D}_a^\chi$ with $\bar{D}_a$ close to $\bar{D}_a^\chi$

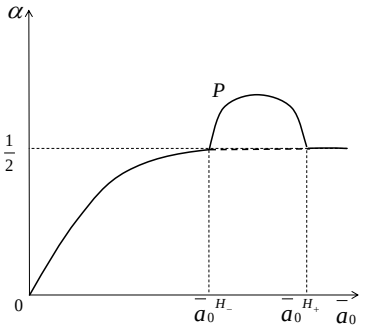

(f) $0 < \bar{D}_a < \bar{D}_a^\chi$ with $\bar{D}_a$ well below $\bar{D}_a^\chi$

Figure 4.10: The full bifurcation diagrams for case (II)(a) and (b) with $\frac{1}{16}\bar{D}_b^2 < \bar{c}_0 < \bar{c}_0^\phi(\bar{D}_b)$ and $\bar{D}_a^*(\bar{D}_a, \bar{c}_0) > \bar{D}_a^\chi(\bar{D}_b, \bar{c}_0)$.

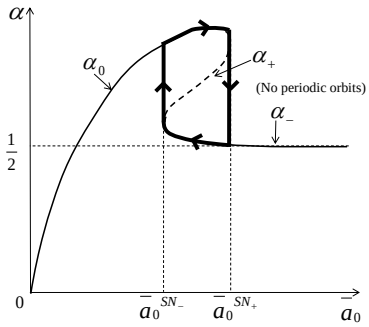

(a) $\bar{D}_a \geq \bar{D}_a^{\chi}$

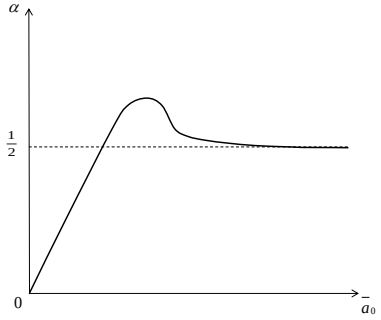

(b) $\bar{D}_a^* < \bar{D} < \bar{D}_a^{\chi}$

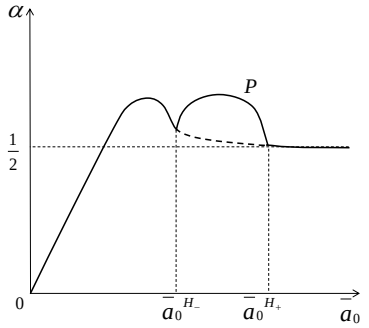

(c) $0 < \bar{D} < \bar{D}_a^*$ with $\bar{D}_a$ close to $\bar{D}_a^*$

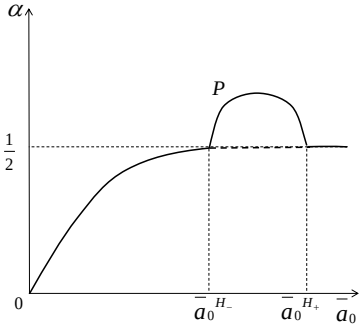

(d) $0 < \bar{D} < \bar{D}_a^*$ with $\bar{D}_a$ well below $\bar{D}_a^*$

Figure 4.11: The full bifurcation diagrams for case (II)(a) and (b) with $\bar{c}_0^{\phi}(\bar{D}_b) < \bar{c}_0 < \bar{c}_0^*(\bar{D}_b)$ and $\bar{D}_a^*(\bar{D}_a, \bar{c}_0) < \bar{D}_a^{\chi}(\bar{D}_b, \bar{c}_0)$.

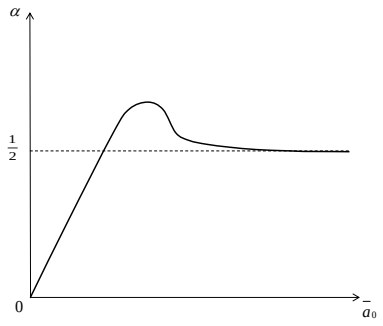

(a) $\bar{D}_a \geq \bar{D}_a^*$

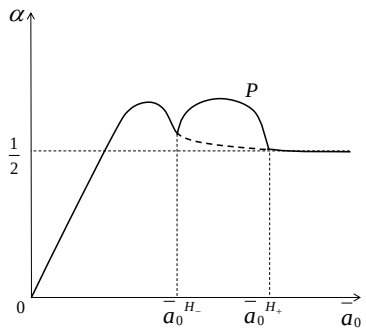

(b) $0 < \bar{D} < \bar{D}_a^*$ with $\bar{D}_a$ close to $\bar{D}_a^*$

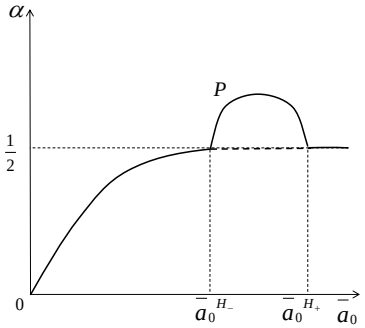

(c) $0 < \bar{D} < \bar{D}_a^*$ with $\bar{D}_a$ well below $\bar{D}_a^*$

Figure 4.12: The full bifurcation diagrams for case (III).

4.4 Numerical Integration

In this section we exhibit sample numerical integrations to $\overline{[\text{D-S}]}$. Taking $\bar{D}_b = 3$ throughout, and selecting $(\bar{a}_0, \bar{D}_a)$ from illustrative regions in the unfolding plane for each of the cases, $\overline{[\text{D-S}]}$ is integrated forward into $t > 0$ from initial conditions $(a_0, b_0) \in \bar{Q}$ using the MATLAB *ode*23*s* solver. The selected regions of the unfolding plane in each of the cases are listed in Table (4.1) using the cases from Section 4.3, along with the initial conditions used for the numerical integrations.

Table 4.1: Initial conditions for the calculated phase paths in each of the cases shown in Figures 4.13-4.16

unfolding plane region	selected point $(\bar{a}_0, \bar{D}_a)$	initial conditions $(a(t=0), b(t=0))$
Case (I) $(\bar{c}_0 = 0.5)$		
(i)	$(4.02, 2)$	$(7.966, 1.605)$ & $(7.043, 1.489)$
(ix) & (xiv)	$(8, 1)$	$(0.9075, 2.950)$ & $(0.3464, 1.361)$
(ii), (v), (xi), (xii) & (xv)	$(10, 2)$	$(4.904, 3.984)$ & $(2.227, 1.209)$
Case (II) $(\bar{c}_0 = 0.7)$ with $\frac{1}{16}\bar{D}_b < \bar{c}_0 < \bar{c}_0^{\phi}(\bar{D}_b)$		
(v)	$(7.5, 0.94)$	$(1.195, 2.702)$ & $(0.3544, 1.684)$
(ii) & (vii)	$(7.5, 1.2)$	$(3.649, 2.675)$ & $(1.059, 1.443)$
(iii) & (x)	$(10, 1.2)$	$(4.556, 3.408)$ & $(2.460, 3.672)$
Case (II) $(\bar{c}_0 = 0.9)$ with $\bar{c}_0^{\phi}(\bar{D}_b) < \bar{c}_0 < \bar{c}_0^{*}(\bar{D}_b)$		
(iii)	$(10, 2.8)$	$(1.880, 6.374)$ & $(1.773, 2.861)$
(vi)	$(10, 0.6)$	$(1.212, 2.547)$
(ii)	$(4, 1.6)$	$(2.420, 1.763)$ & $(1.806, 1.051)$
Case (III) $(\bar{c}_0 = 1.1)$		
(i), (ii) & (iv)	$(5, 0.7)$	$(4.638, 2.100)$ & $(4.131, 0.7551)$
(iii)	$(8, 0.7)$	$(1.458, 2.405)$

Figure 4.13 shows numerical integrations for selected regions of the unfolding plane in case (I). The situation is similar to that in Section 3.2 of Chapter 3, except that the equilibrium point $\mathbf{e_0} = (\alpha_0, \beta_0)$ no longer lies on the a-axis since $\beta_0 > 0$ and $\alpha_0 < \bar{a}_0$. In Figure 4.13a, which corresponds with the region of the unfolding plane given by case (I)(i), all phase paths approach the single stable equilibrium point $\mathbf{e_0} = (\alpha_0, \beta_0)$ as $t \to +\infty$. In Figure 4.13b, which corresponds with the region of the unfolding plane given by cases (I)(ix) & (xiv), all phase paths which start outside the stable manifold $\mathcal{S}$ of the equilibrium point $\mathbf{e}_+$ approach the stable equilibrium point $\mathbf{e_0}$ as $t \to +\infty$. However all phase paths starting inside $\mathcal{S}$ approach the stable limit cycle $\mathcal{C}_\mathcal{S}$ as $t \to +\infty$. Figure 4.13c, which corresponds with the region of the unfolding plane given by cases (I)(ii), (v), (xi), (xii) & (xv), also shows two stable attractors in the phase plane, but now the stable limit cycle $\mathcal{C}_\mathcal{S}$ has collapsed onto the stable equilibrium point $\mathbf{e}_-$. All phase paths which start outside the stable manifold $\mathcal{S}$ of the equilibrium point $\mathbf{e}_+$ approach the stable equilibrium point $\mathbf{e_0}$ as $t \to +\infty$. However all phase paths starting inside $\mathcal{S}$ approach the stable equilibrium point $\mathbf{e}_-$ as $t \to +\infty$.

Figure 4.14 shows numerical integrations for selected regions of the unfolding plane in case (II)(a). Figure 4.14a corresponds with the region of the unfolding plane given by case (II)(a)(v), which exhibits two stable attractors in the phase plane. All phase paths which start outside the stable manifold $\mathcal{S}$ of the equilibrium point $\mathbf{e}_+$ approach the stable equilibrium point $\mathbf{e_0}$ as $t \to +\infty$. However all phase paths starting inside $\mathcal{S}$ approach the stable limit cycle $\mathcal{C}_\mathcal{S}$ as $t \to +\infty$. In Figure 4.14b, which corresponds with the region of the unfolding plane given by cases (II)(a)(ii) & (vii), the situation is similar to that in Figure 4.13c. All phase paths which start outside the stable manifold $\mathcal{S}$ of the equilibrium point $\mathbf{e}_+$ ap-

proach the stable equilibrium point $\mathbf{e_0}$ as $t \to +\infty$. However all phase paths starting inside $\mathcal{S}$ approach the stable equilibrium point $\mathbf{e}_-$ as $t \to +\infty$. Increasing $\bar{a}_0$ we enter the region of the unfolding plane given by cases (II)(a)(iii) & (x), as shown in Figure 4.14c. The system $\overline{\text{[D-S]}}$ has undergone a second saddle-node bifurcation, leaving only the single stable equilibrium point $\mathbf{e}_-$, which attracts all phase paths as $t \to \infty$.

Figure 4.15 shows numerical integrations for selected regions of the unfolding plane in case (II)(b), where now the Hopf and saddle-node curves in the unfolding plane have separated leading to an interesting change in dynamics. Figure 4.15a, which corresponds with the region of the unfolding plane given by case (II)(b)(iii), exhibits, similarly to Figure 4.14c, the single stable equilibrium point $\mathbf{e}_-$ which attracts all phase paths as $t \to \infty$. In Figure 4.15b, which corresponds with the region of the unfolding plane given by case (II)(b)(vi), the only attractor in the phase plane is the stable limit cycle $\mathcal{C}_\mathcal{S}$, which now surrounds the equilibrium point $\mathbf{e_0}$. All phase paths approach $\mathcal{C}_\mathcal{S}$ as $t \to \infty$. Figure 4.15c, which corresponds with the region of the unfolding plane given by case (II)(b)(ii), exhibits similar behaviour to that in Figures 4.13c & 4.14b. All phase paths which start outside the stable manifold $\mathcal{S}$ of the equilibrium point $\mathbf{e}_+$ approach the stable equilibrium point $\mathbf{e_0}$ as $t \to +\infty$. However all phase paths starting inside $\mathcal{S}$ approach the stable equilibrium point $\mathbf{e}_-$ as $t \to +\infty$.

Figure 4.16 shows numerical integrations for the two regions of the unfolding plane in case (III), where now there are just two Hopf bifurcations, and no saddle-node bifurcations in the unfolding plane. In Figure 4.16a, which corresponds with the region of the unfolding plane given by cases (III)(i), (ii) & (iv), all phase paths approach the single stable equilibrium point $\mathbf{e_0}$ as $t \to \infty$. In

Figure 4.16b, which corresponds with the region in the unfolding plane given by case (III)(iii), the system has undergone a Hopf bifurcation causing the single equilibrium point $\mathbf{e_0}$ to become unstable, simultaneously creating a stable limit cycle $\mathcal{C}_S$, which surrounds the equilibrium point $\mathbf{e_0}$, to which all phase paths are attracted as $t \to \infty$.

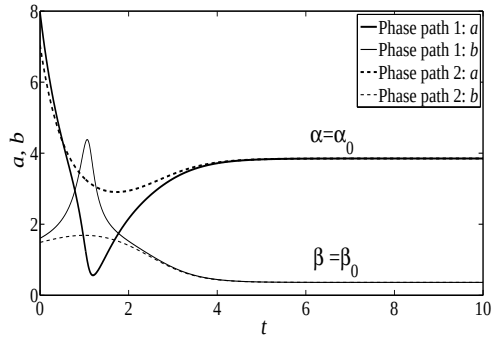

(a) Case (I)(i).

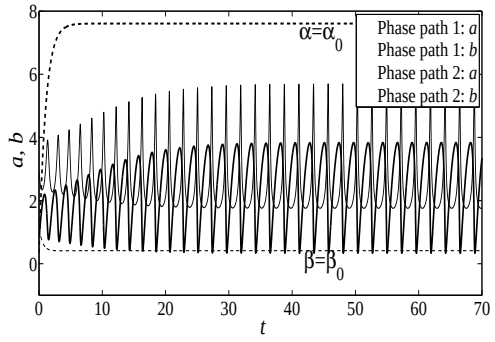

(b) Cases (I)(ix) & (xiv).

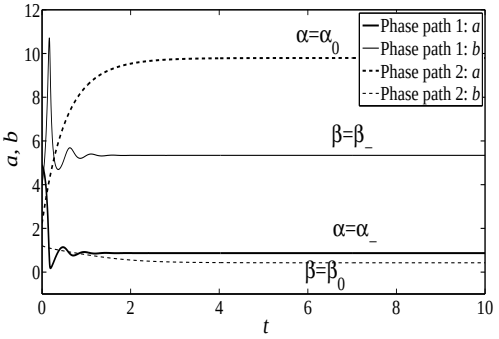

(c) Cases (I)(ii), (v), (xi), (xii) & (xv).

Figure 4.13: Graphs of $a(t)$ and $b(t)$ against $t \geq 0$ with $(\bar{a}_0, \bar{D}_a)$ chosen from selected regions of the unfolding plane for case (I). Initial conditions are given in Table (4.1).

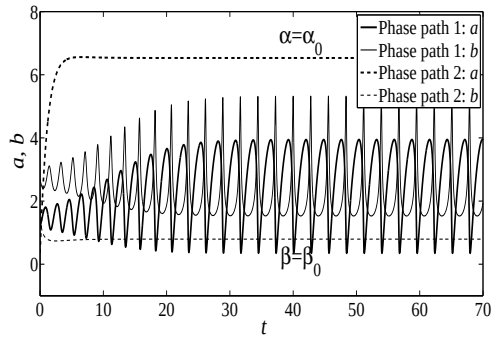

(a) Case (II)(a)(v).

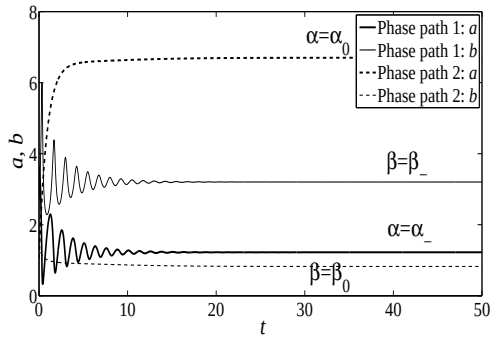

(b) Cases (II)(a)(ii) & (vii).

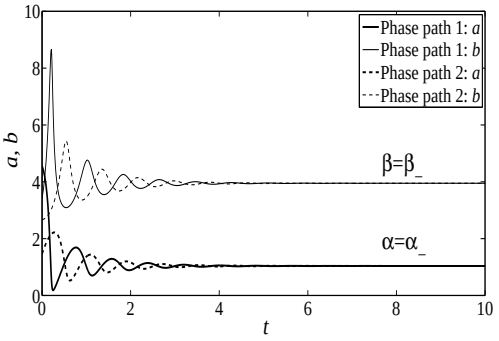

(c) Cases (II)(a)(iii) & (x).

Figure 4.14: Graphs of $a(t)$ and $b(t)$ against $t \geq 0$ with $(\bar{a}_0, \bar{D}_a)$ chosen from selected regions of the unfolding plane for case (II)(a). Initial conditions are given in Table (4.1).

4.5 Discussion

The model presented in Chapter 2 has been analysed for the case when $\bar{c}_0 > 0$, which corresponds with an internal reforming SOFC using methane as the primary fuel, where the fuel stream humidification plays a significant role in the dynamics of the fuel cell. The dynamical system $\overline{[\text{D-S}]}$, given by equations (2.42)-(2.43), describes the temporal dynamics of the concentrations $(a(t), b(t))$, which are respectively the non-dimensional concentrations of methane and hydrogen in

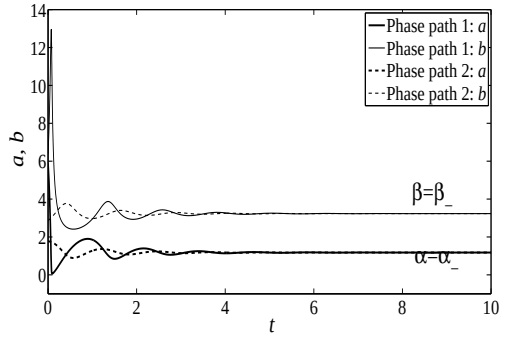

(a) Case (II)(b)(iii).

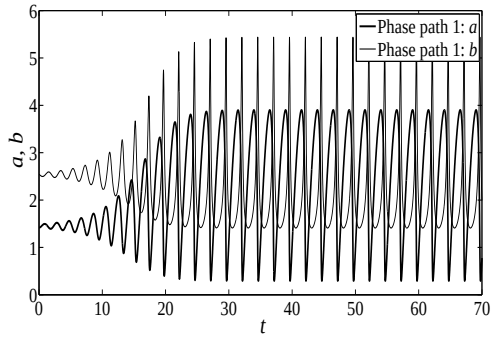

(b) Case (II)(b)(vi).

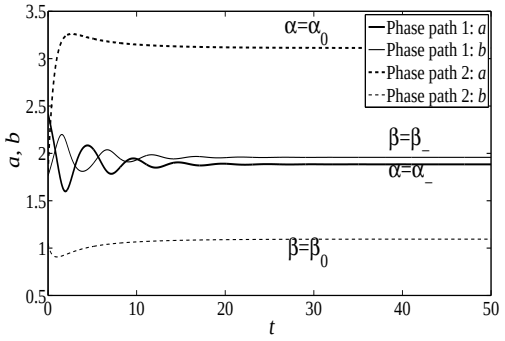

(c) Case (II)(b)(ii).

Figure 4.15: Graphs of $a(t)$ and $b(t)$ against $t \geq 0$ with $(\bar{a}_0, \bar{D}_a)$ chosen from selected regions of the unfolding plane for case (II)(b). Initial conditions are given in Table (4.1).

the SOFC. The full unfolding plane diagrams for each of the cases were presented in Figure 4.8, and sample numerical integrations were performed to illustrate they key features of the unfolding plane, shown in Figures 4.13-4.16.

Having arrived at the dynamical system $\overline{[\text{D-S}]}$, it was established that, simlarly to the weakly humidified case, the quadrant $\bar{Q}$ is a positively invariant region, with the bounds of the ω-limit set of the phase paths Γ^i given by equation (4.3). The equilibrium points of $\overline{[\text{D-S}]}$ were then identified and analysed for stability, leading to three cases depending on the value of $\bar{c}_0$. In case (I), where $0 <$

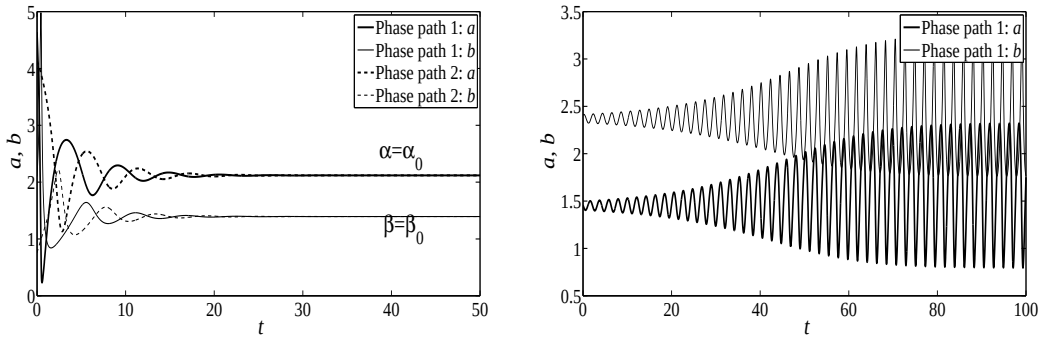

(a) Cases (III)(i), (ii) & (iv). (b) Case (III)(iii).

Figure 4.16: Graphs of $a(t)$ and $b(t)$ against $t \geq 0$ with $(\bar{a}_0, \bar{D}_a)$ chosen from selected regions of the unfolding plane for case (III). Initial conditions are given in Table (4.1).

$\bar{c}_0 < \frac{1}{16}\bar{D}_b^2$, the dynamics of $\overline{\text{[D-S]}}$ are qualitatively the same as that of [D-S]. The fundamental difference being that the equilibrium point $\mathbf{e_0}$ for $\overline{\text{[D-S]}}$ no longer lies on the a-axis since $\beta_0 > 0$ and $\alpha_0 < \bar{a}_0$. The equilibrium point $\mathbf{e_0}$ is stable for all regions of parameter space, whilst the equilibrium point $\mathbf{e}_+$ is a saddlepoint for all $\bar{a}_0 > \bar{a}_0^{SN}(\bar{D}_a)$. The equilibrium point $\mathbf{e}_-$ can be either unstable with a stable limit cycle surrounding it, or stable, with or without an unstable limit cycle surrounding it, depending on the region of the unfolding plane the system parameters imply.

As $\bar{c}_0$ is increased such that $\frac{1}{16}\bar{D}_b^2 < \bar{c}_0 < \bar{c}_0^{\phi}(\bar{D}_b)$, a qualitative change in system dynamics is observed. A second saddle-node bifurcation takes place for all $\bar{D}_a > \bar{D}_a^{\chi}(\bar{D}_b, \bar{c}_0)$, causing the equilibrium points $\mathbf{e_0}$ and $\mathbf{e}_+$ to collide, leaving only the equilibrium point $\mathbf{e}_-$ when $\bar{a}_0 > \bar{a}_0^{SN_+}(\bar{D}_a)$. This region of parameter space contains full hysteresis loops as described in Section 4.3. There are no unstable limit cycles surrounding the equilibrium point $\mathbf{e}_-$ when it is stable, and so there are no periodic saddle-node bifurcations in this case. However,

a stable limit cycle does arise in the phase plane, surrounding the equilibrium point $\mathbf{e}_-$ when it loses stability due to a Hopf bifurcation. Interestingly in this case, for $\bar{D}_a \leq \bar{D}_a^{\chi}(\bar{D}_b, \bar{c}_0)$, the single equilibrium point $\mathbf{e_0}$ becomes unstable when $\bar{a}_0^{H_-} < \bar{a}_0 < \bar{a}_0^{H_+}$, causing a stable limit cycle to appear, surrounding the equilibrium point $\mathbf{e_0}$.

Increasing $\bar{c}_0$ such that $\bar{c}_0^{\phi}(\bar{D}_b) < \bar{c}_0 < \bar{c}_0^{*}(\bar{D}_b)$, the two saddle-node curves separate from the two Hopf curves in the unfolding plane, implying $\bar{D}_a^{*}(\bar{D}_b, \bar{c}_0) < \bar{D}_a^{\chi}(\bar{D}_b, \bar{c}_0)$. Now, stable limit cycles only appear for $\bar{D}_a \leq \bar{D}_a^{*}(\bar{D}_b, \bar{c}_0)$ when $\bar{a}_0^{H_-} < \bar{a}_0 < \bar{a}_0^{H_+}$, which surround the unstable equilibrium point $\mathbf{e_0}$. For $\bar{D}_a^{*}(\bar{D}_b, \bar{c}_0) < \bar{D}_a \leq \bar{D}_a^{\chi}(\bar{D}_b, \bar{c}_0)$ there exists only the stable equilibrium point $\mathbf{e_0}$, to which all phase paths are attracted as $t \to \infty$. For the region of parameter space defined by $\bar{D}_a > \bar{D}_a^{\chi}(\bar{D}_b, \bar{c}_0)$, full hysteresis loops as described in Section 4.3 are observed.

For all $\bar{c}_0 > \bar{c}_0^{\phi}(\bar{D}_b)$, there are no saddle-node bifurcations. There exists only the single equilibrium point $\mathbf{e_0}$ which is stable when $\bar{D}_a > \bar{D}_a^{*}(\bar{D}_b, \bar{c}_0)$ for all $\bar{a}_0 > 0$. When $0 < \bar{D}_a < \bar{D}_a^{*}(\bar{D}_b, \bar{c}_0)$, the equilibrium point $\mathbf{e_0}$ becomes unstable for $\bar{a}_0^{H_-} < \bar{a}_0 < \bar{a}_0^{H_+}$, causing a stable limit cycle to arise in the phase plane due to a Hopf bifurcation, which surrounds the equilibrium point $\mathbf{e_0}$ and attracts all phase paths as $t \to +\infty$.

4.6 Conclusions

From the analysis in this chapter, it is clear that fuel stream humidification plays an important role in the temporal dynamics of an internal reforming SOFC fuelled with methane. For very low humidification, corresponding with $0 < \bar{c}_0 < \frac{1}{16}\bar{D}_b^2$, the dynamics are qualitatively the same as that presented in Chapter 3.

Increasing the humidification beyond $\frac{1}{16}\bar{D}_b^2$, causes an additional saddle-node bifurcation to take place, resulting in hysteresis. Hysteresis has been observed experimentally in PEMFCs, along with both current and voltage oscillations [37, 92]. However, to the author's knowledge, hysteretic behaviour has only been theoretically investigated for SOFCs [69, 116]. A key aspect of the experimentally observed hysteresis in PEMFCs is that one steady state gives a high power output, whilst the other steady state, for the same operating conditions, gives a low power output. This observation is remarkably similar to the two stable steady states predicted by the present model, where the equilibrium point $\mathbf{e}_- = (\alpha_-, \beta_-)$ represents a high power output, whilst the equilibrium point $\mathbf{e_0} = (\alpha_0, \beta_0)$ represents a low power output state. The experiments in [37, 92] show hysteresis between two steady states, namely, the high and low power output states, as the bifurcation parameter is varied. These results parallel the full e-e hysteresis loops described in Section 4.3, which jump between the equilibrium point $\mathbf{e}_- = (\alpha_-, \beta_-)$, representing the high power output state, and the equilibrium point $\mathbf{e_0} = (\alpha_0, \beta_0)$, representing the low power output state. The model also predicts hysteresis loops involving periodic orbits with equilibrium points, however there are currently no results in the literature to verify these predictions.

Additionally, nonlinear, autonomous oscillations are also predicted by the model in certain regions of parameter space. Autonomous oscillations have been observed experimentally [42, 68, 71, 96], although the reaction mechanisms of the SOFC have been different to the standard one adopted here. The significance of this work is apparent in the prediction of autonomous oscillations for one of the most common SOFC setups. Where others have recorded oscillations in,

for example, single chamber conditions, or with sulphur poisoning, the present model has determined criteria for oscillations for a typical non-contaminated, dual chamber, internal reforming SOFC fuelled with methane. In addition to this, Kendall et al. [18] has published work on the importance of methane dilution in SOFCs in order to stop carbon deposition from deactivating the anode surface. In the present work, oscillations have been predicted for low humidification and with very dilute concentrations of methane. Thus a lower bound for methane dilution is implied by the model in order to achieve a stable current output.

In the next chapter, an experimental programme is detailed, which corresponds with the model presented in Chapter 3.

Chapter 5

Experimental Validation

The aim of this chapter is to compare the results of the mathematical model presented in Chapter 2, with an experimental setup, for the case when $\bar{c}_0 \ll 1$, which corresponds with a weakly humidified fuel stream.

5.1 Physical Parameters

We appeal to the literature, in order to obtain the physical parameters of the system as inputs to the model. Structural properties of the cell are required, and empirical data is taken for reaction rate constants and diffusion coefficients.

5.1.1 Diffusion Model

For multi-component diffusion in a porous membrane, the parallel pore model is used [52, 117]. Effective diffusion coefficients for use with a Fickian mass

transport mechanism are obtained. For each species, i,

$$D_i^{eff} = \frac{\phi}{\tau}\left(\frac{1-\alpha_{i,m}X_i}{D_{i,m}} + \frac{1}{D_i^{Kn}}\right)^{-1}, \tag{5.1}$$

where,

$$\alpha_{i,m} = 1 - \left(\frac{M_i}{M_{avg}}\right)^{-1}, \tag{5.2}$$

$$D_{i,m} = \frac{1-X_i}{\sum\limits_{\substack{j \\ j\neq i}} \frac{X_j}{D_{ij}}}. \tag{5.3}$$

Here, ϕ and τ are the anode porosity and tortuousity respectively, X_j is the mole fraction of species j, M_i is the molecular mass of species i, M_{avg} is the average molecular mass of the mixture, D_i^{Kn} is the Knudsen diffusion coefficient of species i, and D_{ij} is the binary diffusion coefficient of species i and j.

The average molecular mass of the mixture is given by the total mass of the mixture divided by the total moles of the mixture [118]. We can hence derive an expression for M_{avg} in terms of the mole fractions of the species and their respective molecular masses, as,

$$M_{avg} = \frac{m}{n} \tag{5.4}$$

$$= \frac{\sum n_i M_i}{n} \tag{5.5}$$

$$= \frac{\sum x_i n M_i}{n} \tag{5.6}$$

$$= \sum x_i M_i \tag{5.7}$$

where x_i is the mole fraction of species i, n_i is the number of moles of species i, m is the total mass of the mixture, and n is the total moles of the mixture.

The Knudsen diffusion coefficient is given by [52],

$$D_i^{Kn} = \frac{2}{3} r_p \left(\frac{8 R_u T}{\pi M_i} \right)^{\frac{1}{2}}, \tag{5.8}$$

where, r_p is the average pore radius of the anode, R_u is the universal gas constant, and T is the temperature in Kelvin.

The binary diffusion coefficients used in equation (5.1) come from the 1^{st} order approximation to the Chapman-Enskog theory for binary mixtures [109], that is,

$$D_{ij} = 0.0018583 \sqrt{T^3 \left(\frac{1}{M_i} + \frac{1}{M_j} \right)} \frac{1}{p \sigma_{ij}^2 \Omega_{ij}}, \tag{5.9}$$

where, p is pressure of the gas mixture and σ_{ij} is the average collision diameter

given by,

$$\sigma_{ij} = \frac{\sigma_i + \sigma_j}{2}. \tag{5.10}$$

The path integral, Ω_{ij}, is empirically derived as,

$$\Omega_{ij} = \frac{1.06036}{(T^*)^{0.15610}} + \frac{0.19300}{e^{0.47635T^*}} + \frac{1.03587}{e^{1.52996T^*}} + \frac{1.76474}{e^{3.89411T^*}} \tag{5.11}$$

where,

$$T^* = \frac{k_B T}{\epsilon_{ij}}, \tag{5.12}$$

and the characteristic energy is,

$$\epsilon_{ij} = \sqrt{\epsilon_i \epsilon_j}. \tag{5.13}$$

Here, k_B is the Boltzmann constant, whilst σ_i, σ_j, ϵ_i, and ϵ_j are Lennard-Jones parameters which are given by Mason & Monchick [113] and Roncin [119], for the species under consideration.

5.1.2 Reaction Kinetic Model

Many studies have been done on the rate of methane steam reforming in SOFCs [64, 103, 105, 120] which indicate that the rate of steam reforming is much higher than the rate of hydrogen oxidation. An expression for the rate constant for the

steam reforming of methane has been given as [105, 121],

$$k_1 = S_A^{Ni} 0.0636 T^2 e^{\frac{-27063}{T}}, \tag{5.14}$$

where, S_A^{Ni} is the specific surface area of the nickel catalyst in the SOFC anode ($\frac{m^2}{m^3}$). Values of S_A^{Ni} generally used in the literature for SOFC modelling are estimated to be between 2×10^5 and 1×10^6, however a comprehensive study of anode structural properties under redox cycling has more recently been done, estimating the specific surface area of nickel to be between 3.56×10^6 and 5.86×10^6 [122]. The study determined the anode structural properties before and after a number of redox cycles using Focussed Ion Beam Scanning Electron Microscopy. The results, in fact, showed that S_A^{Ni} increased monotonically as the number of redox cycles increased.

The reaction rate constant for hydrogen oxidation, k_3, may be estimated via an application of Faraday's law of electrolysis.

$$\frac{i}{VnF} = 2k_3 b^2 x, \tag{5.15}$$

where, i is the current drawn from the cell (A), V is the volume of the anode (m^3), n is the change in valence of the reactant, F is Faraday's constant ($\frac{C}{mol}$), b and x are the concentrations of hydrogen and oxygen respectively ($\frac{mol}{m^3}$), and so,

$$k_3 = \frac{i}{2VnFb^2 x} \tag{5.16}$$

5.1.3 Stoichiometry

Since the cell will be exposed to air at 1073 K, the value of x, which is the concentration of oxygen at the cathode side ($\frac{mol}{m^3}$), is calculated as follows. Assuming air contains approximately 21% oxygen by volume, and taking 100 m^3 of air as a basis, we have,

$$x = \frac{\text{mass of } O_2}{\text{molar mass of } O_2} \frac{1}{\text{volume of air}} \tag{5.17}$$

$$= \frac{\text{density of } O_2 \text{ at } 1073K \times \text{volume of } O_2}{\text{molar mass of } O_2} \frac{1}{\text{volume of air}} \tag{5.18}$$

$$= \frac{0.3633 \frac{kg}{m^3} \times 21 m^3}{0.032 \frac{kg}{mol}} \frac{1}{100 m^3} \tag{5.19}$$

$$= 2.3842 \frac{mol}{m^3}. \tag{5.20}$$

The concentration of methane in the fuel channel, a_0, is calculated as,

$$a_0 = \frac{\text{molar flow rate of } CH_4 \frac{mol}{s}}{\text{total flow rate} \frac{m^3}{s}} \tag{5.21}$$

$$= \frac{\text{mass flow rate of } CH_4 \frac{kg}{s}}{\text{total flow rate} \frac{m^3}{s} \times \text{molar mass of } CH_4 \frac{kg}{mol}} \tag{5.22}$$

$$= \frac{\text{density of } CH_4 \frac{kg}{m^3} \times \text{flow rate of } CH_4 \frac{m^3}{s}}{\text{total flow rate} \frac{m^3}{s} \times \text{molar mass of } CH_4 \frac{kg}{mol}}. \tag{5.23}$$

At high temperatures the ideal gas law may be applied [123], giving,

$$\rho_{CH_4} = \frac{P \times \text{molar mass of } CH_4}{RT}, \tag{5.24}$$

where ρ_{CH_4} is the density of methane, P is the pressure, R is the universal gas constant and T is the temperature. Substituting into equation (5.23) we arrive at,

$$a_0 = \frac{\dot{Q}_{CH_4}}{\dot{Q}_{Tot}} \frac{P}{RT} \tag{5.25}$$

$$= \frac{\dot{Q}_{CH_4}}{\dot{Q}_{Tot}} \frac{101325Pa}{8.314\frac{m^3 Pa}{molK} \times 1073K} \tag{5.26}$$

$$= 11.3581 \times \frac{\dot{Q}_{CH_4}}{\dot{Q}_{Tot}} \frac{mol}{m^3}. \tag{5.27}$$

Here, $\dot{Q}_{CH_4}$ is the volumetric flow rate of methane ($\frac{m^3}{s}$), and $\dot{Q}_{Tot}$ is the total fuel stream flow rate ($\frac{m^3}{s}$). The surface area of transfer, A, and the thickness of the anode, h, are used to calculate the dimensionless parameters that were introduced in Chapter 2.

5.2 Experimental Programme

Since there are very few results in the literature concerning current oscillations in SOFCs, an experimental programme has been implemented, in order to locate the regions of oscillations based on the parameters in the model. The results are compared with model predictions, and the dynamic features of the cell are discussed. A preliminary test was first performed on a microtubular SOFC as was used in [8], whilst subsequent experiments were conducted using tubular

SOFCs, assembled in-house, with the geometry as shown in Figure (5.1).

The experiments performed here were done with low fuel stream humidification, corresponding with the first dynamical system [D-S]. According to the model, introducing higher concentrations of steam creates more variable behaviour, and would require a more comprehensive study than the present experimental programme. The aim of this experimental programme is to establish preliminary results, and test fundamental model predictions for the case of a weakly humidified fuel stream. Thus we start with the experimental conditions which correspond with $\bar{c}_0 \ll 1$.

5.2.1 Cell Assembly

The anode supported microtubular cell came from the same batch of cells that were prepared in [8], and the dimensions were approximately 55mm in length, with an inside diameter of 2.2mm, and outside diameter of 2.8mm. The approximate thicknesses of each layer were, 300μm of Ni anode, 15μm of YSZ electrolyte, and 30μm of LSM cathode. In order to collect the current, a 10mm strip of the YSZ electrolyte was carefully filed down in order to expose the Ni anode beneath. Conducting silver ink was then applied to both electrodes. The exposed anode was completely covered by the ink, whilst the cathode only had 4 bands of silver ink in order to minimise oxygen concentration polarisation. Silver wire was then tightly wrapped around the cell electrodes, in contact with the applied silver ink. The cell manifolds were made from drilled macor blocks, and the cell was held in place using high temperature cement, with silver ink applied over the top in order to minimise leakage. The outlet manifold was connected to an

exhaust pipe and once again sealed with high temperature cement and silver ink. This was to ensure that there was no combustion near the outlet due to leaked fuel, which has been known to damage the cell [124].

The anode supported tubular cells were commercially obtained with the configuration as shown in Figure (5.1). A similar method to the preparation of the microtubular cells was used, with a 10mm strip of anode being exposed by filing down the samarium doped ceria (SDC) barrier and YSZ electrolyte. Silver ink was then applied to the entire exposed anode, and in 4 bands along the cathode. The cell was sintered at 120^oC for 2 hours before tightly wrapping the silver wire around the cell electrodes. More silver ink was then applied on top of the silver wire, carefully filling in the gaps between the wire and the silver-coated electrodes. The cell was again sintered at 120^oC for a further 2 hours in order to enhance the electrical contact. The cell manifolds were made from drilled macor cylinders, and the connecting tubes were made from alumina. At the inlet the alumina tube was connected to the piping coming from the fuel supply, whilst the outlet alumina tube was connected to an exhaust pipe. All the connections were sealed with high temperature cement, and the connections between the cell and the manifolds also had silver ink applied over the top in order to minimise leakage. The cell and manifolds are shown in Figure (5.2).

5.2.2 Test Rig

Gas cylinders were connected to specific mass flow controllers, which in turn were fed into a gas mixer prior to entering the cell. The setup was such that the gas mixture could then either pass through a humidifier, or go directly into the

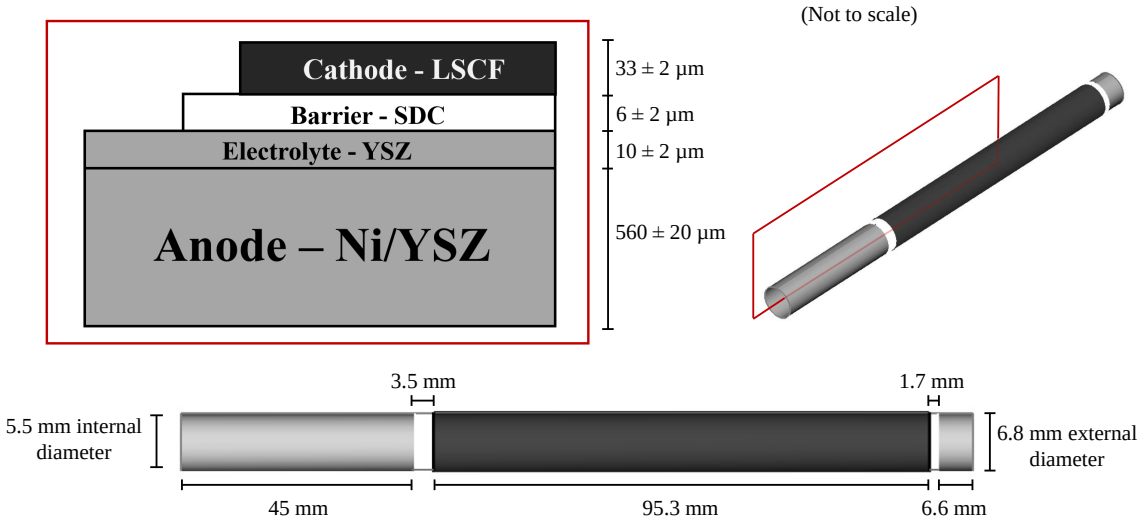

Figure 5.1: Tubular SOFC configuration.

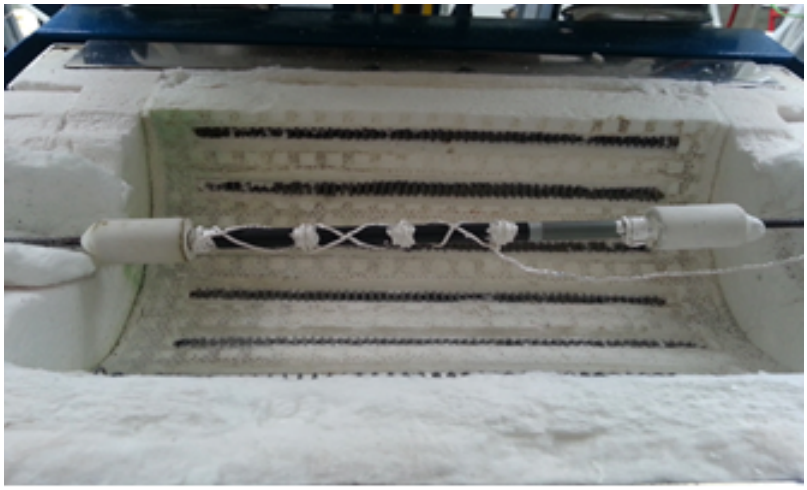

Figure 5.2: Tubular SOFC with manifolds.

cell. The piping from the gas mixer/humidifier was connected to the cell manifolds, whilst the outlet manifolds were connected to an exhaust pipe as described

in Section 5.2.1. The cell was enclosed in a high temperature, programmable furnace, and the silver wire current collectors were connected to a potentiostat. A schematic is shown in Figure (5.3).

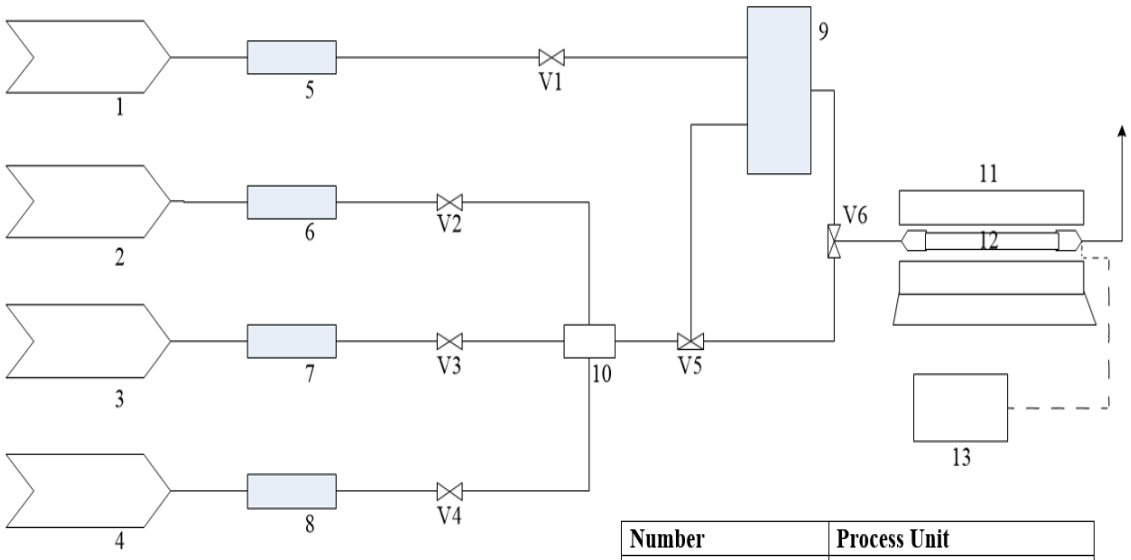

Number	Process Unit
1	N_2
2	H_2
3	CH_4
4	N_2
5-8	mass flow controller
9	evaporator/humidifier
10	gas mixer
11	furnace
12	tubular SOFC
13	potentiostat
V1-V4	quarter turn valve
V5, V6	three-way valve

Figure 5.3: Test rig schematic.

5.2.3 Experimental Procedure

Microtubular SOFC

The microtubular cell was heated up to 700^oC, whilst maintaining a flow of H_2 through the cell at $30\frac{ml}{min}$. This was done in order to prevent the Ni anode from reoxidising. The open circuit voltage (OCV) was then measured for 40 minutes to allow the cell to stabilise. After the OCV test, the fuel stream was switched to a mixture of CH_4 and He, with a flow rate totalling $30\frac{ml}{min}$. The flow was allowed to stabilise, then a potentiostatic test was performed. The potential difference between the 2 cell electrodes was held at 0.5V throughout. This potential difference will henceforth be referred to as the applied voltage, or the voltage applied to the cell. Initially the concentration of CH_4 was kept low, and over regular time intervals the CH_4 flow rate would be increased by $0.5\frac{ml}{min}$, whilst the He flow rate would simultaneously be reduced by $0.5\frac{ml}{min}$ in order to maintain a reasonably constant flow rate. In this experiment there was no fuel stream humidification.

Tubular SOFC

The tubular cells were heated up to 800^oC, while once again, maintaining a flow of H_2 through the cell at $70\frac{ml}{min}$ to prevent the Ni anode from reoxidising. The OCV was then measured for 40 minutes to allow the cell to stabilise. After the OCV test, the fuel stream was switched to a mixture of CH_4, N_2, and H_2O, with a flow rate totalling approximately $100\frac{ml}{min}$. The flow was allowed to stabilise, then a potentiostatic test was performed. Initially the cell was held at an applied voltage of 0.8V. In this experiment the CH_4 flow rate was initially high, and was decreased after the dynamic behaviour of the cell became apparent. The N_2 flow

rate was simultaneously increased by the same amount in order to keep the flow rate approximately the same. The minimum time between flow rate adjustment was set at 20 minutes, in order to ensure the cell had reached a distinct stable, or oscillatory state. The potentiostatic experiment was then repeated for applied voltages of 0.7V and 0.6V, using the same procedure for adjusting the flow rates. Three different tubular cells were tested using this method.

5.2.4 Results

Microtubular SOFC

In what follows, all fuel compositions will be given in $\frac{ml}{min}$. The initial experiment with the microtubular cell utilised very dilute concentrations of dry methane. As can be seen from Figure (5.4), an oscillatory response was observed after an initial settling in period of around 3 minutes. The concentration of methane was increased gradually over time, and the oscillations persisted up until the fuel composition reached 11.5/18.5/0 (CH_4/He/H_2O). At this concentration of methane, the cell was seen to undergo a qualitative change in behaviour. The amplitude of the oscillations decreased, as the average current increased, until a new quasi-steady state was reached at approximately 9380s.

Tubular SOFCs

Results from the potentiostatic experiments performed on 3 tubular SOFCs are presented in Figures (5.5)-(5.13). For the first cell, steady states were observed for intermediate to high concentrations of methane in all potentiostatic experiments. For a fixed composition, the amount of current drawn from the cell increased

as the applied voltage decreased, due to the accelerated forward electrochemical reaction (2.3). Additionally, as the concentration of methane in the fuel stream was decreased, the average current output also decreased due to a reduced flux of reactants into the anode. For applied voltages of $0.8V$ and $0.7V$, the cell began to exhibit small fluctuations in current output at the lower concentrations of methane, and then dropped to a zero current state at compositions 5/93/2 and 5.5/92.5/2 ($CH_4/N_2/H_2O$) respectively. When the applied voltage was decreased to $0.6V$, the cell exhibited self-sustained, autonomous current oscillations at low concentrations of methane. The initial step decrease in methane concentration was $2\frac{ml}{min}$, up until the region of oscillation. After 20 minutes, the concentration of methane was then increased by $0.5\frac{ml}{min}$, which caused the oscillations to decrease in amplitude, whilst the average current increased. After another 40 minutes the methane concentration was again increased by $0.5\frac{ml}{min}$, causing the oscillation amplitude to further decrease, and the average current to increase again. This effect is similar to that observed for the microtubular cell, where the initial state was oscillatory, and increasing the methane concentration through a critical value caused a new quasi-steady state to be reached. Following this, the methane concentration was decreased sufficiently to bring the cell back into the fully oscillatory state, and then further decreased over time in order to observe the effect on the oscillations. At a composition of 5/100/2 ($CH_4/N_2/H_2O$) the cell dropped to a zero current state.

The second and third cells gave very similar performance to each other in terms of electrical output. The cells exhibited the same steady state behaviour as the first cell at intermediate and high concentrations of methane, for all applied voltages. However in these experiments, the step decrease in methane concentra-

tion was much smaller at lower concentrations. This was done in order to induce the oscillatory state before the zero current state was reached. Self-sustained, autonomous current oscillations were observed at all applied voltages in both cells. As the methane concentration was lowered, the oscillations generally increased in amplitude, whilst the average current decreased. In all cases the zero current state was reached for a non-zero concentration of methane in the fuel stream, however the critical values at which the zero current states occurred were lower for the second and third cells than that of the first cell. Additionally, when comparing the performance between the cells at the same fuel composition, the second and third cells provided much more current than the first cell, indicating a much more efficient SOFC. This explains, why at each of the applied voltages, the zero current state was reached at a lower methane concentration for the second and third cells. The difference in performance was no doubt an artefact of the cell assembly process. Interestingly, the peak of the current oscillations was still relatively high for methane-deprived compositions. For example, in the case of the second cell, at an applied voltage of $0.6V$ the current peaked as high as $0.7A$ for compositions as low as $0.5/100/2$ ($CH_4/N_2/H_2O$). Regarding high power output in oscillatory modes of operation, in [89], a PEMFC was observed to oscillate under galvanostatic, but not potentiostatic conditions. The authors point out that for the same fuel compositions, the time-averaged power output density was much higher in the oscillatory state than in the corresponding steady state. This implies that it may be beneficial to operate the cell in oscillatory mode for any application whose power requirements are not strictly time dependent. For example, electrolysis is often used to produce hydrogen for fuel by passing an electric current through water. Since the hydrogen product is generally stored

in gas cylinders for later use, it is not strictly necessary to produce the hydrogen at a constant rate. Thus, a more efficient system is possible by supplying the current from an oscillatory mode of operation, as opposed to that from a steady state current output.

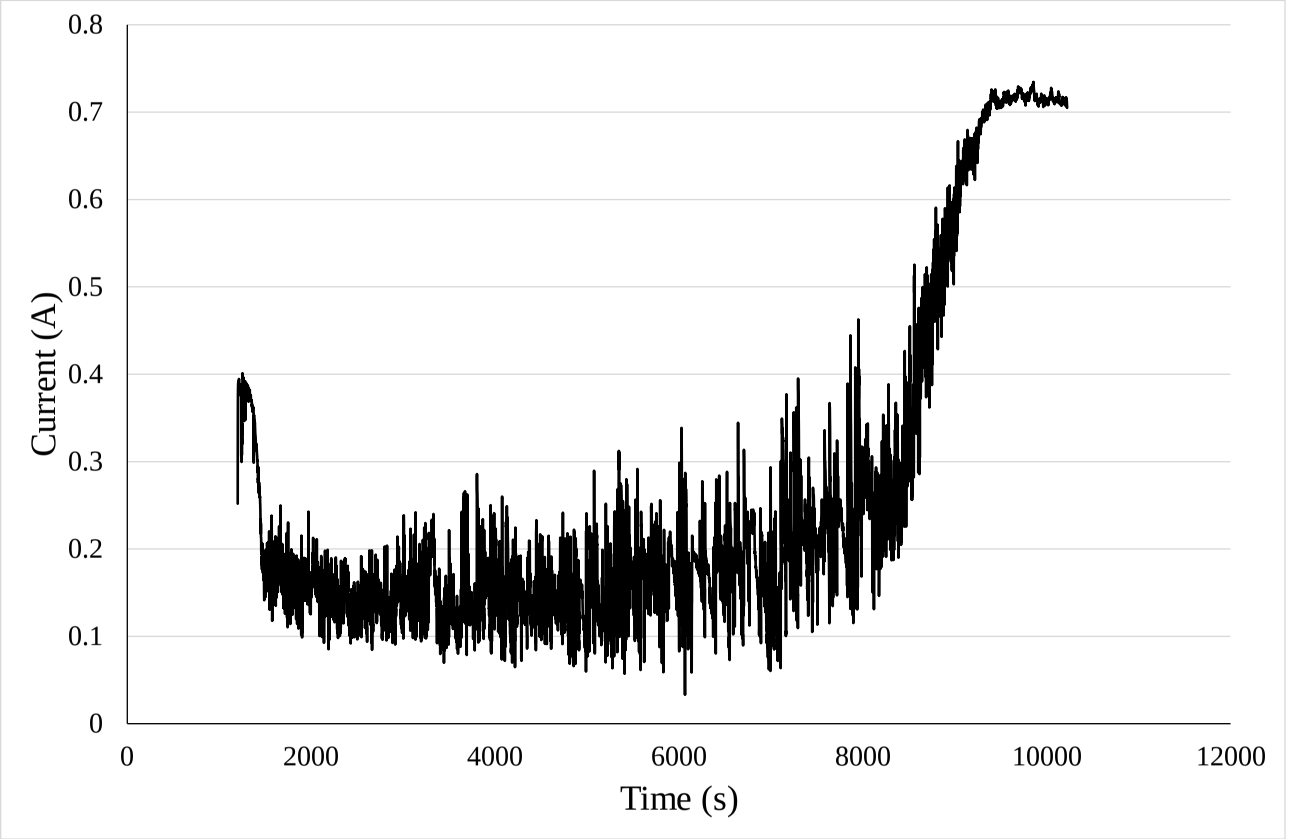

Figure 5.4: Potentiostatic experiment for microtubular cell at 0.5V. Here, the initial concentration of methane, a_0, is increasing with time.

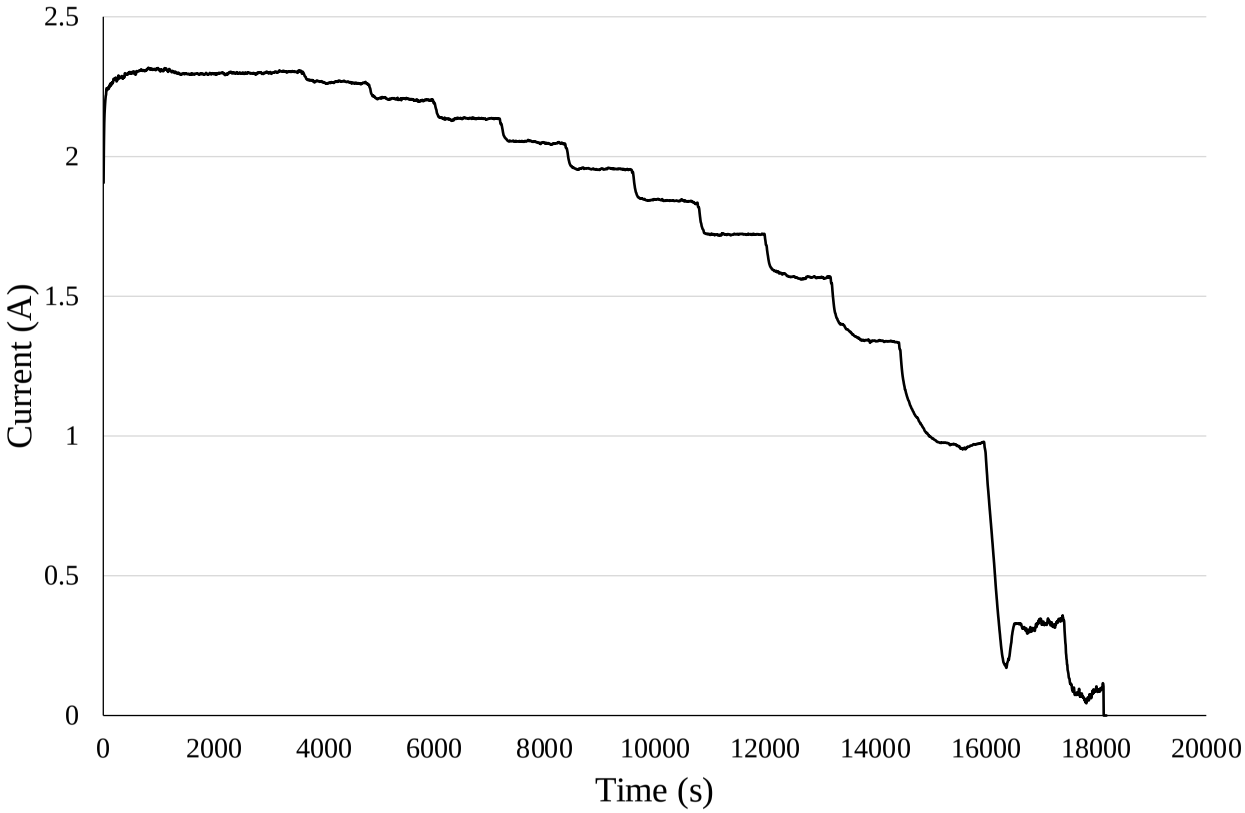

Figure 5.5: Potentiostatic experiment for tubular cell 1 at 0.8V. Here, the initial concentration of methane, a_0, is decreasing with time.

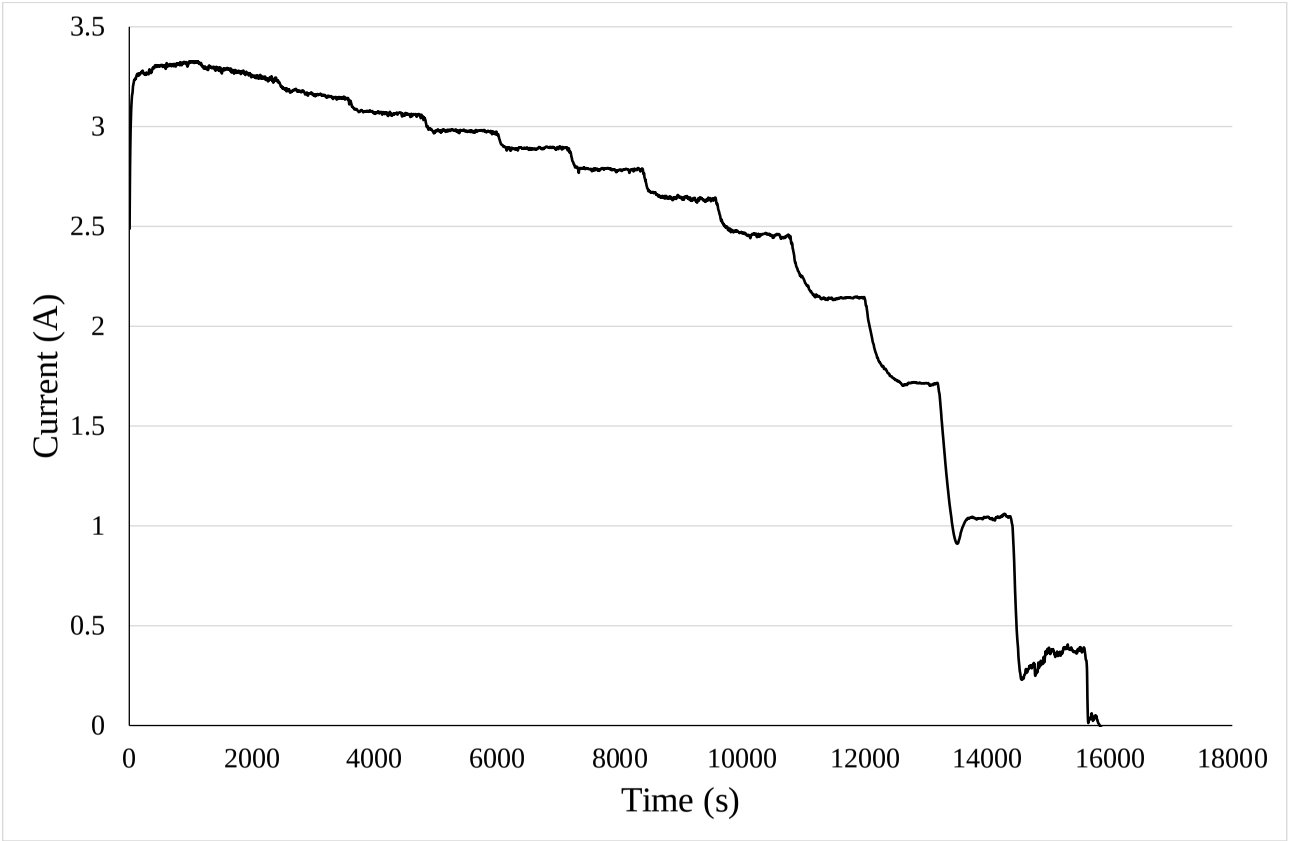

Figure 5.6: Potentiostatic experiment for tubular cell 1 at 0.7V. Here, the initial concentration of methane, a_0, is decreasing with time.

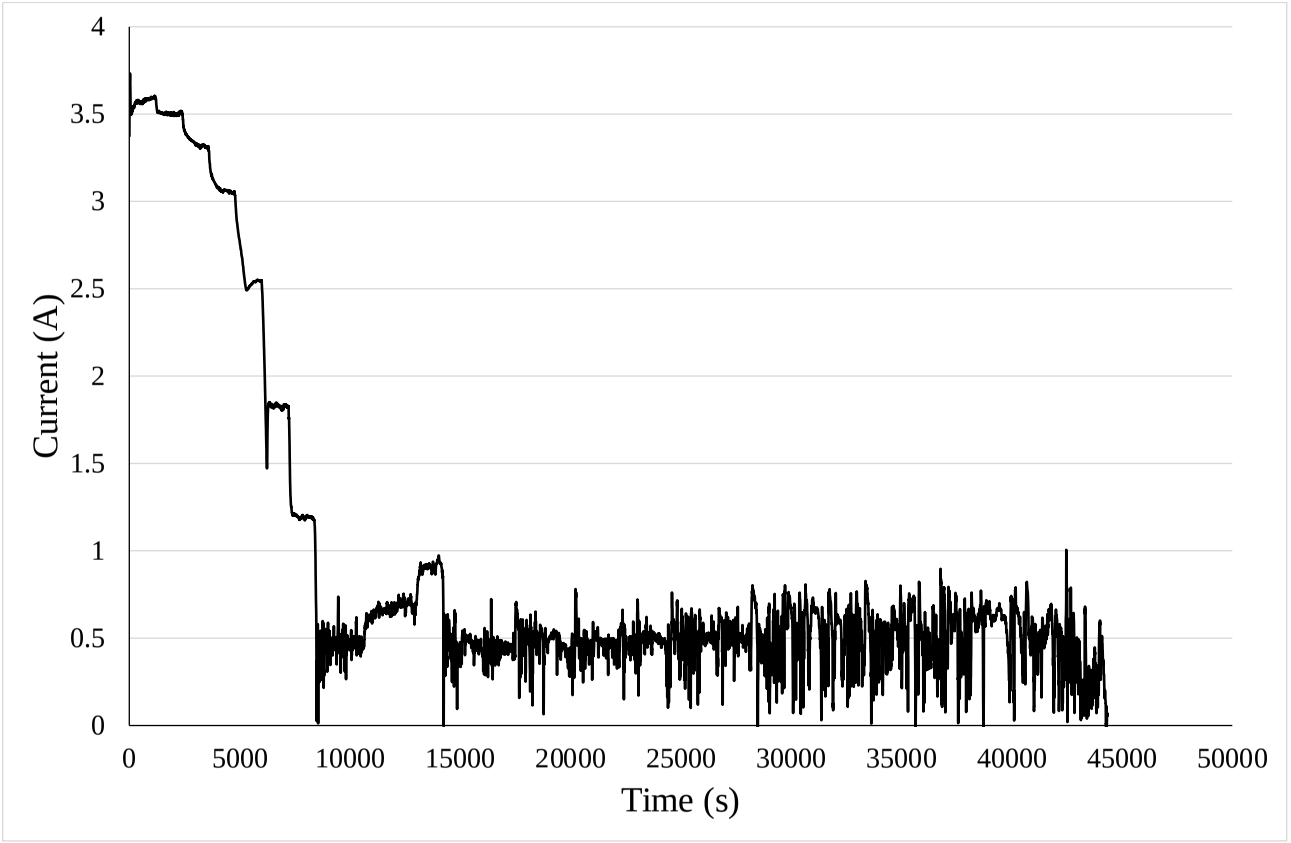

Figure 5.7: Potentiostatic experiment for tubular cell 1 at 0.6V. Here, the initial concentration of methane, a_0, is decreasing with time.

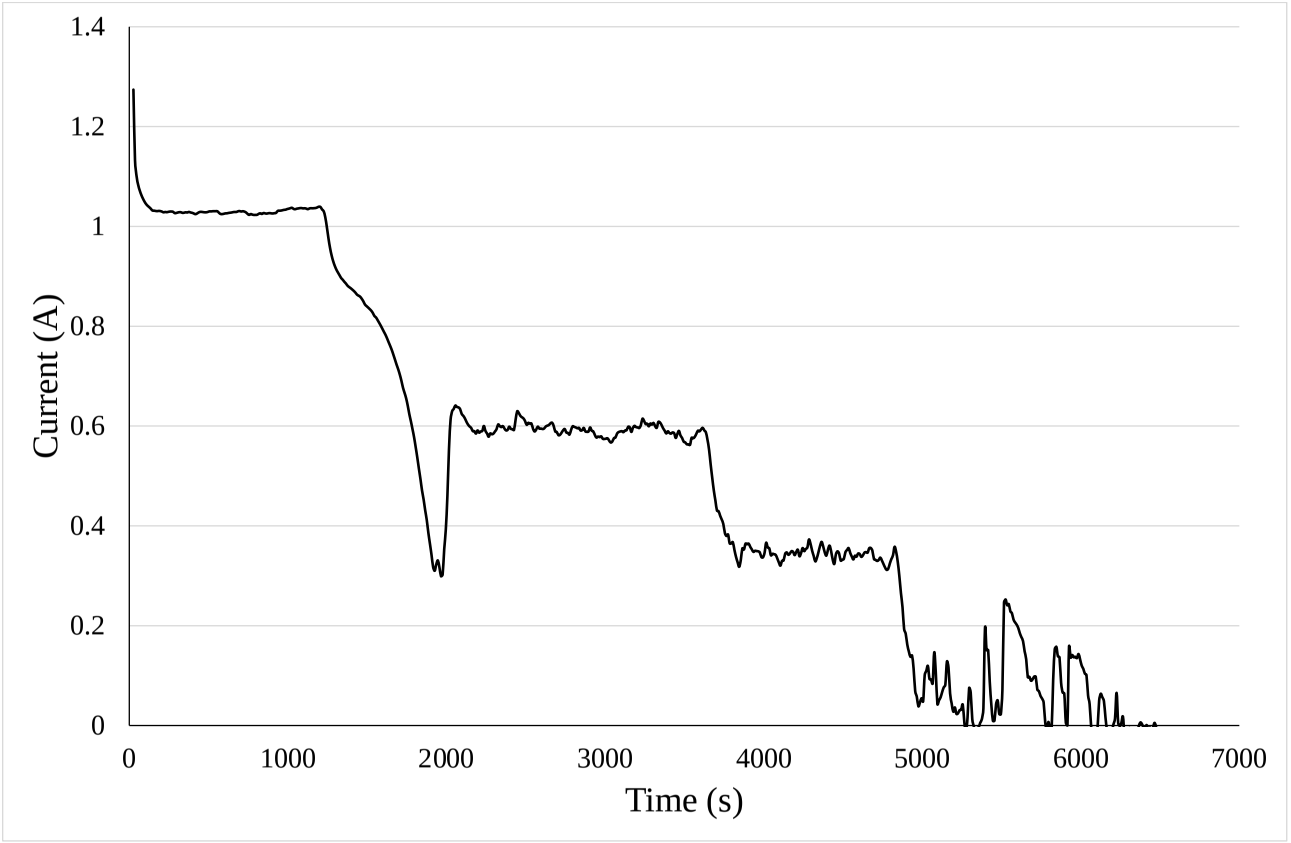

Figure 5.8: Potentiostatic experiment for tubular cell 2 at 0.8V. Here, the initial concentration of methane, a_0, is decreasing with time.

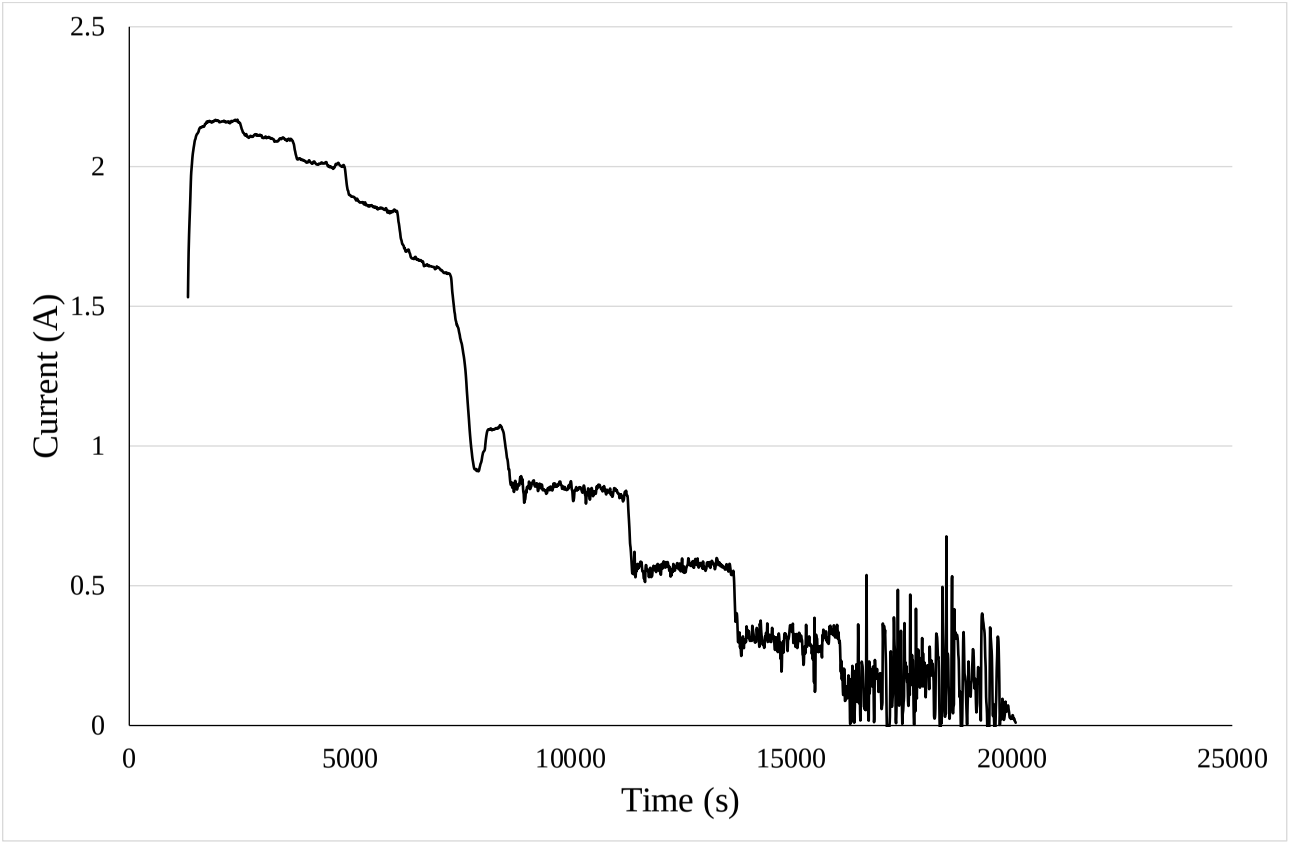

Figure 5.9: Potentiostatic experiment for tubular cell 2 at 0.7V. Here, the initial concentration of methane, a_0, is decreasing with time.

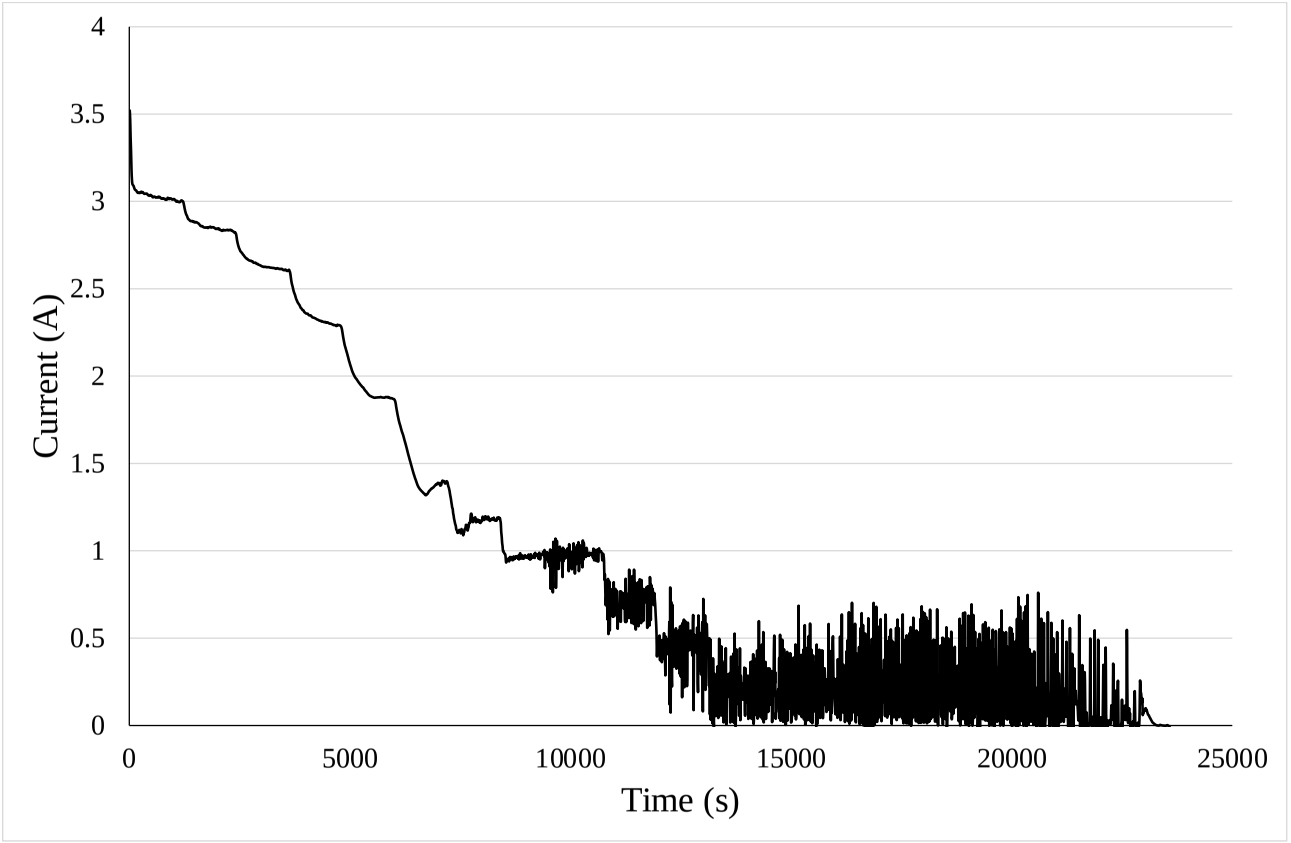

Figure 5.10: Potentiostatic experiment for tubular cell 2 at 0.6V. Here, the initial concentration of methane, a_0, is decreasing with time.

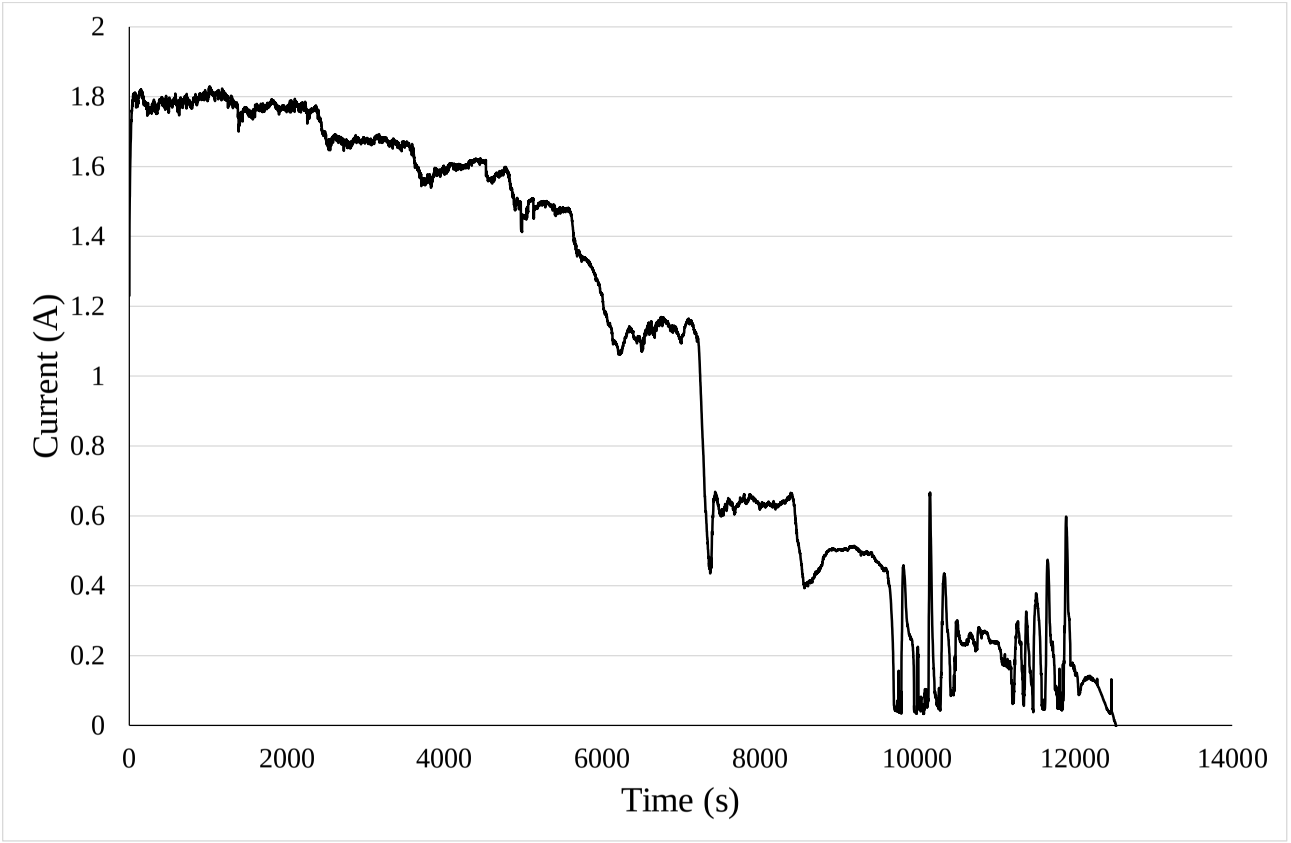

Figure 5.11: Potentiostatic experiment for tubular cell 3 at 0.8V. Here, the initial concentration of methane, a_0, is decreasing with time.

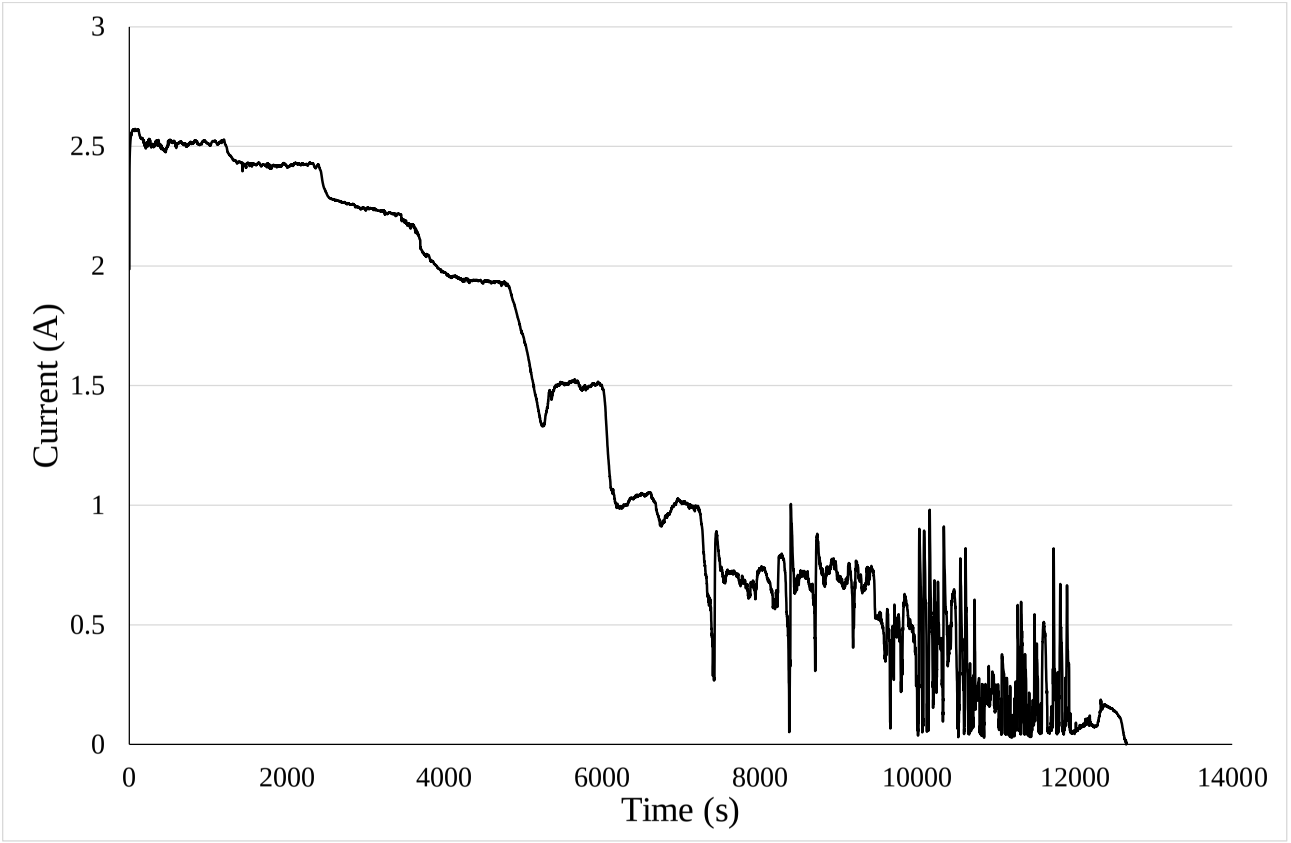

Figure 5.12: Potentiostatic experiment for tubular cell 3 at 0.7V. Here, the initial concentration of methane, a_0, is decreasing with time.

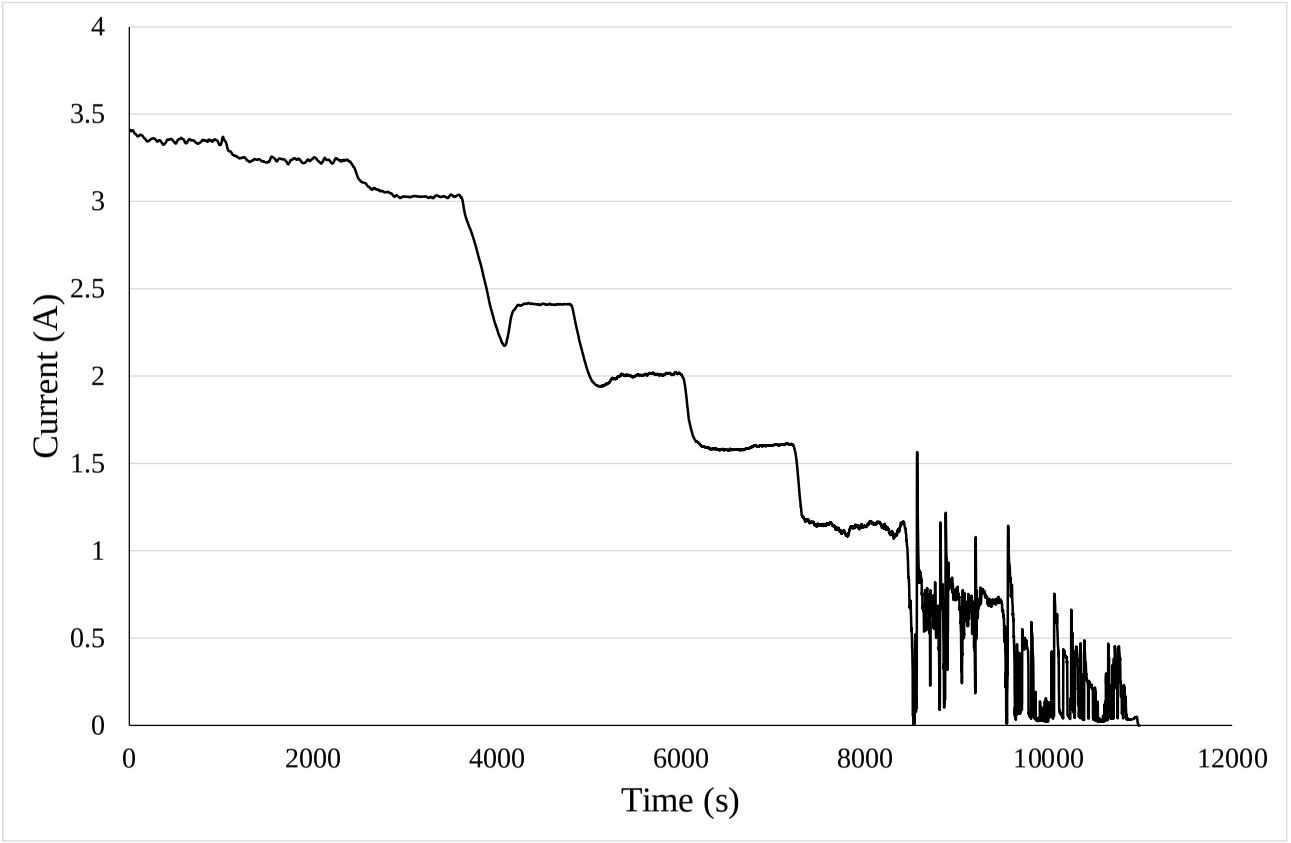

Figure 5.13: Potentiostatic experiment for tubular cell 3 at 0.6V. Here, the initial concentration of methane, a_0, is decreasing with time.

5.3 Model Comparison

The first interesting feature is that the current drops to zero for a non-zero concentration of methane in the fuel stream. In other words, the fuel cell stops producing electric current when the amount of methane in the fuel channel drops below a critical value. This observation is in full accord with the predictions of the model, and the critical value is represented in the model by $\bar{a}_0^{SN}$, $\bar{a}_0^{P}$, or $\bar{a}_0^{\infty}$ in Figures (3.12a)-(3.12f), depending on what region of parameter space the fuel cell system corresponds with. For $\bar{D}_a \geq \bar{D}_a^*(\bar{D}_b)$, there are no limit cycles in the phase plane, and therefore one would not expect to observe an oscillatory response from the cell as is the case in the experiments. Decreasing the methane concentration below $\bar{a}_0^{SN}$ causes the equilibrium points $\mathbf{e}_-$ and $\mathbf{e}_+$ to collide via a saddle-node bifurcation, leaving only the equilibrium point $\mathbf{e_0}$, which corresponds with a zero current output state. Thus we would expect to see the cell go from various stable current states, since the equilibrium point $\mathbf{e}_-$ corresponds with a stable steady state current output, to the zero current state, without exhibiting any oscillations. For all $0 < \bar{D}_a < \bar{D}_a^c(\bar{D}_b)$, stable limit cycles arise in the phase plane, so one would expect to see the cell exhibit autonomous current oscillations. For $\bar{D}_a^{\infty}(\bar{D}_b) < \bar{D}_a < \bar{D}_a^c(\bar{D}_b)$, decreasing the methane concentration below $\bar{a}_0^{P}$ causes the stable and unstable limit cycles to collide via a periodic saddle-node bifurcation, leaving the equilibrium point $\mathbf{e_0}$ as the only stable attractor in the phase plane. Thus one would expect to see the cell go from stable steady states, to an oscillatory state, and then finally to the zero current state. For $0 < \bar{D}_a \leq \bar{D}_a^{\infty}(\bar{D}_b)$, the mechanism would involve the stable limit cycle colliding with the equilibrium point $\mathbf{e}_+$ via a homoclinic bifurcation, leaving the

equilibrium point $\mathbf{e_0}$ as the only stable attractor in the phase plane. Similarly, one would once again expect to see the cell go from stable steady states, to an oscillatory state, and then to the zero current state, as the concentration of methane was lowered. All of these sequences of behaviour are seen in the experiments.

If we now look at the non-dimensional parameters in the model, we can determine the region of parameter space corresponding with the physical fuel cell setup in the experiments, based on the operating conditions and material properties of the fuel cell. We have,

$$\varepsilon = \frac{xk_3}{k_1}\,, \quad \bar{D}_b = \frac{D_b}{D_c\varepsilon}\,, \quad \bar{D}_a = \frac{D_a}{D_c\varepsilon}\,, \quad \bar{a}_0 = \frac{a_0}{a_s}\,, \quad \bar{c}_0 = \frac{c_0}{c_s}\ .$$

From these we obtain the relationship,

$$\bar{D}_a = \frac{D_a}{D_b}\bar{D}_b. \tag{5.28}$$

The parameters D_a and D_b are the dimensional Fickian transfer coefficients, for methane and hydrogen respectively, which can be calculated from equation (5.1). For the operating conditions, and fuel cell materials used in the experiment, we find that,

$$0.3138 < \frac{D_a}{D_b} < 0.3393. \tag{5.29}$$

A graphical user interface, the code for which is given in Appendix B, was created in MATLAB and used to calculate the values of D_a and D_b over the range of operating conditions. The range of $\frac{D_a}{D_b}$ was found by substituting in the upper and lower bounds given in the literature for material properties [66, 103, 121], in conjunction with the flow rates and operating conditions used in the experiments.

From the model we also have the parameterisation, (3.34),

$$\bar{a}_0^* = \alpha + \tfrac{\alpha(2\alpha+1)(2\alpha-1)}{(6\alpha+1)}, \quad \bar{D}_a^* = \tfrac{(2\alpha-1)^3(6\alpha+1)}{32\alpha^2}, \quad \bar{D}_b = \tfrac{(2\alpha-1)^3}{4\alpha}, \quad \alpha > \tfrac{1}{2},$$

for the unfolding point $(\bar{a}_0^*, \bar{D}_a^*)$ in the $(\bar{a}_0, \bar{D}_a)$ unfolding plane. Taking derivatives and applying the chain rule we find that,

$$\frac{d\bar{D}_a^*}{d\bar{D}_b} \to 1, \text{ as } \alpha \to \frac{1}{2}, \tag{5.30}$$

$$\frac{d\bar{D}_a^*}{d\bar{D}_b} \to 0.75, \text{ as } \alpha \to \infty. \tag{5.31}$$

This means that the value of $\bar{D}_a$ obtained from the actual diffusion coefficients in equation (5.28), for each $\bar{D}_b$, will always be less than $\bar{D}_a^*$, for the operating conditions of the fuel cell in this particular experimental programme. Additionally, it has been confirmed through numerical investigation that the curve $\bar{D}_a = \bar{D}_a^c(\bar{D}_b)$ lies between the curve $\bar{D}_a = \bar{D}_a^*(\bar{D}_b)$, and the curve given by equation (5.28). Therefore one would expect to see oscillations, given the right fuel composition, regardless of the applied voltage, as has been confirmed in the experiments. The

situation is shown in Figure (5.14).

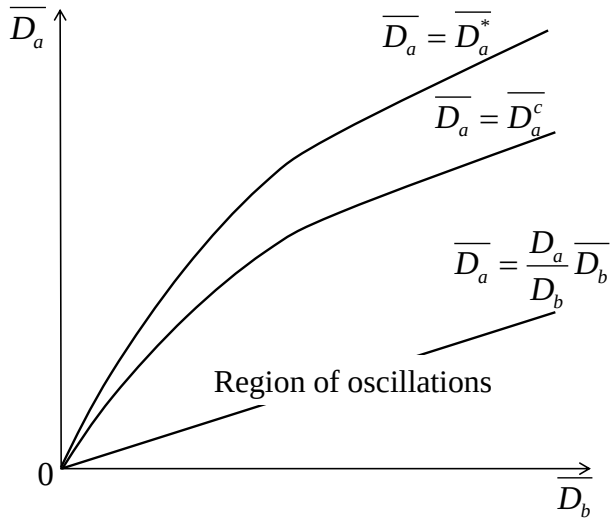

Figure 5.14: Sketch of $(\bar{D}_b, \bar{D}_a)$ plane.

The experiments on the second and third tubular cells indeed show current oscillations at all applied voltages for low methane concentrations. However, the first cell appeared to only exhibit minor current fluctuations before the zero current output state was reached. The absence of larger, distinct oscillations in cell 1 may be down to the step change in methane concentration being too great. The final step size before the cell dropped to zero current was $0.5\frac{ml}{min}$ for the first cell, at applied voltages of $0.8V$ and $0.7V$. However, it is possible that the cell may have started to oscillate if a smaller step size had been used. An indicator of how sensitive the system is to qualitative changes in behaviour can be seen in the potentiostatic test on the second cell at $0.6V$. At step decrease in methane of $0.1\frac{ml}{min}$ was enough to cause the cell to change from exhibiting autonomous current oscillations, where the peak was still approximately $0.5A$,

to a zero current output. Therefore it is reasonable to suggest that oscillations may have occurred in the first cell, if the final step size had been smaller. This is further confirmed by finding oscillations at all applied voltages in the later cells, where a much smaller step change in methane concentration was used.

We can infer other interesting features from the bifurcation diagrams shown in Figure 5.15. Figure 5.15a shows the full bifurcation diagram for fixed $0 < \bar{D}_a \leq \bar{D}_a^{\infty}$ in the $(\bar{a}_0, \alpha)$ plane, with the corresponding full bifurcation diagram in the $(\bar{a}_0, \beta)$ plane shown in Figure 5.15b. The amplitude of the oscillation is represented, in both Figure 5.15a and Figure 5.15b, by the line with an arrow in the centre, pointing in the direction of increasing amplitude. The equilibrium point $\mathbf{e}_- = (\alpha_-, \beta_-)$ corresponds with the stable, current generating state of the SOFC, whilst the equilibrium point $\mathbf{e_0} = (\bar{a}_0, 0)$ corresponds with the zero current output state. The value of β_- thus corresponds with the amount of current being produced in a steady state response from the cell, as given by equation (5.15). It can be seen from Figure 5.15b that as the initial concentration of methane is decreased (corresponding with a decrease in $\bar{a}_0$), the value of β_- also decreases, which, via (5.15), implies a decrease in current output. This trend can be seen in the experimental results for all 3 tubular cells. In each of the Figures 5.5-5.13, as the concentration of methane was decreased, the steady state current output decreased accordingly. To demonstrate this, we plot the steady state current output, against the concentration of methane supplied to the SOFC.

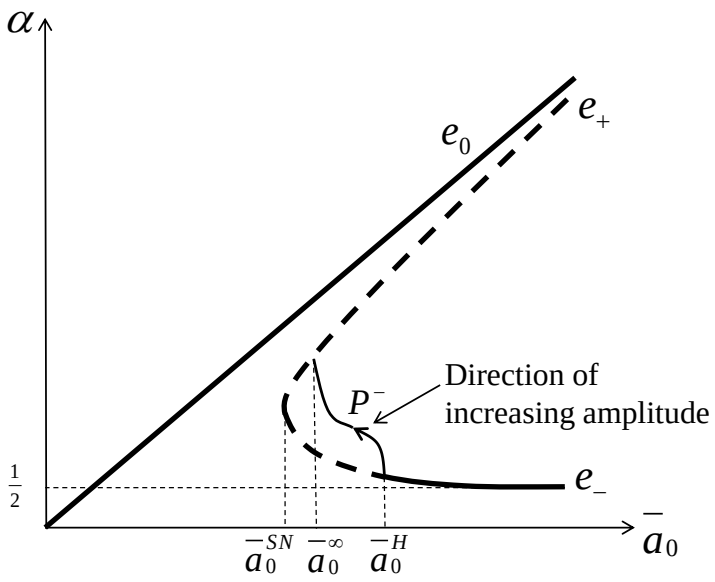

(a) $(\bar{a}_0, \alpha)$ plane.

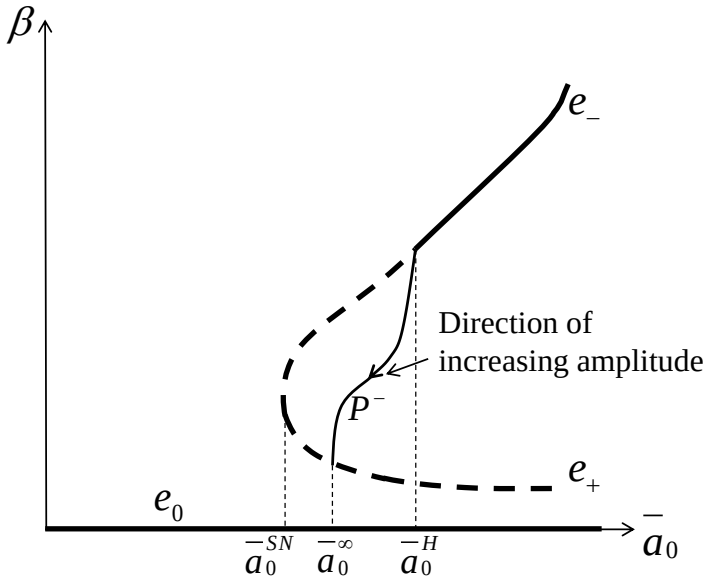

(b) $(\bar{a}_0, \beta)$ plane.

Figure 5.15: Bifurcation diagrams in the $(\alpha, \bar{a}_0)$ and $(\beta, \bar{a}_0)$ planes.

The results for the first cell, with an applied voltage of $0.7V$, are shown in Figure 5.16. The crosses are time averaged current outputs for various fuel compositions, and the dotted line is a cubic polynomial fit. The shape of the curve in Figure 5.16 matches very well with the $\mathbf{e}^-$ curve in Figure 5.15b, validating the assumption that the concentration of hydrogen within the anode is representative of the current drawn from the cell at given operating conditions.

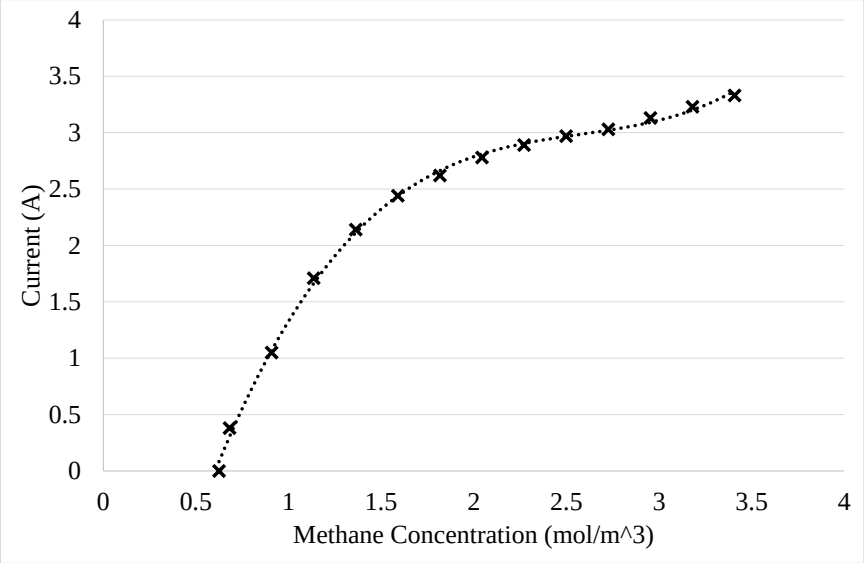

Figure 5.16: Steady state current output vs. methane concentration for cell 1 at an applied voltage of $0.7V$.

With regard to the oscillations, it can be seen from Figure 5.15b that first as the concentration of methane is decreased, the steady state current output de-

creases, then small amplitude oscillations arise in the phase plane surrounding the equilibrium point $\mathbf{e}_- = (\alpha_-, \beta_-)$. Further decreasing the concentration of methane lowers the value of β_-, whilst simultaneously increasing the amplitude of the oscillation. Physically this corresponds with less hydrogen in the anode, and therefore a lower average current output, with a larger amplitude of current oscillation. This trend can be be seen in the results shown in Figures 5.7-5.13. As the cell is transitioning from steady state to oscillatory, the average current drops with each step decrease in methane concentration, whilst the amplitude of the oscillation increases. Conversely, with the microtubular cell, the oscillations start off with large amplitude at low methane concentrations, and as the methane concentration is increased the cell transitions back into a quasi-steady state. As the transition is occurring, the average current output increases whilst the amplitude of the oscillation decreases. In the model, this corresponds with the stable limit cycle $\mathcal{C}_S$ collapsing onto the equilibrium point $\mathbf{e}_-$ as $\bar{a}_0$ increases.

Since the experiments were performed over a long period of time, the sampling rate of the potentiostat was always greater than 1 second. This meant that the shape of the current oscillations could not be deduced from these results. However oscillations can clearly be seen on the order of seconds, rather than minutes or hours. The time scale of the model is given in equation (2.29) and can be calculated using the values for the parameters given in this chapter. For the experimental conditions used in these experiments the time scale ranges from approximately 0.2-1.04, which corresponds with the period of the oscillations observed in the experiments.

5.4 Summary

In this chapter the model presented in Chapter 3 was linked with physical parameters in order to compare with the experimental programme set out in Section 5.2. A diffusion model was implemented based on Lennard-Jones parameters taken from [113] and [119], and expressions for rate constants were presented based on various results from the literature. Additionally, the stoichiometry was detailed in order to link the experimental conditions to the species concentrations in the model.

An experimental programme was carried out using both tubular, and microtubular methane fuelled SOFCs, with a weakly humidified fuel stream. The tubular cells were assembled in-house and the microtubular cell was obtained from the same batch as that in [8]. The test rig and experimental procedure were described in Sections 5.2.2 and 5.2.3, and the results were presented in Section 5.2.4. Finally, the results of the experimental programme were compared with the model in Section 5.3. It was found that the steady state current output of the cells, as the methane concentration was decreased, matched very well with the steady state hydrogen concentration used in the model, represented by β_{-}. Both steady and oscillatory states were induced by varying the concentration of methane in the fuel stream in accordance with the model. For lower concentrations of methane, the amplitude of the oscillations was much larger, with the average current output being lower. As the concentration of methane was increased, the oscillations decreased in size whilst the average current output increased, matching well with model predictions. Additionally, it was seen that each of the SOFCs reached a zero current output for a non-zero concentration of

methane in the fuel stream. This is another interesting feature of the model, and to the author's knowledge, is undocumented in fuel cell literature.

Chapter 6

Conclusions

The objective of this thesis was to investigate the occurrence of nonlinear, autonomous current oscillations in SOFCs, and to elucidate the mechanism driving this behaviour. To this end a model was derived in Chapter 2, based on Fickian mass transfer and fundamental reaction kinetics, resulting in a set of coupled, autonomous, nonlinear ordinary differential equations. These equations were then nondimensionalised with respect to typical scales, and the system was rationally reduced to a planar dynamical system. This system was further simplified by first considering the case where $\bar{c}_0 \ll 1$, which corresponds with a weakly humidified fuel stream in a methane fuelled SOFC. This simplified case was studied in Chapter 3. General properties of the phase portrait were established, then the existence of equilibrium points and equilibrium point bifurcations were identified. Following this, the equilibrium points were analysed for stability, and Hopf bifurcations were identified for specific regions of parameter space. The global phase portraits were sketched, and sample numerical integrations were presented in order to elucidate the dynamic behaviour of the system in the various regions

of parameter space. It was found that multiple steady states occurred, arising from a saddle-node bifurcation. One of the steady states corresponded with a zero current output state of the cell, whilst the other corresponded with a stable current producing state. Particularly, the model predicted that the current drop to zero for a non-zero concentration of methane in the fuel stream. Other predictions were that the steady state current output of the cell would decrease as the concentration of methane was decreased, and eventually enter a region of oscillations. As the transition from steady state to oscillatory was occurring, the model predicted that the average current output would decrease as the amplitude of the oscillations increased until the zero current output state was reached.

In Chapter 4, the model presented in Chapter 2 was analysed for the case of $\bar{c}_0 = O(1)$. A similar analysis to that in Chapter 3 was performed, and key differences in dynamic behaviour were outlined. The key differences were that a second saddle-node bifurcation would occur for larger $\bar{c}_0$, and now also two Hopf bifurcations could be observed. The model indicates that there is a significant change in fuel cell dynamics for a humidified fuel stream. Particularly, various hysteresis loops, including equilibrium point hysteresis and equilibrium-periodic orbit hyteresis, were observed. It is interesting to note that steady state hysteresis has been observed in PEMFCs [37, 92], and has also been theoretically demonstrated to occur in SOFCs in [69, 116].

An experimental programme was implemented in Chapter 5, in order to validate the model for the weakly humidified case. Results in the literature are few and varied for SOFC oscillations, and therefore it was necessary to perform experiments using a fuel cell setup that corresponded with the assumptions in the model. Standard dual chamber, tubular and microtubular SOFCs were used,

fuelled with a noncontaminated supply of methane, diluted with an inert gas, and with weak to zero fuel stream humidification. These conditions matched well with the model in Chapter 3. In order to link the model to the physical setup, expressions for model parameters were presented, based on results from the literature. It was found that the behaviour of the steady states was indeed as expected for decreasing concentrations of methane, and that a zero current output state was reached for a non-zero concentration of methane. This last feature is undocumented in fuel cell literature to the author's knowledge, and is thus a very prominent result. Autonomous current oscillations were found at low methane concentrations before reaching the zero current output state, as predicted by the model, suggesting that the reaction-diffusion dynamics within the anode are indeed the cause of the observed oscillations. In addition, the amplitude of the oscillations was seen to develop in accordance with model predictions, along with the average current output during the oscillatory response.

Of the 4 cells tested, all of them exhibited current oscillations at low methane concentrations, however in the first cell only minor current fluctuations were seen at applied voltages of $0.8V$ and $0.7V$. This can be explained by too large a step decrease in methane concentration, causing the cell to jump immediately to the zero current output state, and bypassing the region of oscillations. This is further confirmed by oscillations being found at all applied voltages for the other cells, where a smaller step change in methane concentration was used.

The significance of this work is apparent when considering the work by Kendall et al. [18], where dilute concentrations of methane were favoured in SOFCs in order to prevent carbon deposition. The present work gives an indication of a lower bound for the dilution of methane during the operation of SOFCs

with a weakly humidified fuel stream, since at lower concentrations, nonlinear, autonomous current oscillations set in. In Chapter 4 it is seen that increasing the fuel stream humidification significantly alters the dynamics of the fuel cell, and shifts the region of oscillation. A more comprehensive experimental programme is required in order to verify this prediction, as well as the effects of altering other operating conditions, such as temperature and material porosity, in relation to the model. Generally, the model was very capable of explaining the dynamic behaviour of a methane fuelled SOFC, and certain model predictions have been experimentally validated. The undocumented phenomenon of reaching a zero current output for a non-zero concentration of methane, was predicted in Chapter 3, and this prediction was verified in Chapter 5. The conditions which induced current oscillations in the fuel cell corresponded well with conditions implied by the model. Additionally, the development of the oscillations during transitions from steady state to oscillatory output matched well with model predictions. Thus it is reasonable to assume, that the model presented in this thesis, has indeed helped elucidate the fundamental mechanisms behind nonlinear, autonomous current oscillations in methane fuelled SOFCs.

6.1 Further Work

Whilst the results from the experimental programme were very promising, a much more comprehensive set of experiments is required in order to verify the predicted changes in dynamic response of the fuel cell, for the case of a humidified fuel stream. The results in Chapter 4 indicate that, rather than reaching a zero current output for low concentrations of methane, the cell will exist in a

low power generating state. Low and high power generating states have been observed to coexist in PEMFCs [37, 92], however have not been observed experimentally in SOFCs as yet. It would be interesting to test for hysteresis in SOFCs, using results from the present model as a guide. Additionally, the effects of different operating conditions can be tested, as these would affect the region of the unfolding plane the fuel cell system would imply. A graphical user interface is presented in Appendix B, which can assist the user in linking model parameters to physical results in future work.

Additionally, since the experiments were performed over a long period of time, a moderate sampling rate was used for the potentiostat when measuring the current over time. Since the period of the oscillations was on the order of seconds, the shape of the oscillations could not be deduced from the results of this experimental programme. In order to see a more accurate picture of the oscillations, experiments should be done using a sample rate of around 10 milliseconds or less.

Since the reactions in a fuel cell include both exothermic and endothermic reactions, a natural progression would be to include these effects in the model, with temperature as an additional variable. Expressions for the rate constants and diffusivities would replace the variables k_{1-4}, D_a, D_b, D_c, using Arrhenius relationships and the diffusion model presented in Section 5.1.1 of Chapter 5.

The model may also be improved upon by considering the spatial domain in conjunction with the time domain. This would involve deriving a system of partial differential equations which account for the changing species concentrations throughout the volume of both the porous anode and the fuel channel. The most important spatial domain to consider is in the longitudinal dimension, as the

various chemical species are changing due to reactions occurring in the anode. The addition of this spatial domain would provide a more accurate description of the dynamic behaviour of the fuel cell. It may then be appropriate to include the other spatial domains to build a full three dimensional, temporal model of the fuel cell. The use of numerical methods and finite element software, such as COMSOL or Open Foam, would be beneficial for this more complicated system of equations.

Bibliography

[1] J. D. Sands, J. Uddin, and D. J. Needham. A Fundamental Model Exhibiting Nonlinear Oscillatory Dynamics in Solid Oxide Fuel Cells. *Proceedings of the Royal Society A-Mathematical Physical and Engineering Sciences*, 470, 2014.

[2] J. D. Sands, D. J. Needham, and J. Uddin. A Fundamental Model Exhibiting Nonlinear Oscillatory Dynamics in Solid Oxide Fuel Cells - The Effects of Fuel Stream Humidification. *Quarterly Journal of Mechanics and Applied Mathematics (under review)*.

[3] J. D. Sands, D. J. Needham, and J. Uddin. Nonlinear Chemical Dynamics Resulting in Current Oscillations in Solid Oxide Fuel Cells. *Journal of Power Sources (under review)*.

[4] L. J. M. J. Blomen and N. Mugerwa. *Fuel Cell Systems*. Springer, 1993.

[5] S. C. Singhal and K. Kendall. *High Temperature Solid Oxide Fuel Cells: Fundamentals, Design and Applications*. Elsevier Advanced Technology, Oxford, 2003.

[6] R. Bove and S. Ubertini. *Modeling Solid Oxide Fuel Cells: Methods, Procedures and Techniques*. Springer, USA, 2008.

[7] N. H. Behling. *Fuel Cells: Current Technology Challenges and Future Research Needs*. Elsevier Science, 2012.

[8] A. Dhir and K. Kendall. Microtubular SOFC Anode Optimisation for Direct Use on Methane. *Journal of Power Sources*, 181:297–303, 2008.

[9] H. Sumi, K. Ukai, Y. Mizutani, H. Mori, C. Wen, H. Takahashi, and O. Yamamoto. Performance of Nickel-Scandia-Stabilized Zirconia Cermet Anodes for SOFCs in 3% H2O-CH4. *Solid State Ionics*, 174:151–156, 2004.

[10] N. Nakagawa, H. Sagara, and K. Kato. Catalytic Activity of Ni $\pm$ YSZ $\pm$ CeO2 Anode for the Steam Reforming of Methane in a Direct Internal-Reforming Solid Oxide Fuel Cell. *Journal of Power Sources*, 92:1–5, 2001.

[11] H. Timmermann, D. Fouquet, A. Weber, E. Ivers-Tiffée, U. Hennings, and R. Reimert. Internal Reforming of Methane at Ni/YSZ and Ni/CGO SOFC Cermet Anodes. *Fuel Cells*, 6(3-4):307–313, 2006.

[12] E. S. Putna, J. Stubenrauch, J. M. Vohs, and R. J. Gorte. Ceria-Based Anodes for the Direct Oxidation of Methane in Solid Oxide Fuel Cells. *Langmuir*, 11:4832–4837, 1995.

[13] J. Hou, Z. Zhu, J. Qian, and W. Liu. A New Cobalt-Free Proton-Blocking Composite Cathode La2NiO4-δ-LaNi0.6Fe0.4O3-δ for BaZr0.1Ce0.7Y0.2O3-δ-Based Solid Oxide Fuel Cells. *Journal Of Power Sources*, 264:67–75, 2014.

[14] R. L. Cook and A. F. Sammells. On The Systematic Selection Of Perovskite Solid Electrolytes For Intermediate Temperature Fuel-Cells. *Solid State Ionics*, 45:311–321, 1991.

[15] Y. Leng, S. Chan, and Q. Liu. Development of LSCF-GDC Composite Cathodes for Low-Temperature Solid Oxide Fuel Cells with Thin Film GDC Electrolyte. *International Journal of Hydrogen Energy*, 33:3808–3817, 2008.

[16] J. Chen, J. Huang, X. Li, Y. Liu, B. Qi, S. Jiang, and X. Wang. Plasma-Sprayed Coating of an Apatite-Type Lanthanum Silicate Electrolyte for Intermediate Temperature Solid Oxide Fuel Cells (IT-SOFCs). *Plasma Science & Technology*, 15:673–676, 2013.

[17] V. D. Belyaev, T. I. Politova, O. A. Marina, and V. A. Sobyanin. Internal Steam Reforming of Methane Over Ni-Based Electrode in Solid Oxide Fuel Cells. *Applied Catalysis A: General*, 133:47–57, 1995.

[18] K. Kendall, C. M. Finnerty, G. Saunders, and J. T. Chung. Effects of Dilution on Methane Entering an SOFC Anode. *Journal of Power Sources*, 106:323–327, 2002.

[19] Y. Lin, Z. Zhan, J. Liu, and S. Barnett. Direct Operation of Solid Oxide Fuel Cells with Methane Fuel. *Solid State Ionics*, 176:1827–1835, 2005.

[20] J. P. Trembly, R. S. Gemmen, and D. J. Bayless. The Effect of IGFC Warm Gas Cleanup System Conditions on the Gas-Solid Partitioning and Form of Trace Species in Coal Syngas and their Interactions with SOFC Anodes. *Journal Of Power Sources*, 163:986–996, 2007.

[21] G. A. Tompsett, C. Finnerty, K. Kendall, T. Alston, and N. M. Sammes. Novel Applications for Micro-SOFCs. *Journal Of Power Sources*, 86:376–382, 2000.

[22] S. McIntosh, J. M. Vohs, and R. J. Gorte. Role of Hydrocarbon Deposits in the Enhanced Performance of Direct-Oxidation SOFCs. *Journal Of The Electrochemical Society*, 150:A470–A476, 2003.

[23] B. Madsen and S. Barnett. Effect of Fuel Composition on the Performance of Ceramic-Based Solid Oxide Fuel Cell Anodes. *Solid State Ionics*, 176:2545–2553, 2005.

[24] M. Noponen, M. Halinen, J. Kiviaho, and J. Saarinen. Feasibility of Autothermally Reformed Natural Gas on Anode Supported Solid Oxide Fuel Cells. *Journal of Fuel Cell Science and Technology*, 3:438–444, 2006.

[25] B. C. H. Steele. Materials for IT-SOFC Stacks 35 Years R&D: The Inevitability of Gradualness. *Solid State Ionics*, 134:3–20, 2000.

[26] R. A. George. Status of Tubular SOFC Field Unit Demonstrations. *Journal Of Power Sources*, 86:134–139, 2000.

[27] A. D. Hawkes and M. A. Leach. Cost-Effective Operating Strategy for Residential Micro-Combined Heat and Power. *Energy*, 32:711–723, 2007.

[28] P. Costamagna, L. Magistri, and A. F. Massardo. Design and Part-Load Performance of a Hybrid System Based on a Solid Oxide Fuel Cell Reactor and a Micro Gas Turbine. *Journal Of Power Sources*, 96:352–368, 2001.

[29] K. Sedghisigarchi and A. Feliachi. Dynamic and Transient Analysis of Power Distribution Systems With Fuel Cells - Part II : Control and Stability Enhancement. *IEEE Transactions on Energy Conversion*, 19:429–434, 2004.

[30] J. Lawrence and M. Boltze. Auxiliary Power Unit Based on a Solid Oxide Fuel Cell and Fuelled with Diesel. *Journal Of Power Sources*, 154:479–488, 2006.

[31] L. Giorgi, M. Carewska, M. Patriarca, S. Scaccia, E. Simonetti, and A. DiBartolomeo. Development and Characterization of Novel Cathode Materials for Molten-Carbonate Fuel-Cell. *Journal Of Power Sources*, 49:227–243, 1994.

[32] N. Di Giulio, B. Bosio, V. Cigolotti, and S. W. Nam. Experimental and Theoretical Analysis of H2S Effects on MCFCs. *International Journal Of Hydrogen Energy*, 37:19329–19336, 2012.

[33] J. R. Davis, R. Johnson, and J. Stepanek. *Fundamentals of Aerospace Medicine*. M - Medicine Series. Lippincott Williams & Wilkins, 2008.

[34] Y. Teow, P. V. Asharani, M. P. Hande, and S. Valiyaveettil. Health Impact and Safety of Engineered Nanomaterials. *Chemical Communications*, 47:7025–7038, 2011.

[35] E. J. Chia, J. B. B. Benziger, and I. G. Kevrekidis. Water Balance and Multiplicity in a Polymer Electrolyte Membrane Fuel Cell. *AIChE Journal*, 50:2320–2324, 2004.

[36] M. Grotsch, R. Hanke-Rauschenbach, and M. Mangold. Bifurcation Analysis of a Two-Phase PEMFC Model. *Journal of Fuel Cell Science and Technology*, 5:1–9, 2008.

[37] A. Katsaounis, S. P. Balomenou, D. Tsiplakides, M. Tsampas, and C. G. Vayenas. The Role of Potential-Dependent Electrolyte Resistance in the Performance, Steady-State Multiplicities and oscillations of PEM fuel cells: Experimental Investigation and Macroscopic Modelling. *Electrochimica Acta*, 50:5132–5143, 2005.

[38] J. H. Wee. Applications of Proton Exchange Membrane Fuel Cell Systems. *Renewable & Sustainable Energy Reviews*, 11:1720–1738, 2007.

[39] P. Fisher, J. Jostins, S. Hilmansen, and K. Kendall. Electronic Integration of Fuel Cell and Battery System in Novel Hybrid Vehicle. *Journal Of Power Sources*, 220:114–121, 2012.

[40] J. Zhang, Z. Xie, J. Zhang, Y. Tang, C. Song, T. Navessin, Z. Shi, D. Song, H. Wang, D. P. Wilkinson, Z. S. Liu, and S. Holdcroft. High Temperature PEM Fuel Cells. *Journal Of Power Sources*, 160:872–891, 2006.

[41] M. Yano, A. Tomita, M. Sano, and T. Hibino. Recent Advances in Single-Chamber Solid Oxide Fuel Cells: A Review. *Solid State Ionics*, 177:3351–3359, 2007.

[42] I. D. Kellogg, U. O. Koylu, V. Petrovsky, and F. Dogan. Effectiveness of Anode in a Solid Oxide Fuel Cell with Hydrogen/Oxygen Mixed Gases. *International Journal of Hydrogen Energy*, 34:5138–5143, 2009.

[43] D. Waldbillig, A. Wood, and D. Ivey. Thermal Analysis of the Cyclic Reduction and Oxidation Behaviour of SOFC Anodes. *Solid State Ionics*, 176:847–859, 2005.

[44] J. E. Hustad and O. K. Sonju. Experimental Studies of Lower Flammability Limits of Gases and Mixtures of Gases at Elevated Temperatures. *Combustion and Flame*, 71:283–294, 1988.

[45] E. Choban, L. J. Markoski, A. Wieckowski, and P. J. A. Kenis. Microfluidic Fuel Cell Based on Laminar Flow. *Journal of Power Sources*, 128:54–60, 2004.

[46] J. D. Sands. Mathematical Modeling of Laminar Flow-based Microfluidic Fuel Cells. Master's thesis, University of Birmingham, 2010.

[47] E. Kjeang, N. Djilali, and D. Sinton. Microfluidic Fuel Cells: A Review. *Journal of Power Sources*, 186:353–369, 2009.

[48] S. C. Singhal. Advances in Solid Oxide Fuel Cell Technology. *Solid State Ionics*, 135:305–313, 2000.

[49] BP Statistical Review of World Energy 2014. Technical report, 2014.

[50] S. Bebelis, A. Zeritis, C. Tiropani, and S. G. Neophytides. Intrinsic Kinetics of the Internal Steam Reforming of CH4 over a Ni-YSZ-Cermet Catalyst-Electrode. *Industrial & Engineering Chemistry Research*, 39:4920–4927, 2000.

[51] T. X. Ho, P. Kosinski, A. C. Hoffman, and A. Vik. Numerical Analysis of a Planar Anode-Supported SOFC with Composite Electrodes. *International Journal of Hydrogen Energy*, 34:3488–3499, 2009.

[52] H. Yakabe, M. Hishinuma, M. Uratani, Y. Matsuzaki, and I. Yasuda. Evaluation and Modeling of Performance of Anode-Supported Solid Oxide Fuel Cell. *Journal of Power Sources*, 86:423–431, 2000.

[53] J. Park, P. Li, and J. Bae. Analysis of Chemical, Electrochemical Reactions and Thermofluid Flow in Methane-Feed Internal Reforming SOFCs: Part I - Modeling and Effect of Gas Concentrations. *International Journal of Hydrogen Energy*, 37:8512–8531, 2012.

[54] E. S. Hecht, G. K. Gupta, H. Zhu, A. M. Dean, R. J. Kee, L. Maier, and O. Deutschmann. Methane Reforming Kinetics Within a Ni-YSZ SOFC Anode Support. *Applied Catalysis A: General*, 295:40–51, 2005.

[55] A. A. Kulikovsky. Temperature and Current Distribution Along the Air Channel in Planar SOFC Stack: Model and Asymptotic Solution. *Journal of Fuel Cell Science and Technology*, 7:1–6, 2010.

[56] Y. Du and N. M. Sammes. Fabrication and Properties of Anode-Supported Tubular Solid Oxide Fuel Cells. *Journal of Power Sources*, 136:66–71, 2004.

[57] D. H. Jeon. A Comprehensive CFD Model of Anode-Supported Solid Oxide Fuel Cells. *Electrochimica Acta*, 54:2727–2736, 2009.

[58] M. F. Serincan, U. Pasaogullari, and N. M. Sammes. Thermal Stresses in an Operating Micro-Tubular Solid Oxide Fuel Cell. *Journal Of Power Sources*, 195:4905–4914, 2010.

[59] K. Yashiro, N. Yamada, T. Kawada, J. O. Hong, A. Kaimai, Y. Nigara, and J. Mizusaki. Demonstration and Stack Concept of Quick Startup/Shutdown SOFC (qSOFC). *Electrochemistry*, 70:958–960, 2002.

[60] P. Sarkar, L. Yamarte, H. Rho, and L. Johanson. Anode-Supported Tubular Micro-Solid Oxide Fuel Cell. *International Journal of Applied Ceramic Technology*, 4:103–108, 2007.

[61] S. B. Beale, Y. Lin, S. V. Zhubrin, and W. Dong. Computer Methods for Performance Prediction in Fuel Cells. *Journal of Power Sources*, 118:79–85, 2003.

[62] M. Poppinger and H. Landes. Aspects of the Internal Reforming of Methane in Solid Oxide Fuel Cells. *Ionics*, 7:7–15, 2001.

[63] P. Iora, P. Aguiar, C. S. Adjiman, and N.P. Brandon. Comparison of Two IT DIR-SOFC models: Impact of Variable Thermodynamic, Physical, and Flow Properties. Steady-State and Dynamic Analysis. *Chemical Engineering Science*, 60:2963–2975, 2005.

[64] E. Achenbach and E. Riensche. Methane/Steam Reforming Kinetics for Solid Oxide Fuel Cells. *Journal of Power Sources*, 52:283–288, 1994.

[65] S. Srinivasan. *Fuel Cells: From Fundamentals to Applications*. Springer, USA, 2006.

[66] M. Bavarian, M. Soroush, I. G. Kevrekidis, and J. B. Benziger. Mathematical Modeling, Steady-State and Dynamic Behavior, and Control of Fuel Cells: A Review. *Industrial & Engineering Chemistry Research*, 49:7922–7950, 2010.

[67] W. Wolf, M. Liibke, M. T. M. Koper, K. Krischer, M. Eiswirth, and G. Ertl. Experimental and Theoretical Description of Potentiostatic Current Oscillations During H2 Oxidation. *Journal of Electroanalytical Chemistry*, 399:185–196, 1995.

[68] T. J. Huang, M. C. Huang, W. J. Chen, and C. L. Chou. Oscillation of Electrical Current During Direct Methane Oxidation over Ni-Added LSCF-GDC Anode of Solid Oxide Fuel Cells. *Chemical Engineering Journal*, 153:164–169, 2009.

[69] M. Mangold, M. Krasnyk, and K. Sundmacher. Theoretical Investigation of Steady State Multiplicities in Solid Oxide Fuel Cells. *Journal of Applied Electrochemistry*, 36:265–275, 2005.

[70] K. Murakami, T. Matsui, R. Kikuchi, H. Muroyama, and K. Eguchi. Activation of LSM Electrode Related to the Potential Oscillation under Cathodic Polarization. *Journal of The Electrochemical Society*, 157:B880–B884, 2010.

[71] T. Yoshizumi, S. Taniguchi, Y. Shiratori, and K. Sasaki. Sulfur Poisoning of SOFCs: Voltage Oscillation and Ni Oxidation. *Journal of the Electrochemical Society*, 159:F693–F701, 2012.

[72] J. H. Merkin, D. J. Needham, and S. K. Scott. On the Creation, Growth and Extinction of Oscillatory Solutions for a Simple Pooled Chemical Reaction Scheme. *SIAM Journal on Applied Mathematics*, 47:1040–1060, 1987.

[73] J. H. Merkin, D. J. Needham, and S. K. Scott. Oscillatory Chemical Reactions in Closed Vessels. *Proceedings of the Royal Society A*, 406:299–323, 1986.

[74] S. K. Scott. *Chemical Chaos*. Clarendon Press, Oxford, 1991.

[75] J. L. Hudson and T. T. Tsotsis. Review Article Reaction Number Dynamics: A Review. *Chemical Emginrering Science*, 49:1493–1572, 1994.

[76] W. Wolf, M. Liibke, and M. Eiswirth. Modelling Oscillations in Galvanostatic. *Journal of Electroanalytical Chemistry*, 385:85–93, 1995.

[77] J. Wojtowicz and B. E. Conway. Oscillatory Kinetics in Fuel Oxidations. *J. Int. Etude Piles Combust.*, 3:171–178, 1969.

[78] N. Fetner and J. L. Hudson. Oscillations During the Electrocatalytic Reduction of Hydrogen Peroxide on a Platinum Electrode. *J. Phys. Chem.*, 94:6506–6512, 1990.

[79] M. R. F. Hurtado, P. T. A Sumodjo, and A. V. Bendetti. Electrochemical Studies with Copper-Based Alloys. Open Circuit Potential Oscillations in Alkaline Media. *J. Electrochem. Soc.*, 140:1567–1582, 1993.

[80] B. E. Conway and D. M. Novak. Oscillatory Kinetics in the Electrochemical Oxidation of Hydrogen in an Almost Anhydrous Solvent. *J. Phys. Chem.*, 81:1459–1464, 1977.

[81] H. Tributsch. Sustained Oscillations During Catalytic Reduction of Hydrogen Peroxide on Copper-Iron-Sulfide Electrodes I. *Ber. Bunsenges Phys. Chem.*, 79:570–580, 1975.

[82] H. Tributsch. Sustained Oscillations During Catalytic Reduction of Hydrogen Peroxide on Copper-Iron-Sulfider Electrodes II. *Ber. Bunsenges Phys. Chem*, 79:580–591, 1975.

[83] H. Tributsch and J. C. Bennet. Hydrogen Peroxide Induced Periodical Catalysis on Copper-Containing Sulfides. *Ber. Bunsenges Phys. Chem.*, 80:321–330, 1976.

[84] A. Katsaounis, M. Tsampas, S. Balomenou, D. Tsiplakides, and C. Vayenas. Potential-Dependent Electrolyte Resistance and Steady-State Multiplicities of PEM Fuel Cells. *Solid State Ionics*, 177:2397–2401, 2006.

[85] A. Mota, P. P. Lopes, E. A. Ticianelli, E. R. Gonzalez, and H. Varela. Complex

Oscillatory Response of a PEM Fuel Cell Fed with H_2/CO and Oxygen. *Journal of The Electrochemical Society*, 157:B1301–B1304, 2010.

[86] J. Zhang and R. Datta. Sustained Potential Oscillations in Proton Exchange Membrane Fuel Cells with PtRu as Anode Catalyst. *Journal of The Electrochemical Society*, 149:A1423–A1431, 2002.

[87] J. Zhang, J. D. Fehribach, and R. Datta. Mechanistic and Bifurcation Analysis of Anode Potential Oscillations in PEMFCs with CO in Anode Feed. *Journal of The Electrochemical Society*, 151:A689–A697, 2004.

[88] H. Lu, L. Rihko-Struckmann, R.chard Hanke-Rauschenbach, and K. Sundmacher. Dynamic Behavior of a PEM Fuel Cell During Electrochemical CO Oxidation on a PtRu Anode. *Topics in Catalysis*, 51:89–97, 2008.

[89] H. Lu, L. Rihko-Struckmann, and K. Sundmacher. Spontaneous Oscillations of Cell Voltage, Power Density, and Anode exit CO Concentration in a PEM Fuel Cell. *Physical Chemistry Chemical Physics : PCCP*, 13:18179–18185, 2011.

[90] T. Kadyk, S. Kirsch, R. Hanke-Rauschenbach, and K. Sundmacher. Autonomous Potential Oscillations at the Pt Anode of a Polymer Electrolyte Membrane Fuel Cell Under CO Poisoning. *Electrochimica Acta*, 56:10593–10602, 2011.

[91] J. R. Atkins, S. C. Savett, and S. E. Creager. Large-Scale Current Fluctuations in PEM Fuel Cells Operating With Reduced Feed Stream Humidification. *Journal of Power Sources*, 128:201–207, 2004.

[92] J. Benziger, E. Chia, J. F. Moxley, and I. G. Kevrekidis. The Dynamic Response of PEM Fuel Cells to Changes in Load. *Chemical Engineering Science*, 60:1743–1759, 2005.

[93] O. A. Marina, L. R. Pederson, C. A. Coyle, E. C. Thomsen, and D. J. Edwards. Polarization-Induced Interfacial Reactions Between Nickel and Selenium in Ni/Zirconia SOFC Anodes and Comparison with Sulfur Poisoning. *Journal of The Electrochemical Society*, 158:B36–B43, 2011.

[94] N. Akhtar, S. P. Decent, D. Loghin, and K. Kendall. Mixed-Reactant, Micro-Tubular Solid Oxide Fuel Cells: An Experimental Study. *Journal of Power Sources*, 193:39–48, 2009.

[95] M. Mangold, M. Krasnyk, and K. Sundmacher. Nonlinear Analysis of Current Instabilities in High Temperature Fuel Cells. *Chemical Engineering Science*, 59:4869–4877, 2004.

[96] Z. Wang, Z. Lü, B. Wei, K. Chen, X. Huang, W. Pan, and W. Su. Redox of Ni/YSZ Anodes and Oscillatory Behavior in Single-Chamber SOFC Under Methane Oxidation Conditions. *Electrochimica Acta*, 56:6688–6695, 2011.

[97] X. L. Zhang, D. M. P. Mingos, and D. O. Hayward. Rate Oscillations During Partial Oxidation of Methane over Chromel-Alumel Thermocouples. *Catalysis Letters*, 72:147–152, 2001.

[98] X. L. Zhang, D. O. Hayward, and D. M. P. Mingos. Oscillatory Behavior During the Partial Oxidation of Methane over Nickel Foils. *Catalysis Letters*, 83:149–155, 2002.

[99] X. L. Zhang, D. O. Hayward, and D. M. P. Mingos. Further Studies on Oscillations over Nickel Wires During the Partial Oxidation of Methane. *Catalysis Letters*, 86:235–243, 2003.

[100] T. Matsui, R. Kishida, J. Y. Kim, H. Muroyama, and K. Eguchi. Performance Deteri-

oration of Ni-YSZ Anode Induced by Electrochemically Generated Steam in Solid Oxide Fuel Cells. *Journal of The Electrochemical Society*, 157:B776–B781, 2010.

[101] J. Yuan and B. Sundén. Analysis of Intermediate Temperature Solid Oxide Fuel Cell Transport Processes and Performance. *Transactions of the ASME*, 127:1380–1390, 2005.

[102] W. Dai, H. Wang, X. Yuan, J.J. Martin, D. Yang, J. Qiao, and J. Ma. A Review on Water Balance in the Membrane Electrode Assembly of Proton Exchange Membrane Fuel Cells. *International Journal of Hydrogen Energy*, 34:9461–9478, 2009.

[103] W. Lehnert, J. Meusinger, and F. Thom. Modelling of Gas Transport Phenomena in SOFC Anodes. *Journal of Power Sources*, 87:57–63, 2000.

[104] K. Sato, Y. Ohmine, K. Ogasa, and S. Tsuji. Solid-Solutioning Effect of the Ni-Based Cermet on the Electrochemical Oxidation of Methane. In Singhal, SC and Dokiya, M, editor, *Solid Oxide Fuel Cells VIII (SOFC VIII)*, number 7 in Electrochemical Society Series, pages 695–703, 2003.

[105] J. M. Klein, Y. Bultel, S. Georges, and M. Pons. Modeling of a SOFC Fuelled by Methane: From Direct Internal Reforming to Gradual Internal Reforming. *Chemical Engineering Science*, 62:1636–1649, 2007.

[106] P. Gray and S. K. Scott. *Chemical Oscillations and Instabilities: Non-Linear Chemical Kinetics*. International Series of Monographs on Chemistry. Clarendon Press, 1994.

[107] R. J. Cooper, J. Billingham, and A. C. King. Flow and Reaction in Solid Oxide Fuel Cells. *J. Fluid Mech.*, 411:233–262, 2000.

[108] A. C. King, J. Billingham, and R. J. Cooper. Performance Modelling of Solid Oxide Fuel Cells. *Combust. Theory Modelling*, 5:639–667, 2001.

[109] R. B. Bird, W. E. Stewart, and E. N. Lightfoot. *Transport Phenomena (2nd edition)*. John Wiley & Sons Inc., New York, 2002.

[110] J. I. Steinfeld, J. S. Francisco, and W. L. Hase. *Chemical Kinetics and Dynamics (2nd edition)*. Prentice Hall, USA, 1999.

[111] L. Segel and G. H. Handelman. *Mathematics Applied to Continuum Mechanics*. Classics in Applied Mathematics. Society for Industrial and Applied Mathematics, 2007.

[112] H. You, A. Abdula, D. Xinwei, and Z. Yihui. Reactions of Low and Middle Concentration Dry Methane over Ni/YSZ Anode of Solid Oxide Fuel Cell. *Journal of Power Sources*, 165:722–727, 2007.

[113] E. A. Mason and L. Monchick. Transport Properties of Polar-Gas Mixtures. *Journal of Chemical Physics*, 36:2746–2757, 1962.

[114] F. Verhulst. *Nonlinear Differential Equations and Dynamical Systems*. Springer, Berlin - Heidelberg, 1990.

[115] D. W. Jordan and P. Smith. *Nonlinear Ordinary Differential Equations: An Introduction for Scientists and Engineers*. Oxford Applied and Engineering Mathematics. Oxford University Press, 2007.

[116] M. Bavarian and M. Soroush. Steady-State Multiplicity in a Solid Oxide Fuel Cell: Practical Considerations. *Chemical Engineering Science*, 67:2–14, 2012.

[117] G. M. Goldin, H. Zhu, R. J. Kee, D. Bierschenk, and S. A. Barnett. Multidimensional Flow, Thermal, and Chemical Behavior in Solid-Oxide Fuel Cell Button Cells. *Journal of Power Sources*, 187:123–135, 2009.

[118] S. M. Vora B. I. Bhatt. *Stoichiometry (4th edition)*. Tata McGraw-Hill, 2006.

[119] J. Y. Roncin. Intermolecular Potential Parameters of Some Electronic Excited States of Atoms and Molecules. *Chemical Physics Letters*, 3:408–410, 1969.

[120] K. Hou and R. Hughes. The Kinetics of Methane Steam Reforming over a Ni/α-Al_2O Catalyst. *Chemical Engineering Journal*, 82:311–328, 2001.

[121] W. Kong, H. Zhu, Z. Fei, and Z. Lin. A Modified Dusty Gas Model in the Form of a Fick's Model for the Prediction of Multicomponent Mass Transport in a Solid Oxide Fuel Cell Anode. *Journal of Power Sources*, 206:171–178, 2012.

[122] H. Sumi, R. Kishida, J. Y. Kim, H. Muroyama, T. Matsui, and K. Eguchi. Correlation Between Microstructural and Electrochemical Characteristics during Redox Cycles for Ni-YSZ Anode of SOFCs. *Journal of The Electrochemical Society*, 157:B1747–B1752, 2010.

[123] R. E. Sonntag, C. Borgnakke, and G. J. Van Wylen. *Fundamentals of Thermodynamics (5th edition)*. John Wiley & Sons, Inc., USA, 1998.

[124] A. Dhir. *Improved Microtubular Solid Oxide Fuel Cells*. PhD thesis, University of Birmingham, 2008.

Appendix A

Experimental Flow Rates

Time (s)	Composition ($\frac{ml}{min}$) ($CH_4/He/H_2O$)
-600	5/25/0
-1220	5.5/24.5/0
-1860	6/24/0
-2500	6.5/23.5/0
-3120	7/23/0
-3830	7.5/22.5/0
-4480	8/22/0
-5120	8.5/21.5/0
-5750	9/21/0
-6410	9.5/20.5/0
-7040	10/20/0
-7680	10.5/19.5
-8340	11/19/0
-9600	11.5/18.5/0
-10222	12/18/0

Table A.1: Experimental flow rates for microtubular cell at 0.5V.

Time (s)	Composition ($\frac{ml}{min}$) ($CH_4/N_2/H_2O$)
-1200	30/68/2
-3600	28/70/2
-4800	26/72/2
-6000	24/74/2
-7200	22/76/2
-8400	20/78/2
-9600	18/80/2
-10800	16/82/2
-12000	14/84/2
-13200	12/86/2
-14400	10/88/2
-16000	8/90/2
-17400	6/92/2
-18100	5.5/92.5/2
-18190	5/93/2

Table A.2: Experimental flow rates for tubular cell 1 at 0.8V.

Time (s)	Composition ($\frac{ml}{min}$) ($CH_4/N_2/H_2O$)
-1200	30/68/2
-2400	28/70/2
-3600	26/72/2
-4800	24/74/2
-6000	22/76/2
-7200	20/78/2
-8400	18/80/2
-9600	16/82/2
-10800	14/84/2
-12000	12/86/2
-13200	10/88/2
-14400	8/90/2
-15600	6/92/2
-15875	5.5/92.5/2

Table A.3: Experimental flow rates for tubular cell 1 at 0.7V.

Time (s)	Composition ($\frac{ml}{min}$) ($CH_4/N_2/H_2O$)
-1200	20/78/2
-2400	18/80/2
-3600	16/82/2
-4800	14/84/2
-6000	12/86/2
-7200	10/88/2
-8400	8/90/2
-10600	6/92/2
-11800	6.5/92/2
-14200	7/91.5/2
-16800	6/92.5/2
-19400	6/93/2
-21800	6/93.5/2
-23200	6/94/2
-25600	6/94.5/2
-28000	6/95/2
-30400	6/95.5/2
-32800	6/96/2
-34600	6/96.5/2
-35800	6/97/2
-37000	6/97.5/2
-38200	6/98/2
-39400	6/98.5/2
-40600	6/99/2
-41800	6/99.5/2
-43000	6/100/2
-44200	5.5/100/2
-44330	5/100/2

Table A.4: Experimental flow rates for tubular cell 1 at 0.6V.

Time (s)	Composition ($\frac{ml}{min}$) ($CH_4/N_2/H_2O$)
-1200	3/95/2
-2400	2/96/2
-3600	2/98/2
-4800	1.5/98/2
-6000	1/98/2
-6476	1/100/2

Table A.5: Experimental flow rates for tubular cell 2 at 0.8V.

Time (s)	Composition ($\frac{ml}{min}$) ($CH_4/N_2/H_2O$)
-1200	8/90/2
-2400	7/91/2
-3600	6/92/2
-4800	5/93/2
-6000	4/94/2
-7200	3/95/2
-8800	2.5/95.5/2
-10000	2.5/96/2
-11200	2/96/2
-12400	2/96.5/2
-13600	1.5/96.5/2
-14800	1.5/97.5/2
-16000	1/97.5/2
-17200	1/98.5/2
-18400	1/100/2
-18590	0.5/100/2

Table A.6: Experimental flow rates for tubular cell 2 at 0.7V.

Time (s)	Composition ($\frac{ml}{min}$) ($CH_4/N_2/H_2O$)
-1200	8/90/2
-2400	7/91/2
-3600	6/92/2
-4800	5/93/2
-6000	4/94/2
-7200	3/95/2
-8400	2.5/95.5/2
-10700	2/96/2
-11900	1.5/96.5/2
-13100	1/97/2
-14300	0.5/97.5/2
-15500	0.5/98/2
-16700	0.5/98.5/2
-17900	0.5/99/2
-19100	0.5/99.5/2
-20300	0.5/100/2
-21500	0.4/100/2
-22700	0.3/100/2
-23580	0.2/100/2

Table A.7: Experimental flow rates for tubular cell 2 at 0.6V.

Time (s)	Composition ($\frac{ml}{min}$) ($CH_4/N_2/H_2O$)
-1200	10/88/2
-2400	8/90/2
-3600	6/92/2
-4800	5/93/2
-6000	4/94/2
-7200	3/95/2
-8400	2/96/2
-9600	1.5/96.5/2
-10800	1/97/2
-12000	1/100/2
-12535	0.5/100/2

Table A.8: Experimental flow rates for tubular cell 3 at 0.8V.

Time (s)	Composition ($\frac{ml}{min}$) ($CH_4/N_2/H_2O$)
-1200	10/88/2
-2400	8/90/2
-3600	6/92/2
-4800	5/93/2
-6000	4/94/2
-7200	3/95/2
-9400	2.5/95.5/2
-10600	2/96/2
-11900	1.5/96.5/2
-12659	1/97/2

Table A.9: Experimental flow rates for tubular cell 3 at 0.7V.

Time (s)	Composition ($\frac{ml}{min}$) ($CH_4/N_2/H_2O$)
-1200	12/86/2
-2400	10/88/2
-3600	8/90/2
-4800	6/92/2
-6000	5/93/2
-7200	4/94/2
-8400	3/95/2
-9600	2/96/2
-10800	1/97/2
-10964	0.5/97.5/2

Table A.10: Experimental flow rates for tubular cell 3 at 0.6V.

Appendix B

Diffusion Coefficient GUI

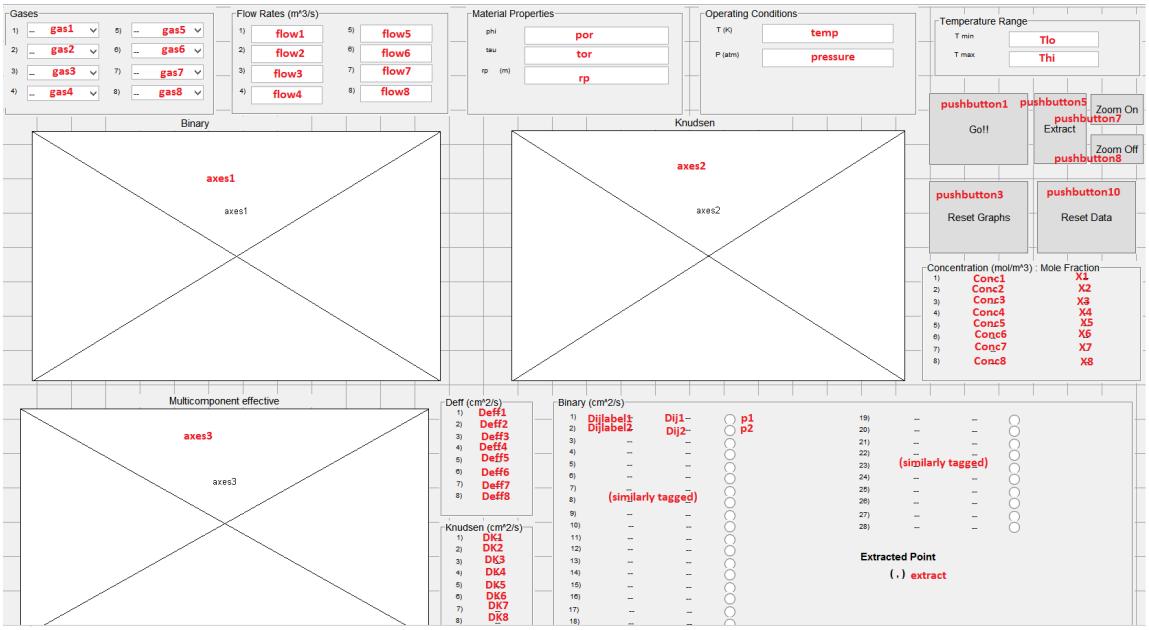

Figure B.1: Matlab GUIDE schematic. Tags for each element are in red.

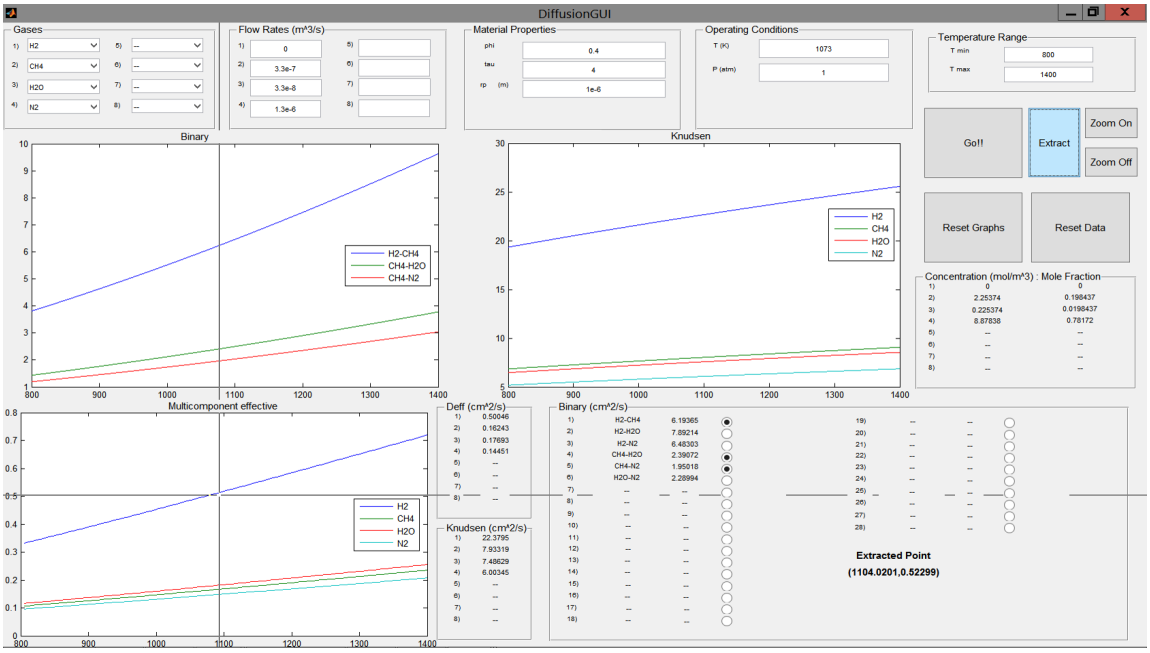

Figure B.2: Graphical user interface for calculating diffusion coefficients.

B.1 Main function file

```
function varargout = DiffusionGUI(varargin)
% Begin initialization code - DO NOT EDIT
gui_Singleton = 0;
gui_State = struct('gui_Name',       mfilename, ...
                   'gui_Singleton',  gui_Singleton, ...
                   'gui_OpeningFcn', @DiffusionGUI_OpeningFcn, ...
                   'gui_OutputFcn',  @DiffusionGUI_OutputFcn, ...
                   'gui_LayoutFcn',  [], ...
                   'gui_Callback',   []);
if nargin && ischar(varargin{1})
   gui_State.gui_Callback = str2func(varargin{1});
end
```

```
if nargout
    [varargout{1:nargout}] = gui_mainfcn(gui_State, varargin{:});
else
    gui_mainfcn(gui_State, varargin{:});
end
% End initialization code - DO NOT EDIT

% --- Executes just before DiffusionGUI is made visible.
function DiffusionGUI_OpeningFcn(hObject, eventdata, handles, varargin)
% Choose default command line output for DiffusionGUI
handles.output = hObject;

% Update handles structure
guidata(hObject, handles);

% --- Outputs from this function are returned to the command line.
function varargout = DiffusionGUI_OutputFcn(hObject, eventdata, handles)
% Get default command line output from handles structure
varargout{1} = handles.output;

% --- Executes when figure1 is resized.
function figure1_ResizeFcn(hObject, eventdata, handles)

% --- Executes on button press in pushbutton1.
function pushbutton1_Callback(hObject, eventdata, handles)
%% Fetch Inputs
% Gases.
Gasall=get(handles.gas1,'string');
```

```
Gas1ind=get(handles.gas1,'value');
Gas1=Gasall{Gas1ind};

Gas2ind=get(handles.gas2,'value');
Gas2=Gasall{Gas2ind};

Gas3ind=get(handles.gas3,'value');
Gas3=Gasall{Gas3ind};

Gas4ind=get(handles.gas4,'value');
Gas4=Gasall{Gas4ind};

Gas5ind=get(handles.gas5,'value');
Gas5=Gasall{Gas5ind};

Gas6ind=get(handles.gas6,'value');
Gas6=Gasall{Gas6ind};

Gas7ind=get(handles.gas7,'value');
Gas7=Gasall{Gas7ind};

Gas8ind=get(handles.gas8,'value');
Gas8=Gasall{Gas8ind};

% Determine number of gases in mixture.
s1='--';
if isequal(Gas1,s1)
    dim=0;
```

```
end
if isequal(Gas1,s1)==0 && isequal(Gas2,s1)
    dim=1;
end
if isequal(Gas1,s1)==0 && isequal(Gas2,s1)==0 && isequal(Gas3,s1)
    dim=2;
end
if isequal(Gas1,s1)==0 && isequal(Gas2,s1)==0 ...
    && isequal(Gas3,s1)==0 && isequal(Gas4,s1)
    dim=3;
end
if isequal(Gas1,s1)==0 && isequal(Gas2,s1)==0 ...
    && isequal(Gas3,s1)==0 && isequal(Gas4,s1)==0 && isequal(Gas5,s1)
    dim=4;
end
if isequal(Gas1,s1)==0 && isequal(Gas2,s1)==0 ...
    && isequal(Gas3,s1)==0 && isequal(Gas4,s1)==0 && isequal(Gas5,s1)==0 ...
    && isequal(Gas6,s1)
    dim=5;
end
if isequal(Gas1,s1)==0 && isequal(Gas2,s1)==0 ...
    && isequal(Gas3,s1)==0 && isequal(Gas4,s1)==0 && isequal(Gas5,s1)==0 ...
    && isequal(Gas6,s1)==0 && isequal(Gas7,s1)
    dim=6;
end
if isequal(Gas1,s1)==0 && isequal(Gas2,s1)==0 ...
    && isequal(Gas3,s1)==0 && isequal(Gas4,s1)==0 && isequal(Gas5,s1)==0 ...
    && isequal(Gas6,s1)==0 && isequal(Gas7,s1)==0 && isequal(Gas8,s1)
    dim=7;
```

```
end
if isequal(Gas1,s1)==0 && isequal(Gas2,s1)==0 ...
    && isequal(Gas3,s1)==0 && isequal(Gas4,s1)==0 && isequal(Gas5,s1)==0 ...
    && isequal(Gas6,s1)==0 && isequal(Gas7,s1)==0 && isequal(Gas8,s1)==0
    dim=8;
end
% Flowrates.
Q1=str2num(get(handles.flow1,'string'));
Q2=str2num(get(handles.flow2,'string'));
Q3=str2num(get(handles.flow3,'string'));
Q4=str2num(get(handles.flow4,'string'));
Q5=str2num(get(handles.flow5,'string'));
Q6=str2num(get(handles.flow6,'string'));
Q7=str2num(get(handles.flow7,'string'));
Q8=str2num(get(handles.flow8,'string'));
if isempty(Q1)==0
    Qmarker=1;
elseif isempty(Q1)
    Qmarker=0;
end
% Material properties.
phi=str2num(get(handles.por,'string'));
tau=str2num(get(handles.tor,'string'));
rp=str2num(get(handles.rp,'string'));
if isempty(phi)==0 && isempty(tau)==0
    matmarker=1;
elseif isempty(phi) || isempty(tau)
    matmarker=0;
end
```

```
% Operating conditions.
T=str2num(get(handles.temp,'string'));
P=str2num(get(handles.pressure,'string'));
Tmin=str2num(get(handles.Tlo,'string'));
Tmax=str2num(get(handles.Thi,'string'));
if isempty(Tmin)==0 || isempty(Tmax)==0
    Tmarker=1;
elseif isempty(Tmin) || isempty(Tmax)
    Tmarker=0;
end
% Binary diffusion plot requests.
p1=get(handles.p1,'Value');
p2=get(handles.p2,'Value');
p3=get(handles.p3,'Value');
p4=get(handles.p4,'Value');
p5=get(handles.p5,'Value');
p6=get(handles.p6,'Value');
p7=get(handles.p7,'Value');
p8=get(handles.p8,'Value');
p9=get(handles.p9,'Value');
p10=get(handles.p10,'Value');
p11=get(handles.p11,'Value');
p12=get(handles.p12,'Value');
p13=get(handles.p13,'Value');
p14=get(handles.p14,'Value');
p15=get(handles.p15,'Value');
p16=get(handles.p16,'Value');
p17=get(handles.p17,'Value');
p18=get(handles.p18,'Value');
```

```
p19=get(handles.p19,'Value');
p20=get(handles.p20,'Value');
p21=get(handles.p21,'Value');
p22=get(handles.p22,'Value');
p23=get(handles.p23,'Value');
p24=get(handles.p24,'Value');
p25=get(handles.p25,'Value');
p26=get(handles.p26,'Value');
p27=get(handles.p27,'Value');
p28=get(handles.p28,'Value');

%% Call Functions
if dim==1
    % Knudsen.
    DKn1=Knudsen(T,rp,Gas1);
    set(handles.DK1,'string',DKn1);
    if Tmarker==1
        Trange=linspace(Tmin,Tmax,(Tmax-Tmin)*10);
        DKn1R=Knudsen(Trange,rp,Gas1);
        axes(handles.axes2);
        fig1=plot(Trange,DKn1R); hold on
    end

    % Concentration.
    set(handles.X1,'string',1);
    % Pure chemical implies concentration = density.
    C=(P*1.01325e5)/(8.31446*T);
    set(handles.Conc1,'string',C);
```

```
elseif dim==2
    % Knudsen.
    DKn1=Knudsen(T,rp,Gas1);
    DKn2=Knudsen(T,rp,Gas2);
    set(handles.DK1,'string',DKn1);
    set(handles.DK2,'string',DKn2);

    if Tmarker==1
        Trange=linspace(Tmin,Tmax,(Tmax-Tmin)*10);
        DKn1R=Knudsen(Trange,rp,Gas1);
        DKn2R=Knudsen(Trange,rp,Gas2);
        axes(handles.axes2);
        fig1=plot(Trange,DKn1R,Trange,DKn2R); hold on
        legend(Gas1,Gas2,'Location','best')
    end

    % Binary.
    Db1=ChapmanEnskog(T,P,Gas1,Gas2);
    set(handles.Dij1,'string',Db1);
    L_Dij1=horzcat(Gas1,'-',Gas2);
    set(handles.Dijlabel1,'string',L_Dij1);
    if Tmarker==1 && p1==1
        Trange=linspace(Tmin,Tmax,(Tmax-Tmin)*10);
        Db1R=ChapmanEnskog(Trange,P,Gas1,Gas2);
        axes(handles.axes1);
        if isempty(Db1R)==0
            fig2=plot(Trange,Db1R); hold on
            legend(L_Dij1,'Location','best')
        end
```

```
end

% Fuel composition.
if Qmarker==1
    F1=molarflow(Q1,P,T,Gas1);
    F2=molarflow(Q2,P,T,Gas2);
    [X C]=concentration(P,T,F1,F2);
    set(handles.Conc1,'string',C(1));
    set(handles.Conc2,'string',C(2));
    set(handles.X1,'string',X(1));
    set(handles.X2,'string',X(2));
end

% Effective.
if Qmarker==1 && matmarker==1
Deff=effectivediff([Q1 Q2],phi,tau,rp,T,P,Gas1,Gas2);
set(handles.Deff1,'string',Deff(1));
set(handles.Deff2,'string',Deff(2));
if Tmarker==1
    Tloop=Tmin;
    Deff1=[]; Deff2=[]; Tr=[];
    while Tloop<Tmax
        Tloop=Tloop+(Tmax-Tmin)/100;
        Deff=effectivediff([Q1 Q2],phi,tau,rp,Tloop,P,Gas1,Gas2);
        Deff1(end+1)=Deff(1);
        Deff2(end+1)=Deff(2);
        Tr(end+1)=Tloop;
    end
    axes(handles.axes3);
```

```
        fig1=plot(Tr,Deff1,Tr,Deff2); hold on
        legend(Gas1,Gas2,'Location','best')
    end
    end

elseif dim==3
    % Knudsen.
    DKn1=Knudsen(T,rp,Gas1);
    DKn2=Knudsen(T,rp,Gas2);
    DKn3=Knudsen(T,rp,Gas3);
    set(handles.DK1,'string',DKn1);
    set(handles.DK2,'string',DKn2);
    set(handles.DK3,'string',DKn3);

    if Tmarker==1
        Trange=linspace(Tmin,Tmax,(Tmax-Tmin)*10);
        DKn1R=Knudsen(Trange,rp,Gas1);
        DKn2R=Knudsen(Trange,rp,Gas2);
        DKn3R=Knudsen(Trange,rp,Gas3);
        axes(handles.axes2);
        fig1=plot(Trange,DKn1R,Trange,DKn2R,Trange,DKn3R); hold on
        legend(Gas1,Gas2,Gas3,'Location','best')
    end

    % Binary.
    Db1=ChapmanEnskog(T,P,Gas1,Gas2);
    set(handles.Dij1,'string',Db1);
    Db2=ChapmanEnskog(T,P,Gas1,Gas3);
    set(handles.Dij2,'string',Db2);
```

```
Db3=ChapmanEnskog(T,P,Gas2,Gas3);
set(handles.Dij3,'string',Db3);

L_Dij1=horzcat(Gas1,'-',Gas2);
set(handles.Dijlabel1,'string',L_Dij1);
L_Dij2=horzcat(Gas1,'-',Gas3);
set(handles.Dijlabel2,'string',L_Dij2);
L_Dij3=horzcat(Gas2,'-',Gas3);
set(handles.Dijlabel3,'string',L_Dij3);

if Tmarker==1
    Trange=linspace(Tmin,Tmax,(Tmax-Tmin)*10);
    Db1R=ChapmanEnskog(Trange,P,Gas1,Gas2);
    Db2R=ChapmanEnskog(Trange,P,Gas1,Gas3);
    Db3R=ChapmanEnskog(Trange,P,Gas2,Gas3);
    DR=[Db1R; Db2R; Db3R];
    legcell={L_Dij1; L_Dij2; L_Dij3};
    Pairs=[p1 p2 p3];
    I=find(Pairs);
    D2plot=DR(I,:);
    leg2plot=legcell(I);
    axes(handles.axes1);
    if isempty(D2plot)==0
        fig2=plot(Trange,D2plot); hold on
        legend(leg2plot,'Location','best')
    end
end

% Fuel composition.
```

```
if Qmarker==1
    F1=molarflow(Q1,P,T,Gas1);
    F2=molarflow(Q2,P,T,Gas2);
    F3=molarflow(Q3,P,T,Gas3);
    [X C]=concentration(P,T,F1,F2,F3);
    set(handles.Conc1,'string',C(1));
    set(handles.Conc2,'string',C(2));
    set(handles.Conc3,'string',C(3));
    set(handles.X1,'string',X(1));
    set(handles.X2,'string',X(2));
    set(handles.X3,'string',X(3));
end

% Effective.
if Qmarker==1 && matmarker==1
Deff=effectivediff([Q1 Q2 Q3],phi,tau,rp,T,P,Gas1,Gas2,Gas3);
set(handles.Deff1,'string',Deff(1));
set(handles.Deff2,'string',Deff(2));
set(handles.Deff3,'string',Deff(3));
if Tmarker==1
    Tloop=Tmin;
    Deff1=[]; Deff2=[]; Deff3=[]; Tr=[];
    while Tloop<Tmax
        Tloop=Tloop+(Tmax-Tmin)/100;
        Deff=effectivediff([Q1 Q2 Q3],phi,tau,rp,Tloop,P,Gas1,Gas2...
            ,Gas3);
        Deff1(end+1)=Deff(1);
        Deff2(end+1)=Deff(2);
        Deff3(end+1)=Deff(3);
```

```
            Tr(end+1)=Tloop;
        end
        axes(handles.axes3);
        fig1=plot(Tr,Deff1,Tr,Deff2,Tr,Deff3); hold on
        legend(Gas1,Gas2,Gas3,'Location','best')
    end
    end

elseif dim==4
    % Knudsen.
    DKn1=Knudsen(T,rp,Gas1);
    DKn2=Knudsen(T,rp,Gas2);
    DKn3=Knudsen(T,rp,Gas3);
    DKn4=Knudsen(T,rp,Gas4);
    set(handles.DK1,'string',DKn1);
    set(handles.DK2,'string',DKn2);
    set(handles.DK3,'string',DKn3);
    set(handles.DK4,'string',DKn4);

    if Tmarker==1
        Trange=linspace(Tmin,Tmax,(Tmax-Tmin)*10);
        DKn1R=Knudsen(Trange,rp,Gas1);
        DKn2R=Knudsen(Trange,rp,Gas2);
        DKn3R=Knudsen(Trange,rp,Gas3);
        DKn4R=Knudsen(Trange,rp,Gas4);
        axes(handles.axes2);
        fig1=plot(Trange,DKn1R,Trange,DKn2R,Trange,DKn3R,Trange,DKn4R); hold on
        legend(Gas1,Gas2,Gas3,Gas4,'Location','best')
    end
```

```
% Binary.
Db1=ChapmanEnskog(T,P,Gas1,Gas2);
set(handles.Dij1,'string',Db1);
Db2=ChapmanEnskog(T,P,Gas1,Gas3);
set(handles.Dij2,'string',Db2);
Db3=ChapmanEnskog(T,P,Gas1,Gas4);
set(handles.Dij3,'string',Db3);
Db4=ChapmanEnskog(T,P,Gas2,Gas3);
set(handles.Dij4,'string',Db4);
Db5=ChapmanEnskog(T,P,Gas2,Gas4);
set(handles.Dij5,'string',Db5);
Db6=ChapmanEnskog(T,P,Gas3,Gas4);
set(handles.Dij6,'string',Db6);

L_Dij1=horzcat(Gas1,'-',Gas2);
set(handles.Dijlabel1,'string',L_Dij1);
L_Dij2=horzcat(Gas1,'-',Gas3);
set(handles.Dijlabel2,'string',L_Dij2);
L_Dij3=horzcat(Gas1,'-',Gas4);
set(handles.Dijlabel3,'string',L_Dij3);
L_Dij4=horzcat(Gas2,'-',Gas3);
set(handles.Dijlabel4,'string',L_Dij4);
L_Dij5=horzcat(Gas2,'-',Gas4);
set(handles.Dijlabel5,'string',L_Dij5);
L_Dij6=horzcat(Gas3,'-',Gas4);
set(handles.Dijlabel6,'string',L_Dij6);

if Tmarker==1
```

```
    Trange=linspace(Tmin,Tmax,(Tmax-Tmin)*10);
    Db1R=ChapmanEnskog(Trange,P,Gas1,Gas2);
    Db2R=ChapmanEnskog(Trange,P,Gas1,Gas3);
    Db3R=ChapmanEnskog(Trange,P,Gas1,Gas4);
    Db4R=ChapmanEnskog(Trange,P,Gas2,Gas3);
    Db5R=ChapmanEnskog(Trange,P,Gas2,Gas4);
    Db6R=ChapmanEnskog(Trange,P,Gas3,Gas4);
    DR=[Db1R; Db2R; Db3R; Db4R; Db5R; Db6R];
    legcell={L_Dij1; L_Dij2; L_Dij3; L_Dij4; L_Dij5; L_Dij6};
    Pairs=[p1 p2 p3 p4 p5 p6];
    I=find(Pairs);
    D2plot=DR(I,:);
    leg2plot=legcell(I);
    axes(handles.axes1);
    if isempty(D2plot)==0
        fig2=plot(Trange,D2plot); hold on
        legend(leg2plot,'Location','best')
    end
end

% Fuel composition.
if Qmarker==1
    F1=molarflow(Q1,P,T,Gas1);
    F2=molarflow(Q2,P,T,Gas2);
    F3=molarflow(Q3,P,T,Gas3);
    F4=molarflow(Q4,P,T,Gas4);
    [X C]=concentration(P,T,F1,F2,F3,F4);
    set(handles.Conc1,'string',C(1));
    set(handles.Conc2,'string',C(2));
```

```
    set(handles.Conc3,'string',C(3));
    set(handles.Conc4,'string',C(4));
    set(handles.X1,'string',X(1));
    set(handles.X2,'string',X(2));
    set(handles.X3,'string',X(3));
    set(handles.X4,'string',X(4));
end

% Effective.
if Qmarker==1 && matmarker==1
Deff=effectivediff([Q1 Q2 Q3 Q4],phi,tau,rp,T,P,Gas1,Gas2,Gas3,Gas4);
set(handles.Deff1,'string',Deff(1));
set(handles.Deff2,'string',Deff(2));
set(handles.Deff3,'string',Deff(3));
set(handles.Deff4,'string',Deff(4));
if Tmarker==1
    Tloop=Tmin;
    Deff1=[]; Deff2=[]; Deff3=[]; Deff4=[]; Tr=[];
    while Tloop<Tmax
        Tloop=Tloop+(Tmax-Tmin)/100;
        Deff=effectivediff([Q1 Q2 Q3 Q4],phi,tau,rp,Tloop,P,Gas1,...
            Gas2,Gas3,Gas4);
        Deff1(end+1)=Deff(1);
        Deff2(end+1)=Deff(2);
        Deff3(end+1)=Deff(3);
        Deff4(end+1)=Deff(4);
        Tr(end+1)=Tloop;
    end
    axes(handles.axes3);
```

```
        fig1=plot(Tr,Deff1,Tr,Deff2,Tr,Deff3,Tr,Deff4); hold on
        legend(Gas1,Gas2,Gas3,Gas4,'Location','best')
    end
    end

elseif dim==5
    % Knudsen.
    DKn1=Knudsen(T,rp,Gas1);
    DKn2=Knudsen(T,rp,Gas2);
    DKn3=Knudsen(T,rp,Gas3);
    DKn4=Knudsen(T,rp,Gas4);
    DKn5=Knudsen(T,rp,Gas5);
    set(handles.DK1,'string',DKn1);
    set(handles.DK2,'string',DKn2);
    set(handles.DK3,'string',DKn3);
    set(handles.DK4,'string',DKn4);
    set(handles.DK5,'string',DKn5);

    if Tmarker==1
        Trange=linspace(Tmin,Tmax,(Tmax-Tmin)*10);
        DKn1R=Knudsen(Trange,rp,Gas1);
        DKn2R=Knudsen(Trange,rp,Gas2);
        DKn3R=Knudsen(Trange,rp,Gas3);
        DKn4R=Knudsen(Trange,rp,Gas4);
        DKn5R=Knudsen(Trange,rp,Gas5);
        axes(handles.axes2);
        fig1=plot(Trange,DKn1R,Trange,DKn2R,Trange,DKn3R,Trange,DKn4R,...
            Trange,DKn5R); hold on
        legend(Gas1,Gas2,Gas3,Gas4,Gas5,'Location','best')
```

```
end

% Binary.
Db1=ChapmanEnskog(T,P,Gas1,Gas2);
set(handles.Dij1,'string',Db1);
Db2=ChapmanEnskog(T,P,Gas1,Gas3);
set(handles.Dij2,'string',Db2);
Db3=ChapmanEnskog(T,P,Gas1,Gas4);
set(handles.Dij3,'string',Db3);
Db4=ChapmanEnskog(T,P,Gas1,Gas5);
set(handles.Dij4,'string',Db4);
Db5=ChapmanEnskog(T,P,Gas2,Gas3);
set(handles.Dij5,'string',Db5);
Db6=ChapmanEnskog(T,P,Gas2,Gas4);
set(handles.Dij6,'string',Db6);
Db7=ChapmanEnskog(T,P,Gas2,Gas5);
set(handles.Dij7,'string',Db7);
Db8=ChapmanEnskog(T,P,Gas3,Gas4);
set(handles.Dij8,'string',Db8);
Db9=ChapmanEnskog(T,P,Gas3,Gas5);
set(handles.Dij9,'string',Db9);
Db10=ChapmanEnskog(T,P,Gas4,Gas5);
set(handles.Dij10,'string',Db10);

L_Dij1=horzcat(Gas1,'-',Gas2);
set(handles.Dijlabel1,'string',L_Dij1);
L_Dij2=horzcat(Gas1,'-',Gas3);
set(handles.Dijlabel2,'string',L_Dij2);
L_Dij3=horzcat(Gas1,'-',Gas4);
```

```
set(handles.Dijlabel3,'string',L_Dij3);
L_Dij4=horzcat(Gas1,'-',Gas5);
set(handles.Dijlabel4,'string',L_Dij4);
L_Dij5=horzcat(Gas2,'-',Gas3);
set(handles.Dijlabel5,'string',L_Dij5);
L_Dij6=horzcat(Gas2,'-',Gas4);
set(handles.Dijlabel6,'string',L_Dij6);
L_Dij7=horzcat(Gas2,'-',Gas5);
set(handles.Dijlabel7,'string',L_Dij7);
L_Dij8=horzcat(Gas3,'-',Gas4);
set(handles.Dijlabel8,'string',L_Dij8);
L_Dij9=horzcat(Gas3,'-',Gas5);
set(handles.Dijlabel9,'string',L_Dij9);
L_Dij10=horzcat(Gas4,'-',Gas5);
set(handles.Dijlabel10,'string',L_Dij10);

if Tmarker==1
    Trange=linspace(Tmin,Tmax,(Tmax-Tmin)*10);
    Db1R=ChapmanEnskog(Trange,P,Gas1,Gas2);
    Db2R=ChapmanEnskog(Trange,P,Gas1,Gas3);
    Db3R=ChapmanEnskog(Trange,P,Gas1,Gas4);
    Db4R=ChapmanEnskog(Trange,P,Gas1,Gas5);
    Db5R=ChapmanEnskog(Trange,P,Gas2,Gas3);
    Db6R=ChapmanEnskog(Trange,P,Gas2,Gas4);
    Db7R=ChapmanEnskog(Trange,P,Gas2,Gas5);
    Db8R=ChapmanEnskog(Trange,P,Gas3,Gas4);
    Db9R=ChapmanEnskog(Trange,P,Gas3,Gas5);
    Db10R=ChapmanEnskog(Trange,P,Gas4,Gas5);
    DR=[Db1R; Db2R; Db3R; Db4R; Db5R; Db6R; Db7R; Db8R;...
```

```
        Db9R; Db10R];
    legcell={L_Dij1; L_Dij2; L_Dij3; L_Dij4; L_Dij5; L_Dij6;...
        L_Dij7; L_Dij8; L_Dij9; L_Dij10};
    Pairs=[p1 p2 p3 p4 p5 p6 p7 p8 p9 p10];
    I=find(Pairs);
    D2plot=DR(I,:);
    leg2plot=legcell(I);
    axes(handles.axes1);
    if isempty(D2plot)==0
        fig2=plot(Trange,D2plot); hold on
        legend(leg2plot,'Location','best')
    end
end

% Fuel composition.
if Qmarker==1
    F1=molarflow(Q1,P,T,Gas1);
    F2=molarflow(Q2,P,T,Gas2);
    F3=molarflow(Q3,P,T,Gas3);
    F4=molarflow(Q4,P,T,Gas4);
    F5=molarflow(Q4,P,T,Gas5);
    [X C]=concentration(P,T,F1,F2,F3,F4,F5);
    set(handles.Conc1,'string',C(1));
    set(handles.Conc2,'string',C(2));
    set(handles.Conc3,'string',C(3));
    set(handles.Conc4,'string',C(4));
    set(handles.Conc5,'string',C(5));
    set(handles.X1,'string',X(1));
    set(handles.X2,'string',X(2));
```

```
    set(handles.X3,'string',X(3));
    set(handles.X4,'string',X(4));
    set(handles.X5,'string',X(5));
end

% Effective.
if Qmarker==1 && matmarker==1
Deff=effectivediff([Q1 Q2 Q3 Q4 Q5],phi,tau,rp,T,P,Gas1,Gas2,Gas3,...
    Gas4,Gas5);
set(handles.Deff1,'string',Deff(1));
set(handles.Deff2,'string',Deff(2));
set(handles.Deff3,'string',Deff(3));
set(handles.Deff4,'string',Deff(4));
set(handles.Deff5,'string',Deff(5));
if Tmarker==1
    Tloop=Tmin;
    Deff1=[]; Deff2=[]; Deff3=[]; Deff4=[]; Deff5=[]; Tr=[];
    while Tloop<Tmax
        Tloop=Tloop+(Tmax-Tmin)/100;
        Deff=effectivediff([Q1 Q2 Q3 Q4 Q5],phi,tau,rp,Tloop,P,Gas1,...
            Gas2,Gas3,Gas4,Gas5);
        Deff1(end+1)=Deff(1);
        Deff2(end+1)=Deff(2);
        Deff3(end+1)=Deff(3);
        Deff4(end+1)=Deff(4);
        Deff5(end+1)=Deff(5);
        Tr(end+1)=Tloop;
    end
    axes(handles.axes3);
```

```
        fig1=plot(Tr,Deff1,Tr,Deff2,Tr,Deff3,Tr,Deff4,Tr,Deff5); hold on
        legend(Gas1,Gas2,Gas3,Gas4,Gas5,'Location','best')
    end
    end

elseif dim==6
    % Knudsen.
    DKn1=Knudsen(T,rp,Gas1);
    DKn2=Knudsen(T,rp,Gas2);
    DKn3=Knudsen(T,rp,Gas3);
    DKn4=Knudsen(T,rp,Gas4);
    DKn5=Knudsen(T,rp,Gas5);
    DKn6=Knudsen(T,rp,Gas6);
    set(handles.DK1,'string',DKn1);
    set(handles.DK2,'string',DKn2);
    set(handles.DK3,'string',DKn3);
    set(handles.DK4,'string',DKn4);
    set(handles.DK5,'string',DKn5);
    set(handles.DK6,'string',DKn6);

    if Tmarker==1
        Trange=linspace(Tmin,Tmax,(Tmax-Tmin)*10);
        DKn1R=Knudsen(Trange,rp,Gas1);
        DKn2R=Knudsen(Trange,rp,Gas2);
        DKn3R=Knudsen(Trange,rp,Gas3);
        DKn4R=Knudsen(Trange,rp,Gas4);
        DKn5R=Knudsen(Trange,rp,Gas5);
        DKn6R=Knudsen(Trange,rp,Gas6);
        axes(handles.axes2);
```

```
    fig1=plot(Trange,DKn1R,Trange,DKn2R,Trange,DKn3R,Trange,DKn4R,...
        Trange,DKn5R,Trange,DKn6R); hold on
    legend(Gas1,Gas2,Gas3,Gas4,Gas5,Gas6,'Location','best')
end

% Binary.
Db1=ChapmanEnskog(T,P,Gas1,Gas2);
set(handles.Dij1,'string',Db1);
Db2=ChapmanEnskog(T,P,Gas1,Gas3);
set(handles.Dij2,'string',Db2);
Db3=ChapmanEnskog(T,P,Gas1,Gas4);
set(handles.Dij3,'string',Db3);
Db4=ChapmanEnskog(T,P,Gas1,Gas5);
set(handles.Dij4,'string',Db4);
Db5=ChapmanEnskog(T,P,Gas1,Gas6);
set(handles.Dij5,'string',Db5);
Db6=ChapmanEnskog(T,P,Gas2,Gas3);
set(handles.Dij6,'string',Db6);
Db7=ChapmanEnskog(T,P,Gas2,Gas4);
set(handles.Dij7,'string',Db7);
Db8=ChapmanEnskog(T,P,Gas2,Gas5);
set(handles.Dij8,'string',Db8);
Db9=ChapmanEnskog(T,P,Gas2,Gas6);
set(handles.Dij9,'string',Db9);
Db10=ChapmanEnskog(T,P,Gas3,Gas4);
set(handles.Dij10,'string',Db10);
Db11=ChapmanEnskog(T,P,Gas3,Gas5);
set(handles.Dij11,'string',Db11);
Db12=ChapmanEnskog(T,P,Gas3,Gas6);
```

```
set(handles.Dij12,'string',Db12);
Db13=ChapmanEnskog(T,P,Gas4,Gas5);
set(handles.Dij13,'string',Db13);
Db14=ChapmanEnskog(T,P,Gas4,Gas6);
set(handles.Dij14,'string',Db14);
Db15=ChapmanEnskog(T,P,Gas5,Gas6);
set(handles.Dij15,'string',Db15);

L_Dij1=horzcat(Gas1,'-',Gas2);
set(handles.Dijlabel1,'string',L_Dij1);
L_Dij2=horzcat(Gas1,'-',Gas3);
set(handles.Dijlabel2,'string',L_Dij2);
L_Dij3=horzcat(Gas1,'-',Gas4);
set(handles.Dijlabel3,'string',L_Dij3);
L_Dij4=horzcat(Gas1,'-',Gas5);
set(handles.Dijlabel4,'string',L_Dij4);
L_Dij5=horzcat(Gas1,'-',Gas6);
set(handles.Dijlabel5,'string',L_Dij5);
L_Dij6=horzcat(Gas2,'-',Gas3);
set(handles.Dijlabel6,'string',L_Dij6);
L_Dij7=horzcat(Gas2,'-',Gas4);
set(handles.Dijlabel7,'string',L_Dij7);
L_Dij8=horzcat(Gas2,'-',Gas5);
set(handles.Dijlabel8,'string',L_Dij8);
L_Dij9=horzcat(Gas2,'-',Gas6);
set(handles.Dijlabel9,'string',L_Dij9);
L_Dij10=horzcat(Gas3,'-',Gas4);
set(handles.Dijlabel10,'string',L_Dij10);
L_Dij11=horzcat(Gas3,'-',Gas5);
```

```
set(handles.Dijlabel11,'string',L_Dij11);
L_Dij12=horzcat(Gas3,'-',Gas6);
set(handles.Dijlabel12,'string',L_Dij12);
L_Dij13=horzcat(Gas4,'-',Gas5);
set(handles.Dijlabel13,'string',L_Dij13);
L_Dij14=horzcat(Gas4,'-',Gas6);
set(handles.Dijlabel14,'string',L_Dij14);
L_Dij15=horzcat(Gas5,'-',Gas6);
set(handles.Dijlabel15,'string',L_Dij15);

if Tmarker==1
    Trange=linspace(Tmin,Tmax,(Tmax-Tmin)*10);
    Db1R=ChapmanEnskog(Trange,P,Gas1,Gas2);
    Db2R=ChapmanEnskog(Trange,P,Gas1,Gas3);
    Db3R=ChapmanEnskog(Trange,P,Gas1,Gas4);
    Db4R=ChapmanEnskog(Trange,P,Gas1,Gas5);
    Db5R=ChapmanEnskog(Trange,P,Gas1,Gas6);
    Db6R=ChapmanEnskog(Trange,P,Gas2,Gas3);
    Db7R=ChapmanEnskog(Trange,P,Gas2,Gas4);
    Db8R=ChapmanEnskog(Trange,P,Gas2,Gas5);
    Db9R=ChapmanEnskog(Trange,P,Gas2,Gas6);
    Db10R=ChapmanEnskog(Trange,P,Gas3,Gas4);
    Db11R=ChapmanEnskog(Trange,P,Gas3,Gas5);
    Db12R=ChapmanEnskog(Trange,P,Gas3,Gas6);
    Db13R=ChapmanEnskog(Trange,P,Gas4,Gas5);
    Db14R=ChapmanEnskog(Trange,P,Gas4,Gas6);
    Db15R=ChapmanEnskog(Trange,P,Gas5,Gas6);
    DR=[Db1R; Db2R; Db3R; Db4R; Db5R; Db6R; Db7R; Db8R;...
        Db9R; Db10R; Db11R; Db12R; Db13R; Db14R; Db15R];
```

```
    legcell={L_Dij1; L_Dij2; L_Dij3; L_Dij4; L_Dij5; L_Dij6;...
        L_Dij7; L_Dij8; L_Dij9; L_Dij10; L_Dij11; L_Dij12; L_Dij13;...
        L_Dij14; L_Dij15};
    Pairs=[p1 p2 p3 p4 p5 p6 p7 p8 p9 p10 p11 p12 p13 p14 p15];
    I=find(Pairs);
    D2plot=DR(I,:);
    leg2plot=legcell(I);
    axes(handles.axes1);
    if isempty(D2plot)==0
        fig2=plot(Trange,D2plot); hold on
        legend(leg2plot,'Location','best')
    end
end

% Fuel composition.
if Qmarker==1
    F1=molarflow(Q1,P,T,Gas1);
    F2=molarflow(Q2,P,T,Gas2);
    F3=molarflow(Q3,P,T,Gas3);
    F4=molarflow(Q4,P,T,Gas4);
    F5=molarflow(Q4,P,T,Gas5);
    F6=molarflow(Q4,P,T,Gas6);
    [X C]=concentration(P,T,F1,F2,F3,F4,F5,F6);
    set(handles.Conc1,'string',C(1));
    set(handles.Conc2,'string',C(2));
    set(handles.Conc3,'string',C(3));
    set(handles.Conc4,'string',C(4));
    set(handles.Conc5,'string',C(5));
    set(handles.Conc6,'string',C(6));
```

```
    set(handles.X1,'string',X(1));
    set(handles.X2,'string',X(2));
    set(handles.X3,'string',X(3));
    set(handles.X4,'string',X(4));
    set(handles.X5,'string',X(5));
    set(handles.X6,'string',X(6));
end

% Effective.
if Qmarker==1 && matmarker==1
Deff=effectivediff([Q1 Q2 Q3 Q4 Q5 Q6],phi,tau,rp,T,P,Gas1,Gas2,Gas3,...
    Gas4,Gas5,Gas6);
set(handles.Deff1,'string',Deff(1));
set(handles.Deff2,'string',Deff(2));
set(handles.Deff3,'string',Deff(3));
set(handles.Deff4,'string',Deff(4));
set(handles.Deff5,'string',Deff(5));
set(handles.Deff6,'string',Deff(6));
if Tmarker==1
    Tloop=Tmin;
    Deff1=[]; Deff2=[]; Deff3=[]; Deff4=[]; Deff5=[];...
        Deff6=[]; Tr=[];
    while Tloop<Tmax
        Tloop=Tloop+(Tmax-Tmin)/100;
        Deff=effectivediff([Q1 Q2 Q3 Q4 Q5 Q6],phi,tau,rp,Tloop,P,Gas1,...
            Gas2,Gas3,Gas4,Gas5,Gas6);
        Deff1(end+1)=Deff(1);
        Deff2(end+1)=Deff(2);
        Deff3(end+1)=Deff(3);
```

```
            Deff4(end+1)=Deff(4);
            Deff5(end+1)=Deff(5);
            Deff6(end+1)=Deff(6);
            Tr(end+1)=Tloop;
        end
        axes(handles.axes3);
        fig1=plot(Tr,Deff1,Tr,Deff2,Tr,Deff3,Tr,Deff4,Tr,Deff5,...
            Tr,Deff6); hold on
        legend(Gas1,Gas2,Gas3,Gas4,Gas5,Gas6,'Location','best')
    end
    end

elseif dim==7
    % Knudsen.
    DKn1=Knudsen(T,rp,Gas1);
    DKn2=Knudsen(T,rp,Gas2);
    DKn3=Knudsen(T,rp,Gas3);
    DKn4=Knudsen(T,rp,Gas4);
    DKn5=Knudsen(T,rp,Gas5);
    DKn6=Knudsen(T,rp,Gas6);
    DKn7=Knudsen(T,rp,Gas7);
    set(handles.DK1,'string',DKn1);
    set(handles.DK2,'string',DKn2);
    set(handles.DK3,'string',DKn3);
    set(handles.DK4,'string',DKn4);
    set(handles.DK5,'string',DKn5);
    set(handles.DK6,'string',DKn6);
    set(handles.DK7,'string',DKn7);
```

```
if Tmarker==1
    Trange=linspace(Tmin,Tmax,(Tmax-Tmin)*10);
    DKn1R=Knudsen(Trange,rp,Gas1);
    DKn2R=Knudsen(Trange,rp,Gas2);
    DKn3R=Knudsen(Trange,rp,Gas3);
    DKn4R=Knudsen(Trange,rp,Gas4);
    DKn5R=Knudsen(Trange,rp,Gas5);
    DKn6R=Knudsen(Trange,rp,Gas6);
    DKn7R=Knudsen(Trange,rp,Gas7);
    axes(handles.axes2);
    fig1=plot(Trange,DKn1R,Trange,DKn2R,Trange,DKn3R,Trange,DKn4R,...
        Trange,DKn5R,Trange,DKn6R,Trange,DKn7R); hold on
    legend(Gas1,Gas2,Gas3,Gas4,Gas5,Gas6,Gas7,'Location','best')
end

% Binary.
Db1=ChapmanEnskog(T,P,Gas1,Gas2);
set(handles.Dij1,'string',Db1);
Db2=ChapmanEnskog(T,P,Gas1,Gas3);
set(handles.Dij2,'string',Db2);
Db3=ChapmanEnskog(T,P,Gas1,Gas4);
set(handles.Dij3,'string',Db3);
Db4=ChapmanEnskog(T,P,Gas1,Gas5);
set(handles.Dij4,'string',Db4);
Db5=ChapmanEnskog(T,P,Gas1,Gas6);
set(handles.Dij5,'string',Db5);
Db6=ChapmanEnskog(T,P,Gas1,Gas7);
set(handles.Dij6,'string',Db6);
Db7=ChapmanEnskog(T,P,Gas2,Gas3);
```

```
set(handles.Dij7,'string',Db7);
Db8=ChapmanEnskog(T,P,Gas2,Gas4);
set(handles.Dij8,'string',Db8);
Db9=ChapmanEnskog(T,P,Gas2,Gas5);
set(handles.Dij9,'string',Db9);
Db10=ChapmanEnskog(T,P,Gas2,Gas6);
set(handles.Dij10,'string',Db10);
Db11=ChapmanEnskog(T,P,Gas2,Gas7);
set(handles.Dij11,'string',Db11);
Db12=ChapmanEnskog(T,P,Gas3,Gas4);
set(handles.Dij12,'string',Db12);
Db13=ChapmanEnskog(T,P,Gas3,Gas5);
set(handles.Dij13,'string',Db13);
Db14=ChapmanEnskog(T,P,Gas3,Gas6);
set(handles.Dij14,'string',Db14);
Db15=ChapmanEnskog(T,P,Gas3,Gas7);
set(handles.Dij15,'string',Db15);
Db16=ChapmanEnskog(T,P,Gas4,Gas5);
set(handles.Dij16,'string',Db16);
Db17=ChapmanEnskog(T,P,Gas4,Gas6);
set(handles.Dij17,'string',Db17);
Db18=ChapmanEnskog(T,P,Gas4,Gas7);
set(handles.Dij18,'string',Db18);
Db19=ChapmanEnskog(T,P,Gas5,Gas6);
set(handles.Dij19,'string',Db19);
Db20=ChapmanEnskog(T,P,Gas5,Gas7);
set(handles.Dij20,'string',Db20);
Db21=ChapmanEnskog(T,P,Gas6,Gas7);
set(handles.Dij21,'string',Db21);
```

```
L_Dij1=horzcat(Gas1,'-',Gas2);
set(handles.Dijlabel1,'string',L_Dij1);
L_Dij2=horzcat(Gas1,'-',Gas3);
set(handles.Dijlabel2,'string',L_Dij2);
L_Dij3=horzcat(Gas1,'-',Gas4);
set(handles.Dijlabel3,'string',L_Dij3);
L_Dij4=horzcat(Gas1,'-',Gas5);
set(handles.Dijlabel4,'string',L_Dij4);
L_Dij5=horzcat(Gas1,'-',Gas6);
set(handles.Dijlabel5,'string',L_Dij5);
L_Dij6=horzcat(Gas1,'-',Gas7);
set(handles.Dijlabel6,'string',L_Dij6);
L_Dij7=horzcat(Gas2,'-',Gas3);
set(handles.Dijlabel7,'string',L_Dij7);
L_Dij8=horzcat(Gas2,'-',Gas4);
set(handles.Dijlabel8,'string',L_Dij8);
L_Dij9=horzcat(Gas2,'-',Gas5);
set(handles.Dijlabel9,'string',L_Dij9);
L_Dij10=horzcat(Gas2,'-',Gas6);
set(handles.Dijlabel10,'string',L_Dij10);
L_Dij11=horzcat(Gas2,'-',Gas7);
set(handles.Dijlabel11,'string',L_Dij11);
L_Dij12=horzcat(Gas3,'-',Gas4);
set(handles.Dijlabel12,'string',L_Dij12);
L_Dij13=horzcat(Gas3,'-',Gas5);
set(handles.Dijlabel13,'string',L_Dij13);
L_Dij14=horzcat(Gas3,'-',Gas6);
set(handles.Dijlabel14,'string',L_Dij14);
```

```
L_Dij15=horzcat(Gas3,'-',Gas7);
set(handles.Dijlabel15,'string',L_Dij15);
L_Dij16=horzcat(Gas4,'-',Gas5);
set(handles.Dijlabel16,'string',L_Dij16);
L_Dij17=horzcat(Gas4,'-',Gas6);
set(handles.Dijlabel17,'string',L_Dij17);
L_Dij18=horzcat(Gas4,'-',Gas7);
set(handles.Dijlabel18,'string',L_Dij18);
L_Dij19=horzcat(Gas5,'-',Gas6);
set(handles.Dijlabel19,'string',L_Dij19);
L_Dij20=horzcat(Gas5,'-',Gas7);
set(handles.Dijlabel20,'string',L_Dij20);
L_Dij21=horzcat(Gas6,'-',Gas7);
set(handles.Dijlabel21,'string',L_Dij21);

if Tmarker==1
    Trange=linspace(Tmin,Tmax,(Tmax-Tmin)*10);
    Db1R=ChapmanEnskog(Trange,P,Gas1,Gas2);
    Db2R=ChapmanEnskog(Trange,P,Gas1,Gas3);
    Db3R=ChapmanEnskog(Trange,P,Gas1,Gas4);
    Db4R=ChapmanEnskog(Trange,P,Gas1,Gas5);
    Db5R=ChapmanEnskog(Trange,P,Gas1,Gas6);
    Db6R=ChapmanEnskog(Trange,P,Gas1,Gas7);
    Db7R=ChapmanEnskog(Trange,P,Gas2,Gas3);
    Db8R=ChapmanEnskog(Trange,P,Gas2,Gas4);
    Db9R=ChapmanEnskog(Trange,P,Gas2,Gas5);
    Db10R=ChapmanEnskog(Trange,P,Gas2,Gas6);
    Db11R=ChapmanEnskog(Trange,P,Gas2,Gas7);
    Db12R=ChapmanEnskog(Trange,P,Gas3,Gas4);
```

```
    Db13R=ChapmanEnskog(Trange,P,Gas3,Gas5);
    Db14R=ChapmanEnskog(Trange,P,Gas3,Gas6);
    Db15R=ChapmanEnskog(Trange,P,Gas3,Gas7);
    Db16R=ChapmanEnskog(Trange,P,Gas4,Gas5);
    Db17R=ChapmanEnskog(Trange,P,Gas4,Gas6);
    Db18R=ChapmanEnskog(Trange,P,Gas4,Gas7);
    Db19R=ChapmanEnskog(Trange,P,Gas5,Gas6);
    Db20R=ChapmanEnskog(Trange,P,Gas5,Gas7);
    Db21R=ChapmanEnskog(Trange,P,Gas6,Gas7);
    DR=[Db1R; Db2R; Db3R; Db4R; Db5R; Db6R; Db7R; Db8R;...
        Db9R; Db10R; Db11R; Db12R; Db13R; Db14R; Db15R;...
        Db16R; Db17R; Db18R; Db19R; Db20R; Db21R];
    legcell={L_Dij1; L_Dij2; L_Dij3; L_Dij4; L_Dij5; L_Dij6;...
        L_Dij7; L_Dij8; L_Dij9; L_Dij10; L_Dij11; L_Dij12; L_Dij13;...
        L_Dij14; L_Dij15; L_Dij16; L_Dij17; L_Dij18; L_Dij19; L_Dij20;...
        L_Dij21};
    Pairs=[p1 p2 p3 p4 p5 p6 p7 p8 p9 p10 p11 p12 p13 p14 p15...
        p16 p17 p18 p19 p20 p21];
    I=find(Pairs);
    D2plot=DR(I,:);
    leg2plot=legcell(I);
    axes(handles.axes1);
    if isempty(D2plot)==0
        fig2=plot(Trange,D2plot); hold on
        legend(leg2plot,'Location','best')
    end
end

% Fuel composition.
```

```
if Qmarker==1
    F1=molarflow(Q1,P,T,Gas1);
    F2=molarflow(Q2,P,T,Gas2);
    F3=molarflow(Q3,P,T,Gas3);
    F4=molarflow(Q4,P,T,Gas4);
    F5=molarflow(Q4,P,T,Gas5);
    F6=molarflow(Q4,P,T,Gas6);
    F7=molarflow(Q4,P,T,Gas7);
    [X C]=concentration(P,T,F1,F2,F3,F4,F5,F6,F7);
    set(handles.Conc1,'string',C(1));
    set(handles.Conc2,'string',C(2));
    set(handles.Conc3,'string',C(3));
    set(handles.Conc4,'string',C(4));
    set(handles.Conc5,'string',C(5));
    set(handles.Conc6,'string',C(6));
    set(handles.Conc7,'string',C(7));
    set(handles.X1,'string',X(1));
    set(handles.X2,'string',X(2));
    set(handles.X3,'string',X(3));
    set(handles.X4,'string',X(4));
    set(handles.X5,'string',X(5));
    set(handles.X6,'string',X(6));
    set(handles.X7,'string',X(7));
end

% Effective.
if Qmarker==1 && matmarker==1
Deff=effectivediff([Q1 Q2 Q3 Q4 Q5 Q6 Q7],phi,tau,rp,T,P,Gas1,Gas2,Gas3,...
    Gas4,Gas5,Gas6,Gas7);
```

```
set(handles.Deff1,'string',Deff(1));
set(handles.Deff2,'string',Deff(2));
set(handles.Deff3,'string',Deff(3));
set(handles.Deff4,'string',Deff(4));
set(handles.Deff5,'string',Deff(5));
set(handles.Deff6,'string',Deff(6));
set(handles.Deff7,'string',Deff(7));
if Tmarker==1
    Tloop=Tmin;
    Deff1=[]; Deff2=[]; Deff3=[]; Deff4=[]; Deff5=[];...
        Deff6=[]; Deff7=[]; Tr=[];
    while Tloop<Tmax
        Tloop=Tloop+(Tmax-Tmin)/100;
        Deff=effectivediff([Q1 Q2 Q3 Q4 Q5 Q6 Q7],phi,tau,rp,Tloop,P,Gas1,...
            Gas2,Gas3,Gas4,Gas5,Gas6,Gas7);
        Deff1(end+1)=Deff(1);
        Deff2(end+1)=Deff(2);
        Deff3(end+1)=Deff(3);
        Deff4(end+1)=Deff(4);
        Deff5(end+1)=Deff(5);
        Deff6(end+1)=Deff(6);
        Deff7(end+1)=Deff(7);
        Tr(end+1)=Tloop;
    end
    axes(handles.axes3);
    fig1=plot(Tr,Deff1,Tr,Deff2,Tr,Deff3,Tr,Deff4,Tr,Deff5,...
        Tr,Deff6,Tr,Deff7); hold on
    legend(Gas1,Gas2,Gas3,Gas4,Gas5,Gas6,Gas7,'Location','best')
end
```

```
    end

elseif dim==8
    % Knudsen.
    DKn1=Knudsen(T,rp,Gas1);
    DKn2=Knudsen(T,rp,Gas2);
    DKn3=Knudsen(T,rp,Gas3);
    DKn4=Knudsen(T,rp,Gas4);
    DKn5=Knudsen(T,rp,Gas5);
    DKn6=Knudsen(T,rp,Gas6);
    DKn7=Knudsen(T,rp,Gas7);
    DKn8=Knudsen(T,rp,Gas8);
    set(handles.DK1,'string',DKn1);
    set(handles.DK2,'string',DKn2);
    set(handles.DK3,'string',DKn3);
    set(handles.DK4,'string',DKn4);
    set(handles.DK5,'string',DKn5);
    set(handles.DK6,'string',DKn6);
    set(handles.DK7,'string',DKn7);
    set(handles.DK8,'string',DKn8);

    if Tmarker==1
        Trange=linspace(Tmin,Tmax,(Tmax-Tmin)*10);
        DKn1R=Knudsen(Trange,rp,Gas1);
        DKn2R=Knudsen(Trange,rp,Gas2);
        DKn3R=Knudsen(Trange,rp,Gas3);
        DKn4R=Knudsen(Trange,rp,Gas4);
        DKn5R=Knudsen(Trange,rp,Gas5);
        DKn6R=Knudsen(Trange,rp,Gas6);
```

```
    DKn7R=Knudsen(Trange,rp,Gas7);
    DKn8R=Knudsen(Trange,rp,Gas8);
    axes(handles.axes2);
    fig1=plot(Trange,DKn1R,Trange,DKn2R,Trange,DKn3R,Trange,DKn4R,...
        Trange,DKn5R,Trange,DKn6R,Trange,DKn7R,Trange,DKn8R); hold on
    legend(Gas1,Gas2,Gas3,Gas4,Gas5,Gas6,Gas7,Gas8,'Location','best')
end

% Binary.
Db1=ChapmanEnskog(T,P,Gas1,Gas2);
set(handles.Dij1,'string',Db1);
Db2=ChapmanEnskog(T,P,Gas1,Gas3);
set(handles.Dij2,'string',Db2);
Db3=ChapmanEnskog(T,P,Gas1,Gas4);
set(handles.Dij3,'string',Db3);
Db4=ChapmanEnskog(T,P,Gas1,Gas5);
set(handles.Dij4,'string',Db4);
Db5=ChapmanEnskog(T,P,Gas1,Gas6);
set(handles.Dij5,'string',Db5);
Db6=ChapmanEnskog(T,P,Gas1,Gas7);
set(handles.Dij6,'string',Db6);
Db7=ChapmanEnskog(T,P,Gas1,Gas8);
set(handles.Dij7,'string',Db7);
Db8=ChapmanEnskog(T,P,Gas2,Gas3);
set(handles.Dij8,'string',Db8);
Db9=ChapmanEnskog(T,P,Gas2,Gas4);
set(handles.Dij9,'string',Db9);
Db10=ChapmanEnskog(T,P,Gas2,Gas5);
set(handles.Dij10,'string',Db10);
```

```
Db11=ChapmanEnskog(T,P,Gas2,Gas6);
set(handles.Dij11,'string',Db11);
Db12=ChapmanEnskog(T,P,Gas2,Gas7);
set(handles.Dij12,'string',Db12);
Db13=ChapmanEnskog(T,P,Gas2,Gas8);
set(handles.Dij13,'string',Db13);
Db14=ChapmanEnskog(T,P,Gas3,Gas4);
set(handles.Dij14,'string',Db14);
Db15=ChapmanEnskog(T,P,Gas3,Gas5);
set(handles.Dij15,'string',Db15);
Db16=ChapmanEnskog(T,P,Gas3,Gas6);
set(handles.Dij16,'string',Db16);
Db17=ChapmanEnskog(T,P,Gas3,Gas7);
set(handles.Dij17,'string',Db17);
Db18=ChapmanEnskog(T,P,Gas3,Gas8);
set(handles.Dij18,'string',Db18);
Db19=ChapmanEnskog(T,P,Gas4,Gas5);
set(handles.Dij19,'string',Db19);
Db20=ChapmanEnskog(T,P,Gas4,Gas6);
set(handles.Dij20,'string',Db20);
Db21=ChapmanEnskog(T,P,Gas4,Gas7);
set(handles.Dij21,'string',Db21);
Db22=ChapmanEnskog(T,P,Gas4,Gas8);
set(handles.Dij22,'string',Db22);
Db23=ChapmanEnskog(T,P,Gas5,Gas6);
set(handles.Dij23,'string',Db23);
Db24=ChapmanEnskog(T,P,Gas5,Gas7);
set(handles.Dij24,'string',Db24);
Db25=ChapmanEnskog(T,P,Gas5,Gas8);
```

```
set(handles.Dij25,'string',Db25);
Db26=ChapmanEnskog(T,P,Gas6,Gas7);
set(handles.Dij26,'string',Db26);
Db27=ChapmanEnskog(T,P,Gas6,Gas8);
set(handles.Dij27,'string',Db27);
Db28=ChapmanEnskog(T,P,Gas7,Gas8);
set(handles.Dij28,'string',Db28);

L_Dij1=horzcat(Gas1,'-',Gas2);
set(handles.Dijlabel1,'string',L_Dij1);
L_Dij2=horzcat(Gas1,'-',Gas3);
set(handles.Dijlabel2,'string',L_Dij2);
L_Dij3=horzcat(Gas1,'-',Gas4);
set(handles.Dijlabel3,'string',L_Dij3);
L_Dij4=horzcat(Gas1,'-',Gas5);
set(handles.Dijlabel4,'string',L_Dij4);
L_Dij5=horzcat(Gas1,'-',Gas6);
set(handles.Dijlabel5,'string',L_Dij5);
L_Dij6=horzcat(Gas1,'-',Gas7);
set(handles.Dijlabel6,'string',L_Dij6);
L_Dij7=horzcat(Gas1,'-',Gas8);
set(handles.Dijlabel7,'string',L_Dij7);
L_Dij8=horzcat(Gas2,'-',Gas3);
set(handles.Dijlabel8,'string',L_Dij8);
L_Dij9=horzcat(Gas2,'-',Gas4);
set(handles.Dijlabel9,'string',L_Dij9);
L_Dij10=horzcat(Gas2,'-',Gas5);
set(handles.Dijlabel10,'string',L_Dij10);
L_Dij11=horzcat(Gas2,'-',Gas6);
```

```
set(handles.Dijlabel11,'string',L_Dij11);
L_Dij12=horzcat(Gas2,'-',Gas7);
set(handles.Dijlabel12,'string',L_Dij12);
L_Dij13=horzcat(Gas2,'-',Gas8);
set(handles.Dijlabel13,'string',L_Dij13);
L_Dij14=horzcat(Gas3,'-',Gas4);
set(handles.Dijlabel14,'string',L_Dij14);
L_Dij15=horzcat(Gas3,'-',Gas5);
set(handles.Dijlabel15,'string',L_Dij15);
L_Dij16=horzcat(Gas3,'-',Gas6);
set(handles.Dijlabel16,'string',L_Dij16);
L_Dij17=horzcat(Gas3,'-',Gas7);
set(handles.Dijlabel17,'string',L_Dij17);
L_Dij18=horzcat(Gas3,'-',Gas8);
set(handles.Dijlabel18,'string',L_Dij18);
L_Dij19=horzcat(Gas4,'-',Gas5);
set(handles.Dijlabel19,'string',L_Dij19);
L_Dij20=horzcat(Gas4,'-',Gas6);
set(handles.Dijlabel20,'string',L_Dij20);
L_Dij21=horzcat(Gas4,'-',Gas7);
set(handles.Dijlabel21,'string',L_Dij21);
L_Dij22=horzcat(Gas4,'-',Gas8);
set(handles.Dijlabel22,'string',L_Dij22);
L_Dij23=horzcat(Gas5,'-',Gas6);
set(handles.Dijlabel23,'string',L_Dij23);
L_Dij24=horzcat(Gas5,'-',Gas7);
set(handles.Dijlabel24,'string',L_Dij24);
L_Dij25=horzcat(Gas5,'-',Gas8);
set(handles.Dijlabel25,'string',L_Dij25);
```

```
L_Dij26=horzcat(Gas6,'-',Gas7);
set(handles.Dijlabel26,'string',L_Dij26);
L_Dij27=horzcat(Gas6,'-',Gas8);
set(handles.Dijlabel27,'string',L_Dij27);
L_Dij28=horzcat(Gas7,'-',Gas8);
set(handles.Dijlabel28,'string',L_Dij28);

if Tmarker==1
    Trange=linspace(Tmin,Tmax,(Tmax-Tmin)*10);
    Db1R=ChapmanEnskog(Trange,P,Gas1,Gas2);
    Db2R=ChapmanEnskog(Trange,P,Gas1,Gas3);
    Db3R=ChapmanEnskog(Trange,P,Gas1,Gas4);
    Db4R=ChapmanEnskog(Trange,P,Gas1,Gas5);
    Db5R=ChapmanEnskog(Trange,P,Gas1,Gas6);
    Db6R=ChapmanEnskog(Trange,P,Gas1,Gas7);
    Db7R=ChapmanEnskog(Trange,P,Gas1,Gas8);
    Db8R=ChapmanEnskog(Trange,P,Gas2,Gas3);
    Db9R=ChapmanEnskog(Trange,P,Gas2,Gas4);
    Db10R=ChapmanEnskog(Trange,P,Gas2,Gas5);
    Db11R=ChapmanEnskog(Trange,P,Gas2,Gas6);
    Db12R=ChapmanEnskog(Trange,P,Gas2,Gas7);
    Db13R=ChapmanEnskog(Trange,P,Gas2,Gas8);
    Db14R=ChapmanEnskog(Trange,P,Gas3,Gas4);
    Db15R=ChapmanEnskog(Trange,P,Gas3,Gas5);
    Db16R=ChapmanEnskog(Trange,P,Gas3,Gas6);
    Db17R=ChapmanEnskog(Trange,P,Gas3,Gas7);
    Db18R=ChapmanEnskog(Trange,P,Gas3,Gas8);
    Db19R=ChapmanEnskog(Trange,P,Gas4,Gas5);
    Db20R=ChapmanEnskog(Trange,P,Gas4,Gas6);
```

```
    Db21R=ChapmanEnskog(Trange,P,Gas4,Gas7);
    Db22R=ChapmanEnskog(Trange,P,Gas4,Gas8);
    Db23R=ChapmanEnskog(Trange,P,Gas5,Gas6);
    Db24R=ChapmanEnskog(Trange,P,Gas5,Gas7);
    Db25R=ChapmanEnskog(Trange,P,Gas5,Gas8);
    Db26R=ChapmanEnskog(Trange,P,Gas6,Gas7);
    Db27R=ChapmanEnskog(Trange,P,Gas6,Gas8);
    Db28R=ChapmanEnskog(Trange,P,Gas7,Gas8);
    DR=[Db1R; Db2R; Db3R; Db4R; Db5R; Db6R; Db7R; Db8R;...
        Db9R; Db10R; Db11R; Db12R; Db13R; Db14R; Db15R;...
        Db16R; Db17R; Db18R; Db19R; Db20R; Db21R;...
        Db22R; Db23R; Db24R; Db26R; Db26R; Db27R; Db28R];
    legcell={L_Dij1; L_Dij2; L_Dij3; L_Dij4; L_Dij5; L_Dij6;...
        L_Dij7; L_Dij8; L_Dij9; L_Dij10; L_Dij11; L_Dij12; L_Dij13;...
        L_Dij14; L_Dij15; L_Dij16; L_Dij17; L_Dij18; L_Dij19; L_Dij20;...
        L_Dij21; L_Dij22; L_Dij23; L_Dij24; L_Dij25; L_Dij26; L_Dij27;...
        L_Dij28};
    Pairs=[p1 p2 p3 p4 p5 p6 p7 p8 p9 p10 p11 p12 p13 p14 p15...
        p16 p17 p18 p19 p20 p21 p22 p23 p24 p25 p26 p27 p28];
    I=find(Pairs);
    D2plot=DR(I,:);
    leg2plot=legcell(I);
    axes(handles.axes1);
    if isempty(D2plot)==0
        fig2=plot(Trange,D2plot); hold on
        legend(leg2plot,'Location','best')
    end
end
```

```
% Fuel composition.
if Qmarker==1
    F1=molarflow(Q1,P,T,Gas1);
    F2=molarflow(Q2,P,T,Gas2);
    F3=molarflow(Q3,P,T,Gas3);
    F4=molarflow(Q4,P,T,Gas4);
    F5=molarflow(Q4,P,T,Gas5);
    F6=molarflow(Q4,P,T,Gas6);
    F7=molarflow(Q4,P,T,Gas7);
    F8=molarflow(Q4,P,T,Gas8);
    [X C]=concentration(P,T,F1,F2,F3,F4,F5,F6,F7,F8);
    set(handles.Conc1,'string',C(1));
    set(handles.Conc2,'string',C(2));
    set(handles.Conc3,'string',C(3));
    set(handles.Conc4,'string',C(4));
    set(handles.Conc5,'string',C(5));
    set(handles.Conc6,'string',C(6));
    set(handles.Conc7,'string',C(7));
    set(handles.Conc8,'string',C(8));
    set(handles.X1,'string',X(1));
    set(handles.X2,'string',X(2));
    set(handles.X3,'string',X(3));
    set(handles.X4,'string',X(4));
    set(handles.X5,'string',X(5));
    set(handles.X6,'string',X(6));
    set(handles.X7,'string',X(7));
    set(handles.X8,'string',X(8));
end
```

```
% Effective.
if Qmarker==1 && matmarker==1
Deff=effectivediff([Q1 Q2 Q3 Q4 Q5 Q6 Q7 Q8],phi,tau,rp,T,P,Gas1,Gas2,Gas3,...
    Gas4,Gas5,Gas6,Gas7,Gas8);
set(handles.Deff1,'string',Deff(1));
set(handles.Deff2,'string',Deff(2));
set(handles.Deff3,'string',Deff(3));
set(handles.Deff4,'string',Deff(4));
set(handles.Deff5,'string',Deff(5));
set(handles.Deff6,'string',Deff(6));
set(handles.Deff7,'string',Deff(7));
set(handles.Deff8,'string',Deff(8));
if Tmarker==1
    Tloop=Tmin;
    Deff1=[]; Deff2=[]; Deff3=[]; Deff4=[]; Deff5=[];...
        Deff6=[]; Deff7=[]; Deff8=[]; Tr=[];
    while Tloop<Tmax
        Tloop=Tloop+(Tmax-Tmin)/100;
        Deff=effectivediff([Q1 Q2 Q3 Q4 Q5 Q6 Q7 Q8],phi,tau,rp,Tloop,P,Gas1,...
            Gas2,Gas3,Gas4,Gas5,Gas6,Gas7,Gas8);
        Deff1(end+1)=Deff(1);
        Deff2(end+1)=Deff(2);
        Deff3(end+1)=Deff(3);
        Deff4(end+1)=Deff(4);
        Deff5(end+1)=Deff(5);
        Deff6(end+1)=Deff(6);
        Deff7(end+1)=Deff(7);
        Deff8(end+1)=Deff(8);
        Tr(end+1)=Tloop;
```

```
        end
        axes(handles.axes3);
        fig1=plot(Tr,Deff1,Tr,Deff2,Tr,Deff3,Tr,Deff4,Tr,Deff5,...
            Tr,Deff6,Tr,Deff7,Tr,Deff8); hold on
        legend(Gas1,Gas2,Gas3,Gas4,Gas5,Gas6,Gas7,Gas8,'Location','best')
    end
    end

end

% --- Executes on button press in pushbutton3.
function pushbutton3_Callback(hObject, eventdata, handles)
cla(handles.axes1,'reset')
cla(handles.axes2,'reset')
cla(handles.axes3,'reset')

% --- Executes on button press in pushbutton5.
function pushbutton5_Callback(hObject, eventdata, handles)
E=ginput(1);
Ewrite=horzcat('(',num2str(E(1)),',',num2str(E(2)),')');
set(handles.extract,'string',Ewrite);

% --- Executes on button press in pushbutton7.
function pushbutton7_Callback(hObject, eventdata, handles)
zoom on

% --- Executes on button press in pushbutton8.
function pushbutton8_Callback(hObject, eventdata, handles)
zoom off
```

```
% --- Executes on button press in pushbutton10.
function pushbutton10_Callback(hObject, eventdata, handles)
s1='--';
set(handles.Conc1,'string',s1);
set(handles.Conc2,'string',s1);
set(handles.Conc3,'string',s1);
set(handles.Conc4,'string',s1);
set(handles.Conc5,'string',s1);
set(handles.Conc6,'string',s1);
set(handles.Conc7,'string',s1);
set(handles.Conc8,'string',s1);
set(handles.X1,'string',s1);
set(handles.X2,'string',s1);
set(handles.X3,'string',s1);
set(handles.X4,'string',s1);
set(handles.X5,'string',s1);
set(handles.X6,'string',s1);
set(handles.X7,'string',s1);
set(handles.X8,'string',s1);
set(handles.Deff1,'string',s1);
set(handles.Deff2,'string',s1);
set(handles.Deff3,'string',s1);
set(handles.Deff4,'string',s1);
set(handles.Deff5,'string',s1);
set(handles.Deff6,'string',s1);
set(handles.Deff7,'string',s1);
set(handles.Deff8,'string',s1);
set(handles.DK1,'string',s1);
```

```
set(handles.DK2,'string',s1);
set(handles.DK3,'string',s1);
set(handles.DK4,'string',s1);
set(handles.DK5,'string',s1);
set(handles.DK6,'string',s1);
set(handles.DK7,'string',s1);
set(handles.DK8,'string',s1);
set(handles.Dijlabel1,'string',s1);
set(handles.Dijlabel2,'string',s1);
set(handles.Dijlabel3,'string',s1);
set(handles.Dijlabel4,'string',s1);
set(handles.Dijlabel5,'string',s1);
set(handles.Dijlabel6,'string',s1);
set(handles.Dijlabel7,'string',s1);
set(handles.Dijlabel8,'string',s1);
set(handles.Dijlabel9,'string',s1);
set(handles.Dijlabel10,'string',s1);
set(handles.Dijlabel11,'string',s1);
set(handles.Dijlabel12,'string',s1);
set(handles.Dijlabel13,'string',s1);
set(handles.Dijlabel14,'string',s1);
set(handles.Dijlabel15,'string',s1);
set(handles.Dijlabel16,'string',s1);
set(handles.Dijlabel17,'string',s1);
set(handles.Dijlabel18,'string',s1);
set(handles.Dijlabel19,'string',s1);
set(handles.Dijlabel20,'string',s1);
set(handles.Dijlabel21,'string',s1);
set(handles.Dijlabel22,'string',s1);
```

```
set(handles.Dijlabel23,'string',s1);
set(handles.Dijlabel24,'string',s1);
set(handles.Dijlabel25,'string',s1);
set(handles.Dijlabel26,'string',s1);
set(handles.Dijlabel27,'string',s1);
set(handles.Dijlabel28,'string',s1);
set(handles.Dij1,'string',s1);
set(handles.Dij2,'string',s1);
set(handles.Dij3,'string',s1);
set(handles.Dij4,'string',s1);
set(handles.Dij5,'string',s1);
set(handles.Dij6,'string',s1);
set(handles.Dij7,'string',s1);
set(handles.Dij8,'string',s1);
set(handles.Dij9,'string',s1);
set(handles.Dij10,'string',s1);
set(handles.Dij11,'string',s1);
set(handles.Dij12,'string',s1);
set(handles.Dij13,'string',s1);
set(handles.Dij14,'string',s1);
set(handles.Dij15,'string',s1);
set(handles.Dij16,'string',s1);
set(handles.Dij17,'string',s1);
set(handles.Dij18,'string',s1);
set(handles.Dij19,'string',s1);
set(handles.Dij20,'string',s1);
set(handles.Dij21,'string',s1);
set(handles.Dij22,'string',s1);
set(handles.Dij23,'string',s1);
```

```
set(handles.Dij24,'string',s1);
set(handles.Dij25,'string',s1);
set(handles.Dij26,'string',s1);
set(handles.Dij27,'string',s1);
set(handles.Dij28,'string',s1);
set(handles.p1,'value',0);
set(handles.p2,'value',0);
set(handles.p3,'value',0);
set(handles.p4,'value',0);
set(handles.p5,'value',0);
set(handles.p6,'value',0);
set(handles.p7,'value',0);
set(handles.p8,'value',0);
set(handles.p9,'value',0);
set(handles.p10,'value',0);
set(handles.p11,'value',0);
set(handles.p12,'value',0);
set(handles.p13,'value',0);
set(handles.p14,'value',0);
set(handles.p15,'value',0);
set(handles.p16,'value',0);
set(handles.p17,'value',0);
set(handles.p18,'value',0);
set(handles.p19,'value',0);
set(handles.p20,'value',0);
set(handles.p21,'value',0);
set(handles.p22,'value',0);
set(handles.p23,'value',0);
set(handles.p24,'value',0);
```

```
set(handles.p25,'value',0);
set(handles.p26,'value',0);
set(handles.p27,'value',0);
set(handles.p28,'value',0);

function rp_Callback(hObject, eventdata, handles)

% --- Executes during object creation, after setting all properties.
function rp_CreateFcn(hObject, eventdata, handles)
if ispc && isequal(get(hObject,'BackgroundColor'), ...
get(0,'defaultUicontrolBackgroundColor'))
    set(hObject,'BackgroundColor','white');
end

function tor_Callback(hObject, eventdata, handles)
% --- Executes during object creation, after setting all properties.
function tor_CreateFcn(hObject, eventdata, handles)
if ispc && isequal(get(hObject,'BackgroundColor'), ...
get(0,'defaultUicontrolBackgroundColor'))
    set(hObject,'BackgroundColor','white');
end

function por_Callback(hObject, eventdata, handles)

% --- Executes during object creation, after setting all properties.
function por_CreateFcn(hObject, eventdata, handles)
if ispc && isequal(get(hObject,'BackgroundColor'), ...
get(0,'defaultUicontrolBackgroundColor'))
    set(hObject,'BackgroundColor','white');
```

```
end

% --- Executes on button press in p1.
function p1_Callback(hObject, eventdata, handles)

% --- Executes on button press in p2.
function p2_Callback(hObject, eventdata, handles)

% --- Executes on button press in p3.
function p3_Callback(hObject, eventdata, handles)

% --- Executes on button press in p4.
function p4_Callback(hObject, eventdata, handles)

% --- Executes on button press in p5.
function p5_Callback(hObject, eventdata, handles)

% --- Executes on button press in p6.
function p6_Callback(hObject, eventdata, handles)

% --- Executes on button press in p7.
function p7_Callback(hObject, eventdata, handles)

% --- Executes on button press in p8.
function p8_Callback(hObject, eventdata, handles)

% --- Executes on button press in p9.
function p9_Callback(hObject, eventdata, handles)
```

```
% --- Executes on button press in p10.
function p10_Callback(hObject, eventdata, handles)

% --- Executes on button press in p11.
function p11_Callback(hObject, eventdata, handles)

% --- Executes on button press in p12.
function p12_Callback(hObject, eventdata, handles)

% --- Executes on button press in p13.
function p13_Callback(hObject, eventdata, handles)

% --- Executes on button press in p14.
function p14_Callback(hObject, eventdata, handles)

% --- Executes on button press in p15.
function p15_Callback(hObject, eventdata, handles)

% --- Executes on button press in p16.
function p16_Callback(hObject, eventdata, handles)

% --- Executes on button press in p17.
function p17_Callback(hObject, eventdata, handles)

% --- Executes on button press in p18.
function p18_Callback(hObject, eventdata, handles)

% --- Executes on button press in p19.
function p19_Callback(hObject, eventdata, handles)
```

```
% --- Executes on button press in p20.
function p20_Callback(hObject, eventdata, handles)

% --- Executes on button press in p21.
function p21_Callback(hObject, eventdata, handles)

% --- Executes on button press in p22.
function p22_Callback(hObject, eventdata, handles)

% --- Executes on button press in p23.
function p23_Callback(hObject, eventdata, handles)

% --- Executes on button press in p24.
function p24_Callback(hObject, eventdata, handles)

% --- Executes on button press in p25.
function p25_Callback(hObject, eventdata, handles)

% --- Executes on button press in p26.
function p26_Callback(hObject, eventdata, handles)

% --- Executes on button press in p27.
function p27_Callback(hObject, eventdata, handles)

% --- Executes on button press in p28.
function p28_Callback(hObject, eventdata, handles)

function Tlo_Callback(hObject, eventdata, handles)
```

```
% --- Executes during object creation, after setting all properties.
function Tlo_CreateFcn(hObject, eventdata, handles)
if ispc && isequal(get(hObject,'BackgroundColor'), ...
get(0,'defaultUicontrolBackgroundColor'))
    set(hObject,'BackgroundColor','white');
end

function Thi_Callback(hObject, eventdata, handles)

% --- Executes during object creation, after setting all properties.
function Thi_CreateFcn(hObject, eventdata, handles)
if ispc && isequal(get(hObject,'BackgroundColor'), ...
get(0,'defaultUicontrolBackgroundColor'))
    set(hObject,'BackgroundColor','white');
end

function temp_Callback(hObject, eventdata, handles)

% --- Executes during object creation, after setting all properties.
function temp_CreateFcn(hObject, eventdata, handles)
if ispc && isequal(get(hObject,'BackgroundColor'), ...
get(0,'defaultUicontrolBackgroundColor'))
    set(hObject,'BackgroundColor','white');
end

function pressure_Callback(hObject, eventdata, handles)

% --- Executes during object creation, after setting all properties.
```

```
function pressure_CreateFcn(hObject, eventdata, handles)
if ispc && isequal(get(hObject,'BackgroundColor'), ...
get(0,'defaultUicontrolBackgroundColor'))
    set(hObject,'BackgroundColor','white');
end

function flow1_Callback(hObject, eventdata, handles)

% --- Executes during object creation, after setting all properties.
function flow1_CreateFcn(hObject, eventdata, handles)
if ispc && isequal(get(hObject,'BackgroundColor'), ...
get(0,'defaultUicontrolBackgroundColor'))
    set(hObject,'BackgroundColor','white');
end

function flow2_Callback(hObject, eventdata, handles)

% --- Executes during object creation, after setting all properties.
function flow2_CreateFcn(hObject, eventdata, handles)
if ispc && isequal(get(hObject,'BackgroundColor'), ...
get(0,'defaultUicontrolBackgroundColor'))
    set(hObject,'BackgroundColor','white');
end

function flow3_Callback(hObject, eventdata, handles)

% --- Executes during object creation, after setting all properties.
function flow3_CreateFcn(hObject, eventdata, handles)
if ispc && isequal(get(hObject,'BackgroundColor'), ...
```

```
get(0,'defaultUicontrolBackgroundColor'))
    set(hObject,'BackgroundColor','white');
end

function flow4_Callback(hObject, eventdata, handles)

% --- Executes during object creation, after setting all properties.
function flow4_CreateFcn(hObject, eventdata, handles)
if ispc && isequal(get(hObject,'BackgroundColor'), ...
get(0,'defaultUicontrolBackgroundColor'))
    set(hObject,'BackgroundColor','white');
end

function flow5_Callback(hObject, eventdata, handles)

% --- Executes during object creation, after setting all properties.
function flow5_CreateFcn(hObject, eventdata, handles)
if ispc && isequal(get(hObject,'BackgroundColor'), ...
get(0,'defaultUicontrolBackgroundColor'))
    set(hObject,'BackgroundColor','white');
end

function flow6_Callback(hObject, eventdata, handles)

% --- Executes during object creation, after setting all properties.
function flow6_CreateFcn(hObject, eventdata, handles)
if ispc && isequal(get(hObject,'BackgroundColor'), ...
get(0,'defaultUicontrolBackgroundColor'))
    set(hObject,'BackgroundColor','white');
```

```
end

function flow7_Callback(hObject, eventdata, handles)

% --- Executes during object creation, after setting all properties.
function flow7_CreateFcn(hObject, eventdata, handles)
if ispc && isequal(get(hObject,'BackgroundColor'), ...
get(0,'defaultUicontrolBackgroundColor'))
    set(hObject,'BackgroundColor','white');
end

function flow8_Callback(hObject, eventdata, handles)

% --- Executes during object creation, after setting all properties.
function flow8_CreateFcn(hObject, eventdata, handles)
if ispc && isequal(get(hObject,'BackgroundColor'), ...
get(0,'defaultUicontrolBackgroundColor'))
    set(hObject,'BackgroundColor','white');
end

% --- Executes on selection change in gas1.
function gas1_Callback(hObject, eventdata, handles)

% --- Executes during object creation, after setting all properties.
function gas1_CreateFcn(hObject, eventdata, handles)
if ispc && isequal(get(hObject,'BackgroundColor'), ...
get(0,'defaultUicontrolBackgroundColor'))
    set(hObject,'BackgroundColor','white');
end
```

```
% --- Executes on selection change in gas2.
function gas2_Callback(hObject, eventdata, handles)

% --- Executes during object creation, after setting all properties.
function gas2_CreateFcn(hObject, eventdata, handles)
if ispc && isequal(get(hObject,'BackgroundColor'), ...
get(0,'defaultUicontrolBackgroundColor'))
    set(hObject,'BackgroundColor','white');
end

% --- Executes on selection change in gas3.
function gas3_Callback(hObject, eventdata, handles)

% --- Executes during object creation, after setting all properties.
function gas3_CreateFcn(hObject, eventdata, handles)
if ispc && isequal(get(hObject,'BackgroundColor'), ...
get(0,'defaultUicontrolBackgroundColor'))
    set(hObject,'BackgroundColor','white');
end

% --- Executes on selection change in gas4.
function gas4_Callback(hObject, eventdata, handles)

% --- Executes during object creation, after setting all properties.
function gas4_CreateFcn(hObject, eventdata, handles)
if ispc && isequal(get(hObject,'BackgroundColor'), ...
get(0,'defaultUicontrolBackgroundColor'))
    set(hObject,'BackgroundColor','white');
```

```
end

% --- Executes on selection change in gas5.
function gas5_Callback(hObject, eventdata, handles)

% --- Executes during object creation, after setting all properties.
function gas5_CreateFcn(hObject, eventdata, handles)
if ispc && isequal(get(hObject,'BackgroundColor'), ...
get(0,'defaultUicontrolBackgroundColor'))
    set(hObject,'BackgroundColor','white');
end

% --- Executes on selection change in gas6.
function gas6_Callback(hObject, eventdata, handles)

% --- Executes during object creation, after setting all properties.
function gas6_CreateFcn(hObject, eventdata, handles)
if ispc && isequal(get(hObject,'BackgroundColor'), ...
get(0,'defaultUicontrolBackgroundColor'))
    set(hObject,'BackgroundColor','white');
end

% --- Executes on selection change in gas7.
function gas7_Callback(hObject, eventdata, handles)

% --- Executes during object creation, after setting all properties.
function gas7_CreateFcn(hObject, eventdata, handles)
if ispc && isequal(get(hObject,'BackgroundColor'), ...
get(0,'defaultUicontrolBackgroundColor'))
```

```
    set(hObject,'BackgroundColor','white');
end

% --- Executes on selection change in gas8.
function gas8_Callback(hObject, eventdata, handles)

% --- Executes during object creation, after setting all properties.
function gas8_CreateFcn(hObject, eventdata, handles)
if ispc && isequal(get(hObject,'BackgroundColor'), ...
get(0,'defaultUicontrolBackgroundColor'))
    set(hObject,'BackgroundColor','white');
end
```

B.2 Function file for calculating binary diffusion coefficients

```
%%%%%%%%%%%%%%%%%%%%%%%%%%%%%%%%%%%%%%%%%%%%%%%%%%%%%%%%%%%%%%%%%%%%%%%%%%%%
%              CHAPMAN-ENSKOG DIFFUSION CALCULATION
%%%%%%%%%%%%%%%%%%%%%%%%%%%%%%%%%%%%%%%%%%%%%%%%%%%%%%%%%%%%%%%%%%%%%%%%%%%%
function Dij=ChapmanEnskog(T,P,Gas1,Gas2)
global sigma_H2O sigma_NH3 sigma_HCL sigma_SO2 sigma_H2S sigma_CH2Cl2...
    sigma_C2H5Cl sigma_C2H5OH sigma_C2H5C2H5O sigma_CH3CH3CO sigma_H2...
    sigma_He sigma_Ne sigma_Ar sigma_N2 sigma_O2 sigma_Air sigma_CO2...
    sigma_CCl4 sigma_CH4 sigma_C2H4 sigma_Xe sigma_Kr sigma_D2...
    sigma_Hg sigma_CO sigma_NO sigma_N2O...
    epsilon_H2O epsilon_NH3 epsilon_HCL epsilon_SO2 epsilon_H2S epsilon_CH2Cl2...
    epsilon_C2H5Cl epsilon_C2H5OH epsilon_C2H5C2H5O epsilon_CH3CH3CO epsilon_H2...
    epsilon_He epsilon_Ne epsilon_Ar epsilon_N2 epsilon_O2 epsilon_Air epsilon_CO2...
    epsilon_CCl4 epsilon_CH4 epsilon_C2H4 epsilon_Xe epsilon_Kr epsilon_D2...
```

```
    epsilon_Hg epsilon_CO epsilon_NO epsilon_N2O...
    M_H2O M_NH3 M_HCL M_SO2 M_H2S M_CH2Cl2...
    M_C2H5Cl M_C2H5OH M_C2H5C2H5O M_CH3CH3CO M_H2...
    M_He M_Ne M_Ar M_N2 M_O2 M_Air M_CO2...
    M_CCl4 M_CH4 M_C2H4 M_Xe M_Kr M_D2...
    M_Hg M_CO M_NO M_N2O

%% Label Input Arguments
G1=Gas1;
G2=Gas2;
sigma1=GasLibrary(horzcat('sigma_',G1));
sigma2=GasLibrary(horzcat('sigma_',G2));
epsilon1=GasLibrary(horzcat('epsilon_',G1));
epsilon2=GasLibrary(horzcat('epsilon_',G2));
M1=GasLibrary(horzcat('M_',G1));
M2=GasLibrary(horzcat('M_',G2));
%% Calculate Intermediates
sigmaAvg=0.5*(sigma1+sigma2);
epsAvg=epsilon1*epsilon2;
TS=T.*sqrt(1/epsAvg);

% Collision integral with N2.
omega=1.06036./(TS.^0.1561)+0.193./exp(0.47635*TS)...
    +1.03587./exp(1.52996*TS)+1.76474./exp(3.89411*TS);

%% Binary Diffusion Coefficient (cm^2/s)
Dij=(0.0018583./(omega.*P*sigmaAvg^2)).*sqrt(((1/M1)+(1/M2)).*T.^3);
```

B.3 Function file for calculating concentration

```
%%%%%%%%%%%%%%%%%%%%%%%%%%%%%%%%%%%%%%%%%%%%%%%%%%%%%%%%%%%%%%%%%%%%%%%%%%%%
%                    CONCENTRATION CALCULATION
%%%%%%%%%%%%%%%%%%%%%%%%%%%%%%%%%%%%%%%%%%%%%%%%%%%%%%%%%%%%%%%%%%%%%%%%%%%%
%{
Takes pressure, P, temperature, T, and variable number of molar flow
rates. Returns concentration, C and mole fraction, X, of each species.
%}
function [X C]=concentration(P,T,varargin)
Ru=8.31446;
p=P*1.01325e5;               % Pressure from atm to pascals.
n=length(varargin);
Ftotal=sum(cell2mat(varargin));
for i=1:n
   X(i)=varargin{i}/Ftotal;
   C(i)=X(i)*p/(Ru*T);
end
```

B.4 Function file for calculating Knudsen diffusion coefficient

```
%%%%%%%%%%%%%%%%%%%%%%%%%%%%%%%%%%%%%%%%%%%%%%%%%%%%%%%%%%%%%%%%%%%%%%%%%%%%
%              KNUDSEN DIFFUSION CALCULATION
%%%%%%%%%%%%%%%%%%%%%%%%%%%%%%%%%%%%%%%%%%%%%%%%%%%%%%%%%%%%%%%%%%%%%%%%%%%%
function DKn=Knudsen(T,rp,Gas)
global sigma_H2O sigma_NH3 sigma_HCL sigma_SO2 sigma_H2S sigma_CH2Cl2...
    sigma_C2H5Cl sigma_C2H5OH sigma_C2H5C2H5O sigma_CH3CH3CO sigma_H2...
    sigma_He sigma_Ne sigma_Ar sigma_N2 sigma_O2 sigma_Air sigma_CO2...
    sigma_CCl4 sigma_CH4 sigma_C2H4 sigma_Xe sigma_Kr sigma_D2...
    sigma_Hg sigma_CO sigma_NO sigma_N2O...
```

```
    epsilon_H2O epsilon_NH3 epsilon_HCL epsilon_SO2 epsilon_H2S epsilon_CH2Cl2...
    epsilon_C2H5Cl epsilon_C2H5OH epsilon_C2H5C2H5O epsilon_CH3CH3CO epsilon_H2...
    epsilon_He epsilon_Ne epsilon_Ar epsilon_N2 epsilon_O2 epsilon_Air epsilon_CO2...
    epsilon_CCl4 epsilon_CH4 epsilon_C2H4 epsilon_Xe epsilon_Kr epsilon_D2...
    epsilon_Hg epsilon_CO epsilon_NO epsilon_N2O...
    M_H2O M_NH3 M_HCL M_SO2 M_H2S M_CH2Cl2...
    M_C2H5Cl M_C2H5OH M_C2H5C2H5O M_CH3CH3CO M_H2...
    M_He M_Ne M_Ar M_N2 M_O2 M_Air M_CO2...
    M_CCl4 M_CH4 M_C2H4 M_Xe M_Kr M_D2...
    M_Hg M_CO M_NO M_N2O

%% Label Input Arguments
G1=Gas;
M1=GasLibrary(horzcat('M_',G1));

% Knudsen Diffusion Coefficient (cm^2/s)
DKn=(sqrt(T)*((2/3)*(rp)*sqrt(8*8.314e3/(pi*M1))))*(10^4);
```

B.5 Function file for calculating effective diffusion coefficient

```
%%%%%%%%%%%%%%%%%%%%%%%%%%%%%%%%%%%%%%%%%%%%%%%%%%%%%%%%%%%%%%%%%%%%%%%%%%%%
%              MULTICOMPONENT DIFFUSION COEFFICIENT
%%%%%%%%%%%%%%%%%%%%%%%%%%%%%%%%%%%%%%%%%%%%%%%%%%%%%%%%%%%%%%%%%%%%%%%%%%%%
%{
Uses the parallel pore model to calculate multicomponent diffusion
coefficients.
%}
function Deff=effectivediff(Q,phi,tau,rp,T,P,varargin)
global sigma_H2O sigma_NH3 sigma_HCL sigma_SO2 sigma_H2S sigma_CH2Cl2...
```

```
    sigma_C2H5Cl sigma_C2H5OH sigma_C2H5C2H5O sigma_CH3CH3CO sigma_H2...
    sigma_He sigma_Ne sigma_Ar sigma_N2 sigma_O2 sigma_Air sigma_CO2...
    sigma_CCl4 sigma_CH4 sigma_C2H4 sigma_Xe sigma_Kr sigma_D2...
    sigma_Hg sigma_CO sigma_NO sigma_N2O...
    epsilon_H2O epsilon_NH3 epsilon_HCL epsilon_SO2 epsilon_H2S epsilon_CH2Cl2...
    epsilon_C2H5Cl epsilon_C2H5OH epsilon_C2H5C2H5O epsilon_CH3CH3CO epsilon_H2...
    epsilon_He epsilon_Ne epsilon_Ar epsilon_N2 epsilon_O2 epsilon_Air epsilon_CO2...
    epsilon_CCl4 epsilon_CH4 epsilon_C2H4 epsilon_Xe epsilon_Kr epsilon_D2...
    epsilon_Hg epsilon_CO epsilon_NO epsilon_N2O...
    M_H2O M_NH3 M_HCL M_SO2 M_H2S M_CH2Cl2...
    M_C2H5Cl M_C2H5OH M_C2H5C2H5O M_CH3CH3CO M_H2...
    M_He M_Ne M_Ar M_N2 M_O2 M_Air M_CO2...
    M_CCl4 M_CH4 M_C2H4 M_Xe M_Kr M_D2...
    M_Hg M_CO M_NO M_N2O

%% Mole Fraction
n=length(varargin);
for i=1:n
    F(i)=molarflow(Q(i),P,T,varargin{i});
end
[X C]=conc(1,700,F);

for i=1:n
    M(i)=GasLibrary(horzcat('M_',varargin{i}));
    Mel(i)=X(i)*M(i);
end
Mavg=sum(Mel);

%% Diffusion Coefficients
```

```
% Knudsen.
for i=1:n
    DK(i)=Knudsen(T,rp,varargin{i});
end

% Binary.
for i=1:n
    for j=1:n
        if j~=i
            Dij(i,j)=ChapmanEnskog(T,P,varargin{i},varargin{j});
        end
    end
end

% Effective.
for i=1:n
    for j=1:n
        if j~=i
            H(j)=X(j)/Dij(i,j);
        end
    end
    Hsum=sum(H);
    Dm(i)=(1-X(i))/Hsum;
    clear Hsum H
    alpham(i)=1-sqrt(M(i)/Mavg);
    Deff(i)=(phi/tau)*(1/(((1-alpham(i)*X(i))/Dm(i))+(1/DK(i))));
end
```

B.6 Function file for calculating molar flow rate

```
%%%%%%%%%%%%%%%%%%%%%%%%%%%%%%%%%%%%%%%%%%%%%%%%%%%%%%%%%%%%%%%%%%%%%%%%%%%%
%                    MOLAR FLOW RATE CALCULATION
%%%%%%%%%%%%%%%%%%%%%%%%%%%%%%%%%%%%%%%%%%%%%%%%%%%%%%%%%%%%%%%%%%%%%%%%%%%%
%{
Takes flow rate, Q, of substance, pressure, P, and temperature, T.
Returns molar flow rate (mol/s).
%}
function F=molarflow(Q,P,T,Gas)
global sigma_H2O sigma_NH3 sigma_HCL sigma_SO2 sigma_H2S sigma_CH2Cl2...
    sigma_C2H5Cl sigma_C2H5OH sigma_C2H5C2H5O sigma_CH3CH3CO sigma_H2...
    sigma_He sigma_Ne sigma_Ar sigma_N2 sigma_O2 sigma_Air sigma_CO2...
    sigma_CCl4 sigma_CH4 sigma_C2H4 sigma_Xe sigma_Kr sigma_D2...
    sigma_Hg sigma_CO sigma_NO sigma_N2O...
    epsilon_H2O epsilon_NH3 epsilon_HCL epsilon_SO2 epsilon_H2S epsilon_CH2Cl2...
    epsilon_C2H5Cl epsilon_C2H5OH epsilon_C2H5C2H5O epsilon_CH3CH3CO epsilon_H2...
    epsilon_He epsilon_Ne epsilon_Ar epsilon_N2 epsilon_O2 epsilon_Air epsilon_CO2...
    epsilon_CCl4 epsilon_CH4 epsilon_C2H4 epsilon_Xe epsilon_Kr epsilon_D2...
    epsilon_Hg epsilon_CO epsilon_NO epsilon_N2O...
    M_H2O M_NH3 M_HCL M_SO2 M_H2S M_CH2Cl2...
    M_C2H5Cl M_C2H5OH M_C2H5C2H5O M_CH3CH3CO M_H2...
    M_He M_Ne M_Ar M_N2 M_O2 M_Air M_CO2...
    M_CCl4 M_CH4 M_C2H4 M_Xe M_Kr M_D2...
    M_Hg M_CO M_NO M_N2O
G1=Gas;
M1=eval(horzcat('M_',G1));
p=P*1.01325e5;              % Pressure from atm to pascals.
Ru=8.31446;
```

```
F=Q*p/(Ru*T);           % Molar flow (mol/s).
```

B.7 Library of Lennard-Jones parameters

```
%%%%%%%%%%%%%%%%%%%%%%%%%%%%%%%%%%%%%%%%%%%%%%%%%%%%%%%%%%%%%%%%%%%%%%%%%%%%
%                      Gas Properties Library
%%%%%%%%%%%%%%%%%%%%%%%%%%%%%%%%%%%%%%%%%%%%%%%%%%%%%%%%%%%%%%%%%%%%%%%%%%%%
function propertyvalue=GasLibrary(property)
global sigma_H2O sigma_NH3 sigma_HCL sigma_SO2 sigma_H2S sigma_CH2Cl2...
    sigma_C2H5Cl sigma_C2H5OH sigma_C2H5C2H5O sigma_CH3CH3CO sigma_H2...
    sigma_He sigma_Ne sigma_Ar sigma_N2 sigma_O2 sigma_Air sigma_CO2...
    sigma_CCl4 sigma_CH4 sigma_C2H4 sigma_Xe sigma_Kr sigma_D2...
    sigma_Hg sigma_CO sigma_NO sigma_N2O...
    epsilon_H2O epsilon_NH3 epsilon_HCL epsilon_SO2 epsilon_H2S epsilon_CH2Cl2...
    epsilon_C2H5Cl epsilon_C2H5OH epsilon_C2H5C2H5O epsilon_CH3CH3CO epsilon_H2...
    epsilon_He epsilon_Ne epsilon_Ar epsilon_N2 epsilon_O2 epsilon_Air epsilon_CO2...
    epsilon_CCl4 epsilon_CH4 epsilon_C2H4 epsilon_Xe epsilon_Kr epsilon_D2...
    epsilon_Hg epsilon_CO epsilon_NO epsilon_N2O...
    M_H2O M_NH3 M_HCL M_SO2 M_H2S M_CH2Cl2...
    M_C2H5Cl M_C2H5OH M_C2H5C2H5O M_CH3CH3CO M_H2...
    M_He M_Ne M_Ar M_N2 M_O2 M_Air M_CO2...
    M_CCl4 M_CH4 M_C2H4 M_Xe M_Kr M_D2...
    M_Hg M_CO M_NO M_N2O

%% Lennard-Jones Parameters
% Taken from Mason & Monchick 1962 "Transport Properties of Polar-Gas
% Mixtures".
sigma_H2O=2.71; sigma_NH3=3.15; sigma_HCL=3.36; sigma_SO2=4.04;
```

```
sigma_H2S=3.49; sigma_CH2Cl2=4.52; sigma_C2H5Cl=4.45; sigma_C2H5OH=4.31;
sigma_C2H5C2H5O=5.49; sigma_CH3CH3CO=4.50; sigma_H2=2.928; sigma_He=2.556;
sigma_Ne=2.789; sigma_Ar=3.418; sigma_N2=3.681; sigma_O2=3.433;
sigma_Air=3.617; sigma_CO2=3.996; sigma_CCl4=5.881; sigma_CH4=3.796;
sigma_C2H4=4.232;

epsilon_H2O=506; epsilon_NH3=358; epsilon_HCL=328; epsilon_SO2=347;
epsilon_H2S=343; epsilon_CH2Cl2=483; epsilon_C2H5Cl=423;
epsilon_C2H5OH=431; epsilon_C2H5C2H5O=362; epsilon_CH3CH3CO=549;
epsilon_H2=37; epsilon_He=10.22; epsilon_Ne=35.7; epsilon_Ar=124;
epsilon_N2=91.5; epsilon_O2=113; epsilon_Air=97; epsilon_CO2=190;
epsilon_CCl4=327; epsilon_CH4=144; epsilon_C2H4=205; % (eps/k)

% From Roncin 1969 "Intermolecular Potential Parameters of Some Electronic
% Excited States of Atoms and Molecules".
sigma_Xe=4.06; sigma_Kr=3.61; sigma_Hg=2.90;...
sigma_CO=3.59; sigma_NO=3.47; sigma_N2O=3.88;

epsilon_Xe=229; epsilon_Kr=190; epsilon_Hg=851;...
epsilon_CO=110; epsilon_NO=119; epsilon_N2O=220;

%% Molar Mass (g/mol)
M_H2O=18.015; M_NH3=17.0305; M_HCL=36.461; M_SO2=64.064;
M_H2S=34.081; M_CH2Cl2=84.933; M_C2H5Cl=64.514; M_C2H5OH=46.0684;
M_C2H5C2H5O=74.1216; M_CH3CH3CO=58.0791; M_H2=2.01588; M_He=4.002602;
M_Ne=20.1791; M_Ar=39.948; M_N2=28.0134; M_O2=31.9988;
M_Air=28.96; M_CO2=44.0095; M_CCl4=153.82; M_CH4=16.0425;
M_C2H4=28.0532;
```

```
M_Xe=131.293; M_Kr=83.798; M_Hg=200.59;...
M_CO=28.0101; M_NO=30.0061; M_N2O=44.0128;

propertyvalue=eval(property);
```